Plasma Physics Reports, Vol. 31, No. 7, 2005, pp. 529–553. Translated from Fizika Plazmy, Vol. 31, No. 7, 2005, pp. 579–603.

TOKAMAKS

Self-Organization of Plasma in Tokamaks

Yu. N. Dnestrovskij, A. Yu. Dnestrovskij, and S. E. Lysenko

Nuclear Fusion Institute, Russian Research Centre Kurchatov Institute, Moscow, 123182 Russia

Received March 22, 2004; in final form, September 2, 2004

Abstract—A review is given of the main ideas regarding self-organization of a tokamak plasma. The analysis begins with a simple model of canonical profiles that was proposed by Kadomtsev for a plasma column with a circular cross section. Kadomtsev's model is then generalized to a tokamak plasma with an arbitrary cross section in toroidal geometry. In the generalized model, the canonical profiles are determined by the minimum of the plasma energy functional under the additional condition that the total current is conserved. The Euler equation for the energy functional leads to a second-order differential equation for the canonical profile of the function $\mu = 1/q$. Transport models are constructed on the basis of a concept of critical gradients defined in terms of the canonical profiles. The structures of the heat and particle fluxes in the Ohmic heating regime and in the conventional L-mode are discussed. Examples of plasma self-organization in experiments are presented and are illustrated by the results of calculations based on the transport models developed. The expressions for the heat and particle fluxes are then generalized to regimes with improved confinement and with transport barriers. L–H transitions and approximate formulas for the transport barrier parameters are discussed in detail. Some unresolved problems are also discussed, namely, those concerning a description of the formation of internal transport barriers in terms of the canonical profile model. In the Appendix, the ranges of variations in the plasma parameters within which the temperature profiles remain stiff are considered. © *2005 Pleiades Publishing, Inc.*

1. INTRODUCTION

The strange property of plasma to conserve the shape of the spatial profiles of the temperature and pressure in response to external actions has been known for a long time. B. Coppi [1] was apparently the first to precisely formulate the idea of optimal, or "canonical," profiles of the plasma parameters. Now that a much better knowledge of plasma behavior has been gained, we can reformulate the profile consistency principle (PCP), proposed by Coppi [1], in the following manner: the spatial distributions of some plasma parameters in many regimes tend to have their shapes close to certain specific profiles, which are called canonical profiles. The evolution of the plasma from arbitrary initial distributions to canonical profiles is usually called relaxation. The physical meaning of the PCP is that the plasma behaves as if it "remembers" a canonical profile and "directs" the relaxation process in the "desired" way by appropriately changing the transport coefficients.

Adopting the PCP, we rule out many conventional concepts of the energy and particle transport. The energy and particle fluxes can be nonlinear functions of the gradients. The transport coefficients can be nonlocal functions of the plasma parameters and can depend on the distribution of the sources. Moreover, in the above formulation, the PCP itself raises more questions than it can answer, e.g.: What are the plasma parameters that obey the PCP? What is the shape of the canonical profiles? And what are the mechanisms that govern the relaxation rate?

It is often assumed that canonical profiles are determined by the extremum of a certain functional, such as the plasma energy [2–5], or the rate of entropy generation [6–7]. Another assumption is that canonical profiles can be determined from the instability conditions for different drift modes, such as the ion temperature gradient (ITG) mode, the electron temperature gradient (ETG) mode, and the trapped electron mode (TEM) [8–10]. It is not quite clear, however, what type the functional or the drift mode should be. But even if the type of the functional is chosen, there is no unique way to find the shape of the canonical profile. As a rule, the number of unknown functions involved is larger than the number of Euler equations; consequently, the canonical profile can only be determined uniquely by making additional assumptions.

The physical interpretation of the PCP also remains fairly uncertain. It is impossible to single out only one physical mechanism that governs the canonical profile shape and relaxation rate. It can only be supposed that the feedbacks between the instabilities occurring at different radii play an important role. Recently, J. Taylor [11] originated the new idea that the current filamentation, being a statistical process, can lead to the establishment of canonical profiles. The process of directed relaxation controlled by stochastic fluctuations is usually called self-organization.

In this study, we develop the ideas of B.B. Kadomtsev [3, 12] and of other authors [4–5] that the canonical profiles are determined by the minimum of the plasma energy functional under the additional condition that

1063-780X/05/3107-0529$26.00

the total current is conserved. This formulation of the problem implies that there are two unknown functions: one describing the poloidal magnetic field and one describing the plasma pressure. The problem is closed by the additional assumption that the canonical profiles of the plasma current and plasma pressure coincide. In this case, a unique solution to the problem of canonical profiles can be constructed by imposing reasonable boundary conditions.

A transport model based on canonical profiles was developed in our earlier papers [13–19]. In this model, canonical profiles are used to determine the critical gradients in the structure of the heat and particle fluxes under the assumption that the canonical profiles of the ion and electron temperatures are the same. If the temperature gradient exceeds a certain critical value, then the corresponding term in the expression for the heat flux is large. If the temperature gradient is less than its critical value, then this term equals zero. The particle flux is described in terms of the canonical pressure profile. The problem so formulated is suitable for describing Ohmically heated discharges and L-mode discharges.

In order to describe regimes of improved confinement, we introduce the concept of the second critical gradient. In Ohmic or L-mode discharges, the temperature gradient is usually larger than the first critical gradient but is smaller than the second critical gradient. If the temperature gradient in a certain region becomes larger than the second critical gradient, then the plasma in this region "forgets" the canonical profile and the corresponding term in the expressions for the heat and particle fluxes vanishes. This indicates that a transport barrier appears there. Within the remaining part of the cross section of the column, the plasma continues to remember the canonical profile and the structure of the heat and particle fluxes there does not change.

Note that the forgetting effect is analogous to the nonlinear Hooke's law of elasticity. When a solid body is stretched, the elastic force is proportional to extension until the plastic limit is overcome. When this happens, the elastic force decreases and the solid body forgets its original shape.

Since the transport model under consideration is phenomenological in essence, it does not unambiguously dictate the choice of the structure of the heat and particle fluxes. This choice can be justified *a posteriori*, by comparing the calculated results with the experimental data. However, there are a number of favorable factors that reduce possible large errors due to the poor choice of the structure of the fluxes. Thus, the final results of calculations do not depend radically on the shape of the canonical profile in the L-mode. The reason is that, in the L-mode, the temperature profile differs markedly from the canonical one. In addition, the transport model chosen for analysis is stiff because the transport coefficient in front of the difference between the temperature gradients and the critical gradient is large. Therefore, a twofold change in this transport coefficient leads merely to a 20–30% change in the global plasma parameters (such as the energy confinement time).

Our goal here is to construct the simplest possible model, i.e., a model that involves the minimum number of empirical parameters. An additional requirement is that, for a conventional L-mode discharge, the model should be linear in the temperature and density gradients.

At this point, we should say a few words about the use of other variational principles. In [6, 7], it was assumed that, in the relaxed state, the magnetic entropy S is time-independent, $dS/dt = 0$. The condition for this assumption to be consistent with the equilibrium Grad–Shafranov equation leads to a second-order differential equation that describes the toroidal current density and contains two arbitrary functions. The solution to this equation supplemented with Ohm's law determines the canonical profiles of the plasma current and electron temperature. For a fixed magnetic configuration, the pressure profile depends only on one parameter. In [6], the peakedness of the experimental profiles of the electron temperature T_e in the TCV tokamak was compared to that calculated numerically for a steady-state Ohmic regime. In [7], a comparison was made between the measured and calculated T_e profiles in an ECRH discharge. Note that the condition that the magnetic entropy be steady-state naturally leads to the PCP.

Tamano *et al.* [20] analyzed discharges in which the kinetic energy of toroidal plasma rotation is compared to the plasma thermal energy. They assumed that, during relaxation, the total energy of the plasma is conserved and only the relationship between its thermal and kinetic energies changes. Another assumption was that, in the relaxed state, the thermal energy of the plasma is minimum, i.e., the kinetic energy of its rotation is maximum. They constructed the Euler equation for the maximum kinetic energy under the condition that the total angular momentum of toroidal rotation and the number of particles are conserved. An analytic two-parameter solution to this equation relates the profiles of the plasma density and rotation velocity. When applied to the steady-state regimes with an internal transport barrier (ITB) in the DIII-D and JT-60U tokamaks, the formulas obtained in [20] produce reasonable results. Note that, in [6, 7], as well as in [20], no attempts were made to construct a transport model and to trace the evolution of the discharge parameters.

In the present paper, we review the main ideas about the self-organization of tokamak plasmas. In Section 2, we consider Kadomtsev's model of canonical profiles for a plasma cylinder with a circular cross section. In Section 3, we generalize the idea of canonical profiles to a tokamak plasma with an arbitrary cross section in toroidal geometry. In particular, we derive a second-order differential equation for the canonical profile of the function $\mu = 1/q$. In Section 4, we construct trans-

port models on the basis of the concept of critical gradients defined in terms of the canonical profiles. We analyze the structures of the heat and particle fluxes in Ohmic discharges and in conventional L-mode discharges. We also present examples of plasma self-organization in experiments and illustrate them by the calculations based on the set of transport equations obtained. In Section 5, we examine regimes with improved confinement and with transport barriers and discuss in detail the L–H transition, the conditions under which this transition occurs, and the approximate formulas for the parameters of the transport barrier. At the end of the section, we discuss some unresolved problems concerning a description of the ITB formation in terms of the canonical profile model. Finally, in Section 6, we summarize the main results of applying the idea of plasma self-organization to the description of transport processes. In the Appendix, we analyze the ranges of variations in the plasma parameters within which the temperature profiles remain stiff.

2. CANONICAL PROFILES FOR A CIRCULAR PLASMA CYLINDER

2.1. Euler Equation

Our main hypothesis is that, under the action of different instabilities, the plasma parameters will slowly and steadily relax to canonical profiles. Since the driving force for instabilities is the plasma energy, the shape of the canonical profiles is determined by the minimum of the plasma energy functional under the condition that the total current is conserved. If this condition is not imposed, then the minimum of the energy functional will be zero.

The toroidal magnetic field in a tokamak stabilizes large-scale MHD instabilities, which develop on characteristic time scales much shorter than the relaxation time. The plasma in turn has an insignificant impact on the toroidal magnetic field. Consequently, the energy of this field can be excluded from the energy reservoir of the transport processes in the plasma. As a result, the energy functional for a plasma column with a circular cross section assumes, in cylindrical geometry, the following form:

$$F = 2\pi\int_0^a [B_\theta^2/8\pi + p/(\gamma-1) + \lambda j]r dr. \quad (1)$$

Here, r and θ are the radial and poloidal coordinates, a is the minor plasma radius, $B_\theta = B_\theta(r)$ is the poloidal magnetic field, $p = p(r)$ is the plasma pressure, $j = j(r)$ is the current density, λ is the Lagrange multiplier, and γ is the adiabatic index.

We assume that, in the vicinity of the minimum of the functional F, the functions B_θ/r, p, and j are mutually interdependent, so the function $\mu = 1/q$ can be used as an independent variable. This assumption implies that

$$p = p(\mu), \quad j = j(\mu), \quad B_\theta/r = (B_0/R)\mu, \quad (2)$$

where B_0 is the toroidal magnetic field and R is the major radius of the plasma column. For a plasma cylinder with a circular cross section, we have $q = rB_0/RB_\theta$.

For convenience in varying the functional F, we introduce the magnetic field potential $\psi = \psi(r)$ through the relationship $B_\theta = (1/(2\pi R))d\psi/dr$. We denote the variation of ψ by $\delta\psi$ and assume that $\delta\psi(0) = 0$ and $\delta\psi(a) = 0$. We also set

$$\delta p = (dp/d\mu)\delta\mu, \quad \delta j = (dj/d\mu)\delta\mu, \quad \delta\mu = (1/(2\pi B_0 r))d/dr(\delta\psi). \quad (3)$$

We can now vary the functional F and determine its minimum by equating the variation to zero:

$$\delta F = -2\pi R/B_0\int_0^a \delta\psi(d\Phi/dr)dr = 0, \quad (4)$$

where

$$\Phi = B_0^2 r^2\mu/(4\pi R^2) + 1/(\gamma-1)dp/d\mu + \lambda dj/d\mu. \quad (5)$$

Formula (4) yields the Euler equation for the functional F:

$$d\Phi/dr = 0. \quad (6)$$

We also take into account the fact that the functions j and μ are related by Maxwell's equation

$$j = B_0/(\mu_{00}R)1/rd/dr(r^2\mu), \quad (7)$$

where μ_{00} is the vacuum magnetic permeability. As a result, we have arrived at a set of two equations (Eqs. (6) and (7)) for the three functions μ, j, and p. As the third equation, we will use the profile consistency principle; in other words, we assume that the current and pressure profiles are the same:

$$j(\mu)/j_0 = p(\mu)/p_0, \quad j_0 = j(\mu_0), \quad p_0 = p(\mu_0), \quad \mu_0 = \mu(0). \quad (8)$$

Using Eq. (7) and relationships (8), we eliminate the current density and pressure in Eq. (6) and obtain the Euler equation for the function μ

$$d/dr[(B_0\mu_{00}/4\pi R)(r^2/\mu')d/dr(\mu^2 + \lambda_1 d\mu/d(r^2))] = 0, \quad (9)$$

where $\mu' = d\mu/dr$ and λ_1 is the renormalized Lagrange multiplier. In what follows, the solutions to Eq. (9) will be called canonical profiles and will be denoted by $\mu_c = \mu_c(r)$.

2.2. Boundary Conditions

Equation (9) is a third-order differential equation and contains the parameter λ_1. Consequently, in order

to single out the unique solution to this equation, we need four boundary conditions. The symmetry condition at the magnetic axis $r = 0$ implies that $\mu_c'(0) = 0$. The requirement for the total current to be conserved gives $\mu_c(a) = \mu_a = 0.2IR/(a^2B_0)$. These conditions are written in practical units: the current is in MA, the length is in m, and the magnetic field is in T. In a paper by Kadomtsev [3], the remaining two conditions were chosen to be $\mu_c(0) = \mu_0 \sim 1$ and $\mu_c(r) \longrightarrow 0$ as $r \longrightarrow \infty$. This set of four boundary conditions can thus be written as

$$\begin{gathered}\mu_c'(0) = 0,\\ \mu_c(0) = \mu_0 \sim 1,\\ \mu_c(a) = \mu_a = 0.2IR/(a^2B_0),\\ \mu_c(r) \longrightarrow 0 \quad \text{as} \quad r \longrightarrow \infty.\end{gathered} \tag{10}$$

Integrating Eq. (9) yields

$$(r^2/\mu')d/dr[\mu^2 + \lambda_1 d\mu/d(r^2)] = C_1. \tag{11}$$

In order to determine the constant C_1, we consider how the solution to Eq. (11) behaves in the vicinity of the magnetic axis $r = 0$. The first two of conditions (10) lead us to the following representation of the solution in this vicinity:

$$\mu = \mu_0(1 + \alpha_2 r^2 + \alpha_4 r^4 + \ldots). \tag{12}$$

With solutions of type (12), the left-hand side of Eq. (11) approaches zero as $r \longrightarrow 0$. This gives $C_1 = 0$. Hence, the Euler equation for $\mu_c(r)$ has the form

$$d/dr[\mu^2 + \lambda_1 d\mu/d(r^2)] = 0. \tag{13}$$

For the solutions to Eq. (13), the first of boundary conditions (10) is satisfied automatically. We are thus left with the remaining three conditions, which play an essential role in further analysis:

$$\begin{gathered}\mu_c(0) = \mu_0 \sim 1,\\ \mu_c(a) = \mu_a = 0.2IR/(a^2B_0),\\ \mu_c(r) \longrightarrow 0 \quad \text{as} \quad r \longrightarrow \infty.\end{gathered} \tag{14}$$

The solution to Eq. (13) that satisfies boundary conditions (14) was obtained by Kadomtsev in [3]. Hereafter, we will denote this solution by the superscript K:

$$\mu_c^{\mathrm{K}} = \mu_0/(1 + r^2/a_j^2), \tag{15}$$

where

$$\begin{aligned}a_j &= a[\mu_a/(\mu_0 - \mu_a)]^{1/2},\\ \lambda_1 &= \mu_0 a_j^2 = \mu_a a^2(1 - \mu_a/\mu_0)^{-1}.\end{aligned} \tag{16}$$

Function (15) is usually called the Kadomtsev canonical profile. Using Maxwell's equation (7) and relationships (8), one can easily find the Kadomtsev canonical profiles of the current and pressure:

$$j_c^{\mathrm{K}} = j_0(\mu_c^{\mathrm{K}}/\mu_0)^2, \quad p_c^{\mathrm{K}} = p_0(\mu_c^{\mathrm{K}}/\mu_0)^2. \tag{17}$$

Using the obtained solution to Eq. (13) with boundary conditions (14), we can now easily reformulate the last of these boundary conditions by replacing it with a boundary condition at the plasma surface. To do this, it is convenient to introduce the surface impedance

$$X = i_a/2\mu_a, \tag{18}$$

where the dimensionless current i is given by Eq. (7) and has the form

$$i = 1/rd/dr(r^2\mu), \quad i_a = i(a). \tag{19}$$

Using expressions (15) and (19), we can readily find the impedance for the Kadomtsev canonical profile:

$$X^{\mathrm{K}} = \mu_a/\mu_0. \tag{20}$$

Hence, in the Kadomtsev problem, we can use the following boundary conditions, which are equivalent to conditions (14):

$$\begin{gathered}\mu_c(0) = \mu_0 \sim 1,\\ \mu_c(a) = \mu_a = 0.2IR/(a^2B_0),\\ X_c = X^{\mathrm{K}} = \mu_a/\mu_0.\end{gathered} \tag{21}$$

Boundary conditions (14), one of which is imposed at infinity, can naturally be called "soft," since they incompletely reflect the physical processes at the plasma surface. Now, we consider a plasma exposed to a strong external action that changes its boundary temperature, density, and edge radiation loss. Such action can be provided, e.g., by pulsed gas puffing, impurity seeding, peripheral injection of hydrogen pellets, and surface current drive. It is obvious that boundary conditions (14) or (21) do not reflect such processes. On the other hand, many experiments show that the plasma responds rapidly over its entire cross section to the peripheral action. It is apparent that the boundary conditions for the canonical profiles should be somehow related to the boundary conditions for the actual plasma parameters. As an example of such a relation, we can mention the "rigid" boundary conditions proposed in [21]:

$$\begin{gathered}\mu_c(a) = \mu(a),\\ \mu_c'(a) = \mu'(a),\\ \mu_c''(a) = \mu''(a).\end{gathered} \tag{22}$$

Here, $\mu(r)$ is the solution to the set of transport equations for the actual (rather than canonical) profiles of the temperature, density, and poloidal magnetic field. All boundary conditions (22), in contrast to conditions (21), are imposed at the plasma surface. Such a problem is usually called the Cauchy problem. Boundary conditions (22) have the following physical meaning: it is actually assumed that the canonical profiles $\mu_c(r)$ in a

thin boundary layer satisfy both Maxwell's equation (7) and Ohm's law. This follows from the fact that the function $\mu(r)$ satisfies the equation and the law over the entire plasma cross section and from the fact that the first and the second derivatives of $\mu_c(r)$ and $\mu(r)$ at the plasma boundary are equal.

It is an easy matter to determine how the parameter λ_1 is related to the function μ and its derivatives at the plasma boundary. To do this, we consider Eq. (13) at the boundary. It is legitimate to do so because boundary conditions (22) contain the second derivative of this function. After simple manipulations, we obtain

$$\lambda_1 = 4\mu_a a^2(1 - a\mu''(a)/\mu'(a)). \quad (23)$$

Like conditions (21), boundary conditions (22) can be written in terms of the surface impedances:

$$\begin{aligned} &\mu_c(a) = \mu_a, \\ &X_c = X, \\ &Y_c = Y. \end{aligned} \quad (24)$$

Here, the impedance X is determined by formula (18) and Y is the second-order surface impedance, which is defined as

$$Y = i_a'/4\mu_a'. \quad (25)$$

For the Kadomtsev problem, we have $Y^K = \mu_a/\mu_0$.

The third of boundary conditions (24) contains the second derivative of the function $\mu(r)$, i.e., the third spatial derivative of the function $\psi(r)$ at the boundary of the plasma column. In transport models, however, the function ψ is usually described by a second-order parabolic differential equation, so it is incorrect to solve for the third derivative of this function. The problem can be made regular by using Ohm's law

$$j = \sigma E \quad (26)$$

(where σ is the plasma conductivity) and the assumption that the current diffusion in the edge plasma is quasi-steady,

$$dE/dr(r = a) = 0 \quad (27)$$

(where E is the toroidal electric field). This assumption is valid for a low edge electron temperature and slow variations in the total current. By virtue of Eqs. (26) and (27), we have

$$j_a'/j_a = i_a'/i_a \approx \sigma_a'/\sigma_a,$$

which leads to the following approximate expression for the second-order impedance:

$$Y = i_a'/(4\mu_a') \approx (\sigma_a'/\sigma_a)(i_a/4\mu_a'). \quad (28)$$

This expression does not contain third-order derivatives and can be used in boundary conditions (24).

The question naturally arises about the ranges of applicability of soft boundary conditions (21) and rigid boundary conditions (24). A comparison with the experimental data [21] shows that the applicability ranges are distinguished by the inequality

$$Y < Y^K = \mu_a/\mu_0. \quad (29)$$

Using approximate expression (28), we can rewrite this inequality as

$$(\sigma_a'/\sigma_a)(i_a/4\mu_a') < \mu_a/\mu_0. \quad (30)$$

Hence, the rigid boundary conditions should be used when the electron temperature gradient in the edge plasma is sufficiently small, $\sigma_a'/\sigma_a \sim 3/2(T_a'/T_a)$.

3. CANONICAL PROFILES FOR A TOROIDAL PLASMA WITH AN ARBITRARY CROSS SECTION

3.1. Euler Equation

We assume that the equilibrium problem (i.e., the Grad–Shafranov equation for the poloidal magnetic flux function ψ) with prescribed boundary conditions has been solved for given distributions of the currents and pressure in a toroidal plasma column with an arbitrary cross section. The solution ψ = const to this problem determines the magnetic surfaces.

We denote by r, z, and φ polar coordinates whose axis coincides with the symmetry axis of the torus. We also introduce the natural coordinates ρ, θ, and ζ such that ρ is the coordinate of the magnetic surface in terms of the toroidal magnetic field flux Φ,

$$\pi\rho^2 B_0 = \Phi, \quad \Phi = \int_S \mathbf{B}\,d\mathbf{S}, \quad (31)$$

with B_0 being the vacuum toroidal magnetic field at the center of the chamber, θ is the poloidal angle, and $\zeta = r\varphi$. The plasma surface is determined by the equation $\rho = \rho_{max} = a_{eff}$, where a_{eff} is the effective plasma radius. For a low pressure and large aspect ratio $A = R/a$, we have $a_{eff} = \sqrt{k}a$, where a is the minor plasma radius and $k = b/a$ is the ellipticity (elongation) of the plasma cross section (the ratio between its major and minor semiaxes). We denote by the angle brackets $\langle \ldots \rangle$ the operation of averaging over a magnetic surface,

$$\langle f \rangle = 2\pi/V' \int_0^{2\pi} \sqrt{g} f\,d\theta, \quad (32)$$

where V' is the plasma volume and g is the determinant of the metric tensor in the polar coordinates,

$$\sqrt{g} = r\frac{D(r, z)}{D(\rho, \vartheta)}. \quad (33)$$

We assume that, as in the case of a circular plasma cylinder, the canonical profiles are determined by the minimum of the free energy functional,

$$F = \int_V (B_\theta^2/8\pi + p/(\gamma-1))dV + \lambda \int_S j_\varphi dS, \qquad (34)$$

where the last term reflects the conservation of the total plasma current $I_p = \int_S j_\varphi dS$.

In order to reduce the problem of minimizing functional (34) to a one-dimensional one, we utilize profile consistency conditions (8), where

$$\mu = \partial\psi/\partial\Phi = 1/(2\pi B_0\rho)\partial\psi/\partial\rho. \qquad (35)$$

The equation μ = const determines the magnetic surfaces. Conditions (8) should be satisfied for the whole class of functions in which functional (34) is to be minimized, but they are of course not necessary for the actual current and pressure profiles.

Functional (34) can now be represented as a sum of one-dimensional integrals,

$$F = F_B + F_p + F_j. \qquad (36)$$

Here, [22]

$$F_B = \int_V B_\theta^2/8\pi dV = 1/(8\pi 4\pi^2 R^2)\int_0^{\rho_{max}} V'(\partial\psi/\partial\rho)^2 G d\rho, \qquad (37)$$

$$F_p = \int_0^{\rho_{max}} V' p/(\gamma-1) d\rho, \qquad (38)$$

$$F_j = \lambda_{11}\int_0^{\rho_{max}} V' j_\varphi d\rho, \qquad (39)$$

where λ_{11} is the renormalized Lagrange multiplier,

$$V'(\rho) \equiv \partial V/\partial\rho = 2\pi\int_0^{2\pi}\sqrt{g}\,d\theta, \qquad (40)$$

$B_\theta = (|\nabla\rho|/2\pi r)\partial\psi/\partial\rho$, j_φ is the averaged current density, V' and

$$G = R^2\langle(\nabla\rho)^2/r^2\rangle, \quad G_2 = GV' \qquad (41)$$

are the metric coefficients, and G is a dimensionless coefficient. From Maxwell's equation we obtain

$$j_\varphi = (B_0/(\mu_{00}V'R))\partial/\partial\rho(V'G\rho\mu). \qquad (42)$$

For a circular plasma cylinder, we have $V \longrightarrow 2\pi^2 R\rho^2$, $V' \longrightarrow 4\pi^2 R\rho$, $G \longrightarrow 1$, and $G_2 \longrightarrow 4\pi^2 R\rho$.

We vary the functional F with respect to the potential ψ, treating the latter as an independent variable. As a result, we obtain

$$\delta F = -\int_0^{\rho_{max}} \delta\psi\partial/\partial\rho\{V'/\rho(B_0^2\rho^2/(4\pi R^2))G\mu + \partial p/\partial\mu/(\gamma-1) + \lambda_{11}\partial j_\varphi/\partial\mu)\}d\rho = 0. \qquad (43)$$

This yields the following Euler equation for functional (34):

$$\partial/\partial\rho\{V'/(\rho\mu')[\rho^2 G\partial\mu^2/\partial\rho + (\lambda_1/2)\partial/\partial\rho((1/V')\partial/\partial\rho(G_2\rho\mu))]\} = 0. \qquad (44)$$

In deriving this equation, we used Eq. (42), introduced the notation $\mu' = \partial\mu/\partial\rho$, and again renormalized the Lagrange multiplier. As in the case of a circular plasma cylinder, Euler equation (44) is a third-order differential equation containing the parameter λ_1. Integrating Eq. (44) yields a second-order equation with an arbitrary constant C:

$$\rho^2 G\partial\mu^2/\partial\rho + (\lambda_1/2)\partial/\partial\rho((1/V')\partial/\partial\rho(G_2\rho\mu)) = C\rho\mu'/V'. \qquad (45)$$

Equation (45) was first derived in [18]. It corresponds to Eq. (11) for a circular plasma cylinder. Consequently, the constant C can be found in essentially the same manner, by using expansion (12) for the solution near the magnetic axis $\rho = 0$ and by comparing the terms in Eq. (45). It is also necessary to use the expansions of the metric coefficients V' and G:

$$V' = V''(0)\rho(1 + O(\rho^2)), \quad G(\rho) = 1 + G'(0)\rho + 1/2G''(0)\rho^2. \qquad (46)$$

Substituting expansions (12) and (46) into Eq. (45) and equating the coefficients of the same powers of ρ, we obtain

$$3G'(0) = 0 \quad (\rho^0), \qquad (47)$$

$$(\lambda_1/2)(8\alpha_2 G(0) + G''(0)) = 2\alpha_2 C/V''(0) \quad (\rho^1). \qquad (48)$$

For a circular plasma cylinder, we have G = const = 1, which gives $G'(0) = 0$ and $G''(0) = 0$. Numerical calculations show that these equalities remain also valid for a toroidal plasma column. As a result, Eq. (47) is satisfied automatically and Eq. (48) is homogeneous in α_2. The value of the constant C should be chosen so as to satisfy the condition $\alpha_2 \neq 0$. This requires that the following equality be met:

$$C = 4(\lambda_1/2)G(0)V''(0). \qquad (49)$$

We substitute this equality into Eq. (45) and take into account expansions (46) to arrive at the final equation for the canonical profile [18]:

$$L[\mu] \equiv \rho^2 G \partial\mu^2/\partial\rho + (\lambda_1/2)\partial/\partial\rho((1/V')\partial/\partial\rho(V'G\rho\mu)) - 4(\lambda_1/2)V''(0)\rho\mu'/V' = 0. \quad (50)$$

For a circular plasma cylinder, Eq. (50) takes the form

$$\rho^2 \partial\mu^2/\partial\rho + (\lambda_1/2)(-\partial\mu/\partial\rho + \rho\partial^2\mu/\partial\rho^2) = 0, \quad (51)$$

which is equivalent to Eq. (13).

3.2. Boundary Conditions

Let us consider whether Kadomtsev boundary conditions (14) can be applied to a toroidal plasma with an arbitrary cross section. In this case, the plasma region with closed magnetic surfaces is bounded by a separatrix, so the radial coordinate ρ cannot be defined on a semi-infinite interval. This is why the third of boundary conditions (14) should be reformulated to refer to the plasma surface. As in the case of a circular plasma cylinder, this can be conveniently done by introducing the first-order surface impedance for a toroidal plasma column:

$$X = i_S/(2G_S\mu_S), \quad (52)$$

where $i = i(\rho)$ is the dimensionless current,

$$i = (1/V')\partial/\partial\rho(V'G\rho\mu), \quad (53)$$

and the subscript S stands for the values of the quantities at the plasma surface.

We assume that the boundary conditions for a toroidal plasma column with an arbitrary cross section have the same form as boundary conditions (21), which single out the special Kadomtsev solutions for a circular cylindrical plasma:

$$\mu_c(0) = \mu_0 \sim 1, \quad \mu_c(\rho_{max}) = \mu_S, \quad X_c = \mu_S/\mu_0, \quad (54)$$

where μ_S is the value of the function μ at the plasma surface S that was obtained from the solution to the equilibrium problem.

In order to determine the Lagrange multiplier λ_1, we rewrite Eq. (50) in terms of dimensionless current (53),

$$\rho^2 G\partial\mu^2/\partial\rho + (\lambda_1/2)i' - 4(\lambda_1/2)V''(0)\rho\mu'/V' = 0. \quad (55)$$

Taking the limit $\rho \longrightarrow \rho_{max}$ in Eq. (55), we arrive at the following expression relating the parameter λ_1 to the boundary values of the functions μ and i and their derivatives:

$$\lambda \equiv \lambda_1/(\rho_{max}^2\mu_S) = \frac{G_S}{\xi(1-Y)}, \quad (56)$$

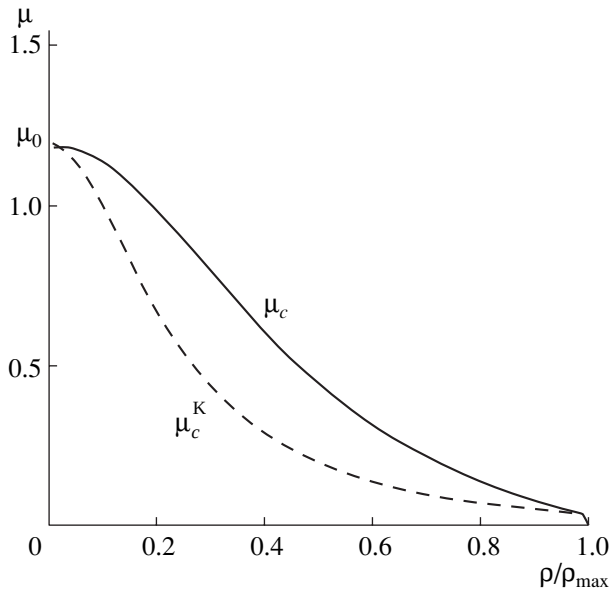

Fig. 1. Canonical profile $\mu_c(\rho)$ for a toroidal plasma with the aspect ratio $A = 1.5$ for $q_S = 7$, the elongation and triangularity being $k = 1.6$ and $\delta = 0.3$, respectively. The dashed curve shows the Kadomtsev canonical profile $\mu_c^K(\rho)$.

where

$$Y = i_S'/(4\xi\mu_S') \quad (57)$$

is the second-order impedance and $\xi = \rho_{max}V''(0)/V_S'$, $(\xi \geq 1)$.

Let us say a few words about the numerical algorithm for solving the problem given by Eqs. (50) and (54). With soft boundary conditions (54), the right-hand side of relationship (56) is undefined because the quantity Y is unknown. Accordingly, the quantity λ is unknown too. Boundary conditions (54), however, determine the values μ_{cS} and $(\partial\mu_c/\partial\rho)_S$. Consequently, the boundary-value problem for Eq. (50) can be solved by applying a shooting method that assumes integration from the plasma surface to the plasma center and by adjusting the parameter λ_1 so as to fit the first of boundary conditions (54). Figure 1 shows the canonical profile $\mu_c(\rho)$ calculated for a small-aspect-ratio tokamak ($A = 1.5$) and the Kadomtsev canonical profile $\mu_c^K(\rho)$ calculated for $q_S = 7$. We can see that the canonical profile $\mu_c(\rho)$ is markedly wider than the Kadomtsev profile $\mu_c^K(\rho)$. As the aspect ratio increases, the canonical profile becomes narrower and approaches the Kadomtsev profile, which is independent of A.

With rigid boundary conditions (24), namely,

$$\mu_c(\rho_{max}) = \mu_S, \quad X_c(\rho_{max}) = X_S, \quad Y_c(\rho_{max}) = Y_S, \quad (58)$$

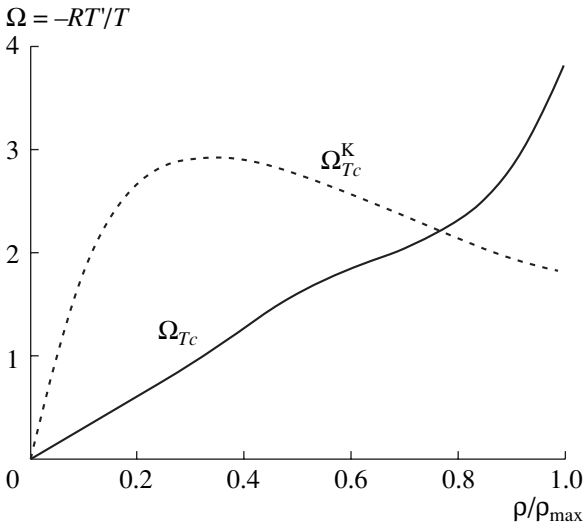

Fig. 2. Profiles of the critical temperature gradient $\Omega_{Tc} = -(R/T_c)dT_c/d\rho$ (solid curve) and the Kadomtsev critical gradient $\Omega^{\mathrm{K}}_{Tc} = -(R/T^{\mathrm{K}}_c)dT^{\mathrm{K}}_c/d\rho$ (dashed curve) for a tokamak plasma with the same parameters as in Fig. 1.

the quantity Y is known and the parameter λ_1 is determined from formula (56). In this case, Eq. (50) is defined and thus can be readily solved by direct numerical integration, because the functions μ_{cS} and $(\partial\mu_c/\partial\rho)_S$ are given in boundary conditions (58).

3.3. Difficulties in Numerical Solution of the Above Problems

If the plasma surface S coincides with the separatrix, then the value of q at this surface is formally equal to infinity and the value μ_S vanishes there, so a question arises about the physical meaning of boundary conditions (54) and (58) and, accordingly, about the necessity of their regularization. Note, however, that expressions (42) and (53) for the current density and definition (52) of the impedance contain not the function μ but the product $G\mu$, which is regular and does not vanish at the separatrix. Consequently, the second of boundary conditions (54) and the first of boundary conditions (58) should be regularized by equating to its boundary value the product $G\mu$ rather than the function μ. In practice, however, the required regularization is performed in solving the equilibrium equation. If the Grad–Shafranov equation is solved in finite differences, then the separatrix containing corner points is approximated by a smooth closed curve at which the value of q is bounded. In the ASTRA code, the Grad–Shafranov equation is solved by the method of moments, in which the plasma boundary, too, is approximated by a smooth curve. This numerical regularization turns out to be sufficient for boundary conditions (54) and (58) to be used without any corrections.

Real difficulties associated with Eq. (50) arise in the vicinity of the magnetic axis $\rho = 0$. The reason is that the functions $V'(\rho)$ and $G(\rho)$, as well as their derivatives, are calculated by solving the two-dimensional equilibrium equation and thereby inevitably contain errors. We determined the constant C in Eq. (45) by using the condition $G''(0) = 0$. In differentiating the function $G(\rho)$ numerically, however, this condition can be violated. As a result, in numerical integration of Eq. (50) from the surface of the plasma to its center, the boundary symmetry condition at the magnetic axis, $\mu_c'(0) = 0$, may fail to hold.

In order to overcome this difficulty, it is necessary to return from Eq. (50) to Eq. (45), which contains two parameters, λ_1 and C, and to supplement boundary conditions (54) with the condition $\mu_c'(0) = 0$. The problem in question can then be solved by employing a shooting method that assumes integration from the plasma surface inward and by adjusting these two parameters so as to satisfy two boundary conditions at the magnetic axis, $\mu_c(0) = \mu_0$ and $\mu_c'(0) = 0$. In this way, formula (49) can be used as an initial approximation. Of course, errors in calculating the function $G''(\rho)$ also will show up in the solution obtained by using a two-parameter algorithm. For instance, the function $\mu_c''(\rho)$ can falsely change sign in the vicinity of the magnetic axis $\rho = 0$. In this case, the function $\mu_c(\rho)$ has to be smoothed to a greater extent by additional numerical procedures.

3.4. Temperature and Density Canonical Profiles and Critical Gradients

Knowing the canonical profile $\mu_c(\rho)$, we can construct the canonical profile of the temperature $T_c(\rho)$ in the following way: In a relaxed quasi-steady state, the profiles of the current and electron temperature are close to their canonical profiles,

$$j_\varphi(\rho) \approx j_c(\rho), \quad T_e(\rho) \approx T_c(\rho). \tag{59}$$

On the other hand, the profiles $j_\varphi(\rho)$ and $T_e(\rho)$ are related by Ohm's law,

$$j_\varphi(\rho) \sim T_e^{3/2}(\rho). \tag{60}$$

By virtue of the consistency of profiles (8), as well as of profiles (59) and (60), we have

$$p_c(\rho) = n_c(\rho)T_c(\rho) \sim j_c(\rho) \sim T_e^{3/2} \sim T_c^{3/2}, \tag{61}$$

which yields the relationships

$$T_c \sim j_c^{2/3}, \quad n_c \sim T_c^{1/2} \sim j_c^{1/3}. \tag{62}$$

We introduce the dimensionless critical gradients of the temperature, density, and pressure through the formulas

$$\begin{aligned} \Omega_{Tc} &= -RT_c'/T_c, \quad \Omega_{nc} = -Rn_c'/n_c, \\ \Omega_{pc} &= -Rp_c'/p_c \quad (f' = \partial f/\partial\rho), \end{aligned} \tag{63}$$

and, by virtue of relationships (62), obtain

$$\Omega_{Tc} = 2/3\Omega_j, \quad \Omega_{nc} = 1/3\Omega_j, \quad \Omega_{pc} = \Omega_j, \qquad (64)$$

where

$$\Omega_j = -Rj_c'/j_c. \qquad (65)$$

Figure 2 shows the profile of the critical temperature gradient Ω_{Tc} for a small-aspect-ratio tokamak ($A = 1.5$) and also the Kadomtsev canonical profile of the critical temperature gradient Ω_{Tc}^{K} for $q_S = 7$, which can be calculated from solution (15)–(17). We can see that, in the gradient zone $0.2 < \rho/\rho_{max} < 0.8$, these two profiles deviate substantially from one another. Figure 3 shows the profiles of the critical temperature gradient calculated for three different values of the aspect ratio, $A = 1.5$, 3, and 5, and for $k = 1.6$, $\delta = 0.3$, and $q_S = 7$. It is seen that, in the gradient zone, the critical gradients computed for $A = 1.5$ and 5 differ by a factor of 8–10. Figure 4 presents the values of the critical temperature gradient Ω_{Tc} at mid-radius, $\rho/\rho_{max} = 0.5$, calculated for many shots on seven different tokamaks. The parameters of the shots were chosen from the ITER database [23]. As an independent argument, we use the value of Ω_{Tc}^{K} at mid-radius divided by the vertical elongation k of the plasma; the argument so defined is equal to $Aq/(k(q + 4))$. We can see that the values of the critical temperature gradient at mid-radius vary over a wide range, $1 < \Omega_{Tc} < 12$. In subsequent sections, the critical gradients are used in the expressions for the heat and particle fluxes in the transport equations.

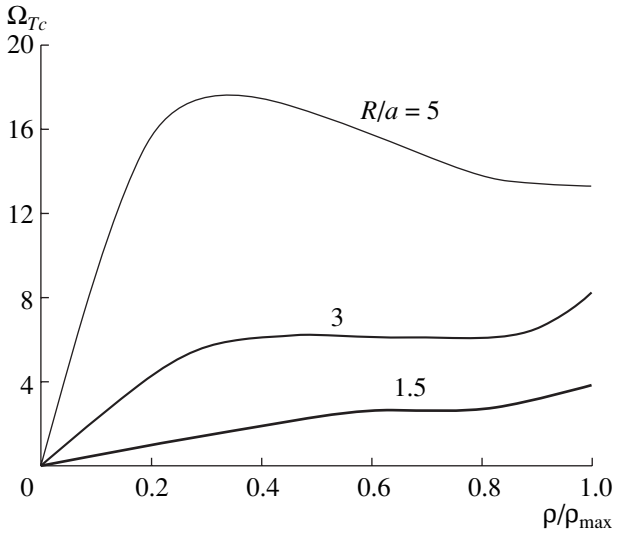

Fig. 3. Profiles of the critical temperature gradient for three different values of the aspect ratio, $A = 1.5$, 3, and 5, and for $k = 1.6$, $\delta = 0.3$, and $q_S = 7$.

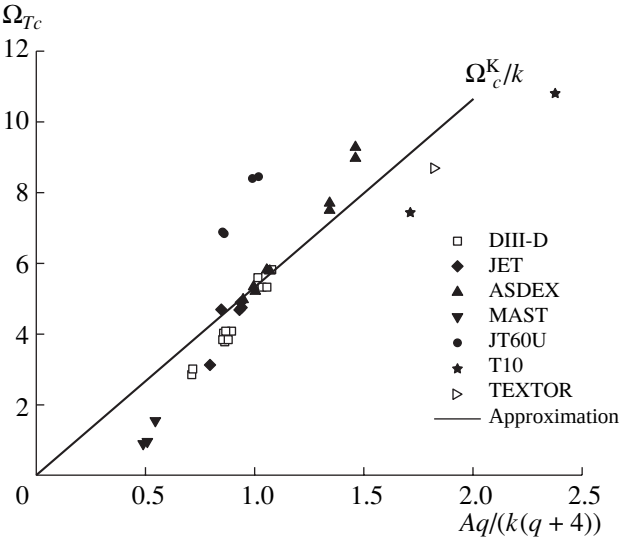

Fig. 4. Critical temperature gradient at mid-radius, $\rho = \rho_{max}/2$, calculated for a set of shots on seven different tokamaks. The straight line is the approximating linear function that is determined by the Kadomtsev canonical profile and is divided by the elongation k of the plasma cross section.

4. SET OF TRANSPORT EQUATIONS

4.1. Transport Equations

To simplify the analysis, we assume that the vacuum toroidal magnetic field does not change with time. Under this assumption, the set of transport equations for the plasma density n, the electron and ion temperatures T_e and T_i, and the potential ψ of the poloidal magnetic field in the above natural coordinates has the form [22]

$$\partial n/\partial t + \mathrm{div}_\rho(G_1\Gamma_n) = S_n, \qquad (66)$$

$$3/2\partial(nT_k)/\partial t + \mathrm{div}_\rho(G_1\Gamma_k) = P_k, \qquad (67)$$

$$\sigma_\parallel\partial\psi/\partial t = 1/(\mu_{00}B_0\rho)\partial/\partial\rho(V'G\partial\psi/\partial\rho). \qquad (68)$$

Here, Γ_n is the particle flux, Γ_k ($k = e, i$) are the electron and ion heat fluxes, S_n is the particle source term, P_k are the heat source terms and the ion–electron energy exchange terms,

$$\mathrm{div}_\rho(.) = (1/V')\partial/\partial\rho(V'(.)) \qquad (69)$$

is the radial component of the operator of divergence, $\sigma_\parallel$ is the longitudinal plasma conductivity, and $G_1 = \langle(\nabla\rho)^2\rangle$ is the metric coefficient. The metric coefficients V' and G were defined above by formulas (40) and (41).

Equations (66) and (67) describe the conservation of the number of particles and heat conservation, respectively. Equation (68) represents Ohm's law. In order to close the set of equations (66)–(68), it is necessary to determine the relationships between the fluxes and the unknown functions n, T_k, and ψ.

4.2. Heat and Particle Fluxes in Ohmic and L-mode Discharges

The structures of the heat and particle fluxes were chosen based on the following experimental facts:

(i) In Ohmic and L-mode discharges, the profiles of the electron and ion temperatures T_e and T_i, as well as the profiles of the plasma pressure $p = n(T_e + T_i)$, are conserved when the plasma is exposed to external actions. The profile of the plasma density n is more sensitive to the experimental conditions.

(ii) In a steady state, the profiles of the temperatures and pressure are close to their canonical profiles.

(iii) The heat pinch, if it ever exists, is very small.

Hence, the structure of the fluxes should be such that the dominant terms in the expressions for the fluxes lead to the relaxation of the electron and ion temperatures and plasma pressure to canonical profiles. This can be conveniently achieved by using critical gradients (63). If the relative temperature and pressure gradients are larger than the critical gradients, then the fluxes should increase considerably; in this case, the profiles will be close to the canonical ones. If the relative gradients are smaller than the critical gradients, then the flux associated with the canonical profiles should vanish by virtue of the smallness of the heat pinch. Supplementing these conditions with the requirement for the fluxes to depend linearly on the temperature and density gradients, we can almost unambiguously determine the structure of the heat fluxes. As a result, the electron and ion heat fluxes (which will be denoted by the subscripts e and i, respectively) have the form

$$\begin{aligned} -\Gamma_{e,i} &= -\kappa_{e,i}(T_{e,i}/R)(\Omega_{Te,Ti} - \Omega_{Tc}) \\ &\times H(\Omega_{Te,Ti} - \Omega_{Tc}) + \kappa_{0e,0i}\partial T_{e,i}/\partial\rho - 3/2T_{e,i}\Gamma_n, \end{aligned} \tag{70}$$

where $H(x)$ is the Heaviside step function, defined as $H(x) = 1$ for $x > 0$ and $H(x) = 0$ for $x < 0$.

An unambiguous expression for the particle flux is still lacking. The steady states, as well as transient processes occurring during pulsed gas puffing or during the injection of hydrogen pellets, can be described by using the following simple expression for the particle flux:

$$\begin{aligned} -\Gamma_n &= -\Gamma_{nn} + D_0\partial n/\partial\rho - nv_{\text{neo}}, \\ \Gamma_{nn} &= -D_n n/R(\Omega_n - \Omega_{nc}), \end{aligned} \tag{71a}$$

where $\Omega_n = -R(\partial n/\partial\rho)/n$ and nv_{neo} is the Ware pinch. However, in order to describe the transient processes that occur during plasma heating, it is necessary to utilize an additional "off-diagonal" term. The form of this term can be chosen with allowance for the conservation of the pressure profile,

$$-\Gamma_{np} = -D_p n/R(\Omega_p - \Omega_{pc}), \tag{71b}$$

so we can write

$$-\Gamma_n = -(\Gamma_{nn} + \Gamma_{np}) + D_0\partial n/\partial\rho. \tag{71c}$$

Here,

$$\begin{aligned} \Omega_{Te,Ti} &= -R(\partial T_{e,i}/\partial\rho)/T_{e,i}, \\ \Omega_p &= -R(\partial p/\partial\rho)/p, \quad \Omega_p = \Omega_n + \Omega_T, \\ \Omega_T &= -R(\partial(T_e + T_i)/\partial\rho)/(T_e + T_i)), \end{aligned} \tag{72}$$

and Ω_{Tc}, Ω_{nc}, and Ω_{pc} are the critical gradients given by formulas (63). Expressions (71a)–(71c) for the particle flux do not contain the Heaviside function. This indicates that, under the condition $\Omega_n < \Omega_{nc}$ or $\Omega_p < \Omega_{pc}$, a particle pinch appears. The second term in expression (70) accounts for the "background" heat flux. It contains both neoclassical fluxes and possible turbulent fluxes, which are independent of the canonical profiles. The third term in expression (70) accounts for the convective heat flux driven by the particle flux. Expressions (71a)–(71c) for the particle flux have a similar structure.

Note that Eqs. (66)–(68) and expressions (70) and (71) for the fluxes have a paradoxical property. In the previous sections, the canonical profiles to which the plasma relaxes were obtained for the parameters of the poloidal magnetic field μ_c and j_c. At the same time, transport equation (68) for ψ does not contain canonical profiles and the conductivity $\sigma_\parallel$ is normal (i.e., classical or neoclassical). In contrast, expressions (70) and (71) for the heat and particle fluxes are largely dominated by the terms with the turbulent fluxes, i.e., those containing the critical gradients Ω_{Tc} and Ω_{pc}. Consequently, during the evolution of the temperatures and density, the functions μ and j relax to their canonical profiles μ_c and j_c through the influence of the normal conductivity, which depends on the electron temperature.

4.3. Transport Coefficients

The heat transport coefficients, $\kappa_{e,i}$ and $\kappa_{0e,0i}$, and particle transport coefficients, $D_{n,p}$ and D_0, determine the relaxation rate; they have to be found from a comparison of calculations with experiment. The ratio $\kappa_{e,i}/\kappa_{0e,0i}$ is usually large and lies in the range $\kappa_{e,i}/\kappa_{0e,0i} = 6$–$15$. This indicates that the set of equations (66)–(68) is stiff because the parameter in front of the difference $\Omega_{Te,Ti} - \Omega_{Tc}$ is large. The diffusion coefficients $D_{n,p}$ are usually several times lower than the coefficients $\kappa_{e,i}$, and little is yet known about the coefficient D_0.

We will describe the coefficients κ by the expression adopted in [16, 19]:

$$\begin{aligned} \kappa_{e,i} &= \alpha_{e,i}/M(1/A)^{3/4}q(\rho_{\max}/2)q_{\text{cyl}}(\rho_{\max}) \\ &\times T_{e,i}^{1/2}(\rho_{\max}/4)\bar{n}/B(3/R)^{1/4}. \end{aligned} \tag{73}$$

Here, it is assumed that the coefficients $\kappa_{e,i}$ are independent of ρ. Expression (73) is written in the following practical units: $\kappa_{e,i}$ are in 10^{19} m^{-1} s^{-1}, $\alpha_e = 3.5$, $\alpha_i = 5$,

M is the relative mass of an ion, the temperatures $T_{e,i}$ are in keV, the chord-averaged plasma density $\bar{n}$ is in 10^{19} m^{-3}, the magnetic field B is in T, and the major plasma radius R is in m. For moderate-aspect-ratio tokamaks, we have $A = R/a = 3$–5 and $\kappa_{e,i} \sim 5$–15. For devices with a small aspect ratio A and weak magnetic field B (spherical tokamaks), we have $\kappa_{e,i} \sim 20$–30.

The coefficients κ_0 can be estimated from the expression

$$\kappa_{0e,0i} = C_0 T_{e,i}^{1/2}(\rho)\bar{n}/(BR^{1/4}), \qquad (74)$$

where $C_0 = 2$–3. Finally, the approximate values of the coefficients $D_{n,p}$ can be deduced from the estimate

$$D_n = (0.1\text{–}0.2)\kappa_{e,i} \quad D_p = (0.05\text{–}0.1)\kappa_{e,i}, \qquad (75)$$

where the coefficients $\kappa_{e,i}$ are given by formula (73). Note that formulas (73)–(75) satisfy the invariance conditions for a quasineutral plasma [24].

For discharges with on-axis heating, the dominant term in expression (70) for the heat flux is the first term, which contains the product $\kappa_{e,i}(\Omega_{Te,Ti} - \Omega_{Tc})$. It is this term that is responsible for the conservation (stiffness) of the temperature profile under changes of the total deposited power, plasma density, and boundary temperature. When the power is mainly deposited in the edge plasma (and, accordingly, the deposited power profile is hollow), the temperature profile may lose its stiffness because of the presence of the Heaviside function in the expression for the heat flux. In the Appendix, this point will be considered in more detail.

4.4. Structure of the Complete Transport Model

The structure of a complete model for describing transport processes in a tokamak is illustrated in Fig. 5. The model consists of three parts. The first part is represented by the set of transport equations for the electron and ion temperatures T_e and T_i, plasma density n, function μ, and current density j. If the values of these parameters and the shape of the plasma column at a certain time are prescribed, then the geometry of the magnetic surfaces and the values of the coordinate ρ and of the required metric coefficients V', G, and G_1 are determined by solving the Grad–Shafranov equation in the second part of the model. Finally, in the third part of the model, the functions μ_c and j_c and the critical gradients are found by solving Eqs. (45) or (50) for the canonical profiles. The evolution of the plasma parameters is calculated by repeating this procedure as many times as necessary.

We stress that, in this model, the canonical profiles (i.e., the final profiles to which the plasma tends to relax) change during relaxation. The relaxation rate, however, is much faster than the rate of change of the canonical profiles; consequently, the actual profiles of the plasma parameters sooner or later will approach their canonical profiles. Because of the presence of energy and particle sources, and because of the difference in the boundary conditions, the actual profiles will not exactly coincide with the canonical profiles.

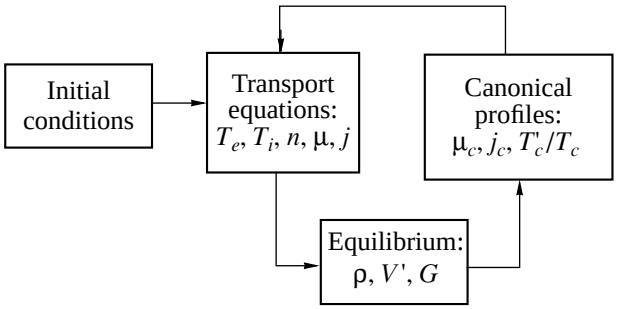

Fig. 5. Structure of the complete transport model.

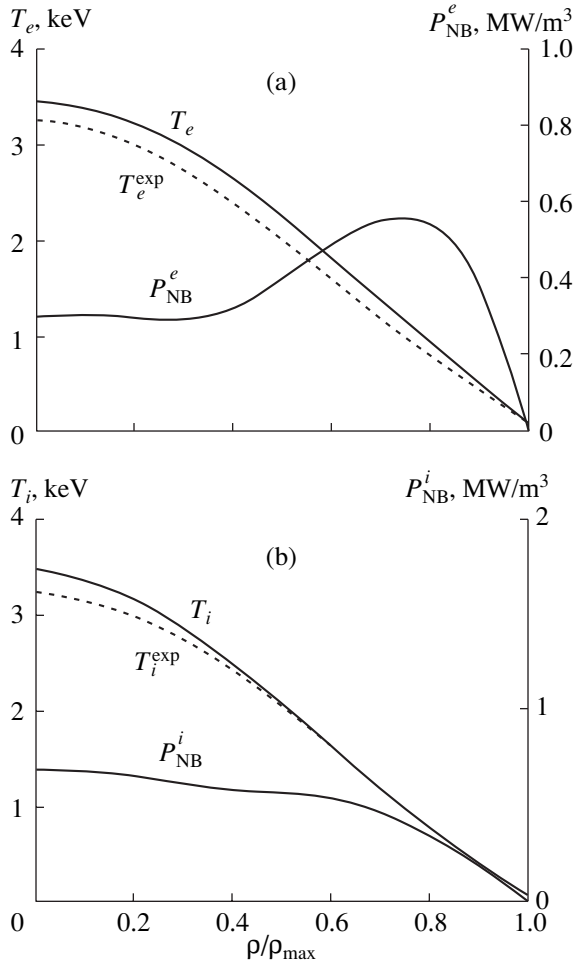

Fig. 6. Experimental and calculated profiles of the (a) electron and (b) ion temperatures for DIII-D shot no. 71 384 with a high density ($\bar{n} = 9.6 \times 10^{19}$ m^{-3}), a high NBI power ($P_{NB} = 14$ MW), a moderate boundary value of q ($q_S = 3$), and a low triangularity ($\delta = 0.16$). Also shown are the calculated profiles of the power deposited in the electrons (P^e_{NB}) and the ions (P^i_{NB}).

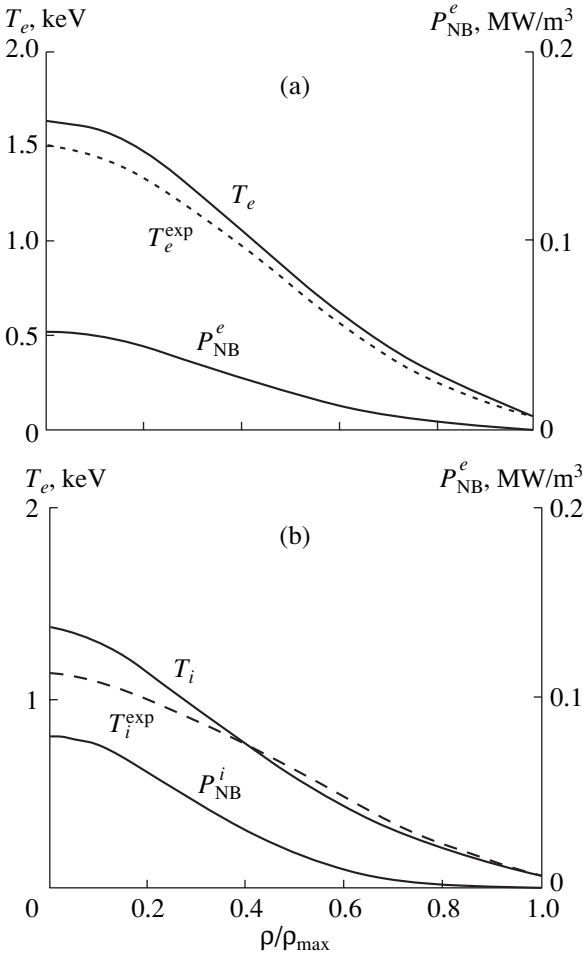

Fig. 7. The same as in Fig. 6, but for DIII-D shot no. 78 283 with a low density ($\bar{n} = 1.2 \times 10^{19}$ m^{-3}), a low NBI power ($P_{NB} = 0.46$ MW), a large boundary value of q ($q_S \sim 12$), and a high triangularity ($\delta = 0.6$).

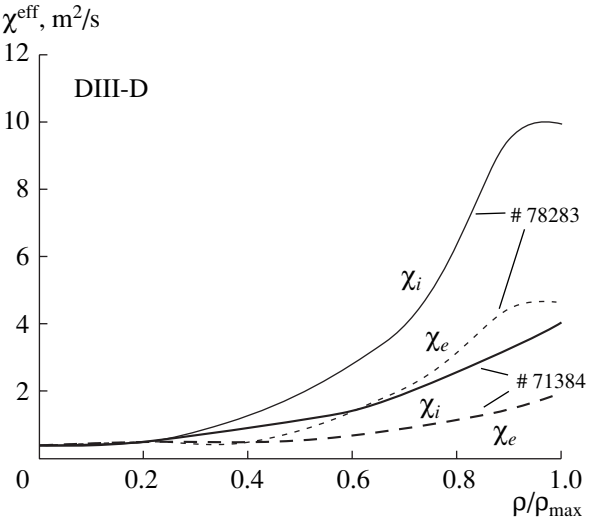

Fig. 8. Profiles of the effective thermal diffusivity of the electrons and ions, χ_e and χ_i, for the shots illustrated in Figs. 6 and 7.

4.5. Examples

The next four figures exemplify the results obtained by numerically solving Eqs. (67) and (68) with heat fluxes (70). In order to simplify the problem, we did not integrate Eq. (66) for the plasma density but instead used experimental density profiles. The calculated results were compared to the ITER database [25]. Figures 6a and 6b show the measured and calculated profiles of the electron and ion temperatures, $T_{e,i}$ and $T^{exp}_{e,i}$ for DIII-D shot no. 71384. The characteristic features of this shot are a high chord-averaged plasma density, $\bar{n} = 9.6$; a high power of neutral beam injection (NBI), $P_{NB} \sim 14$ MW; and a moderate boundary value of the parameter q, $q_S = 3.7$, the elongation and triangularity also being moderate ($k = 1.6$ and $\delta = 0.16$). The profiles of the power deposited in the electrons and ions that are shown in Figs. 6a and 6b were also taken from the ITER database. Since the plasma density is high, the neutral beam does not penetrate deep into the plasma, so the profile of the power deposited in the electrons is peaked at the plasma edge.

Figures 7a and 7b show the same profiles but for DIII-D shot no. 78 283. In this shot, the plasma density and NBI power are both low, $\bar{n} = 1.2$ and $P_{NB} \sim 0.46$ MW, while the q_S value and triangularity are large, $q_S \sim 12$ and $\delta \sim 0.6$. From Figs. 6 and 7, we can see that, although the parameters of the two shots are very different, the model reliably describes the experiment. It should be emphasized that the model does not contain any adjustable parameters. In order to make better estimates of the reliability of the simulation results, it is also necessary to take into account the following factors:

(i) The experimental errors in measuring the electron and ion temperatures are difficult to estimate from the ITER database because it typically contains smoothed data and does not provide direct information about the measurement errors.

(ii) In the ITER database, the profiles of the NBI power deposited in the plasma were obtained from complicated computations carried out by the investigators of the discharges with allowance for the geometry of neutral beams, the tokamak geometry, a large number of beams in tokamaks (e.g., more than ten beams in the JT-60U device), multispecies composition of the beams, losses of hot ions that follow "bad" trajectories and their losses due to the secondary charge exchange with cold neutrals, etc. Since the error in such involved calculations of the deposited power is difficult to estimate, it is not, as a rule, included in the database. In addition, it is impossible to check the calculated results because the required information is lacking.

It has become common practice to quantitatively characterize heat transport in terms of the so-called

effective thermal diffusivity,

$$\chi_{e,i}^{\text{eff}} = -\Gamma_{e,i}/(n\partial T_{e,i}/\partial\rho). \quad (76)$$

Figure 8 shows the profiles of $\chi_{e,i}^{\text{eff}}$ for both of the shots in question. We can see that, for both shots, $\chi^{\text{eff}} \sim 0.4$–$0.6$ m^2/s in the central plasma region ($\rho/\rho_{\max} < 0.3$). In the gradient zone ($0.3 < \rho/\rho_{\max} < 0.8$), the effective thermal conductivity χ^{eff} increases monotonically toward the plasma edge, where it reaches values of $\chi^{\text{eff}} \sim 4$–8 m^2/s at a low plasma density and values of $\chi^{\text{eff}} \sim 2$–4 m^2/s at a high density. In other tokamaks, the thermal conductivity χ^{eff} in the L-mode discharges is observed to exhibit similar behavior.

Up to this point, we have compared calculation and experiment only for one tokamak. A comparison made for many devices with different plasma geometries is illustrated in Fig. 9, which presents the measured and calculated values of the relative electron temperature gradient, $\Omega_{Te}^{\text{exp}} = -(R/T_e^{\text{exp}})\partial T_e^{\text{exp}}/\partial\rho$ and $\Omega_{Te} = -(R/T_e)\partial T_e/\partial\rho$, at mid-radius, $\rho = \rho_{\max}/2$. For one of the ASDEX-U shots, a typical experimental error is shown [26]. This error is seen to be fairly large because, in calculating Ω_{Te}^{exp}, we had to differentiate the experimental data. Nevertheless, Fig. 9 shows that the calculated temperature gradients, too, satisfactorily agree with the measured ones.

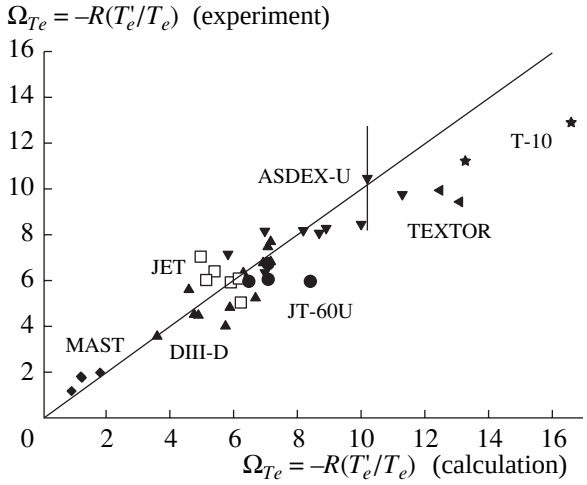

Fig. 9. Comparison between the experimental and calculated values of the relative electron temperature gradient at midradius for a set of shots on seven different tokamaks. The vertical bar shows the measurement error for one of the shots.

5. SET OF TRANSPORT EQUATIONS FOR IMPROVED CONFINEMENT REGIMES

5.1. Regimes of Improved Confinement

By improved confinement regimes we will mean those during which transport barriers form. A regime with a transport barrier in the edge plasma—a so-called edge transport barrier (ETB)—is usually referred to as the H-mode. During the L–H transition, transport coefficients inside the barrier decrease by a factor of 5–10 and, outside the barrier, they decrease by a factor of 1.5–2. A transport barrier can form in the plasma interior (ITB formation). A special name for the regime with an ITB is still lacking. Inside the ITB, transport coefficients usually decrease severalfold.

In order to describe regimes of improved confinement in the canonical profile model, we introduce the concept of the second critical gradient. Experiments show that this gradient exists for the plasma pressure profile. If the pressure gradient in a certain plasma region is larger than the second critical gradient, then the plasma in this region undergoes a bifurcation to a new state, which is accompanied by the formation of transport barriers. In this case, the plasma behaves as if it has forgotten the canonical profile within the barrier.

During the discharge evolution, a barrier forms not immediately after the required power is switched on but with a certain time delay, when the pressure gradient has become larger than the second critical gradient. The time delay depends on the extent to which the deposited power exceeds a certain threshold power. If this extent is small, the barrier can build up after a significant time delay.

In the H-mode, ETBs form simultaneously for the electron and ion temperatures and plasma density, presumably because of a strong coupling between the ions and electrons when the latter have a low temperature. As for ITBs, they develop differently in different tokamaks. For instance, in the TFTR tokamak, the existence of an ITB was confirmed only for the ion temperature and plasma density (iITB and nITB, respectively), whereas the electron ITB (eITB) was not revealed. In other tokamaks, an ITB for the electron temperature also formed. When the heating power is sufficiently high, ITBs can build up for all three main transport parameters: the electron and ion temperatures and plasma density. It was established that the iITB, eITB, and nITB occur in the same place, which, however, can vary with time. In some cases, two ITBs for the ion temperature were observed. It was also found that an internal and an edge transport barrier may exist simultaneously. In this case, it is common to speak of the H-mode with an ITB.

5.2. Heat and Particle Fluxes in Improved Confinement Regimes

The fact that barriers can exist separately for the electron and ion heat transport channels necessitates a proper reformulation of the transport model. We assume that the second critical gradients exist separately for the electron and ion pressures, $p_e = nT_e$ and $p_i = nT_i$. We also assume that the canonical profiles of

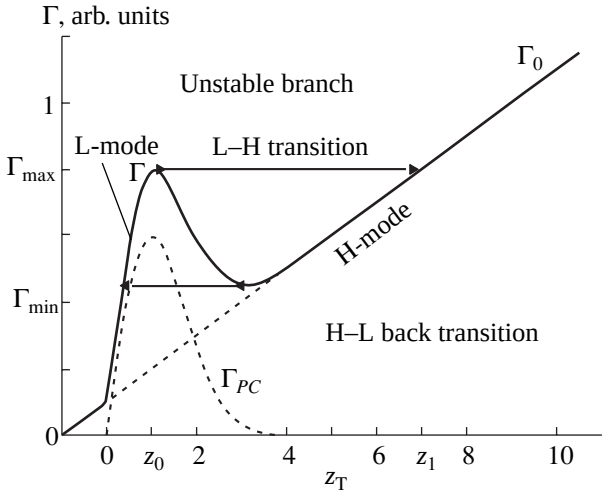

Fig. 10. Dependence of the heat fluxes Γ_{PC}, Γ_0, and $\Gamma = \Gamma_{PC} + \Gamma_0$ on the deviation z_T of the temperature profile from the critical one. The range $\Gamma > \Gamma_{\max}$ corresponds to the L–H transition, and the range $\Gamma < \Gamma_{\min}$ corresponds to the H–L back transition.

the partial electron and ion pressures, p_{ec} and p_{ic}, coincide with canonical profile (61) of the total pressure p_c.

We introduce the deviations of the partial pressure profiles from the canonical profiles through the relationship

$$z_{pk} = (\rho_{\max}/(A\rho))(\Omega_{pk} - \Omega_{pc}) \quad (k = e, i), \tag{77}$$

where

$$\Omega_{pk} = -R\,p_k'/p_k \tag{78}$$

and the critical gradient Ω_{pc} is defined in formulas (63). In relationship (77), we use the normalizing factor $\rho_{\max}/\rho$ in order for the deviations z_{pk} not to vanish at the magnetic axis $\rho = 0$. We suppose that a transport barrier forms in a certain plasma region where deviation (77) exceeds the second critical gradient z_{0k},

$$|z_{pk}| > z_{0k}. \tag{79}$$

Here, $z_{0k} = z_{0k}(\rho)$ are positive functions that should be determined by comparing the calculated results to the experimental data. The functions $z_{0k}(\rho)$ may be related to the profile of the function $q(\rho)$, but this relationship has not yet been established. Below, we will say a few words about this point.

Let us introduce the "forgetting" factor,

$$F_k = \exp(-z_{pk}^2/2z_{0k}^2). \tag{80}$$

We note that $F_k \approx 1$ inside the region in which the plasma forgets the canonical pressure profile (below, such a region will be referred to as the forgetting zone, for brevity) and $F_k \ll 1$ outside this region. Inside the forgetting zone, the first terms in expressions (70), (71a), and (71c) for the fluxes should be small. This indicates that the electron and ion heat fluxes and the particle flux can now be written as

$$\begin{aligned} -\Gamma_{e,i} &= -\kappa_{e,i}(T_{e,i}/R)(\Omega_{Te,Ti} - \Omega_{Tc}) \\ &\times H(\Omega_{Te,Ti} - \Omega_{Tc})F_{e,i} + \kappa_{0e,0i}\partial T_{e,i}/\partial\rho \\ &+ 3/2\,T_{e,i}\Gamma_n, \end{aligned} \tag{81}$$

$$-\Gamma_n = -(\Gamma_{nn} + \Gamma_{np})F_eF_i + D_0\partial n/\partial\rho - n\nu_{\text{neo}}. \tag{82}$$

Here, in accordance with experiment, we assume that the transport barrier for the density appears together with barriers for the electron and/or ion heat transport.

Let us consider how expression (81) for the heat fluxes depends on the temperature gradients. For simplicity, we omit the subscripts *e* and *i*, as well as the convective term, and denote the first and second terms in expression (81) by Γ_{PC} (with the subscript *PC* being an abbreviation of "profile consistency") and Γ_0,

$$\Gamma_{PC} = \kappa(T/R)(\Omega_T - \Omega_{Tc})H(\Omega_T - \Omega_{Tc})F, \tag{83}$$

$$\Gamma_0 = -\kappa_0\partial T/\partial\rho. \tag{84}$$

We also assume that the density profile coincides with its canonical profile. As a result, we obtain

$$z_p = z_T = (\rho_{\max}/\rho)(\Omega_T - \Omega_{Tc})/A, \tag{85}$$

and arrive at the following expression for the heat flux:

$$\begin{aligned} \Gamma &= \Gamma_{PC} + \Gamma_0 = \kappa(T/R)(\rho/\rho_{\max})z_T \\ &\times \exp(-z_T^2/2z_0^2)H(z_T) + \kappa_0(C_1z_T + C_2), \end{aligned} \tag{86}$$

where the functions $C_1 = \rho T/(\rho_{\max}R)$ and $C_2 = -T_c'T/T_c$ are independent of the temperature gradient. As an example, Fig. 10 shows the dependence of the fluxes Γ, Γ_{PC}, and Γ_0 on the deviation z_T at the plasma boundary $\rho = \rho_{\max}$. We can see that the flux Γ depends on z_T nonmonotonically: it has a maximum near the point $z_T = z_0$ and a minimum in the range $z_T > z_0$. Within the interval between the maximum and minimum, the derivative $d\Gamma/dz_T$ is negative, so the corresponding quasi-steady solution to heat conduction equation (67) is unstable. In the initial stage, when the total deposited power is low ($z_T < z_0$), the flux Γ is less than $\Gamma(z_0) = \Gamma_{\max}$ and the plasma evolves along the left branch, corresponding to the L-mode. If the total deposited power P_{tot} increases, then, at a certain time at which it becomes equal to the threshold power ($P_{\text{tot}} = P_{\text{thr}}$), the flux Γ reaches its maximum value $\Gamma_{\max}$. At this time, the solution makes a discontinuous transition from the left to the right branch (Fig. 10), the deviation z_T increases in a jumplike manner from z_0 to a value $z_1 \gg z_0$, and the temperature gradient in the vicinity of the magnetic surface $\rho_{\max}$ increases sharply. This corresponds to a transition to the H-mode and to the formation of a temperature pedestal at the plasma edge. We also see that, in the model adopted, the plasma exhibits a hysteresis effect with respect to H–L and L–H transitions. As the deposited

power decreases, the transition from the H-mode back to the L-mode occurs at a power lower than its threshold value, $P_{tot} < P_{thr}$, when the flux decreases to its minimum value, $\Gamma = \Gamma_{min}$ (Fig. 10). The formation of an ITB is accompanied by a similar process.

5.3. Approximate Analytic Criterion for the L–H Transition

Hence, during the L–H transition, a transport barrier appears at the plasma edge. The qualitative behavior of the temperature profiles and effective thermal diffusivity (76) (in which the electron and ion heat fluxes are denoted by Γ) in the L- and H-modes is illustrated in Figs. 11a and 11b, where T_L and T_H are the temperature profiles in the L- and H-modes, T_c is the canonical temperature profile, and χ_L^{eff} and χ_H^{eff} are the effective thermal diffusivities in the L- and H-modes. In the L-mode, the deviation z_T (see expression (85)) of T_L from T_c in the outer part of plasma column is large because the profile $T(\rho)$ is more peaked than the canonical profile $T_c(\rho)$ and the boundary temperature $T(\rho_{max})$ in the experiment is low. Because of the large deviation z_T in the outer part of plasma column, the flux Γ_{PC} is large there and the effective thermal diffusivity χ^{eff} is high. During the L–H transition, a narrow transport barrier (the forgetting zone) builds up near the plasma boundary and, in the remaining region of plasma column, the temperature profile $T(\rho)$ approaches the canonical profile $T_c(\rho)$ and the deviation z_T decreases. As a result, the effective thermal diffusivity decreases both inside and outside the transport barrier. Inside the barrier, the thermal diffusivity χ_H^{eff} is four to ten times lower than χ_L^{eff} and $\Gamma_{PC} = 0$. On the temperature profile $T(\rho)$, there is a pedestal with the temperature T_{ped}, which takes on very different values depending on the discharge conditions: it varies from $T_{ped} \sim 150$ eV in MAST to 7 keV in JET. In the plasma core, the ratio $\chi_L^{eff}/\chi_H^{eff}$ is typically equal to 1.5–2.

Since the transport barrier appears nearby the plasma boundary, the condition for its onset at $z_{pk} > 0$ has the form

$$z_p(\rho_{max}) > z_0. \quad (87)$$

Here, we omit the *e* and *i* subscripts for the electron and ion temperatures because, near the plasma boundary, the electrons and ions are strongly coupled, $T_e \approx T_i = T$, and, accordingly, the transport barriers develop simultaneously for all the transport parameters. By virtue of definition (77) for z_p, condition (87) can be rewritten as

$$-aT'/T > z_0 + (\Omega_{pc} - \Omega_n)/A. \quad (88)$$

In the L-mode, the temperature profile at the edge differs strongly from the canonical one ($\Omega_T \gg \Omega_c$, see Fig. 11a), so heat flux (70) can be approximately represented as

$$\Gamma = 2\kappa(T/R)\Omega_T = -2\kappa T'(\rho_{max}) = P_{tot}/S. \quad (89)$$

Here, P_{tot} is the total deposited power and S is the area of the plasma surface. Resolving relationship (89) with respect to T' and substituting the results into inequality (88), we obtain the following condition for the transition to the H-mode:

$$P_{tot} > P_{thr}, \quad (90)$$

where

$$P_{thr} = 2\kappa T_S(S/a)(z_0 + (\Omega_{pc} - \Omega_n)/A)_S. \quad (91)$$

The subscript S implies that all the quantities on the right-hand side of formula (91) should be treated in terms of their values at the plasma boundary $\rho = \rho_{max}$. In the practical units adopted in the ITER project, formula (91) reads

$$P_{thr} = 0.0032\kappa T_S(S/a)(z_0 + (\Omega_{pc} - \Omega_n)/A)_S, \quad (91a)$$

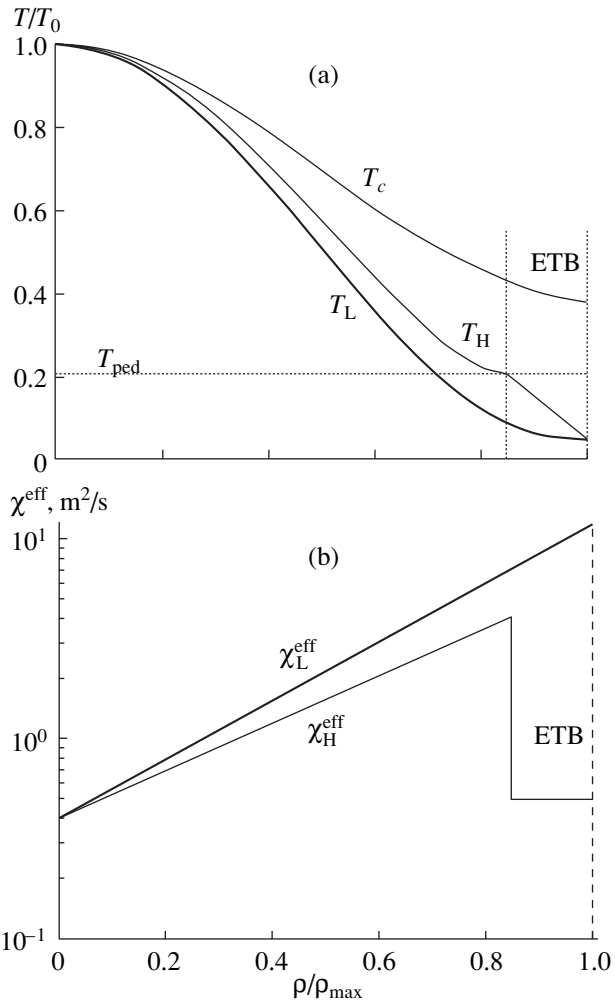

Fig. 11. Behavior of the profiles of (a) the electron temperature and (b) the effective thermal diffusivity in the L- and H-modes (T_{ped} is the pedestal temperature).

where P_{thr} is in MW, κ is in 10^{19} m^{-1} s^{-1}, T is in keV, S is in m^2, and a is in m. Since the parameter κ defined by expression (73) is independent of radius, we have

$$P_{thr} \sim \bar{n}[q(\rho_{max}/2)(q_S/B)]\{R^{3/4}T^{1/2}(\rho_{max}/4)\} \times T_S(z_0 + (\Omega_{pc} - \Omega_n)_S/A)(l/2\pi a), \quad (92)$$

where T_S is the boundary temperature and l is the length of the boundary of the meridional plasma cross section. This relationship does not contradict the ITER scaling [23]

$$P_{thr} = 0.7\, n_{20}^{0.94} B^{0.8} R^{2.12}, \quad (93)$$

because the powers of the density in scalings (92) and (93) are essentially the same, the factor in the square brackets of scaling (92) increases with magnetic field, and the factor in parentheses increases sharply with the geometric dimensions of the device. Scaling (92), however, also involves dependence on the boundary temperature, the density gradient at the plasma edge (through the critical gradient Ω_{nS}), and the shape of the plasma cross section (through the ratio $l/2\pi a$). In scaling (93), the symbol n_{20} denotes the mean plasma density in units of 10^{20} m^{-3}.

5.4. Estimates of the Transport Barrier Parameters in the H-Mode

For H-mode discharges, we can distinguish between two regions of plasma column:

(I) the main inner plasma region, $0 < \rho < \rho_{max} - \Delta$, in which $F_{e,i} \approx 1$, and

(II) the ETB zone, $\rho_{max} - \Delta < \rho < \rho_{max}$, in which $F_{e,i} \ll 1$.

Here, Δ is the width of the transport barrier. At the edge, we have $T_e \sim T_i = T$. To simplify the estimates, we assume that, at the edge, the electron and ion heat fluxes are also the same, $\kappa_e = \kappa_i = \kappa$. In the expression for the forgetting factor, we use the quantity z_p in place of z_T and ignore specific features of the density profile in the H-mode. As a result, expression (70) for the heat flux at the periphery of region (I), i.e., near the transport barrier, takes the form

$$\Gamma^- = -\kappa T\partial/\partial\rho \ln(T/T_c) = 1/2P_{tot}/S, \quad T = T_{ped}. \quad (94)$$

Here, the numerical factor 1/2 stands for the power deposited in the electrons or in the ions. Within the transport barrier, the heat fluxes are as follows:

$$\Gamma^+ = -\kappa_0 \partial T/\partial\rho = 1/2P_{tot}/S, \quad \Gamma^+ = \Gamma^- = \Gamma. \quad (95)$$

At the boundary between regions (I) and (II), we have

$$z_T = z_{0S}/2, \quad \text{or} \quad -ad/d\rho \ln(T/T_c) = z_{0S}/2, \quad (96)$$

where z_{0S} is the value of the function z_0 at the plasma boundary. Substituting relationships (96) into formula (94), we obtain

$$T_{ped} = aP_{tot}/(S\kappa z_{0S}), \quad (97)$$

or, in practical units,

$$T_{ped}\ [\text{keV}] = 16P_{tot}\ [\text{MW}](2\pi a/l)/(R\kappa z_{0S}). \quad (98)$$

Note that the pedestal temperature does not depend on how the temperature behaves inside the barrier. Integrating formula (95) over the transport barrier taking into account the inequality $T_S/T_{ped} \ll 1$ yields

$$\kappa_0 T_{ped} \approx 1/2\Delta P_{tot}/S. \quad (99)$$

Using expression (97), we find

$$\Delta/a = 2\kappa_0/(\kappa z_{0S}). \quad (100)$$

Formulas (98) and (100) give upper estimates for the pedestal temperature and barrier width in a steady-state discharge. For discharges with edge localized modes (ELMs), the pedestal temperature T_{ped} will be lower.

In some experimental situations, the pressure or temperature gradient within the barrier can be somehow restricted, e.g., by ballooning instabilities. If the absolute value of the temperature gradient is restricted by the value $T_b' > 0$, then we should distinguish between two possible cases.

(i) The temperature gradient inside the barrier is smaller in absolute value than T_b'; i.e.,

$$\Gamma/\kappa_0 < T_b'. \quad (101)$$

In this case, formulas (95) and (100) remain valid.

(ii) The inequality opposite to inequality (101) holds,

$$\Gamma/\kappa_0 > T_b'. \quad (102)$$

In this case, formulas (95) and (100) fail to hold, but formula (97) for T_{ped} remains valid. Consequently, the barrier width Δ should be described by the obvious expression

$$\Delta/a = T_{ped}/(aT_b') = P_{tot}/(S\kappa z_{0S}T_b'). \quad (103)$$

We thus see that the width of the transport barrier is proportional to the deposited power. This behavior of the barrier parameters was observed in Alcator C-Mod [27].

5.5. Some Remarks about the Second Critical Gradient z_{0k}

In our model, the first critical temperature gradient Ω_{Tc} is determined in terms of the canonical pressure profile in accordance with formulas (63)–(65), specifically, $\Omega_{Tc} = 2/3\Omega_{pc}$. We have derived differential equation (50) for the canonical profiles and have formulated boundary conditions (54). Hence, the first critical gradient is determined by means of a closed theory. Nothing of this kind has been done for the second critical gradient. Even the general question of whether it is possible to describe the physics of the complex process of transport barrier formation by a relatively simple phenomenological model with forgetting remains open.

We will discuss this issue in two steps. First, we consider the problem of finding the two functions $z_{0e}(\rho)$ and $z_{0i}(\rho)$ by comparing the calculated results to the experimental data. To do this, we parameterize these functions and then determine their parameters by simulating discharges with improved confinement. Second, knowing how the functions $z_{0e}(\rho)$ and $z_{0i}(\rho)$ behave in space, we compare their behavior to the spatial behavior of different parameters of the poloidal magnetic field in order to establish whether there is a relation between these functions and the poloidal field.

We begin by considering whether the functions z_{0e} and z_{0i} at the very edge of the plasma can be determined by analyzing the L–H transition. Since the transport barrier is narrow and occurs near the boundary, its formation is described in the model only by the quantities $z_{0e}(\rho_{max})$ and $z_{0i}(\rho_{max})$. Since the electrons and ions at the edge are strongly coupled, it is natural to assume that $z_{0e}(\rho_{max}) = z_{0i}(\rho_{max})$. For brevity, the quantities on both sides of this equality have been denoted by z_{0S}. Consequently, in our model, the L–H transition is described in terms of only one quantity, which has to be determined by comparing the calculations to experiment. This comparison was carried out in [15], where it was shown that $z_{0S} = 8$–9 for DIII-D and $z_{0S} = 6$–7 for JET. Our simulations for the MAST small-aspect-ratio tokamak ($A \sim 1.5$), yielded the values $z_{0S} = 5$–6. We thus can conclude that the quantity z_{0S} lies in the range $6 < z_{0S} < 8$, within which it probably increases slightly with increasing aspect ratio.

The behavior of the functions $z_{0e}(\rho)$ and $z_{0i}(\rho)$ in the plasma core and in the gradient zone can be determined by analyzing discharges with ITBs. Such an analysis was carried out in [15] for JET and in [28, 29] for JT-60U. It was shown that the functions $z_{0e}(\rho)$ and $z_{0i}(\rho)$ within the plasma column are markedly smaller than z_{0S}; this especially concerns the ion component. The results of the analysis can conveniently be represented in the form of a continuous piecewise linear function of radius:

$$z_{0k}(\rho) = \begin{cases} \alpha_{k1} & \text{for } 0 < \rho < \rho_1, \\ \alpha_{k1} + (\alpha_{k2} - \alpha_{k1})(\rho - \rho_1)/(\rho_2 - \rho_1) & \\ \quad \text{for } \rho_1 < \rho < \rho_2, & \\ \alpha_{k2} \quad \text{for } \rho_2 < \rho < \rho_{max}, & \end{cases} \tag{104}$$

where

$$z_{0e}(0) = \alpha_{e1} = 4\text{–}5, \quad z_{0i}(0) = \alpha_{i1} = 2\text{–}3,$$

$$\alpha_{e2} = \alpha_{i2} = z_{0S} = 6\text{–}8,$$

$$\rho_1/\rho_{max} = 0.5\text{–}0.6, \quad \rho_2/\rho_{max} = 0.8\text{–}0.9.$$

Examples of the functions $z_{0e}(\rho)$ and $z_{0i}(\rho)$ for JET are presented in Figs. 12a and 12b.

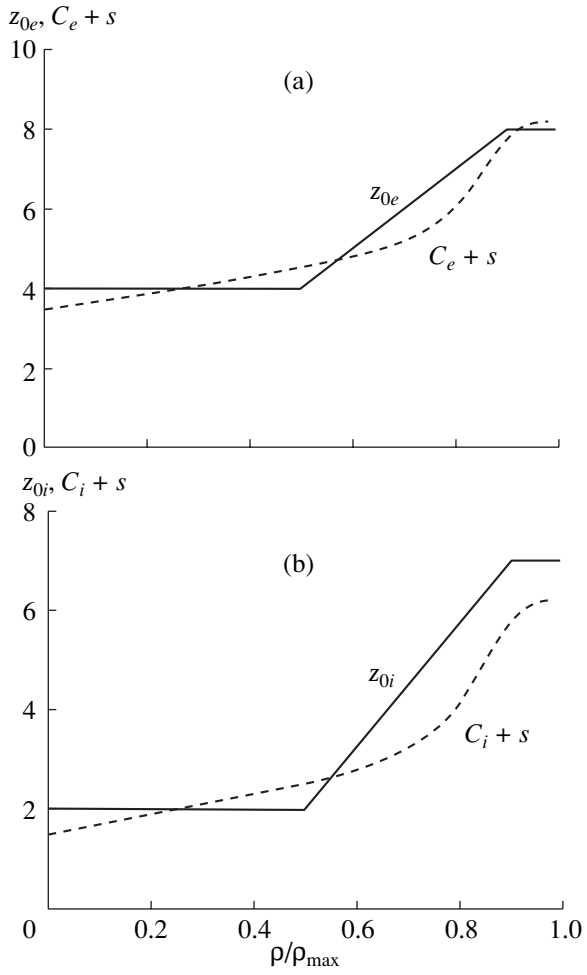

Fig. 12. Profiles of the deviations of the (a) electron temperature gradient and (b) ion temperature gradient from the second critical gradients z_{0e} and z_{0i} and profiles of the functions (a) $C_e + s$ and (b) $C_i + s$.

Let us compare the conditions for the formation of an ITB and an ETB. General condition (79) for the build-up of a barrier can be rewritten in the form

$$a\rho_{max}/\rho\left|p_k'/p_k - p_c'/p_c\right| > z_{0k}. \tag{105}$$

This condition implies the following three requirements for the development of the transport barrier:

(i) the peak in deposited power profile should be sharp enough,

(ii) the power deposited within an ITB should exceed a certain threshold value, and

(iii) the increase in the plasma density gradient inside the barrier favors a decrease in the threshold power.

For the L–H transition, as well as for the buildup of an ETB, the first condition is not necessary. The fact that the pressures p_k at the plasma boundary are relatively low and remain essentially unchanged makes condition (ii) easier to satisfy. However, the threshold

gradient at the boundary, z_{0S}, is two to three times larger than the gradients z_{0k} in the gradient zone. This is why the onset of an ITB is not necessarily accompanied by the onset of an ETB, and vice versa. Of course, in some discharges, both of the barriers (ITB and ETB) can arise simultaneously.

Now, we discuss the physical mechanisms that can govern the behavior of the functions $z_{0k}(\rho)$ ($k = e, i$). At the present stage of research, most attention is focused on the following two effects: first, the toroidal and poloidal plasma rotation in a narrow zone inside the barrier and, second, a negative or a small positive magnetic shear $s = (\rho/q)\partial q/\partial\rho$ in the plasma interior.

In order to find out how plasma rotation is related to transport processes, we consider the force balance equation for the ion component, ignoring the viscosity and omitting the term proportional to the velocity squared:

$$\partial p_i/\partial\rho = enE_\rho + en/c(v_{i\theta}B_\varphi - v_{i\varphi}B_\theta), \qquad (106)$$

where $p_i = nT_i$ is the ion pressure, E_ρ is the radial electric field, B_θ and B_φ are the poloidal and toroidal magnetic-field components, and $v_{i\theta}$ and $v_{i\varphi}$ are the poloidal and toroidal ion velocities. Equation (106) is a relationship between the four unknown functions (p_i, E_ρ, $v_{i\theta}$, $v_{i\varphi}$) and therefore can only be used for a qualitative description. From this equation we see that the large pressure gradient inside the barrier inevitably produces a strong radial electric field and can force the plasma ions to move with high velocities $v_{i\theta}$ and $v_{i\varphi}$; the strong radial electric field, in turn, can set the plasma into drift motion with the velocity $\mathbf{v}_d = c(\mathbf{E}\times\mathbf{B})/B^2$, which generates a highly sheared poloidal flow. This poloidal rotation is usually thought to be the major cause of the suppression of turbulence and of the associated reduction in anomalous transport.

In this connection, many experiments were aimed at revealing the internal mechanisms for the L–H transition. The underlying logic behind such investigations was quite simple: if one event occurs before the other, then this first event was thought to be a cause, and the other, a consequence. However, there is no unique answer to the question of what happens earlier—the L–H transition or the onset of the poloidal plasma rotation. The strong coupling between the L–H transition and the radial electric field was confirmed in biasing experiments, in which charged electrodes were inserted into the plasma to a depth of 1–2 cm. In such experiments, observations revealed effects resembling the L–H transition. The L–H transitions, however, can also be artificially triggered by other means, provided that the plasma (in the parameter space) is near the threshold for the transition. For instance, a transition to the H-mode can be initiated by a low-intensity pulsed hydrogen puffing (as in Tuman-3M) or even by displacing the plasma column toward the high-field side (as in T-10).

At this point, we focus attention on what is important for the modeling of the L–H transition. The experiments have not yet revealed any immediate cause of the transition. The complex processes whereby the plasma parameters changes during the transition proceed almost simultaneously. The experimental criterion for the transition, $P_{tot} > P_{thr}$, contains only one parameter, P_{tot}, and coincides in structure with criterion (90). We thus can conclude that, although the canonical profile model does not involve the parameters of the plasma motions, it is likely to provide a consistent description of the L–H transition.

The problem of ITB formation is more complicated. Already in the early stage of research (1993–1995), it was shown that the criterion for ITB formation depends on the profile $q(\rho)$ and on the magnetic shear s. When the shear in the plasma core is negative, $s < 0$, an ITB forms at a lower deposited power. Moreover, such an ITB is a strong boxlike narrow barrier with very low transport coefficients. The strength of the barrier is usually characterized by the relative temperature gradient (72), i.e., by the value of the ratio $R/L_T = -RT'/T = \Omega_T$, within it. For a strong barrier, we have $\Omega_T = 30$–40.

When the shear in the plasma core is positive but low, $0 < s < 0.2$, an ITB can form too, but presumably at a higher level of the deposited power. In this case, the ITB is, as a rule, weak and wide, the characteristic relative temperature gradient being smaller, $\Omega_T = 20$–25.

There is evidence that ITBs develop near the resonant magnetic surfaces $q = m/n$ with small n and m ($q = 1, 3/2, 2, 3$). This is clear from a very elegant JET experiment in which, during the evolution of a nonmonotonic current profile, the $q = 2$ magnetic surface was split into two resonant surfaces, and a single ITB, which was initially close to the $q = 2$ surface, was split into two barriers, each confined to its own $q = 2$ surface. Measurements of the plasma rotation velocity near ITBs showed the presence of zonal plasma flows. After the transport barrier has appeared, it can be somewhat displaced toward the edge, but, as a rule, it stops moving in the vicinity of the magnetic surface $\rho/\rho_{max} \sim 0.65$–$0.7$.

Summarizing the above remarks, we can draw the following conclusions:

(i) At the plasma boundary, the magnetic shear is large. At the edge of a plasma column with a large aspect ratio, $A = 5$, and a circular cross section (as in T-10), the shear is equal to $s = 2$. For $A = 1.5$ and an elongation of $k \sim 2$ (as in MAST), the shear at the plasma edge is $s = 5$–6. For such a large shear, the details of its behavior, as well as the presence of resonant magnetic surfaces in the edge plasma, are likely to be of secondary importance. A key role in the formation of an ETB is played by the radial electric field and by the zonal flow nearby the plasma boundary. With allowance for these factors, the canonical profile model developed above can provide a reliable description of the L–H transition and the radial electric field can be estimated from Eq. (106), provided that the ion pres-

sure gradient $\partial p_i/\partial\rho$ is known. In order to close the model, it is necessary to determine only one parameter, z_{0S}, by comparing the calculations with experiment. This parameter can depend on the plasma geometry.

(ii) The development of an ITB within the plasma column and its position there are governed by the magnitude and sign of the magnetic shear s, the positions of the resonant magnetic surfaces (r_{s1}, $r_{s3/2}$, r_{s2}, …), and also by the magnitude and profile of the deposited power. In our model, the criterion for the onset of an ITB is given by inequality (105). The magnitude and profile of the deposited power are contained on the left-hand side of this inequality. The remaining dependences should enter the right-hand side of inequality (105); i.e., they should be taken into account in choosing the functions $z_{0k}(\rho)$ ($k = e, i$) for the plasma core. In doing so, it is expedient to compare the behavior of the functions $z_{0k}(\rho)$ with that of the shear s of the poloidal magnetic field. Figures 12a and 12b show the behavior of the function $s(\rho)$ for one of the JET operating modes. We can see that both of the functions, $z_{0k}(\rho)$ and $s(\rho)$, increase sharply in the same region. This allows the function $z_{0k}(\rho)$ to be approximated by

$$z_{0k}(\rho) \approx C_k + D_k s(\rho). \quad (107)$$

Function (107) contains four parameters, which are to be determined from experiment. Good approximations to these parameters are provided by the estimates proposed above:

$$C_e = 4\text{–}5,\ C_i = 2\text{–}3,\ D_e = D_i = 1\text{–}2. \quad (108)$$

Model function (107), in particular, reliably describes the possible displacement of a fully developed ITB. From Fig. 12 it is seen that, in the vicinity of the magnetic surface $\rho/\rho_{max} \sim 0.7$, the shear increases abruptly and thereby stops the motion of the barrier.

Let us estimate the difference between the first and the second critical gradients. The first critical gradient is given by the formula $\Omega_{T1} = \Omega_{Tc}$ (see Eqs. (64), (65)). The second critical gradient is determined by inequality (79) and approximate expression (85) for z_p,

$$\Omega_{Tk} - \Omega_{Tc} > (\rho/\rho_{max})Az_{0k}. \quad (109)$$

As a result, we obtain

$$\Omega_{Tk} > \Omega_{T2} = \Omega_{T1} + (\rho/\rho_{max})Az_{0k}. \quad (110)$$

We thus see that the difference between the second and the first critical gradients, Ω_{T2} and Ω_{T1}, is equal to $(\rho/\rho_{max})Az_{0k}$. For instance, for an iITB ($z_{0k} = 3$) formed at mid-radius in JET (with $A = 3$), we have $\Omega_{T2} - \Omega_{T1} = 4.5$. From Figs. 3 and 4 it follows that $\Omega_{T1} \approx 5$; consequently, $\Omega_{T2} \approx 9.5$, so $\Omega_{T2}/\Omega_{T1} \sim 1.9$. In this case, the second critical gradient is almost two times larger than the first one.

It is expedient to compare the above estimates with the empirical criterion for ITB formation in JET [30]:

$$\rho_S/L_T \geq 0.014, \quad L_T = -T/T', \quad (111)$$

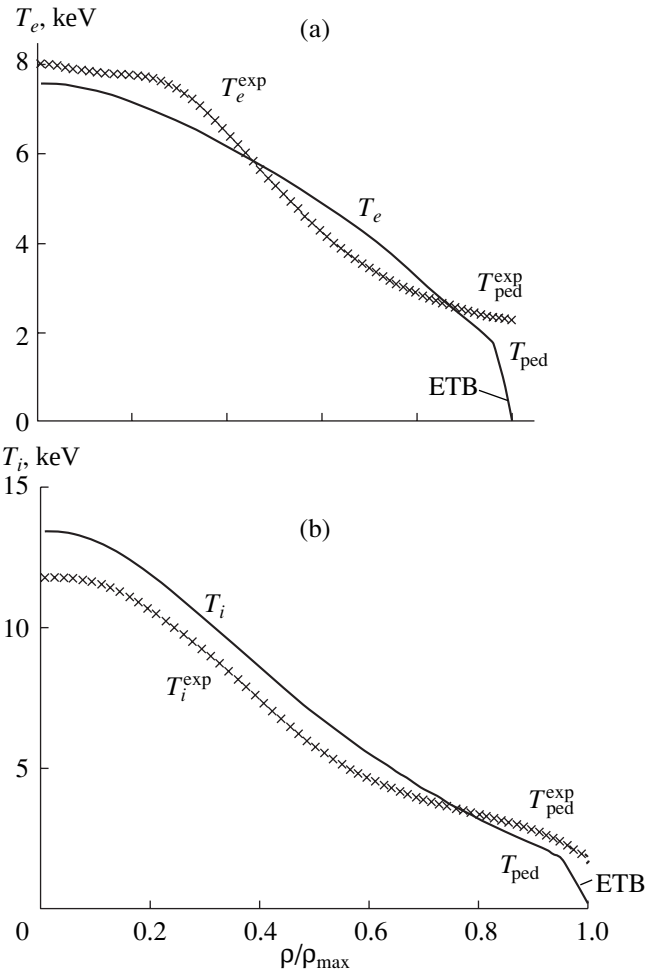

Fig. 13. Measured and calculated profiles of the (a) electron and (b) ion temperatures in the H-mode for JET shot no. 26087.

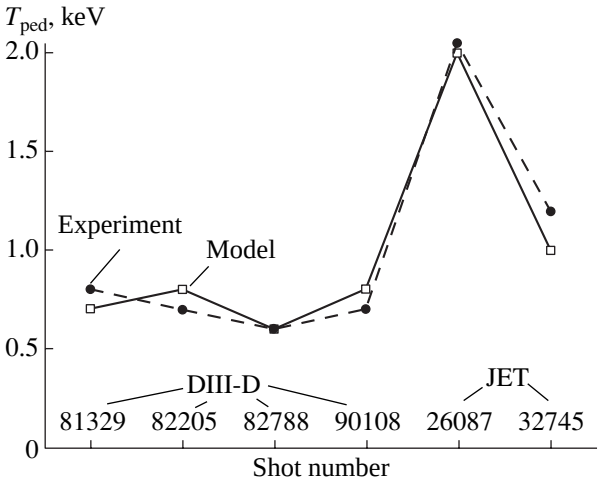

Fig. 14. Comparison between the measured and calculated pedestal temperatures for four DIII-D shots and for two JET shots.

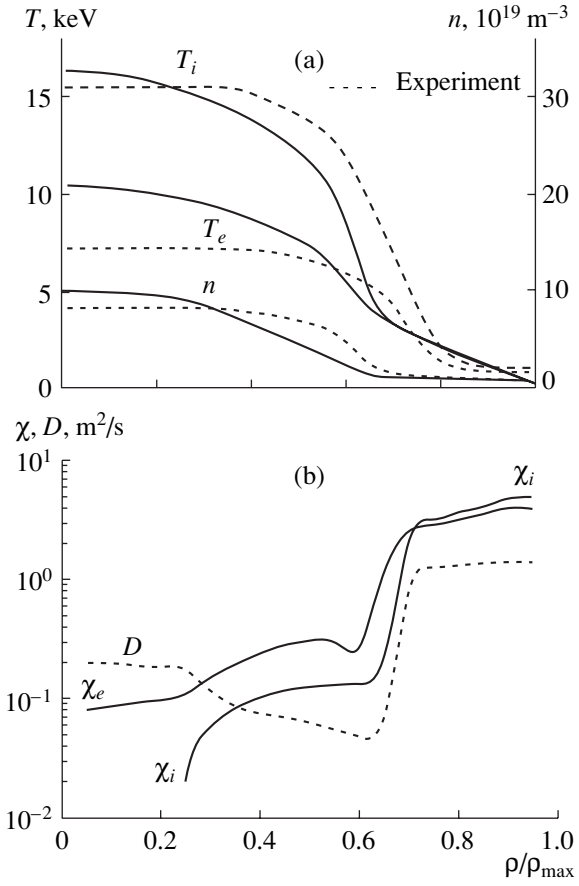

Fig. 15. Measured and calculated profiles of (a) the electron and ion temperatures and plasma density and of (b) the effective diffusivities for JT-60U shot no. E27 302 with an ITB.

where, in practical units,

$$\rho_S = 0.0046\sqrt{T_e}/B_0\,. \tag{112}$$

Criterion (111) can be rewritten in the form

$$\Omega_T = -R/L_T > \Omega_{T2}^{\rm JET}\,, \tag{113}$$

where $\Omega_{T2}^{\rm JET} = 3RB_0/\sqrt{T_e}$.

Substituting the typical values of the JET parameters (T_e = 9 keV, B_0 = 3 T) into criterion (113) yields the following experimental estimate for the second critical gradient: $\Omega_{T2}^{\rm JET}$ = 9. Our model gives Ω_{T2} = 9.5; this value deviates from the experimental value by less than 10%. Up to this point, we have assumed that the functions z_{0k} are independent of the plasma parameters. The JET experiments, however, show that the functions z_{0k} can be proportional to $B_0/\sqrt{T_e}$.

The question then arises: how can the model proposed (the set of equations (66)–(68) with fluxes (81) and (82)) be generally capable of reliably describing discharge modes with a nonmonotonic current profile (a negative magnetic shear), especially in view of our assumption that profile consistency principle (8) is satisfied for the canonical profile problem?

In Section 3.1, we have already shown, however, that only the canonical profiles of the current and pressure (targets of relaxation) should coincide. As for the actual current and pressure profiles, they can differ appreciably from one another. Equation (68), which describes the evolution of the current profile, does not contain the parameters of the canonical profiles. On the other hand, the actual current profile is incorporated in the equilibrium Grad–Shafranov equation and thereby is taken into account through the plasma geometry and metric coefficients. The canonical profiles are included only in the expressions for the heat and particle fluxes through the critical gradients. The discharge modes with a nonmonotonic current profile are unstable, but the plasma of such discharges relaxes toward canonical profiles; however, the current relaxes very slowly.

5.6. Examples

Here, we present the results obtained by numerically solving the set of transport equations (67) and (68) with heat fluxes (81) for H-mode discharges and discharges with ITBs. The calculated results were tested against discharges from the ITER database [25]. All simulations were carried out for z_{0S} = 6.

Figures 13a and 13b show the experimental and calculated profiles of the electron and ion temperatures for JET shot no. 26087 with moderate parameter values: $\bar{n}$ = 3.2, $P_{\rm NB}$ = 12.8 MW, and $q_S \sim 4.1$. Unfortunately, the ITER database contains no information about the temperature within the ETB and about the barrier width. From Fig. 13 we can see that the calculated and experimental values of the pedestal temperature are nearly the same and are approximately equal to 2 keV. The calculated and experimental central temperatures are also close to one another.

In Fig. 14, we compare the calculated and measured pedestal temperatures in a steady state for four DIII-D shots and for two JET shots. The parameters of these six shots are very different. We can see that the pedestal temperatures differ by no more than 10%. It should be emphasized that the relevant model calculations were carried out without any adjustable parameters.

Figure 15 illustrates the results of calculating all the three main parameters (the electron and ion temperatures and plasma density) for JT-60U shot no. E27302 with an ITB. In this shot, the NBI power deposited in the electrons was $P_{\rm NB}^e$ = 4 MW and that deposited in the ions was $P_{\rm NB}^i$ = 9 MW. Figure 15a shows the numerical and experimental steady-state profiles of T_e, T_i, and n, and Fig. 15b shows the calculated profiles of the transport coefficients. The calculations were performed using the complete model given by Eqs. (66)–(68),

including the equation for the plasma density, and by formula (104) for z_{0k}. We can see that, on the whole, the model reasonably well describes the position of the inner side of the ITB (the foot point), as well as the behavior of the electron and ion temperature profiles and the central electron and ion temperatures. Within the barrier, the effective diffusivities $\chi_{e,i}^{\text{eff}}$ and D^{eff} decrease by a factor of more than 10. The experimentally measured barrier width, however, is markedly less than the calculated one. A possible reason for this is that formula (104) is too rough: it does not reflect such features of the magnetic field as nonmonotonic behavior of $q(\rho)$, negative shear $s(\rho)$ in the plasma core, and the positions of resonant magnetic surfaces $q(\rho) = m/n$.

6. CONCLUSIONS

About 25 years ago, it became clear that a tokamak plasma is well self-organized in the sense that the temperature and pressure profiles are conserved when the deposited power or the plasma density changes, whereas the profile shape itself depends on the q value at the plasma boundary. The greater the q value and the plasma density, the stiffer the shape of the profiles. Such plasma behavior, which is often called the "profile consistency," has been confirmed experimentally in many tokamaks.

Self-organization processes are attributed to the plasma turbulence. In the present study, transitions to different turbulent regimes are described by means of such a control parameter as the relative temperature gradient $\Omega_T = -RT'/T$. When this parameter exceeds a certain critical value, the mode of transport changes. For low values of Ω_T (flat temperature profiles), such that $\Omega_T < \Omega_{T1}$ (where $\Omega_{T1} = -RT_c'/T_c$ is the first critical gradient), the plasma is in a low-transport mode, which usually takes place in the plasma core during off-axis heating. For $\Omega_T > \Omega_{T1}$, the discharge is in the L-mode, in which the profile self-consistency is very pronounced and the plasma is subject to self-organization. Consequently, it is the discharges with enhanced transport of energy and particles that are well self-organized. As the parameter Ω_T further increases and becomes greater than the second critical gradient Ω_{T2}, the discharge undergoes a transition to an improved confinement regime. In this case, a barrier in which the transport is reduced forms in a certain layer within the plasma or at the plasma edge, while the transport in the remaining part of the plasma is still as large as that before the transition.

In order to describe self-organization of the plasma, different variational principles have been repeatedly offered in the literature. Among these are the principle of minimum magnetic or free energy [2–5], the principle of the stationarity of entropy [6–7], and the principle of maximum kinetic energy [20]. The most highly developed of them is the principle of minimum free energy, which has been discussed in the present paper. Studies in this way succeeded in constructing the Euler equation for the canonical profiles that minimize the free energy functional provided that the total current is conserved (see Section 3), as well as in developing the relevant transport model. For a fully self-organized plasma (in the L-mode), the model contains critical gradients calculated in terms of the canonical profiles (Section 4). Many calculations carried out on the basis of this model [16–19, 21] have confirmed its predictability.

In Section 5, a mathematical apparatus has been worked out for describing the partial violation of the profile consistency principle and the transition to a regime of improved energy confinement. The transport model constructed in that section contains the second critical gradient. It provides a reasonable description of the L–H transition in terms of bifurcation in a nonlinear system and also in terms of ETB formation. However, the attempt to describe the formation of ITBs with this model encounters difficulties. The second critical gradient in the inner plasma layers is obtained by comparing the calculated results to the experimental data. The model seems to be of limited predictability. Its further development requires considering the dependence of the second critical gradient on the profiles $q(\rho)$ and $s(\rho)$ and on the position of the resonant magnetic surfaces $q(\rho_{mn}) = m/n$.

ACKNOWLEDGMENTS

We are grateful to A.M. Stefanovskiĭ, who drew our attention to the fact that free energy functional (1) may not have a minimum if we choose too wide a class of allowable functions. This work was supported in part by the RF Presidential Program for State Support of Leading Scientific Schools (project nos. NSh-1608.2003.2 and NSh-2024.2003.3).

APPENDIX

STIFFNESS OF THE TEMPERATURE PROFILE IN A TOKAMAK

It was noted above that, in experiment, the temperature profiles are conserved in spite of changes in the external influence on the plasma. This property is often called the stiffness of the temperature profiles. Now, we consider in more detail how this property manifests itself in the temperature profiles that are solutions to Eq. (67) with heat fluxes (70).

In order to give a more exact definition of the profile stiffness, we introduce the peakedness coefficient

$$S = (T(0.4\rho_{\max}) - T_a)/(T(0.8\rho_{\max}) - T_a), \qquad \text{(A.1)}$$

where T is the electron or ion temperature and $T_a = T(\rho_{\max})$ is the value of this temperature at the plasma boundary. The temperature profile is called stiff if ratio (A.1) depends weakly on the plasma density n, the total

deposited power P_{tot}, and the boundary temperature T_a. Of course, the temperature profile can depend on the profile of the deposited power.

We begin by performing analytic estimates. As an example, we consider how a plasma cylinder with a circular cross section of radius a is described by Eq. (67), in which the heat flux Γ is given by simplified expression (70) with $H = 1$ and $\Gamma_n = 0$:

$$-\Gamma = \kappa[dT/dr - (dT_c/dr)T/T_c] + \kappa_0 dT/dr. \quad (A.2)$$

Collecting the terms with the derivative dT/dr, we obtain

$$-\Gamma = ((\kappa + \kappa_0)/a)[dT/d\rho + \lambda T]. \quad (A.3)$$

Here,

$$\lambda = (\kappa/(\kappa + \kappa_0))\lambda_0, \quad \lambda_0 = \Omega_c/A \quad (\lambda < \lambda_0), \quad (A.4)$$

where $\rho = r/a$ and $A = R/a$ is the aspect ratio. The parameter λ describes the rate of exponential growth of the solution from the boundary of the plasma toward its center.

We will assume that the functions κ, κ_0, and λ are constant over the cross section of the plasma cylinder and are independent of T. Under this assumption, the temperatures are described by a linear time-independent equation

$$-(1/\rho)d/d\rho\{\rho(\kappa + \kappa_0)/a^2[dT/d\rho + \lambda T]\} = P, \quad (A.5)$$

which can be solved analytically. In this equation, $P = P(\rho) = P_0 f(\rho)$ is the density of the deposited power, $f(\rho)$ is a dimensionless function, $P_0 = P_{tot}/(2VF(1))$,

$$F(\rho) = \int_0^\rho f(\rho')\rho' d\rho', \quad (A.6)$$

and P_{tot} is the total deposited power. Integrating Eq. (A.5) once yields

$$dT/d\rho + \lambda T = -T^*, \quad (A.7)$$

where

$$T^* = T^*(\rho) = T_a^* g(\rho),$$
$$T_a^* = P_{tot}/(R(\kappa + \kappa_0)(2\pi)^2),$$
$$g(\rho) = P_{tot}(\rho)/(\rho P_{tot}), \quad (g(0) = 0, g(1) = 1), \quad (A.8)$$
$$P_{tot}(\rho) = \int_{V_\rho} P dV = P_{tot}F(\rho)/F(1).$$

The last of these relationships is the power deposited within a magnetic surface of radius ρ.

We consider the boundary-value problem for Eq. (A.7) with the boundary condition

$$T(\rho = 1) = T_a. \quad (A.9)$$

Since Eq. (A.7) is linear, the solution to the boundary-value problem can be represented as the sum

$$T = T_1 + T_2, \quad (A.10)$$

where

$$T_1 = T_a \exp(\lambda(1 - \rho)) \quad (A.11)$$

$$T_2 = T_a^* G(\rho),$$
$$G(\rho) = \int_\rho^1 \exp(\lambda(\rho' - \rho))g(\rho')d\rho' \geq 0. \quad (A.12)$$

The solution T_1 depends linearly on the boundary temperature and its profile nearly (to within the replacement of $\kappa + \kappa_0$ by κ) coincides with the canonical temperature profile $T_c = \exp(\lambda_0(1 - \rho))$. That this solution increases toward the plasma center is attributed to the presence of the heat pinch. The solution T_2 depends on the magnitude and profile of the deposited power and is independent of the boundary temperature.

Substituting relationships (A.10)–(A.12) into expression (A.1), we obtain the peakedness parameter:

$$S = \exp(0.4\lambda)S_0, \quad (A.13)$$

where

$$S_0 = \{1 - \exp(-0.6\lambda) + \gamma G(0.4)\exp(-0.6\lambda)\}/\{1 - \exp(-0.2\lambda) + \gamma G(0.8)\exp(-0.2\lambda)\}, \quad (A.14)$$

$$\gamma = T_a^*/T_a = 15.6P_{tot}/(R(\kappa + \kappa_0))/T_a. \quad (A.15)$$

Formula (A.15) is written in practical units. Expressions (A.13) and (A.14) for S contain two independent physical parameters, λ and γ. The first of them, λ, given by formulas (A.4), depends on the plasma geometry and on the parameter q. The second parameter, γ, depends on the total deposited power, on the boundary temperature, and on the plasma density (through the thermal conductivity). By the definition of stiffness, the temperature profile is stiff if the parameter S is independent of γ. Since the numerator and denominator in expression (A.14) are linear in the parameter γ, the γ dependence of the parameter S is, generally speaking, weak. In the L-mode, the boundary temperature is low, so we have $\gamma \gg 1$. In this case, the parameter γ drops out of the expression for S. For the H-mode, the parameter γ may decrease to values on the order of unity or even less, provided that by the boundary temperature is meant the pedestal temperature. In this case, the heat flux should be described by an expression more general than expression (A.2). To do this, we write expression (A.2) in terms of the Heaviside step function:

$$-\Gamma = \kappa[dT/dr - (dT_c/dr)T/T_c] \times H(-[(dT/dr)/T - (dT_c/dr)/T_c]) + \kappa_0 dT/dr. \quad (A.16)$$

This expression for the heat flux is strongly nonlinear. However, in the region where $H = 1$, Eq. (A.7) remains linear. In what follows, we denote the normalized argument of the Heaviside function by $\Delta = [\Omega_T - \Omega_c]$.

If we everywhere have

$$\Delta > 0, \tag{A.17}$$

then the Heaviside function H in expression (A.16) is equal to unity over the entire plasma column. If inequality (A.17) fails to hold in a certain region, $\Omega_T < \Omega_c$, then, in this region, the temperature profile is not stiff because it is flatter than the canonical profile. Using the definitions of Ω_T and Ω_c, we can reduce inequality (A.17) to

$$T^*(\rho)/T(\rho) > \lambda/\beta, \tag{A.18}$$

where

$$\beta = \kappa/\kappa_0 \gg 1. \tag{A.19}$$

We substitute expressions (A.8) and (A.10)–(A.12) for T^* and T into inequality (A.18) and resolve it in terms of the parameter γ. We thus arrive at a new inequality that is equivalent to inequality (A.17):

$$\gamma > \gamma^{\min}(\rho), \tag{A.20}$$

where

$$\gamma^{\min}(\rho) = \lambda\exp(\lambda(1-\rho))/[g(\rho)\beta - \lambda G(\rho)]. \tag{A.21}$$

At the plasma boundary ($\rho = 1$), we have $g = 1$, $G = 0$, and $\gamma^{\min}(1) = \lambda/\beta$, so inequality (A.20) takes the form

$$\gamma > \lambda/\beta. \tag{A.22}$$

This inequality is usually satisfied for the H-mode. This indicates that, at the edge, the temperature gradient exceeds its critical value and the Heaviside function in this region is equal to unity.

For sufficiently large values $\lambda > 1$, the function $\gamma^{\min}(\rho)$ increases exponentially toward the plasma center; therefore, within a certain magnetic surface of radius $\rho = \rho_0$, inequality (A.20) should fail to hold. In the region $\rho < \rho_0$, the Heaviside function is equal to zero, $H = 0$, and the temperature profile becomes flatter. It is obvious that, for this effect to be pronounced, the magnetic surface ρ_0 should occur in the gradient zone (typically, at $\rho = 0.5$). This is why we consider the value of $\gamma^{\min}(\rho)$ precisely at this radius:

$$\begin{aligned}\gamma^{\min}(0.5) &\equiv \gamma^{\min} \\ &= \lambda\exp(\lambda/2)/[g(0.5)\beta - \lambda G(0.5)].\end{aligned} \tag{A.23}$$

For $\gamma < \gamma^{\min}$, the temperature profile fails to be stiff. Hence, the stiffness condition for the profile is given by the inequality

$$\gamma > \gamma^{\min}. \tag{A.24}$$

The values of the parameters S, given by formula (A.13), and $\gamma^{\min}$, given by formula (A.23), depend on the deposited power profile through the functions $g(\rho)$ and $G(\rho)$. We consider four characteristic types of profiles: a localized profile,

$$\begin{aligned} f &= f_l = 1 \quad (\rho < \rho_0), \\ f_l &= 0 \quad (\rho > \rho_0), \quad \rho_0 \sim 0.1 \ll 1, \end{aligned} \tag{A.25}$$

and three power-law profiles,

$$f = f_j = \rho^{j-2} \quad (0 < \rho < 1, j = 1, 2, 3). \tag{A.26}$$

The corresponding functions $g(\rho)$ have the form

$$g_l(\rho) = \rho/\rho_0^2 \quad (\rho < \rho_0), \quad g_l(\rho) = 1/\rho \quad (\rho > \rho_0),$$

$$g_j = \rho^{j-1} \quad (0 < \rho < 1, j = 1, 2, 3).$$

Note that the dimensionless parameter

$$\xi = 2P(1)V/P_{\text{tot}} \tag{A.27}$$

characterizes the deposited power profile and is equal to zero for a localized profile and to j for power-law profiles.

Formula (A.23) contains the parameter β. Here, we assume that the coefficient β is constant over the plasma cross section and is equal to $\beta = \kappa/\kappa_0 = 6$. Note that this assumption does not contradict the experimental data. The value of λ can be estimated with the help of Fig. 4. For JET discharges, we have $\Omega_c \sim 4$, $A \sim 3$, and, consequently, $\lambda \sim 1.5$. The dependence of $\gamma^{\min}$ on the parameter ξ for the β and λ values chosen above is shown in Fig. 16, in which the range $\gamma > \gamma^{\min}$ corresponds to stiff temperature profiles. Accordingly, the range $\gamma < \gamma^{\min}$ is that of "flexible" profiles. In this case, in the plasma core, the Heaviside function is equal to zero and thereby nullifies the term with the critical gradient, so the profiles in this region are flat.

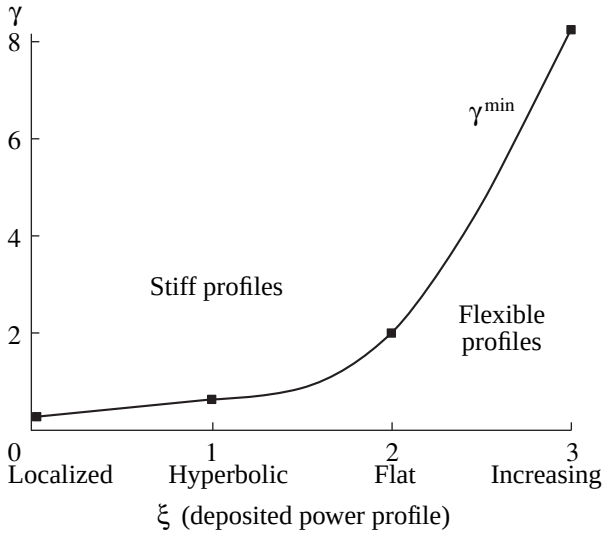

Fig. 16. Dependence of $\gamma^{\min}$ on the parameter ξ for the adopted values $\beta = 6$ and $\lambda = 1.5$.

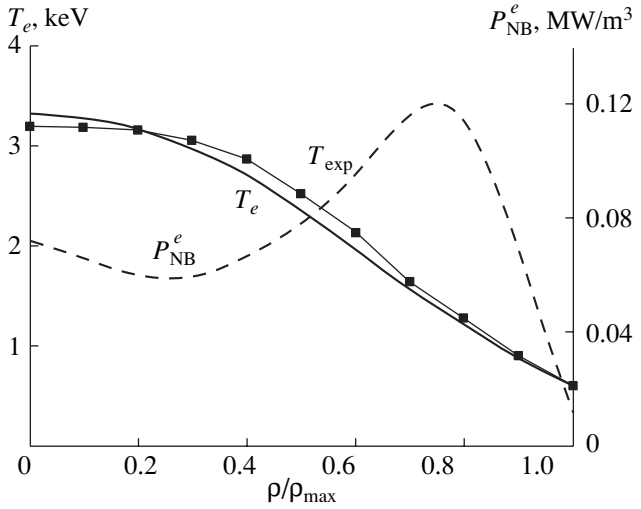

Fig. 17. Measured and calculated electron temperature profiles and profile of the density of the power P^e_{NB} deposited in the electrons for JET shot no. 52022.

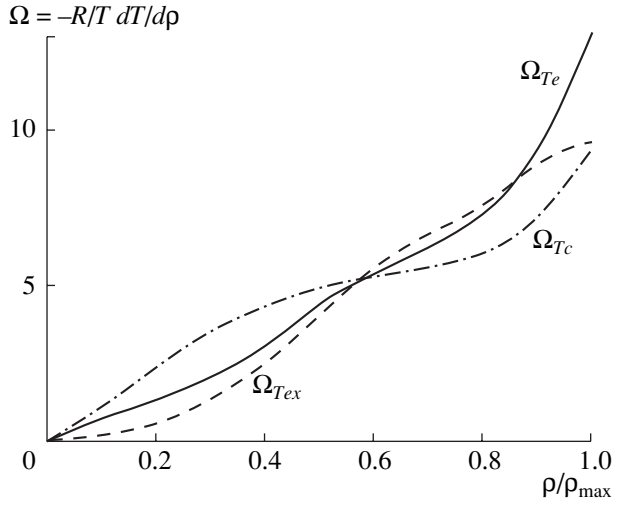

Fig. 18. Profiles of the relative gradients Ω_{Te}, Ω_{Tex}, and Ω_{Tc} for the same shot as in Fig. 17.

Now, we describe the results obtained by numerically solving Eqs. (67) and (68) with heat fluxes (70). The central value of the plasma density and its profile were assumed to be known from experiment. The results of calculating an H-mode JET discharge (specifically, shot no. 52 022 with I = 2.48 MA, density of $\bar{n} = 8.93 \times 10^{19}$ m^{-3}, and P_{NB} = 14.2 MW at the time t = 60.44 s [25]) are illustrated in the subsequent figures. Figure 17 shows the calculated and experimental electron temperature profiles and the profile of the specific power P^e_{NB} deposited in the electrons. We can see that the deposited power profile P^e_{NB} is peaked at the plasma edge, because the high pedestal in the plasma density, $n_{ped} \sim 5.5 \times 10^{19}$ m^{-3}, prevents the neutral beam from penetrating into the plasma core. Figure 18 shows the profiles of the relative gradients Ω_{Te}, Ω_{Tex}, and Ω_{Tc}. It can be seen that, in the region $\rho < \rho_1 \sim 0.6$, Ω_{Te} and Ω_{Tex} lie below that of the critical gradient Ω_{Tc}. In this region, the Heaviside function is equal to zero and the temperature profile is not stiff.

Hence, experiments confirm the formation of flexible temperature profiles when the pedestal temperature is sufficiently high and when the deposited power profiles are either flat or peaked at the plasma edge. In turn, the existence of flexible profiles confirms that there is no substantial heat pinch.

REFERENCES

1. B. Coppi, Comments Plasma Phys. Control. Fusion **5**, 26 (1980).
2. J. B. Taylor, Phys. Rev. Lett. **33**, 1139 (1974).
3. B. B. Kadomtsev, Fiz. Plazmy **13**, 443 (1987) [Sov. J. Plasma Phys. **13**, 443 (1987)].
4. D. Biskamp, Comments Plasma Phys. Control. Fusion **10**, 165 (1986).
5. J. Y. Hsu and M. S. Chu, Phys. Fluids **30**, 1221 (1987).
6. E. Minardi and H. Weisen, Nucl. Fusion **41**, 113 (2001).
7. E. Minardi, E. Lazzaro, C. Sozzi, and S. Cirant, Nucl. Fusion **43**, 369 (2003).
8. M. Kotschenreuther, W. Dorland, G. W. Hammet, and M. A. Beer, Phys. Plasmas **2**, 2381 (1995).
9. H. Nordman, J. Weiland, and A. Jarmen, Nucl. Fusion **30**, 983 (1990).
10. R. E. Waltz, G. M. Staebler, W. Dorland, *et al.*, Phys. Plasmas **4**, 2482 (1997).
11. J. B. Taylor, Phys. Fluids B **5**, 4378 (1993).
12. B. B. Kadomtsev, Rep. Prog. Phys. **59**, 91 (1996).
13. Yu. N. Dnestrovskij and G. V. Pereverzev, Plasma Phys. Controlled Fusion **30**, 47 (1988).
14. Yu. N. Dnestrovskij, E. L. Berezovskij, S. E. Lysenko, *et al.*, Nucl. Fusion **31**, 1877 (1991).
15. Yu. N. Dnestrovskij, S. E. Lysenko, and K. N. Tarasyan, Nucl. Fusion **35**, 1047 (1995).
16. Yu. N. Dnestrovskij, Yu. V. Esipchuk, N. A. Kirneva, *et al.*, Fiz. Plazmy **23**, 614 (1997) [Plasma Phys. Rep. **23**, 566 (1997)].
17. Yu. N. Dnestrovskij, M. P. Gryaznevich, A. Yu. Dnestrovskij, *et al.*, Fiz. Plazmy **26**, 579 (2000) [Plasma Phys. Rep. **26**, 539 (2000)].
18. Yu. N. Dnestrovskij, A. Yu. Dnestrovskij, S. E. Lysenko, and S. V. Cherkasov, Fiz. Plazmy **28**, 963 (2002) [Plasma Phys. Rep. **28**, 887 (2002)].
19. Yu. N. Dnestrovskij, A. Yu. Dnestrovskij, S. E. Lysenko, and S. V. Cherkasov, in *Proceedings of the19th IAEA Fusion Energy Conference, Lyon, 2002,* Paper IAEA-CN-94/TH/P1-04.

20. T. Tamano, I. Katanuma, and Y. Sakamoto, in *Proceedings of the19th IAEA Fusion Energy Conference, Lyon, 2002*, Paper IAEA-CN-94/TH/P1-15.

21. Yu. N. Dnestrovskij, S. V. Cherkasov, S. E. Lysenko, *et al.*, Nucl. Fusion **38**, 373 (1998).

22. G. V. Pereverzev and P. N. Yushmanov, Report No. IPP 5/98 (Max-Planck Inst. for Plasma Physics, Garching, 2001).

23. *ITER Physics Basis*, Nucl. Fusion **39** (12) (1999).

24. J. W. Connor and J. B. Taylor, Nucl. Fusion **17**, 1047 (1977).

25. D. Boucher, J. W. Connor, W. A. Houlberg, *et al.*, Nucl. Fusion **40**, 1955 (2000); http://tokamak-profiledb.ukaea.org.uk/.

26. F. Ryter, C. Angioni, M. Beurskens, *et al.*, Plasma Phys. Controlled Fusion **43**, A323 (2001).

27. A. E. Hubbard, B. Lipschultz, D. Mossessian, *et al.*, in *Proceedings of the 26th EPS Conference on Controlled Fusion and Plasma Physics, Maastricht, 1999*, ECA **23J**, 13 (1999).

28. Yu. N. Dnestrovskij, S. E. Lysenko, and K. N. Tarasyan, Fiz. Plazmy **24**, 867 (1998) [Plasma Phys. Rep. **24**, 805 (1998)].

29. Yu. N. Dnestrovskij, S. E. Lysenko, K. N. Tarasyan, *et al.*, Nucl. Fusion **39**, 2089 (1999).

30. G. Tresset, X. Litaudon, D. Moreau, *et al.*, Nucl. Fusion **42**, 520 (2002).

Translated by I.A. Kalabalyk

Plasma Physics Reports, Vol. 31, No. 7, 2005, pp. 554–561. Translated from Fizika Plazmy, Vol. 31, No. 7, 2005, pp. 604–611.

STELLARATORS

The Use of Doppler Reflectometry in the L-2M Stellarator

A. A. Pshenichnikov, L. V. Kolik, N. I. Malykh, A. E. Petrov, M. A. Tereshchenko, N. K. Kharchev, and Yu. V. Khol'nov

Prokhorov Institute of General Physics, Russian Academy of Sciences, ul. Vavilova 38, Moscow, 119991 Russia

Received April 21, 2004; in final form, October 21, 2004

Abstract—Results are presented from measurements of the plasma rotation velocity and plasma density fluctuations in the L-2M stellarator by the method of Doppler reflectometry. Specific problems that arise when applying this diagnostics to the stellarator are revealed. The poloidal plasma velocity at the periphery of the plasma column is determined. The results of measurements are well reproducible. © *2005 Pleiades Publishing, Inc.*

1. INTRODUCTION

In recent years, increased interest in anomalous transport mechanisms in tokamaks and stellarators has stimulated the development of Doppler [1–5] and correlation [6–8] reflectometry for measuring the plasma rotation velocity and plasma density fluctuations. In this paper, we present results from experiments on the use of Doppler reflectometry in the L-2M stellarator in the ohmic heating (OH) and electron cyclotron resonance heating (ECRH) regimes. The results of measurements in these two regimes were found to differ qualitatively. In the course of experiments, some general physics and engineering problems, as well as those related to the specific stellarator geometry, were revealed.

2. LAYOUT OF THE DIAGNOSTICS AND THE SPECIFIC FEATURES OF THE STELLARATOR PLASMA GEOMETRY

The geometry and parameters of the L-2M stellarator were described, e.g., in [9, 10]. The diagnostic facility was mounted in the standard diagnostic cross section, where the plasma column was turned by certain angles with respect to the major and minor axes of the vacuum chamber (see Fig. 1). The quadrature scheme of signal detection [1, 11] employed in our experiments included an 8-mm microwave oscillator (MO) with an

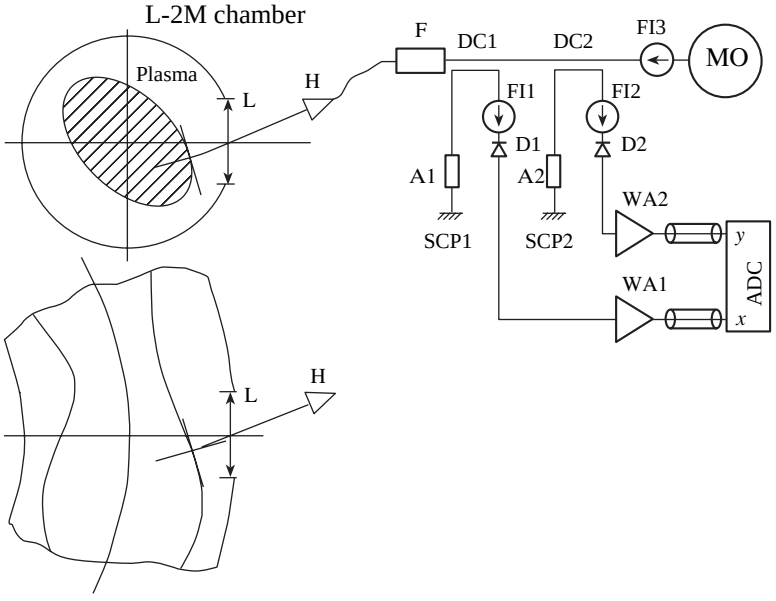

Fig. 1. Schematic of the reflectometry diagnostics in the L-2M stellarator.

1063-780X/05/3107-0554$26.00 © 2005 Pleiades Publishing, Inc.

output power of 5 mW, a waveguide transmission line, two directional couplers (DC1, DC2) with short-circuited plugs (SCP1, SCP2), two 3-dB attenuators (A1, A2), and two detector units (D1, D2). Three ferrite isolators (FI1, FI2, FI3) served to suppress standing waves in the measuring system. The probing microwave beam was launched into the plasma by a horn antenna (H) through a teflon lens (L) mounted on the diagnostic port of the stellarator. The horn–lens system formed a slightly converging Gaussian beam with a diameter (at the half-height of the radial power profile) of about 3 cm; the waist of the beam lay at a distance of 20 cm from the lens. The scattering region was located at a distance of 6–10 cm from the lens. Provision was made for linear and angular displacements of the antenna horn in the toroidal and poloidal directions; for this reason, the transmission line was ended near the horn with a flexible (annealed copper) waveguide (FW). The horn was displaced so that its axis always passed through the center of the diagnostic window. For this purpose, a laser pointer was used. The microwave beam was incident normally onto the plasma when the horn axis was inclined at an angle of about 12° to the horizontal plane and its projection onto this plane was inclined at an angle of 12° to the major radius. To suppress the stray signal from the heating gyrotron radiation, a waveguide resonance filter (F) with an attenuation of 30 dB at a frequency of 75.3 GHz was used. The polarization of the probing radiation in the plasma corresponded to an ordinary wave. The signals from microwave diodes were fed to wideband amplifiers (WA1, WA2) with an amplification factor of 10 and were recorded by a 10-bit analog-to-digital converter (ADC) with a sampling rate of 2.5 MHz. The time resolution of the diagnostic system was 400 ns.

The use of this diagnostics in the stellarator is hampered by the complicate shape of the stellarator magnetic surfaces. It can be seen from Fig. 1 that the projection of the wave vector of the probing radiation onto a stellarator magnetic surface depends on both the poloidal and toroidal tilt angles of the antenna and also on the radial position of the scattering region. This makes it rather difficult to determine the components of the wave vector and complicates the interpretation of the experiment.

3. MEASUREMENT TECHNIQUES

The diagnostics operated during several experimental campaigns in the L-2M stellarator under OH and ECRH conditions. The radial plasma density profile was measured by an HCN interferometer [12]. Using the interferometric data, we calculated the location of the critical plasma density (Fig. 2). The radial and angular resolutions of the diagnostics were estimated from the average magnitudes of the plasma parameters and the widths of their distributions along the ray trajectories calculated with the help of a code developed in [13]. The microwave beam was modeled by a set

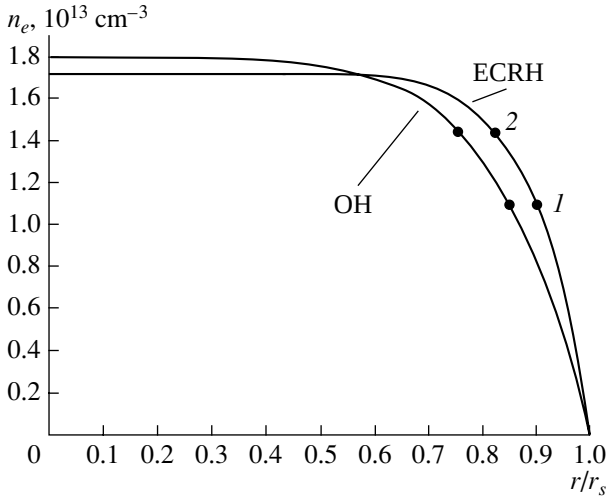

Fig. 2. Radial profiles of the electron density in the quasi-steady phase of an OH discharge and an ECRH discharge. The circles show the positions of the critical density n_c for probing frequencies of (*1*) 30.2 and (*2*) 34.6 GHz and for an angle of incidence of the microwave beam of 4°.

(bunch) of elementary beams. When averaging over the trajectory of an elementary beam, the quantity $1/\sqrt{1-(\omega_{pe}/\omega_0)^2}$, approximately proportional to the local beam intensity, was used as a weighting function (here, ω_{pe} is the electron plasma frequency and ω_0 is the probing frequency). Assuming that the spatial distribution of the magnitudes of plasma density fluctuations was uniform, this function approximated the intensity of radiation scattered from an elementary plasma volume on the beam path. For each trajectory, we also introduced an additional weighting factor corresponding to the fraction of the incident power carried by an elementary beam. Estimates showed that the spread in the poloidal wavenumbers of the probing radiation (i.e., the resolution in poloidal wavenumbers) was $(0.15\ldots0.3)k_0$, depending on the radial plasma density profile and the angle of incidence of the microwave beam. The radial size of the scattering region was 0.2–1 cm. The angular resolution was also estimated experimentally from a change in the reflectometer signal when varying the antenna tilt angle. Thus, the waveform of the recorded signals and their spectrum changed appreciably when the tilt angle was changed by 1°–2°. However, the low-frequency spectral component corresponding to the radiation reflected from the plasma disappeared completely only when the deviation of the antenna from its normal position exceeded 8°–12° (depending on the stellarator operating regime). This is consistent with the above theoretical estimate for the resolution in poloidal wavenumbers.

The poloidal velocity was calculated by the formula

$$v_\theta = \Delta f/(2k_\theta),$$

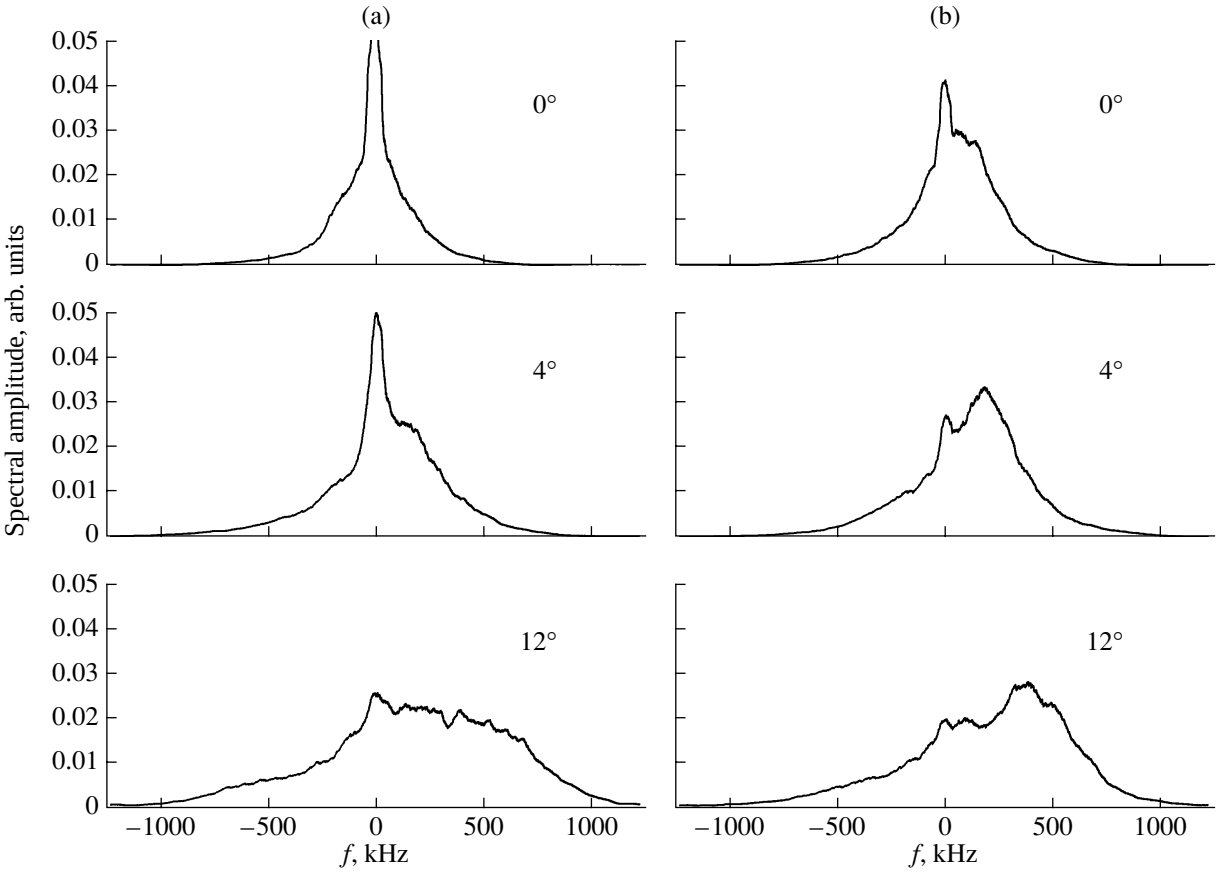

Fig. 3. Scattered spectra for an average plasma density of 1.6×10^{13} cm^{-3} and probing frequencies of (a) 34.6 and (b) 30.2 GHz in the OH regime with a plasma current of 21 kA (shot nos. 57 078–57 098). The angle is counted from the normal to the magnetic surface. The frequency of the complex signal (the difference between the frequency of the scattered signal and the probing frequency) is plotted on the abscissa.

where Δf is the Doppler shift and k_θ is the average (along the ray trajectory) poloidal component of the wave vector of the probing wave.

The Doppler shift Δf was determined from the shift of the Fourier spectrum of the complex signal [1, 11]

$$z = x + iy,$$

where x and y are the readings of the first and second channels of the reflectometer (Fig. 1) and i is the imaginary unit.

The Doppler shift was also determined from the rate of change of the phase of the complex signal:

$$\Delta f = \Delta\varphi/(2\pi\Delta t),$$

where $\Delta\varphi$ is the increment in the argument of z over a time Δt.

4. OH REGIME

Experiments in the OH regime were performed at an average plasma density of 1.6×10^{13} cm^{-3} and a plasma current of 21 kA. We used three probing frequencies: 30.2, 34.6, and 35.9 GHz, which corresponded to the critical plasma densities of 1.1×10^{13}, 1.5×10^{13}, and 1.6×10^{13} cm^{-3}, respectively.

The scattered spectra were rather simple in structure and had only one pronounced peak (Fig. 3). The spectrum was similar in shape to a Gaussian. When the antenna was inclined at a small angle with respect to its normal position, the spectrum also contained an intense low-frequency component. As the deviation of the antenna from its normal position increased, the spectrum broadened and shifted over frequency nearly in proportion to the deviation angle. From this shift and also from the rate of change of the phase of the complex signal (Fig. 4), we determined the poloidal plasma velocity (see table). Positive velocities in the table correspond to the drift in an electric field directed toward the axis of the plasma column.

It can be seen from the table that the poloidal plasma velocity deduced from the spectral shift differs quantitatively from that deduced from the rate of change of the phase of the complex signal but has a similar dependence on the antenna tilt angle. The reason for this quantitative difference is that the spectra are asymmetric and that the location of the scattering region depends

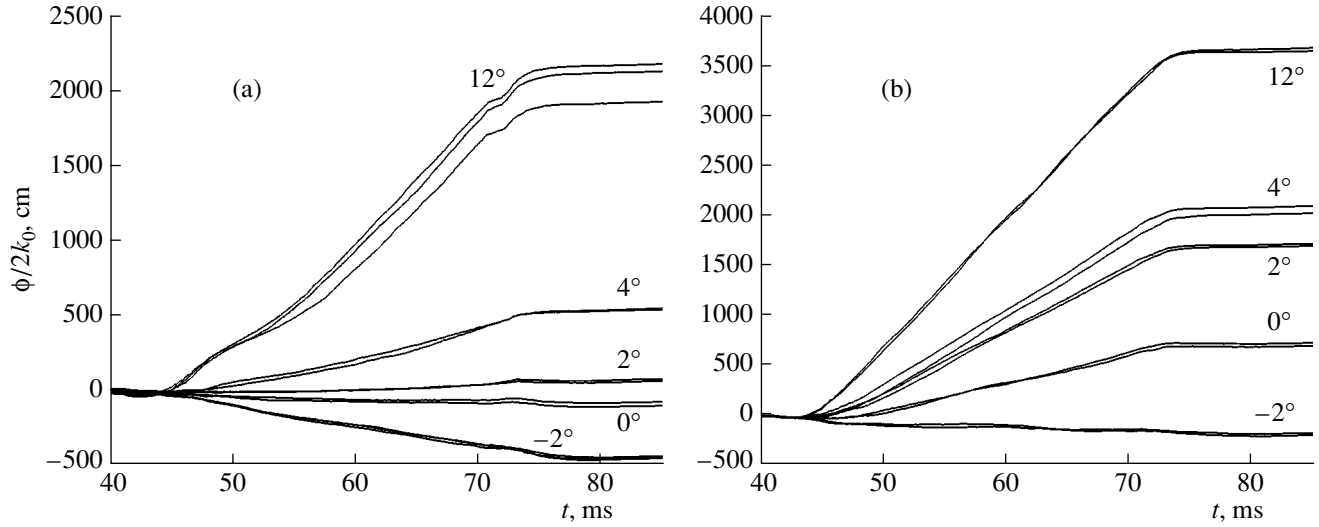

Fig. 4. Phase of the complex signal normalized to the doubled wavenumber of the probing wave in vacuum for probing frequencies of (a) 34.6 and (b) 30.2 GHz in the OH regime (shot nos. 57078–57098). The time is counted from the beginning of the discharge.

on the tilt angle. The spread in velocities for different tilt angles characterizes the measurement accuracy and the spatial resolution of the diagnostics. Judging from this spread, the calculation of the poloidal velocity from the spectral shift is more reliable. The monotonic variation in the phase during a discharge (Fig. 4), as well as an almost linear dependence of its growth rate on the antenna tilt angel, indicates the correct and rather reliable operation of the diagnostics and allows a relatively simple interpretation of the results obtained. This is also confirmed by the change in the sign of the phase at a certain tilt angle. Since the shape of a stellarator magnetic surface depends on its average radius, this angle is different for different probing frequencies (different probing radii). Thus, for a frequency of 34.6 GHz, this angle is 0°–1°, whereas for 30.2 GHz it lies within the interval from –2° to –1°.

5. ECRH REGIME

ECRH experiments were performed at average plasma densities of 1.6×10^{13} and 2.5×10^{13} cm^{-3} and heating powers of 190 and 300 kW, respectively.

Typical spectra of the complex signals are shown in Fig. 5. These spectra differ markedly from those observed in the OH regime. Typically, the spectrum has three local maxima (peaks): one lies near the zero frequency, and two others are shifted almost symmetrically from the zero frequency by 100–200 kHz. As the antenna tilt angle varies within ±4°, only the magnitudes of these three peaks change, whereas their positions vary only slightly. At large deviations of the antenna from its normal position, a considerable fraction of the spectrum falls in the high-frequency range. Only the two side peaks shift over frequency (the shift not being proportional to the angle of incidence of the

Poloidal plasma velocities calculated from the growth rate of the phase of the complex signal and from the shift of the scattered spectrum in the OH regime for an average plasma density of 1.6×10^{13} cm^{-3} and a plasma current of 21 kA (shot nos. 57078–57098)

34.62-GHz probing frequency			30.20-GHz probing frequency		
antenna tilt angle, degree	poloidal velocity, 10^5 cm/s		antenna tilt angle, degree	poloidal velocity, 10^5 cm/s	
	from phase	from spectrum		from phase	from spectrum
12	3.7	5.0	12	5.0	8.4
4	1.9	5.0	4	5.2	7.0
2	0.87	4.3	2	7.2	9.4
0	0.49	–	0	11	1.5
–2	1.59	3.8	–2	0.27	–
		$v_\theta = (4.5 \pm 0.6) \times 10^5$ cm/s			$v_\theta = (8.3 \pm 1.0) \times 10^5$ cm/s

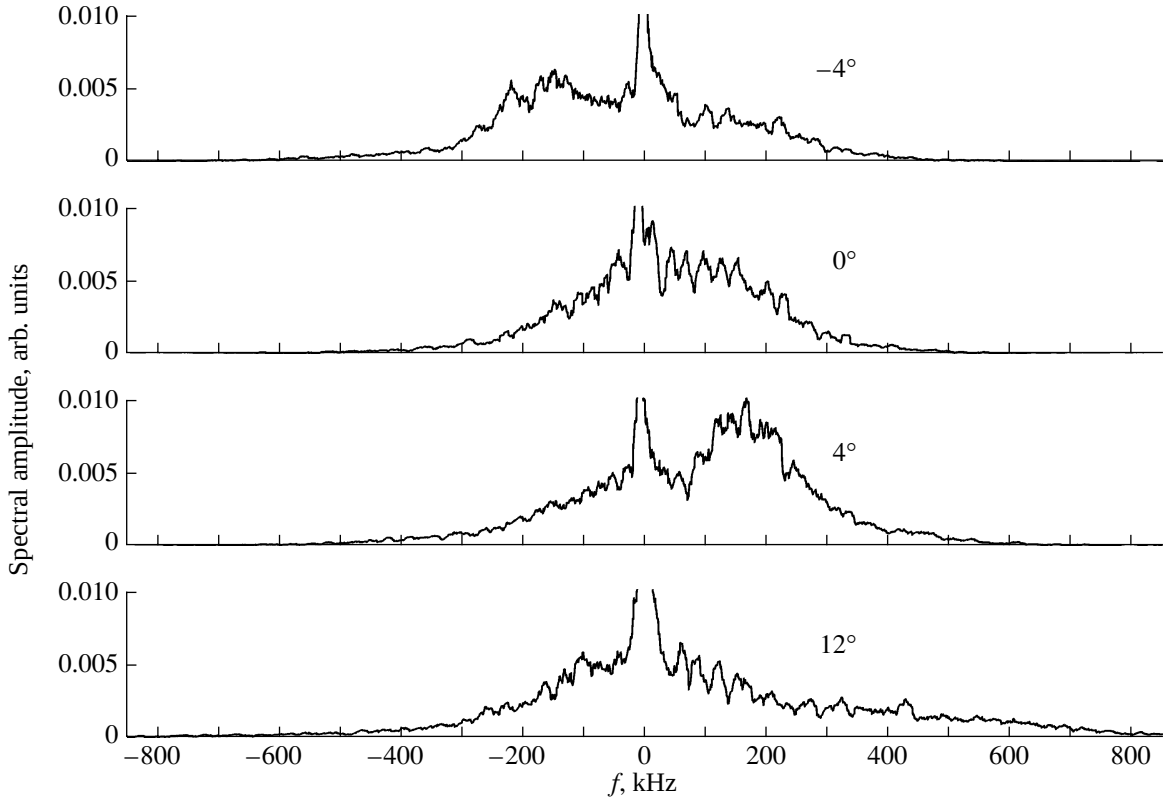

Fig. 5. Scattered spectra in the ECRH regime for a radiation frequency of 34.6 GHz, $\bar{n} = 1.6 \times 10^{13}$ cm^{-3}, $P_{\mathrm{ECRH}} = 190$ kW, and different antenna tilt angles (shot nos. 57 371–57 396). The spectra were measured over the time interval 58–59 ms after the beginning of the discharge.

probing beam onto the plasma), while the central (low-frequency) component of the spectrum changes only slightly. This indicates that the formation of the central component is apparently unrelated to the backscattering of the microwave beam by small-scale fluctuations drifting in the poloidal direction. The presence of this component may be attributed to the finite width of the directional pattern of the horn antenna and the large curvature of the magnetic flux surfaces. Under these conditions, a fraction of the probing radiation is always reflected backward to the antenna. This is also confirmed by ray-tracing calculations. Thus, the central component is merely stray radiation and must be ignored when calculating the poloidal plasma velocity from the shift of the spectrum. For the same reason, we failed to determine the poloidal plasma velocity from the growth rate of the phase of the complex signal because its time behavior was irregular. To eliminate the stray component, the spectra were approximated by a sum of Lorentzian functions (see Fig. 6) and only the satellites were taken into account in calculating the shift of the spectrum. We analyzed various versions of calculating this shift. The most reliable (stable) results were obtained when the Doppler shift was calculated by the formula

$$\Delta f = \int_{-f_s/2}^{f_s/2} f A^2(f) df \Big/ \int_{-f_s/2}^{f_s/2} A^2(f) df,$$

where $f_s = 2.5$ MHz is the ADC sampling rate and $A(f)$ is the absolute value of the Fourier component (in our case, the value of the approximating Lorentzian function). Figure 7 shows the frequency shifts calculated in this way for several instants during a stellarator discharge. It can be seen from Fig. 7 that the frequency shift varies over a wide rage with time and that the Doppler shift is not proportional to the antenna tilt angle. The radial location of the scattering region was estimated using the ray-tracing method. The estimates show that, when the axis of the probing beam is inclined at an angle of 12°–18° with respect to the normal to the magnetic surface, the reflection region is displaced by 3–5 mm toward the plasma boundary. The change in the frequency from 34.6 to 30.2 GHz corresponds to a displacement of 10–12 mm. Figure 8 shows the velocities calculated for small (±4°–5°) and large (12°–18°) antenna tilt angles for two probing frequencies. It can be seen that the velocity decreases toward

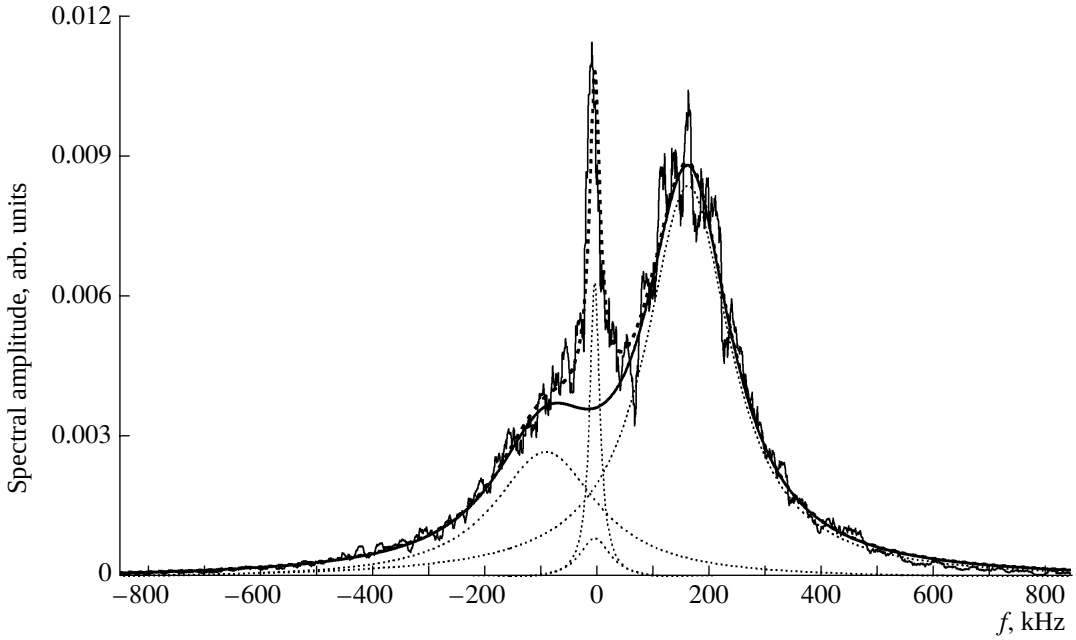

Fig. 6. Approximation of the spectrum by a sum of Lorentzian functions. The solid polygonal line shows the Fourier spectrum of the recorded signal, the dotted lines show the summands of the approximating function, and the dashed line shows their sum. The part of the Fourier spectrum used to calculate the Doppler shift is shown by the heavy solid line.

the plasma boundary. Figure 9 shows the time evolution of the radius of the critical surface for the same shots as in Fig. 8. The relative position of the critical surface was determined with the help of the reflectometer at small angles of incidence of the probing beam, whereas the absolute position was determined with the help of an HCN laser interferometer. A comparison of Figs. 8 and 9 shows that the poloidal plasma velocity varies both when the density profile is quasi-steady (the velocity increases by the end of the heating pulse) and when it varies. The latter may be related to the radial displacement of the scattering region. Figure 10 shows the time evolution of the poloidal plasma velocity in a stellarator discharge with a higher plasma density and higher heat-

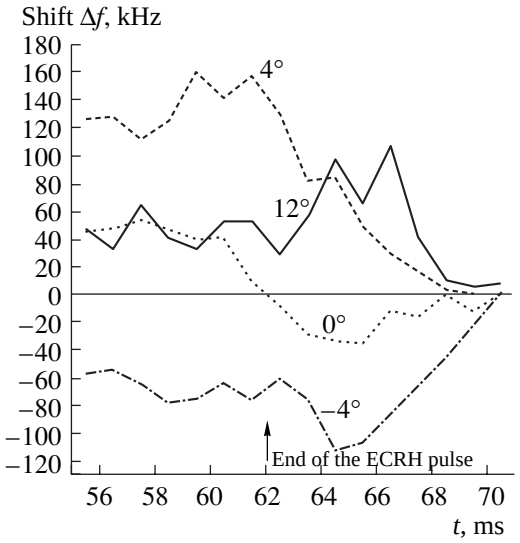

Fig. 7. Doppler shift of the scattered spectra for different antenna tilt angles for a probing frequency of 34.62 GHz, $\bar{n} = 1.6 \times 10^{13}$ cm^{-3}, and $P_{ECRH} = 190$ kW (shot nos. 57390–57396). The shift is averaged over two shots for each angle.

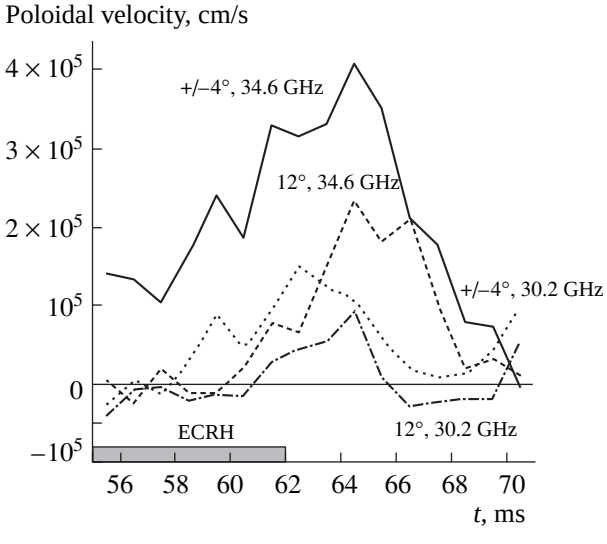

Fig. 8. Poloidal plasma velocities measured at four different radii for $\bar{n} = 1.6 \times 10^{13}$ cm^{-3} and $P_{ECRH} = 190$ kW (shot nos. 57 371–57 396). The position of the scattered region is varied by varying the probing frequency and the antenna tilt angle.

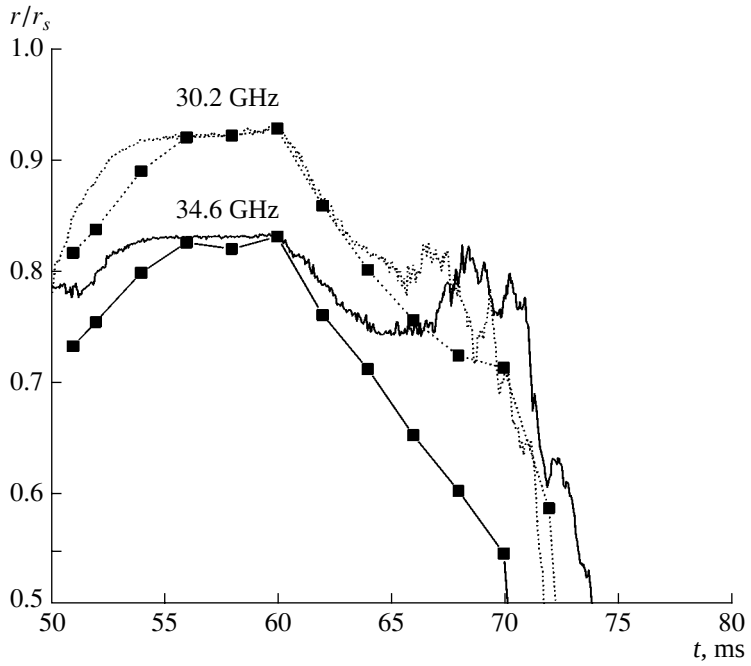

Fig. 9. Time evolution of the radial position of the critical surface calculated from the interferometric (squares) and reflectometric data for two probing frequencies (shot nos. 57371–57396). The reflectometric data are normalized to the interferometric data at t = 60 ms; r_s is the radius of the last closed magnetic surface.

ing power. It can be seen that, in this case, the spatiotemporal behavior of the poloidal velocity remains qualitatively the same as in the previous case.

Unfortunately, the very large plasma density gradient in the edge plasma and an insufficiently high accuracy of measurements of the plasma density profile (see Fig. 9) did not allow us to exactly determine the location of the scattering region and the corresponding poloidal wavenumbers of the scattered radiation. The measured poloidal velocities, as well as probe measurements, show the presence of a strongly inhomogeneous radial electric field (i.e., a large velocity shear) in the edge plasma. It is interesting that, according to our measurements, the sign of the velocity shear is different in the OH and ECRH regimes. Another problem (already mentioned in this paper) is that the mechanism for the formation of the recorded spectrum is not yet completely understood. It is likely that the antenna receives not only the backscattered radiation, but also the radiation repeatedly reflected from the plasma and the construction elements of the stellarator chamber. Note that the reflected radiation provides information about radial plasma fluctuations (in particular, fluctuations of the critical surface).

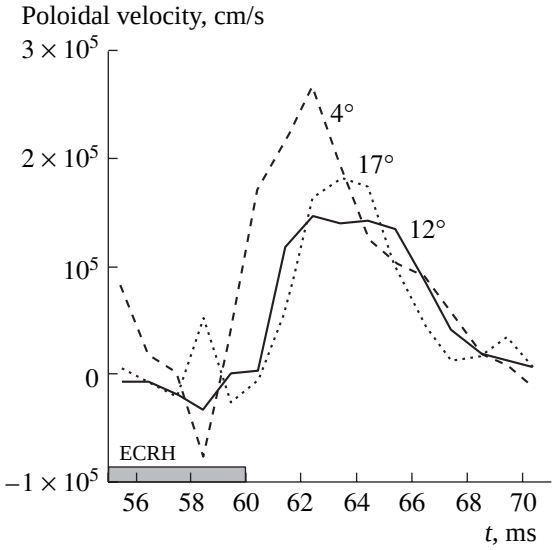

Fig. 10. Poloidal plasma velocities measured at three different radii for $\bar{n} = 2.5 \times 10^{13}$ cm^{-3} and $P_{\mathrm{ECRH}} = 300$ kW (shot nos. 57 498–57 520). The position of the scattered region is varied by varying the probing frequency and the antenna tilt angle.

6. CONCLUSIONS

Our experiments have demonstrated the possibility of using Doppler reflectometry in the L-2M stellarator. The time evolution of the poloidal velocity in the edge plasma has been measured in the OH and ECRH regimes at several different radii. An analysis of the scattered spectra has shown that the plasma density fluctuations and the radial profile of the poloidal plasma velocity in these two regimes differ qualitatively.

The experiments have revealed that the use of this diagnostics in L-2M is hampered by the complicated topology of the stellarator magnetic field and by the presence of strong spatial inhomogeneities of the electric field and plasma density in the edge plasma.

ACKNOWLEDGMENTS

We are grateful to V.V. Bulanin, K.A. Sarksyan, and G.M. Batanov for fruitful discussions. This work was supported in part by the Russian Foundation for Basic Research (project nos. 03-02-06628, 03-02-17269, and 04-02-16571) and the RF Presidential program for Support of Leading Scientific Schools (grant no. Nsh-1965.2003.2).

REFERENCES

1. V. V. Bulanin, S. V. Lebedev, L. S. Levin, and V. S. Roĭtershteĭn, Fiz. Plazmy **26**, 867 (2000) [Plasma Phys. Rep. **26**, 813 (2000)].
2. V. V. Bulanin, *XXX Zvenigorod Conference on Plasma Physics and Controlled Nuclear Fusion, Zvenigorod, 2003*, Abstracts of Papers, p. 8.
3. B. Brañas, M. Hirsch, J. Sánchez, and V. Zhuravlev, Rev. Sci. Instrum. **70**, 1025 (1999).
4. M. Hirsh, E. Holzhauer, J. Baldzuhn, and B. Kurzan, in *Proceedings of the 4th International Reflectometry Workshop, Cadarache, 1999.*
5. M. Hirsh and E. Holzhauer, Plasma Phys. Controlled Fusion **46**, 593 (2004).
6. V. A. Vershkov, D. A. Shelukhin, and K. A. Razumova, in *Proceedings of the 30th EPS Conference on Controlled Fusion and Plasma Physics, St. Petersburg, 2003*, ECA **27A**, 3.115 (2003).
7. A. O. Urazbaev, V. A. Vershkov, D. A. Shelukhin, *et al.*, in *Stochastic Models of Plasma Structural Turbulence*, Ed. by V. Yu. Korolev and N. N. Skvortsova (MAKS, Moscow, 2003), p. 62.
8. E. Z. Gusakov and A. V. Surkov, *XXX Zvenigorod Conference on Plasma Physics and Controlled Nuclear Fusion, Zvenigorod, 2003*, Abstracts of Papers, p. 92.
9. V. V. Abrakov, D. K. Akulina, E. D. Andryuhina, *et al.*, Nucl. Fusion **37**, 233 (1997).
10. S. E. Grebenshchikov, V. V. Abrakov, D. K. Akulina, *et al.*, in *Proceedings of the 15th International Conference on Plasma Physics and Controlled Nuclear Fusion Research, Seville, 1994* (IAEA, Vienna, 1995), Vol. 2, p. 327.
11. V. V. Bulanin and D. O. Korneev, Fiz. Plazmy **20**, 20 (1994) [Plasma Phys. Rep. **20**, 14 (1994)].
12. A. V. Knyazev, A. A. Letunov, and V. P. Logvinenko, Prib. Tekh. Éksp., No. 2, 5 (2004) [Instrum. Exp. Tech. **47**, 329 (2004)].
13. M. A. Tereshchenko, K. A. Sarksian, G. M. Batanov, *et al.*, in *Proceedings of the 30th EPS Conference on Controlled Fusion and Plasma Physics, St. Petersburg, 2003*, ECA **27A**, 1.18 (2003).

Translated by N.F. Larionova

Plasma Physics Reports, Vol. 31, No. 7, 2005, pp. 562–569. Translated from Fizika Plazmy, Vol. 31, No. 7, 2005, pp. 612–620.

DUSTY PLASMA

Formation of Quasi-Two-Dimensional Dust Structures in an External Electric Field

O. S. Vaulina, K. G. Adamovich, and I. E. Dranzhevskiĭ

Institute for High Energy Densities, Russian Academy of Sciences, Izhorskaya ul. 13/19, Moscow, 125412 Russia

Received May 31, 2004; in final form, September 15, 2004

Abstract—Conditions are considered under which quasi-two-dimensional extended structures are formed consisting of charged dust grains that are suspended in a gravitational field by an external electric field. Formulas are derived that describe the relationships between the parameters of the intergrain interaction potential, the number of dust grains, and the gradients of the linear electric field of the device. A criterion is proposed that determines the onset of a new dust layer in a quasi-two-dimensional dust system. © *2005 Pleiades Publishing, Inc.*

1. INTRODUCTION

Laboratory plasma, with its unique features, is an excellent experimental model for studying the properties of a strongly nonideal plasma and for providing a deeper understanding of the processes of the self-organization of matter in nature. Most of the experiments on the properties of dusty plasmas are carried out with discharges in gases (usually, in noble gases) at pressures P of 0.03–3 torr [1–7]. Such a plasma is a partially ionized gas in which the ion temperature ($T_i \sim 0.03$ eV) is much lower than the electron temperature ($T_e \sim 1$–7 eV) and the ion and electron densities, n_i and n_e, are on the order of 10^8–10^9 cm^{-3}. The radii of the dust grains that are usually used in terrestrial laboratory experiments lie in the range $a_d = 0.5$–5 μm, and the radii of the polymer or glass spherical grains are $a_d \approx 30$–40 μm. Owing to the high electron mobility, nonemitting dust grains introduced into a gas-discharge plasma acquire a substantial negative charge of $Z_d \approx (2\text{–}4)a_dT_e/e^2$ (about 10^3–10^5 times the elementary charge e) and can form liquid-like or solid-like quasi-steady dust structures with a dust number density n_d of 10^3–10^5 cm^{-3}. Depending on the experimental conditions, such structures either can be nearly uniform three-dimensional configurations or can be strongly anisotropic one-dimensional or quasi-two-dimensional configurations similar, e.g., to the chains of dust grains observed in a dc glow discharge plasma [6, 7] or to individual dust layers (usually, from one to ten layers) observed in the electrode region of an rf discharge [1–4, 8]. (For fixed discharge parameters, the maximum number of dust layers depends on the number of grains introduced into the discharge and on their equilibrium density within the layer.) The formation of such one-dimensional or quasi-two-dimensional structures is largely governed by the anisotropic nature of the distribution of electric fields in a (usually cylindrical) gas-discharge chamber.

Gas-discharge chambers are widely used to study the properties of a dusty plasma because the electric fields in them are capable of suspending negatively charged grains in the Earth's gravitational field and of confining grains in the radial direction (perpendicular to the gravitational field). Since discharges in noble gases are usually dominated by ambipolar diffusion processes, the gas-discharge plasma has a small excess of positive charge ($\delta n = (n_i - n_e) > 0$, $\delta n/n_i \lesssim 10^{-2}$), which balances the repulsion between negatively charged grains [9]. In dc discharges, a radial electric trap confining a cloud of dust grains in a direction perpendicular to the Earth's gravitational field is formed at the expense of the space charge distribution of plasma electrons and ions that is established as a result of their ambipolar diffusion toward the wall of the gas-discharge chamber. In gas-discharge chambers for initiating rf capacitive discharges, the rf electrodes are often positioned at fairly large distances from the chamber wall; this is why, in such discharges, a radial trap is formed by using a lower electrode that has a dip on its surface or is equipped with a metal ring several millimeters in height [1–4]. Experimental investigations show that, in the axial region of a gas-discharge chamber, $r < 0.6R^*$, the radial electric field strength $E(r)$ depends almost linearly on the distance r from the axis, whereas, at shorter distances from the chamber wall, it obeys the dependence $E(r) \propto r^3$ [10] (here, R^* is a characteristic spatial scale of the device, e.g., the radius of the electrode above which the dust grains are suspended or the radius of the gas-discharge tube). The grains are suspended in the positive space charge sheath just above the lower electrode (in an rf capacitive discharge plasma) or in the electric field of a striation (in a dc glow discharge plasma), mainly at the expense of the balance between the gravitational and electric forces. The role of other forces (namely, the thermophoretic force and the ion drag force) in the formation of a trap for negatively charged dust grains was considered in a

number of theoretical papers, where it was shown that, in most terrestrial laboratory experiments with dusty plasmas, the balance of forces acting in the system is almost completely governed by the electric field of the space charge of the surrounding plasma and by the gravitational force $m_d g$ [10, 11].

It is now generally accepted that the dust grains in a plasma interact through a screened Coulomb potential $U = (eZ_d)^2 \exp(-l/\lambda)/l$ (where l is the distance and λ is the screening length). This suggestion is well supported by the data from measurements of the radial interaction forces between two dust grains in an rf discharge chamber [12] and also by the results of numerical calculations of the structure of the screening cloud [13] at small distances from the grain, $l < 4$–$5\lambda_D$ (where λ_D is the Debye length). The larger the distance l from the grain, the weaker the screening effect; at distances $l \gg \lambda_D$, the potential $U(l)$ behaves as a power function, $U \propto l^{-2}$ [14]. Existing studies deal with solitary grains in a plasma. For extended plasma–dust structures, the pair additivity principle, which implies that the interaction potential in a system of particles is the sum of the potentials of interaction between two particles in isolated pairs, can fail to hold because of the processes that affect the spatiotemporal distribution of the grain density, i.e., various collective effects, perturbations of the external fields, etc. There is as yet no final explanation of how the shape of the intergrain interaction potential $U(l)$ is affected by the presence of other particles in a dust cloud, ionization processes in the surrounding plasma, collisions of electrons and ions with the neutral gas particles, and a host of other factors. The only way to solve this problem is to use model interaction potentials that should be modified to best fit those under actual experimental conditions (and, accordingly, can be checked experimentally by comparing theoretical predictions with the measurement data).

Based on an analytic model, Hebner *et al.* [15] constructed the equation of state for a quasi-two-dimensional crystal of dust grains interacting by means of a screened Coulomb potential in the linear electric field of a radial trap. The model proposed in that paper made it possible to determine the relationship between the gradient of the radial electric field, the number of dust grains, and the parameters of the intergrain interaction potential and to achieve good agreement between the calculated parameters of a dust layer forming in the electrode sheath of an rf discharge and the experimental data. This model has a number of drawbacks, however. Thus, its predictions are in rather poor agreement with the results of numerical simulations of systems in which the dust grains interact through a screened potential (Yukawa systems) such that $\kappa < 1$, where $\kappa = l_d/\lambda$ is the screening parameter and l_d is the characteristic distance between the grains [16]. This model is also incapable of predicting the onset of a new dust layer in the system under analysis.

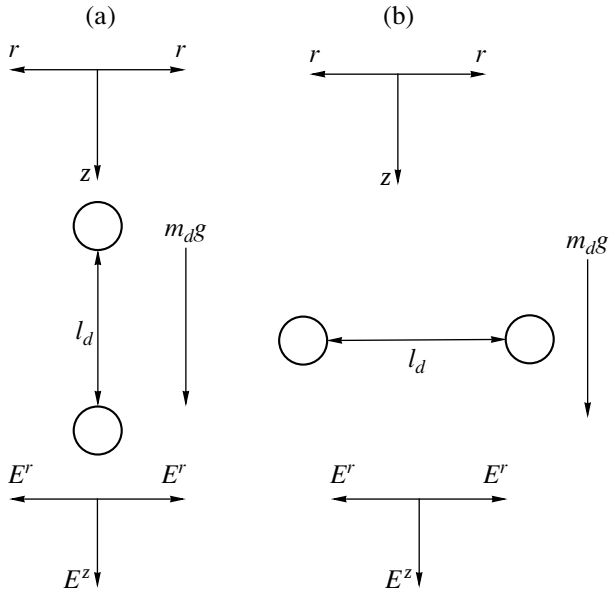

Fig. 1. Schematic illustration of (a) a vertical and (b) a horizontal configuration of two grains in the field of a trap.

The processes of the formation of extended layers of dust grains interacting through a screened potential in a gravitational field and a one-dimensional linear electric field were investigated by Totsuji *et al.* [17]. They found that a new dust layer forms when the dust density (the number of grains) in the original layer grows, the electric field gradient becomes gentler, and the screening length and dust charge increase. However, they did not propose an analytic condition that would combine these parameters into a criterion for the formation of a new dust layer.

2. TWO GRAINS

Before proceeding to an analysis of the formation of extended dust structures, we consider the problem about a horizontal or a vertical stable position of a pair of interacting dust grains of equal mass m_d and equal negative charge $Q = -eZ_d$, staying in a cylindrical trap a distance l from one another, in a gravitational field and in a linear electric field $E(r, z)$ with a radial component $E_r = \alpha r$ and a vertical component $E_z = E_z^0 + \beta z$ (see Fig. 1). Here, $r \equiv (x^2 + y^2)^{1/2}$ is the radial coordinate, z is the vertical coordinate in the direction of the gravitational field, α and β are the electric field gradients, and the field E_z^0 is determined by the balance of the forces acting in the system. Analogous investigations were carried out by Vladimirov and Samarian [18], who, however, gave no insight into some important aspects of the stability of a vertical and a horizontal configuration of two grains.

We denote by U_{12} the potential of the force exerted on the first grain by the second one (the potential of the force exerted on the latter by the former being U_{21}, accordingly), so this force is equal to $F_{21} = -dU_{21}/dl$ (the force acting on the second grain being $F_{12} = -dU_{12}/dl$). For an isotropic pair interaction, we have $U_{12} = U_{21}$ and $F_{21} \equiv F_{12}$; in the case of attractive interaction, the forces F_{21} and F_{12} are positive. The pair interaction can be anisotropic ($F_{21} \neq F_{12}$) in a vertical configuration of two grains in the electrode sheath of an rf discharge because of the attractive forces associated with ion focusing effects [19, 20].

We assume that, in the field of the trap, a vertical configuration of two dust grains separated by a distance l from one another is stable (Fig. 1a). Under this assumption, we consider the response of the system to small deviations (r_1, z_1) and (r_2, z_2) of grains 1 and 2 from their equilibrium positions in the **z** direction,

$$m_d d^2 z_1/dt^2 = -m_d \nu_{fr} dz_1/dt - eZ_d \beta z_1 + (z_1 - z_2) dF_{21}/dl, \quad (1a)$$

$$m_d d^2 z_2/dt^2 = -m_d \nu_{fr} dz_2/dt - eZ_d \beta z_2 + (z_2 - z_1) dF_{12}/dl, \quad (1b)$$

and in the radial direction,

$$m_d d^2 r_1/dt^2 = -m_d \nu_{fr} dr_1/dt - eZ_d \alpha r_1 + (r_1 - r_2) F_{21}/l, \quad (2a)$$

$$m_d d^2 r_2/dt^2 = -m_d \nu_{fr} dr_2/dt - eZ_d \alpha r_2 + (r_2 - r_1) F_{12}/l. \quad (2b)$$

Here, ν_{fr} is the grain friction coefficient. The equations describing the response of a horizontal configuration of two grains to their deviations from equilibrium positions can be written in a similar form. (To do this, in Eqs. (1a) and (1b), the derivatives dF_{21}/dl and dF_{12}/dl should be replaced by the ratios F_{21}/l and F_{12}/l and, accordingly, in Eqs. (2a) and (2b), the ratios F_{21}/l and F_{12}/l should be replaced by the derivatives dF_{21}/dl and dF_{12}/dl.) Thereby, the investigation of the stability of the two (vertical and horizontal) configurations of a pair of grains can be reduced to an analysis of the stability problem given by the following set of ordinary differential equations:

$$d^2 r_1/dt^2 = -\nu_{fr} dr_1/dt + a_{11} r_1 + a_{12} r_2, \quad (3)$$

$$d^2 r_2/dt^2 = -\nu_{fr} dr_2/dt + a_{22} r_2 + a_{21} r_1, \quad (4)$$

where a_{ij} are the corresponding coefficients of the terms describing the radial (r_1, r_2) and vertical (z_1, z_2) displacements of the grains. Note that a number of problems about the stable position of grains in an extended dust cloud can be reduced to differential equations similar to Eqs. (3) and (4) [21]. A dust system described by Eqs. (3) and (4) can become unstable because of the onset of dissipative or dispersive instabilities, whose development depends on the sign of the quantity

$$\delta = (a_{22} - a_{11})^2 + 4a_{12}a_{21}. \quad (5)$$

The condition for the onset of a dissipative instability ($\delta > 0$) can be written as

$$(a_{22} + a_{11}) + \{(a_{22} - a_{11})^2 + 4a_{12}a_{21}\}^{1/2} > 0. \quad (6)$$

A dispersive instability develops when $\delta < 0$, or, equivalently, under the condition

$$-2(a_{22} + a_{11})\nu_{fr}^2 + (a_{22} - a_{11})^2 + 4a_{12}a_{21} < 0. \quad (7)$$

Let us examine the stability of a vertical and a horizontal configuration of two grains by substituting the values of the corresponding coefficients a_{ij} into conditions (6) and (7). Since, in the problem in question, the quantity δ is always positive, the dispersive instability can be excluded from consideration. As for the originally equilibrium vertical grain configuration described by Eqs. (1a) and (1b) (see Fig. 1a), it may be subject to a dissipative instability under the condition

$$eZ_d\beta - d(F_{21} + F_{12})/dl < 0. \quad (8)$$

This condition implies that, being slightly displaced ($\Delta z \ll l$) from its equilibrium position in the **z** direction, the grain does not experience a restoring force. In the problem given by Eqs. (2a) and (2b), the condition for the onset of a dissipative instability can be written in the form

$$eZ_d\alpha - (F_{21} + F_{12})/l < 0. \quad (9a)$$

Under this condition, a charged grain that undergoes radial displacement does not experience a restoring force; accordingly, a vertical configuration of dust grains changes into a qualitatively new one—a horizontal stable configuration. With allowance for the fact that, according to the balance equations for the electric forces in a gravitational field, the distance between the grains in a vertically oriented configuration is equal to $l = (F_{12} + F_{21})/(\beta|eZ_d|)$, condition (9a) takes the form

$$\alpha < \beta. \quad (9b)$$

An analysis of the above relationships shows that two dust grains experiencing an attractive force, $F_{12} + F_{21} < 0$, can form a vertical configuration only for $\beta < 0$. Such a situation is unlikely to occur in the electrode region of an rf discharge, but it can take place in a dc discharge. Since the gas-discharge plasma in this case is usually electropositive ($\delta n = (n_i - n_e) > 0$, $\nabla \cdot \mathbf{E} > 0$), we can readily see that, for a cylindrical trap, the following inequality should hold:

$$2\alpha + \beta > 0. \quad (10)$$

For an initially equilibrium horizontal configuration of dust grains (see Fig. 1b), the conditions for the onset of a dissipative instability have the form

$$eZ_d\alpha - d(F_{21} + F_{12})/dl < 0, \quad (11)$$

$$eZ_d\beta - (F_{21} + F_{12})/l < 0. \quad (12a)$$

Since, for such a configuration, the distance between two grains can be expressed as $l = (F_{12} + F_{21})/(\alpha|eZ_d|)$, condition (12a) can be rewritten as

$$\alpha > \beta. \tag{12b}$$

Condition (11) implies that a grain that is displaced from its equilibrium position in the radial direction ($\Delta r \ll l$) does not experience a restoring force. Condition (12a) describes a qualitative change of a horizontal configuration of dust grains into a new (vertical) stable configuration. In the presence of an attractive force between two grains, $F_{12} + F_{21} < 0$, the configuration can be horizontal only when $\alpha < 0$. This indicates that the radial electric field is negative, which is impossible in discharges dominated by ambipolar plasma diffusion.

Hence, the conditions for the existence of a certain equilibrium configuration of two interacting dust grains are independent of the shape of the potential of pair interaction between them. The stability criterion for a vertical configuration of two grains can be written as $\beta < \alpha$; the opposite inequality, $\beta > \alpha$, is the stability criterion for a horizontal configuration. These considerations are confirmed by numerical simulations. When the linear field gradients are the same, $\alpha = \beta$, the two configurations in question are neutrally stable. Numerical simulations with $\alpha = \beta$ show that the system will not reach a steady state but rather will undergo a continuous sequence of bifurcations.

3. FORMATION OF A QUASI-TWO-DIMENSIONAL DUST LAYER IN A LINEAR ELECTRIC FIELD

It was pointed out above that, in numerical and laboratory experiments, a new dust layer forms when the vertical electric field gradient becomes gentler, the dust density grows, and the screening length and dust charge increase. Hence, when these parameters change, the configuration of a dust cloud can lose its stability and can evolve into a new stable configuration having a different number of dust layers. The stability problem for a uniform dust layer in a linear electric field can be solved in much the same way as the problem of the stability of a horizontal configuration of two dust grains. For a system with an isotropic pair interaction, the condition for the position of an individual grain 1 in a single dust layer to become unstable can be written in a form analogous to condition (12a):

$$eZ_d\beta - 2\sum_{i=1}^{N_d}[F_i(l_i)/l_i] < 0, \tag{13}$$

where F_i is the force of interaction between two dust grains separated by distance l_i ($i = 1$–N_d, with N_d being the total number of grains).

Let us consider a discrete problem for a plane extended crystalline system of dust grains interacting by means of a screened Coulomb potential. We assume that the system is axisymmetric and that the probability for a second grain to occur at the distance $l_j = jl_d$ from a first one is equal to $2\pi jl_d/N$, where l_d is the characteristic distance between two neighboring grains and $N = R/l_d \propto (N_d/\pi)^{1/2}$ is the number of characteristic distances along the radius R of the dust layer. Such a system can be regarded as being extended if $N \gg 2$ or, accordingly, if $N_d \gg 4\pi$. In this case, the second term in condition (13) can be written approximately as

$$\begin{aligned} &2\sum_{i=1}^{N_d}[F_i(l_i)/l_i] \\ &\approx 4\pi(eZ_d)^2\sum_{j=1}^{N}[(1 + j\kappa)\exp(-\kappa j)/j^2]/(\sqrt{2}l_d^3), \end{aligned} \tag{14}$$

where $\kappa = l_d/\lambda$ is the characteristic value of the screening parameter, $j = 1$–N, and the coefficient $1/\sqrt{2}$ accounts for the probability for the grains to be displaced from the position of the center of mass of the dust layer. Since the sum of the series in relationship (14) cannot be represented by a single analytic expression, we introduce the notation

$$\Sigma_E(N, \kappa) \equiv \sum_{j=1}^{N}[(1 + j\kappa)\exp(-\kappa j)/j^2],$$

and rewrite condition (13) for the formation of a new (second) dust layer in the form

$$\beta < 4\pi eZ_d\Sigma_E(N, \kappa)/(\sqrt{2}l_d^3). \tag{15}$$

Note that condition (15) also holds for a nonlinear electric field distribution E_z, provided that the quantity β is understood as the gradient of this field at the position where the dust layer is suspended. For a linear dependence of the field E_z on the z coordinate, condition (15) can easily be rewritten in a form suitable for describing the onset of any new layer of dust grains regardless of the initial number of dust layers. For instance, the criterion for the formation of a third layer in an equilibrium configuration consisting of two dust layers can be obtained by taking the sum of the gradient β in inequality (15) and the quantity $(\beta l_c/\lambda) \equiv -(2dF_c/dl_c)/|eZ_d|$. Here l_c is the distance between the neighboring layers and F_c is the force exerted by one dust layer on the dust grains of another layer. For a uniform extended layer of dust grains interacting through a Yukawa potential, this force can be written as $F_c = 2\pi(eZ_d/l_d)^2\exp(-l_c/\lambda)$; in this case, the distance between the layers can be obtained from the relationship $l_c = 2F_c/(\beta|eZ_d|)$.

For the values of the screening parameter such that $\kappa > 2$–3, which are typical of most terrestrial experiments with dusty plasmas, it is sufficient to take into account only the first term in the sum $\Sigma_E(N, \kappa)$. In this

case, condition (15) can be rewritten in a simple analytic form,

$$\beta < 4\pi e Z_d (1 + \kappa)\exp(-\kappa)/(\sqrt{2} l_d^3). \quad (16)$$

For a fairly extended, radially bounded, equilibrium dust layer in the form of a disk, the relationship between the radial gradient α of the external electric field and the parameters of the intergrain interaction potential can be obtained from the equation of state of the layer,

$$\sum_{i=1}^{N_d} \alpha r_i^2/2 = 2N_d T_d + N_d \sum_{i=1}^{N_d} [F_i l_i]/4. \quad (17)$$

The left-hand side of this equation is a virial describing the action of the external forces on the ith grain at the radial position r_i, and the right-hand side is the sum of the kinetic energy of a two-dimensional grain system and the virial of the intergrain interaction forces.

For a circularly symmetric crystalline dust layer in which the grains do not execute thermal motion ($T_d \longrightarrow 0$), this equation has the form

$$2\pi\alpha e Z_d \sum_{j=1}^{N} j^3 l_d^2 \approx (\pi N e Z_d)^2 \sum_{j=1}^{N} [(1 + j\kappa)\exp(-\kappa j)]/l_d. \quad (18)$$

Using analytic expressions for the sums in this equation, we can write the radial charge gradient as

$$\alpha \approx \frac{2\pi e Z_d}{(N-1)^2 l_d^3}\left\{\frac{1 - [1 + (N-1)\kappa]\exp(-N\kappa)}{1 - \exp(-\kappa)} + \frac{\kappa\exp(-\kappa)[1 - \exp(-(N-1)\kappa)]}{[1 - \exp(-\kappa)]^2} - 1\right\}. \quad (19a)$$

If we then introduce the notation $\Sigma_W(N, \kappa)$ for the factor that depends on the parameters N and κ, we obtain

$$\alpha \approx 2\pi e Z_d \Sigma_W(N, \kappa)/l_d^3. \quad (19b)$$

For a system of grains interacting by means of a Coulomb potential ($\kappa \longrightarrow 0$), relationship (19a) reduces to

$$\alpha \approx \frac{2\pi e Z_d}{(N-1) l_d^3}, \quad (20)$$

and, for $N\kappa \gg 1$, it becomes

$$\alpha \approx \frac{2\pi e Z_d}{(N-1)^2 l_d^3}\left(\frac{\exp(\kappa)(1 + \kappa) - 1}{[\exp(\kappa) - 1]^2}\right). \quad (21)$$

If the characteristic distance l_d is approximately equal to the most probable distance l_m between the neighboring grains at the points of a hexagonal lattice, $l_d \approx l_m = [2\pi R^2/(N_d\sqrt{3})]^{1/2}$, then we have $(N-1)^2 \approx R^2/l_d^2 = \sqrt{3} N_d/(2\pi)$ and formula (21) corresponds to the relationship that was proposed in [15] for the radial charge gradient in a disk-shaped dust cloud. If the characteristic distance l_d is close to the mean intergrain distance $\langle l \rangle$ ($l_d \approx \langle l \rangle = (S/N_d)^{1/2}$, where $S = \pi R^2$ is the area of the structure), then we have $(N-1)^2 \approx N_d/\pi$. In both these cases, expression (21) has a singularity at $\kappa \longrightarrow 0$. Accordingly, when this formula is used for small values of the screening parameter, $\kappa < 0.1$, it produces significant errors and leads to a deviation, δ, from the results of solving the problem numerically (for $\kappa \longrightarrow 0.02$, the deviation is as large as $\delta \longrightarrow$ 50–100%) [16]. Hence, for small values of the screening parameter ($\kappa < 0.1$), it is necessary to utilize a more exact formula (19a).

As a result, for a uniform quasi-two-dimensional system, condition (15) for the formation of a new dust layer can be represented as

$$\beta < \alpha\sqrt{2}\,\Sigma_E(N, \kappa)/\Sigma_W(N, \kappa) \propto \alpha/N_d. \quad (22)$$

For the range $\kappa >$ 2–3, the rapid convergence of the above series expansions allows this condition to be rewritten in the form

$$\beta < \alpha\sqrt{2}\,\pi/N_d. \quad (23)$$

We conclude this section with the following remark. Numerical simulations of quasi-two-dimensional finite-size dust structures in a linear electric field show that the mean distance between the grains changes (increases) in the radial direction (from the center of the dust disk toward its edge) [16]. A similar situation is observed in laboratory experiments [15]. Hence, criterion (22) for the formation of a new dust layer should be modified to include the nonuniformity of the dust density distribution within the system. This can be done with the help of numerical simulations.

4. SIMULATION OF THE DYNAMICS OF THE FORMATION OF QUASI-TWO-DIMENSIONAL DUST STRUCTURES

The conditions for the formation of quasi-two-dimensional dust structures were investigated by the molecular dynamics method based on solving a set of ordinary differential equations that consists of N_d equations of motion (where N_d is the number of grains) and takes into account the Langevin force $\mathbf{F}_{br}$, which drives the grains into stochastic (thermal) motion with a given kinetic temperature T_d. In numerical simulations, account was taken of the pair intergrain interaction force F_{int}, the external electric forces $\mathbf{F}_{\text{ext}} = eZ_d\mathbf{E}(r, z)$ of a cylindrically symmetric trap, and the gravitational

force $|\mathbf{F}_g| = m_d g$ acting on the grains in a dust cloud in the **z** direction,

$$m_d \frac{d^2\mathbf{l}_k}{dt^2} = \sum_j F_{\text{int}}(l)\big|_{l=|\mathbf{l}_k-\mathbf{l}_j|} \frac{\mathbf{l}_k-\mathbf{l}_j}{|\mathbf{l}_k-\mathbf{l}_j|} - m_d \nu_{\text{fr}} \frac{d\mathbf{l}_k}{dt} + \mathbf{F}_{\text{ext}} + \mathbf{F}_g + \mathbf{F}_{br}, \quad (24)$$

where $l = |\mathbf{l}_k - \mathbf{l}_j|$ is the intergrain distance, $F_{\text{int}}(l) = -eZ_d\partial\varphi/\partial l$, and $\varphi = eZ_d\exp(-l/\lambda)/l$ is the screened Coulomb potential.

The problem given by Eqs. (24) was solved numerically for two different cases: (i) for a system bounded in the radial direction by the linear electric field $E_r = \alpha r \neq 0$ and (ii) for a uniform extended dust layer with periodic boundary conditions in the **x** and **y** directions ($E_r = 0$). In both cases, the grains were assumed to be suspended in a gravitational field $F_g = m_d g$ by a linear electric field $E_z = E_z^0 + \beta z$ (where $E_z^0 = m_d g/(eZ_d)$) and the kinetic temperature of the grain was chosen so that the coupling parameter of the system satisfied the inequality $\Gamma^* = (eZ_d)^2(1 + \kappa + \kappa^2/2)\exp(-\kappa)/(l_d T_d) \gg \Gamma_c^*$, where $\Gamma_c^* = 106$ is the melting point of a three-dimensional Yukawa system [22].

In the first series of simulations ($E_r \neq 0$), the number of grains N_d was varied from 125 to 2500, the screening parameter was varied from 0 to about 9, and the external electric field gradients α and β were varied from ~100 V/cm^2 to ~10^{-4} V/cm^2. The formation of a new layer in a finite-size dust system is illustrated in Fig. 2, which shows the positions of the grains calculated for $\beta \gtrsim \beta_c \equiv 4\pi eZ_d\Sigma_E(N, \kappa)/(\sqrt{2}\langle l\rangle^3)$ (see condition (15)), $\beta = 0.8\beta_c$, and $\beta = 0.45\beta_c$. We can see that the formation of a new layer begins with the separation of grains in the central region of the structure. As the parameter β further decreases, the structure evolves into two parabolic layers consisting of approximately the same number of grains.

An analysis of the numerical results shows that, in this case, the condition for the formation of a new dust layer is close to condition (15) and the best agreement between the analytical and numerical results is achieved when the characteristic distance between the grains is chosen to be equal to the mean intergrain distance, $l_d = \langle l\rangle \equiv (\pi R^2/N_d)^{1/2}$ (see Fig. 3). It was also found that formula (19a) describes well the relationship between the number of grains in the system and the radial electric field gradient; in this case, however, the characteristic distance between the grains in the layer is determined by the most probable distance between them, $l_d = l_m \equiv [2\pi R^2/(N_d\sqrt{3})]^{1/2}$ (see Fig. 4). The fact that approximating formulas (15) and (19a) should be used with different characteristic intergrain distances stems primarily from the aforementioned nonuniformity of the dust density in the linear electric field of a cylindrical trap. This is why the relationship between the electric field gradients that corresponds to the conditions for the formation of a new layer in a quasi-two-dimensional dust system bounded by external radial electric fields differs from condition (22) and can be written as

$$\beta < \alpha\sqrt{2}\Sigma_E(N = (N_d/\pi)^{1/2}, \quad \kappa = \langle l\rangle/\lambda)/\Sigma_W(N = (\sqrt{3}N_d/2\pi)^{1/2}, \kappa = l_m/\lambda). \quad (25)$$

For $\kappa > 2$–3, we can take into account only the interaction between the nearest neighboring grains (see Figs. 3, 4) and reduce condition (25) to

$$\beta < \alpha 2\sqrt{2}\pi(1 + \langle l\rangle/\lambda) \times \exp(-\langle l\rangle/\lambda)/(\sqrt{3}N_d(1 + l_m/\lambda)\exp(-l_m/\lambda)). \quad (26)$$

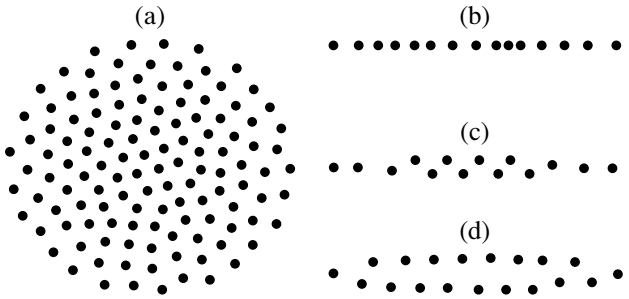

Fig. 2. Schematic illustration of the formation of a new layer in a finite-size system of grains for $N_d = 125$ and $\kappa = 0$: (a) the top view of the grain system for $\beta \gtrsim \beta_c$ and a cross section of the system along its axis for (b) $\beta \gtrsim \beta_c$, (c) $\beta = 0.8\beta_c$, and (d) $\beta = 0.45\beta_c$.

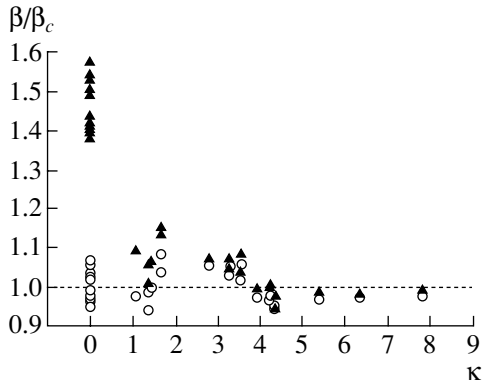

Fig. 3. The ratio of the vertical electric field gradient β on the line of the formation of a new dust layer in a finite-size dust system to the analytic parameter β_c defined by $\beta_c = 4\pi eZ_d\Sigma_E(N, \kappa)/(\sqrt{2}\langle l\rangle^3)$ (circles), according to condition (15), and by $\beta_c = 4\pi eZ_d(1 + \kappa)\exp(-\kappa)/(\sqrt{2}\langle l\rangle^3)$ (triangles), according to condition (16), as a function of the screening parameter $\kappa = \langle l\rangle/\lambda$.

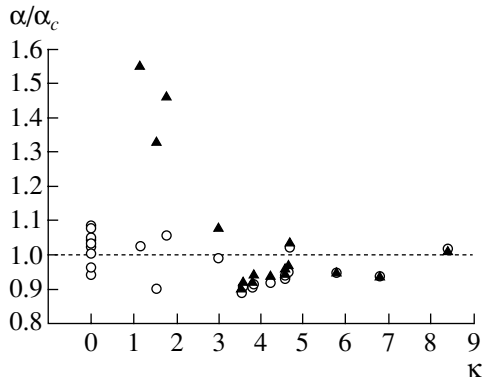

Fig. 4. The ratio of the radial electric field gradient α on the line of the formation of a new dust layer in a finite-size dust system to the analytic parameter α_c defined by $\alpha_c = 2\pi e Z_d \Sigma_W(N, \kappa)/l_m^3$ (circles), according to relationships (19a) and (19b), and by $\alpha_c = 2\pi e Z_d(1 + \kappa)\exp(-\kappa)/(\sqrt{3}N_d l_m^3)$ (triangles) as a function of the screening parameter $\kappa = l_m/\lambda$.

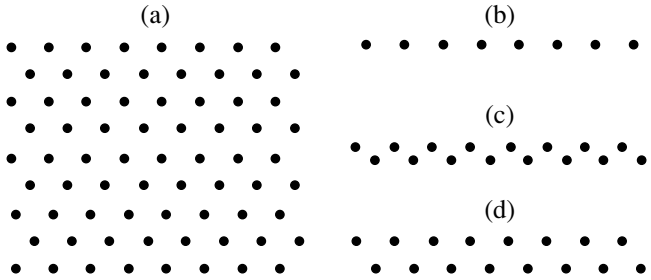

Fig. 5. Schematic illustration of the formation of a new layer in a uniform system of grains for $N_d = 100$ and $\kappa \approx 0.6$: (a) the top view of the grain system for $\beta \gtrsim \beta_c$ and a cross section of the system along its axis for (b) $\beta \gtrsim \beta_c$, (c) $\beta = 0.8\beta_c$, and (d) $\beta = 0.45\beta_c$.

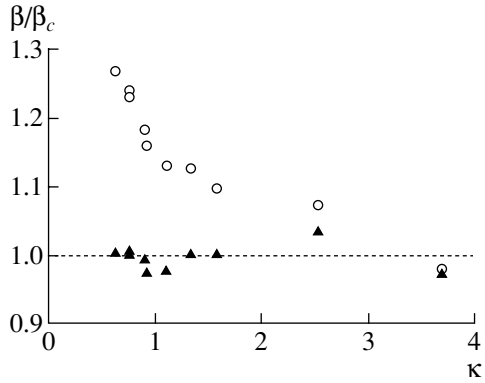

Fig. 6. The ratio of the vertical electric field gradient β on the line of the formation of a new dust layer in a uniform extended dust system to the analytic parameter β_c defined by $\beta_c = 4\pi e Z_d \Sigma_E(N, \kappa)/(\sqrt{2}\langle l\rangle^3)$ (circles), according to condition (15), and by $\beta_c = 4\pi e Z_d(1 + \kappa)\exp(-\kappa)/(\sqrt{2}\langle l\rangle^3)$ (triangles), according to condition (16) as a function of the screening parameter $\kappa = \langle l\rangle/\lambda$.

The equilibrium processes occurring in one-dimensional and three-dimensional extended dust systems are modeled by imposing periodic boundary conditions in the **x**, **y**, and **z** directions. In this case, the intergrain interaction potential is often cut off at a distance $l = l_{\text{cut}}$, which is determined by the condition for an electrically neutral system to be perturbed only slightly. Such a system has an excess of positive energy and the relevant problem is equivalent to that of the confinement of dust grains in a trap created by external electric fields or by other forces ensuring that a constant number of grains are trapped within a volume V at a pressure P [23], in accordance with the virial equation for the external forces.

Recall that we simulated a uniform extended dust layer by imposing periodic boundary conditions only in the **x** and **y** directions and by assuming that a gravitational force $m_d g$ acting on the grains in the **z** direction is balanced by the electric field force. The number of independent grains N_d in a computational cell was varied from 50 to 1000, the screening parameter κ was varied from about 0.6 to about 6, the cutoff distance for the interaction potential l_{cut} was varied from $5\langle l\rangle$ to $25\langle l\rangle$, and the external electric field gradient β was varied from about 100 V/cm^2 to about 10^{-2} V/cm^2. In contrast to the formation of quasi-two-dimensional dust structures in a radial electric field, the characteristic intergrain distance was found to be the same for all grains (the crystalline grain structure corresponds to a regular hexagonal lattice) and the separation of one dust layer into two similar layers (with a regular hexagonal structure) was found to occur simultaneously over the entire area of the computational cell (see Fig. 5). The relationship between the parameters of the system under the conditions of the formation of a new dust layer is shown in Fig. 6. The results obtained agree with those calculated for a nonuniform dust layer bounded by a radial electric field. Hence, in both cases, the criterion for the formation of a new dust layer is represented by condition (15) in which the characteristic distance between the grains is close to the mean distance between them: $l_d = \langle l\rangle \equiv (S/N_d)^{1/2}$, where S is the area of the computational cell in the case of an extended system or $S = \pi R^2$ is the area of a disk-shaped structure with a finite radius R.

5. CONCLUSIONS

We have considered the conditions for the existence of a vertical and a horizontal equilibrium configuration of a pair of interacting dust grains in the Earth's gravitational field and in the external electric field of a trap and have found that these conditions are independent of the shape of the potential of pair interaction between the grains and are governed exclusively by the relationship between the gradients of the external electric field. We have shown that it is the onset of dissipative insta-

bility that causes one configuration of two grains to change into another configuration.

We have analyzed the conditions for the formation of quasi-two-dimensional extended layers of charged dust grains that are suspended in a gravitational field by an external electric field and have determined the relationships between the parameters of the intergrain interaction potential, the number of grains, and the gradients of the linear electric field in the trap. We have also proposed a criterion for the onset of a new dust layer in a quasi-two-dimensional system of dust grains. The results obtained can readily be generalized to any modified analytic pair interaction potential and may be useful for passive diagnostics of the intergrain interaction parameters in quasi-two-dimensional structures forming in the electrode sheath of an rf discharge.

ACKNOWLEDGMENTS

This work was supported in part by the Russian Foundation for Basic Research (project no. 04-02-16326), INTAS (grant no. 01-0391), the US Civilian Research and Development Foundation for the Independent States of the Former Soviet Union (CRDF) (grant no. RU-P2-2593-MO-04), and the Russian Foundation for Support of Domestic Science.

REFERENCES

1. J. Chu and L. I, Phys. Rev. Lett. **72**, 4009 (1994).
2. H. Thomas, G. Morfill, V. Demmel, *et al.*, Phys. Rev. Lett. **73**, 652 (1994).
3. A. Melzer, T. Trottenberg, and A. Piel, Phys. Lett. A **191**, 301 (1994).
4. Y. Hayashi and K. Tachibana, Jpn. J. Appl. Phys. **33**, 804 (1994).
5. V. E. Fortov, A. P. Nefedov, V. M. Torchinskiĭ, *et al.*, Pis'ma Zh. Éksp. Teor. Fiz. **64**, 86 (1996) [JETP Lett. **64**, 92 (1996)].
6. A. M. Lipaev, V. I. Molotkov, A. P. Nefedov, *et al.*, Zh. Éksp. Teor. Fiz. **112**, 2030 (1997) [JETP **85**, 1110 (1997)].
7. A. P. Nefedov, O. F. Petrov, V. I. Molotkov, *et al.*, Pis'ma Zh. Éksp. Teor. Fiz. **72**, 313 (2000) [JETP Lett. **72**, 218 (2000)].
8. V. N. Tsytovich, Fiz. Plazmy **26**, 712 (2000) [Plasma Phys. Rep. **26**, 668 (2000)].
9. Yu. P. Raizer, *Gas Discharge Physics* (Nauka, Moscow, 1987; Springer-Verlag, Berlin, 1991).
10. O. S. Vaulina, A. A. Samaryan, O. F. Petrov, *et al.*, Fiz. Plazmy **30**, 988 (2004) [Plasma Phys. Rep. **30**, 918 (2004)].
11. T. Nitter, Plasma Sources Sci. Technol. **5**, 93 (1996).
12. U. Konopka, G. E. Morfill, and L. Ratke, Phys. Rev. Lett. **84**, 891 (2000).
13. J. E. Daugherty, R. K. Porteous, M. D. Kilgore, *et al.*, J. Appl. Phys. **72**, 3934 (1992).
14. J. Allen, Phys. Scr. **45**, 497 (1992).
15. G. A. Hebner, M. E. Riley, and K. E. Greenberg, Phys. Rev. E **66**, 046407 (2002).
16. H. Totsuji, C. Totsuji, and K. Tsuruta, Phys. Rev. E **64**, 066402 (2001).
17. H. Totsuji, T. Kishimoto, Y. Inoue, *et al.*, Phys. Lett. A **221**, 215 (1996).
18. S. V. Vladimirov and A. A. Samarian, Phys. Rev. E **65**, 046416 (2002).
19. S. V. Vladimirov and M. Nambu, Phys. Rev. E **52**, 2172 (1995).
20. A. V. Ivlev and G. Morfill, Phys. Rev. E **63**, 016409 (2001).
21. O. S. Vaulina, A. P. Nefedov, O. F. Petrov, *et al.*, Zh. Éksp. Teor. Fiz. **118**, 1325 (2000) [JETP **91**, 1147 (2000)].
22. O. S. Vaulina, S. V. Vladimirov, O. F. Petrov, *et al.*, Phys. Rev. Lett. **88**, 245002 (2002).
23. R. T. Farouki and S. Hamaguchi, Appl. Phys. Lett. **61**, 2973 (1992).

Translated by O.E. Khadin

Plasma Physics Reports, Vol. 31, No. 7, 2005, pp. 570–576. Translated from Fizika Plazmy, Vol. 31, No. 7, 2005, pp. 621–627.

DUSTY PLASMA

Vortex Dust Structures in the Track Plasma of a Proton Beam

V. E. Fortov*, V. A. Rykov, V. S. Filinov*, V. I. Vladimirov*, L. V. Deputatova*, O. F. Petrov*, V. I. Molotkov*, A. P. Budnik**, P. P. D'yachenko**, K. V. Rykov**, and A. V. Khudyakov****

**Institute for High Energy Densities, Russian Academy of Sciences, Moscow, 127412 Russia*

***Leĭpunskiĭ Research Institute for Physics and Power Engineering, Russian State Scientific Center, Obninsk, Kaluga oblast, 249020 Russia*

Received April 28, 2004; in final form, October 14, 2004

Abstract—Results are presented from experimental and theoretical investigations of the behavior of dust grains in a track plasma produced by a beam of accelerated protons. The dynamic ordered dust structures in a proton-beam-produced plasma are obtained for the first time. The processes leading to the formation of such structures are simulated numerically. The experimentally obtained dynamic vortex dust structures in a track plasma of a proton beam are explained theoretically, and the theoretical model developed to describe such a plasma is verified experimentally. Numerical investigations carried out by the method of Brownian dynamics made it possible to qualitatively explain the characteristic features of the formation of vortex dust structures. © *2005 Pleiades Publishing, Inc.*

1. INTRODUCTION

A fundamental property of a plasma produced by accelerated ions is its track structure [1–3]. When charged particles with initial velocities much higher than the Bohr velocity $v_B = 2.18 \times 10^8$ cm/s pass through matter, they create electron–ion pairs in a very narrow region around their trajectories. The energy of an ion during its deceleration decreases in an essentially continuous fashion because, every time the ion collides with an atom, it loses a small fraction of its energy. As a result, the intensity of a beam of monoenergetic ions remains essentially unchanged along their entire path length. The production of plasma by ion beams from accelerators provides radically new experimental conditions: in this case, the divergence of a beam of ionizing particles due solely to their numerous collisions with atoms is small and the beam current can be made high enough for the ion tracks to overlap substantially during their lifetime and thereby to produce a quasi-homogeneous plasma.

The objective of the present paper is to experimentally investigate the behavior of dust grains in a track plasma created by a beam of accelerated protons, to obtain dynamic ordered dust structures in a proton-beam-produced plasma, and to numerically simulate the processes leading to the formation of such structures.

The results of these investigations made it possible to reveal for the first time new effects related to collective phenomena in plasma–dust structures. Studying these phenomena may be of interest not only for fundamental science but also for their practical applications in rapidly developing plasma and beam technologies.

The experimentally obtained dynamic vortex dust structures in a track plasma produced by a proton beam are explained theoretically, and the theoretical model of such a plasma is verified experimentally. Numerical investigations carried out by the method of Brownian dynamics make it possible to explain the characteristic features of the formation of vortex dust structures. The results of calculations agree qualitatively with the experimental data.

2. EXPERIMENTAL INVESTIGATIONS

The experiments were performed on the ÉG-2.5 accelerator at the Leĭpunskiĭ Research Institute for Physics and Power Engineering (Obninsk, Russia). A schematic of the experimental setup is shown in Fig. 1. A 2-MeV proton beam was injected into the experimental cell along a horizontal path through a 1.2-cm-diameter window, which was covered by a 10-μm titanium foil and served also as a diaphragm and as a reference electrode. The beam current was $I = 1$ μA. In passing through the foil, the protons lost about 0.5 MeV of their energy and heated the foil to a temperature of 150°C.

The experimental cell had the form of a rectangular parallelepiped with a base of 8 cm and a height of 12 cm. The side faces of the cell were made of glass. The cell was irradiated by a planar laser ray with a waist of width from 100 to 200 μm. The laser light scattered by the grains was recorded by a charge-coupled device (CCD) camera and was converted into video images.

Inside the experimental cell, there was a 3-cm-diameter high-voltage electrode, positioned a distance of 7 cm from the reference electrode. The high-voltage

1063-780X/05/3107-0570$26.00 © 2005 Pleiades Publishing, Inc.

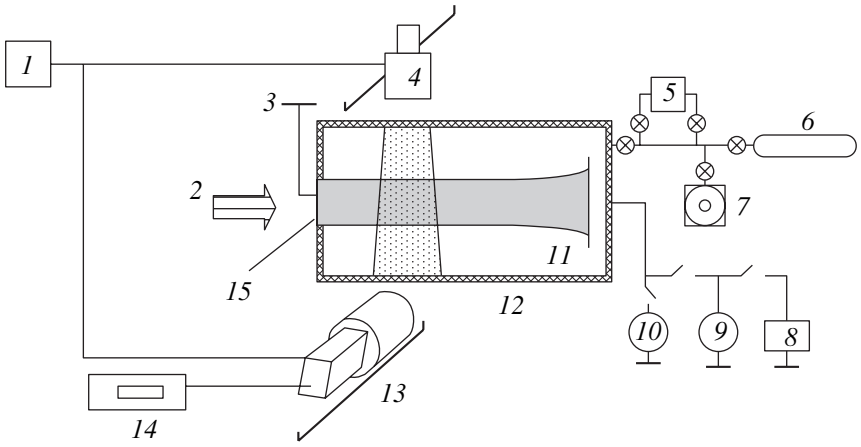

Fig. 1. Schematic of the experimental device: (*1*) servomotor, (*2*) proton beam, (*3*) ground, (*4*) laser, (*5*) container with dust grains, (*6*) container with a plasma-producing gas, (*7*) vacuum pump, (8) dc power supply, (*9*) voltmeter, (*10*) ammeter, (*11*) negative electrode, (*12*) experimental cell, (*13*) CCD camera, (*14*) video recorder, and (*15*) titanium foil.

electrode had three main functions. First, when a constant (positive or negative) potential was applied to the electrode, it created the electric field in the experimental cell. Second, it was used to measure the proton current in the evacuated cell. Finally, it was used as a probe to estimate the plasma floating potential in the gas-filled cell. For the gases under investigation (He, Kr, and Xe), the floating potential U_f in the absence of the applied external electric field was found to lie within the range from –0.5 to –0.4 V. The charge q of a dust grain was estimated from the formula

$$q = CU_f, \quad (1)$$

where C is the grain capacitance. The experiments were carried out with polydisperse cerium dioxide grains having a mean diameter of 1 μm. The negative grain charges calculated for the mean diameter from formula (1) were found to range from 140 to 170 units of the electron charge.

The gas–dust mixture was created by a pulsed injection of a gas jet from a fixed-volume injector into a metal-grid-bottomed container precontaminated with dust grains.

The results of experiments with krypton at two different pressures are illustrated in Figs. 2 and 3. In the first case (Fig. 2), the pressure (870 torr) was chosen so that the protons in their decelerated motion did not fly to the high-voltage electrode, which produced the external electric field. In Fig. 2, we clearly see the vol-

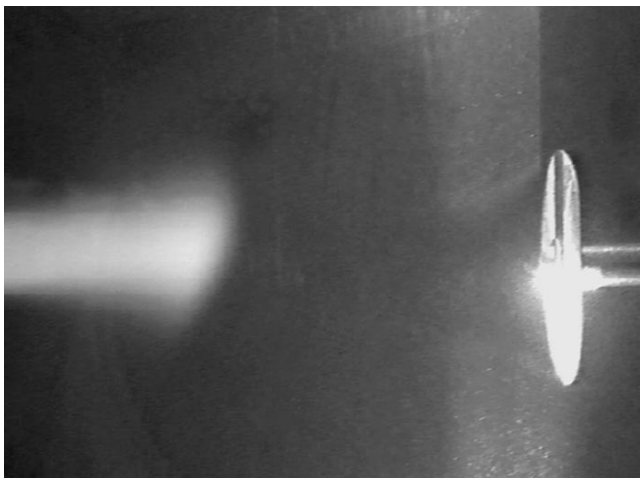

Fig. 2. Formation of a void in a dust structure. The experimental parameters and conditions are as follows: the working gas is krypton at a pressure of 870 torr, the dust grains are made of CeO_2, the electrode potential is –300 V, the energy of the beam protons is 2 MeV, and the beam current is 1 μA.

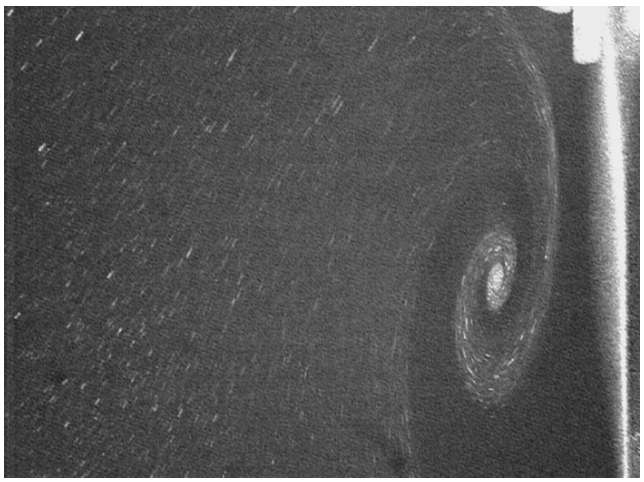

Fig. 3. Vortex in a dust structure. The experimental parameters and conditions are as follows: the working gas is krypton at a pressure of 128 torr, the dust grains are made of CeO_2, the electrode potential is –200 V, the energy of the beam protons is 2 MeV, and the beam current is 1 μA.

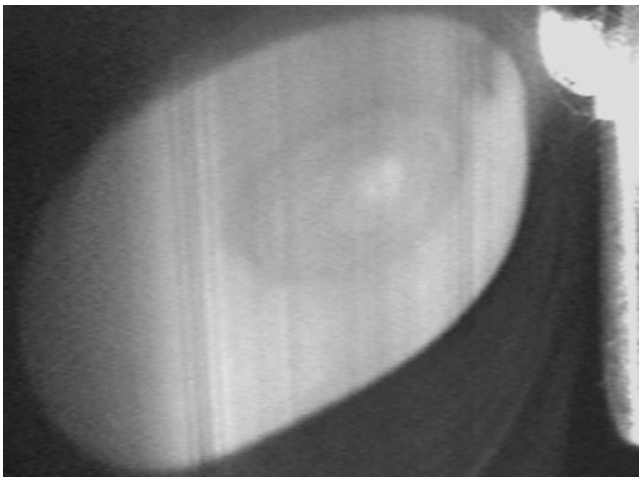

Fig. 4. Dust grain cloud. The experimental parameters and conditions are as follows: the working gas is helium at a pressure of 523 torr, the dust grains are made of CeO_2, the electrode potential is –200 V, the energy of the beam protons is 2 MeV, and the beam current is 1 μA.

ume occupied by the recombining track plasma, which emits radiation characteristic of krypton. When the high-voltage electrode is held at a negative potential of several hundred volts (from –100 to –500 V), an extended void is seen to form, which is more pronounced at a higher negative potential. When the electrode potential is zero or when the electrode is held at a positive potential, the void is seen to become contaminated with dust grains.

At lower pressures (100–400 torr), protons reach the high-voltage electrode. In this case, after the injection of a gas–dust mixture, dust grains form a vortex near the high-voltage electrode and below the proton beam (Fig. 3); the higher the absolute value of the applied potential, the greater the rotation velocity of the vortex. At higher dust densities, the dust grains group together into a cloud with sharp boundaries (Fig. 4); this process takes several minutes. The cloud has a smooth, streamlined shape; the instabilities that occur periodically within the cloud change its shape and again restore it. An important point is that the grains in the vortex and those in the cloud do not strike the electrode but rather flow around it a distance of several millimeters near the plane part of its surface and move away from its ends. All the structures persist for several tens of minutes; in the absence of an external electric field, the dust plasma component becomes stratified, as was mentioned in [4].

In a low-temperature plasma with a relatively low degree of ionization, such as, for example, a nuclear-track plasma or a track plasma, the main mechanism for neutralizing charged particles is dissociative recombination. During a time interval on the order of 1 ns, the atomic ions of inert gases become molecular ions, and the recombination proceeds via the reaction

$$e + A_2^+ \longrightarrow A + A^*, \quad (2)$$

where A is the atom of a noble gas, A_2^+ is its molecular ion, and A* is the atom in an excited state. Under steady-state conditions, the number of electron–ion pairs produced by protons is equal to the number of recombination events. This leads to the following equation for the electron and ion densities:

$$\frac{IE}{ewV} = \alpha n_- n_+, \quad (3)$$

where I is the proton current, E is the proton energy, e is the charge of a proton, w is the energy required for a fast ion to produce an electron–ion pair (for all gases, this energy is approximately equal to 30 eV), α is the dissociative recombination coefficient, $n_\pm$ are the electron and ion densities (which were set at equal magnitude), and V is the volume occupied by the plasma. In the experimental cell, this plasma volume was observed visually because the electron–ion recombination excites the emission of radiation characteristic of the gas under investigation. Estimates of the electron and ion densities from Eq. (3) give $n_+ \approx n_- \approx 10^{11}$ cm^{-3}. The electron temperature was estimated from the magnitude of the floating potential using the relationship [5]

$$T_e\,(\text{eV}) \approx e|U_f|/10. \quad (4)$$

The ion temperature was set equal to the room temperature. We numerically solved the following equation for the charging of dust grains:

$$\frac{dq}{dt} = I_+ - I_-. \quad (5)$$

The currents of positive ions and electrons to a grain, I_+ and I_-, were calculated in the same way as in [6]. The grain charges calculated for the mean grain diameter were found to lie in the range from 130 to 160 units of the electron charge, which correlates well with the estimate obtained from formula (1).

In order to explain the behavior of dust grains in a track plasma, the following circumstances should be kept in mind. First, protons deposit energy in the experimental cell at a rate of about 2 J/s; second, the convective gas flow drags the dust grains upward; and finally, the ions accelerated by the electric field transfer their momentum to the gas atoms in numerous collisions with them and thereby cause the gas to move toward the negative electrode [7, 8]. In addition, each of the grains is penetrated by a proton within a time of about 10 μs; in this case, two to five secondary electrons with an energy of ~2 eV are knocked out of it, and each proton can pass through several grains. This grain charging mechanism plays a role at low gas pressures, whereas, under actual experimental conditions, the main mechanism for grain charging is that described by Eq. (5).

Estimates show that, in experiment, the external electric field near the high-voltage electrode can be as strong as several thousands of V/m. The electric field

produced by the high-voltage electrode in its function as a probe when it is held at a negative potential expels negatively charged dust grains from the axial region of the experimental cell (Fig. 2). When the grains come into the proton beam, they are moved upward by convection. If the proton beam occupies the entire axial region of the experimental cell, then, far from the high-voltage electrode, the main mechanisms that cause the dust grain to move (together with the gas) toward the electrode are the acceleration of the gas by ions and the drag of the grains. This is evidenced by the increase in the velocity of the grains as the negative potential is increased in absolute value. Near the high-voltage electrode, however, the field becomes strong enough to repel the grains, which is confirmed by the presence of a grain-free layer near the electrode; the width of the layer is maximum near the electrode ends, where the field is the strongest. In the external electric field, the convective flows put the grains into vertical motion.

Hence, our experiments made it possible to reveal for the first time a new effect: the collective motion of cerium dioxide dust grains in a plasma produced during the deceleration of a proton beam from an accelerator. We observed compact vortex structures consisting of many dust grains and rotating about their axes. We also observed evolving dense dust clouds with sharp boundaries. Under fixed conditions, both types of dust structures were found to persist for several tens of minutes. The behavior of the dust grains was found to depend substantially on the strength of the external electric field.

3. COMPUTER SIMULATIONS OF THE FORMATION OF DYNAMIC DUST STRUCTURES

In the present paper, we make the first attempt to describe the formation of vortex dust structures in a track plasma produced by a proton beam. This is why the theoretical approach adopted for these purposes cannot pretend to completely describe the dust behavior under the conditions of our experiments. Our main aim here is to choose a reasonable model for describing the most characteristic features of the behavior of dust grains in a track plasma and to reveal the main physical mechanisms that ensure the levitation of the grains. Therefore, it is expedient to carry out computer simulations for the experimental conditions under which vortex structures in the gases under investigation (such as Kr) at the pressures of interest to us (e.g., at 128 torr) are stable. Such structures are shown in Fig. 3.

In order to investigate the levitation of dust grains and their mutual interactions, it is necessary not only to establish the mechanism for their charging but also to reveal the nature of the forces acting upon them. At present, several different mechanisms are being discussed in the literature that affect both the balance between the gravitational and electrostatic forces experienced by the levitated dust grains and the interactions between them (see [9–11] for details). Here, because of the complexity of the dynamic problem in question, we utilize a simplified approach that makes it possible to trace the formation of dynamic vortex structures and their evolution using a reasonable amount of computer time.

Dust grain motion was described by a set of Langevin equations that involve a stochastic force and take into account random collisions of plasma particles with dust grains. We also account for such factors as regular forces of interaction among the grains, the interaction of grains with the electrode bombarded by the beam protons, the ion drag force, the heat-convection-driven force, and the gravitational force. The resulting set of Langevin equations has the form

$$m_d \frac{d^2\mathbf{q}_k}{dt^2} = \sum_j \mathbf{F}_{\text{int}}(|\mathbf{q}_k - \mathbf{q}_j|) + \mathbf{F}_k^{\text{el}}(\mathbf{q}_k)$$

$$+ \mathbf{F}_k^{\text{drag}}(\mathbf{q}_k) + \mathbf{F}_k^{\text{convec}}(\mathbf{q}_k) + m_d\mathbf{g} - m_d\nu_{\text{fric}}\frac{d\mathbf{q}_k}{dt} + \mathbf{F}_k^{\text{Br}},$$

where m_d is the mass of a dust grain, $\mathbf{F}_{\text{int}}(|\mathbf{q}_k - \mathbf{q}_j|)$ is the force of the pair interaction between the grains, ν_{fric} is the characteristic friction rate, $\mathbf{F}_k^{\text{el}}$ is the force of interaction of the grains with the electrode, $\mathbf{F}_k^{\text{convec}}$ is the force exerted on the grains by heat convection, $\mathbf{F}_k^{\text{Br}}$ is the stochastic Langevin force originating from collisions of plasma particles with a dust grain, and $m_d\mathbf{g}$ is the gravitational force.

Although the negative charge of dust grains is relatively small and the characteristic distances between them are comparatively large, the coupling between the grains through a Coulomb screened potential was completely taken into account in solving the equations of their motion because the intergrain interaction parameter under the conditions of our experiments was on the order of unity. As was mentioned above, the grains also interacted with the electrode bombarded by the beam protons; in our simulations, this electrode was at a negative potential and thus repelled the oncoming dust grains.

Since the power of the proton beam was sufficiently high and since the degree of ionization of the plasma produced by it was low, we took into account the drag force $\mathbf{F}^{\text{drag}}$ exerted on dust grains by drift ion flows and by the flows of neutrals dragged by the ions. According to [12], the drag force $\mathbf{F}^{\text{drag}}$ is described by the expression

$$\mathbf{F}^{\text{drag}} \cong \frac{4}{3}\frac{|z|^2 e^4}{T_i^2} n m_i \nu_{T_i} \mathbf{U}\sqrt{2\pi}\ln\Lambda,$$

where z is the charge number of a dust grain, T_i is the ion temperature, M is the mass of an ion, n is the unper-

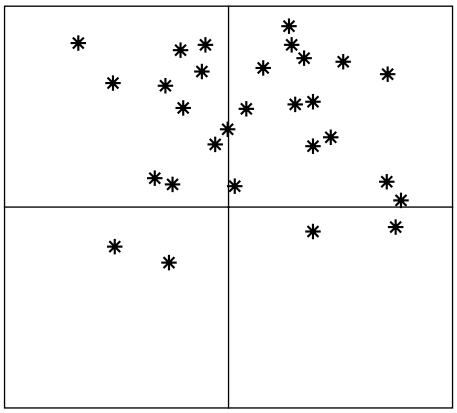

Fig. 5. Initial configuration ($t = 0$) of a dust cloud before the formation of a vortex.

turbed ion density, V_{T_i} is the ion thermal velocity, **U** is the ion drift velocity, $\ln\Lambda = \ln(\lambda/R_c)$ is the Coulomb logarithm, λ is the ion Debye radius, and $R_c = |z|^2e^2/m_iV_{Ti}^2$ is the Coulomb length. Because of the closed (finite) volume of the experimental cell and the continuity of the neutral fluxes within it, the lines of the force field $\mathbf{F}^{\text{drag}}$ are closed: inside the beam, they are predominantly directed toward the electrode and, outside the beam (at distances on the order of several beam diameters from it), they point in the opposite direction. The force field $\mathbf{F}^{\text{drag}}$ is axisymmetric about the axis of the proton beam. In numerical simulations, we used the following approximating formula:

$$\mathbf{F}_y^{\text{drag}} = \mathbf{F}_k^{\text{drag}}[\exp(-(\rho/\sigma_b)^4) - \alpha(1 - \exp(-(\rho/\sigma_b)^4))\exp(-(\rho/\sigma_c)^2)],$$

where σ_b is the beam radius; ρ is the distance from a grain to the beam axis in a perpendicular plane; σ_c is the sum of the beam and vortex radii; $\mathbf{F}_x^{\text{drag}} = \mathbf{F}_z^{\text{drag}} = 0$; $\alpha \approx (\sigma_c/\sigma_b)^2$ is the coefficient of attenuation of the reverse flow; and the indices *x*, *y*, and *z* stand for the corresponding projections of the force $\mathbf{F}^{\text{drag}}$ on the coordinate axes.

Recall that the heat released from the proton beam gives rise to heat convection, which is described in our model by the vector field $\mathbf{F}^{\text{convec}}$. By virtue of the closed volume of the experimental cell and the continuity of neutral fluxes, the stream lines of this vector field are also closed. The lines of the heat-convection-driven drag force are directed upward in the middle (axial) region of the horizontally passed proton beam; in the peripheral region (near the vertical side walls of the experimental cell and near the electrode surface), they are directed downward. For numerical simulations, the characteristic magnitude of the force $\mathbf{F}^{\text{convec}}$ was adjusted in such a manner that, in an infinite free space, the grains of a given weight moved upward with the experimentally observed characteristic velocity (on the order of 1 cm/s). The vector field of the convective force $\mathbf{F}^{\text{convec}}$ in the closed experimental cell was described by the approximating formula

$$\mathbf{F}_z^{\text{convec}} = \mathbf{F}^{\text{convec}}\{\exp[-((x/\sigma_b)^2 + \zeta(0.5 - y/L)^2)^2] - \beta(1 - \exp[-((x/\sigma_b)^2 + \zeta(0.5 - y/L)^2)^2])\} \times \exp(-(z/\sigma_c)^4),$$

where *x* and *z* are the corresponding distances from a grain to the beam axis in a perpendicular plane, *y* is the coordinate of the grain on the beam axis, β is the coefficient of attenuation of the reverse flow, ζ is a numerical coefficient on the order of unity, $\mathbf{F}_x^{\text{convec}} = \mathbf{F}_y^{\text{convec}} = 0$, and *L* is the distance from the diaphragm to the electrode.

The set of Langevin equations describing the motion of dust grains was solved numerically by the standard Brownian dynamics method. This method usually assumes calculations for a finite number *N* of particles in a computational cell of size *L* with periodic boundary conditions. In order for the computations to take a reasonable amount of time on the available computers, we restricted our simulations to $N = 200$–1000. Note that, for a smaller size *L*, as well as for a smaller number of dust grains in comparison to that in the experiments, the requirements on computational resources can be substantially reduced; this made it possible to reduce the run time of the code to about ten hours. The initial spatial distribution of dust grains and their initial velocities were specified with the help of a random-number generator.

4. DISCUSSION OF THE CALCULATED RESULTS

Here, we discuss the results from numerical simulations carried out by the standard method of Brownian dynamics. Figures 5–9 show the configurations of dust grains inside a thin planar vertical axial layer, calculated for three successive times.

Initially, the grains are distributed uniformly over the computational cell and move chaotically within it. As time elapses, the forces considered above, first, cause the motion of the grains to become more regular and then gradually put them into vortex circulation just below the proton beam. This vortex motion entrains a progressively larger number of grains that come down from the upper part of the cell to its lower part, where a stable vortex forms. Let us consider the motion of dust grains and the forces acting on them in more detail.

In Figs. 5–9, the proton beam propagates from left to right in the immediate vicinity of a horizontal axis. Recall that, in this region, the grains are subject to a

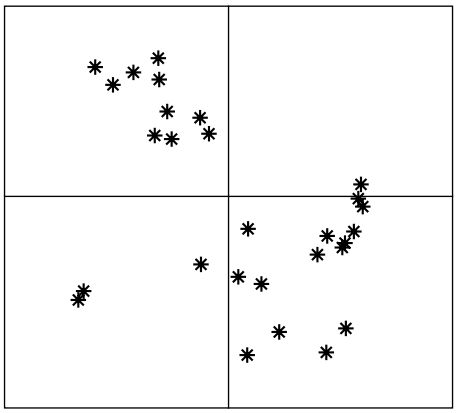

Fig. 6. Intermediate stage (t = 0.5 s) of the developing dust cloud during the formation of a vortex.

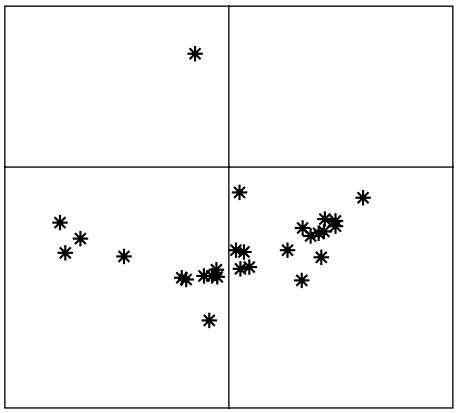

Fig. 7. Evolution of a dust vortex (t = 1 s).

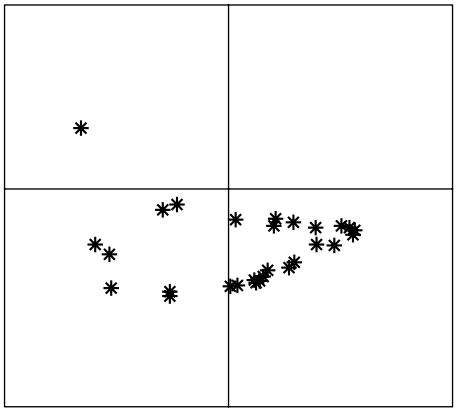

Fig. 8. Evolution of a dust vortex (t = 1.5 s).

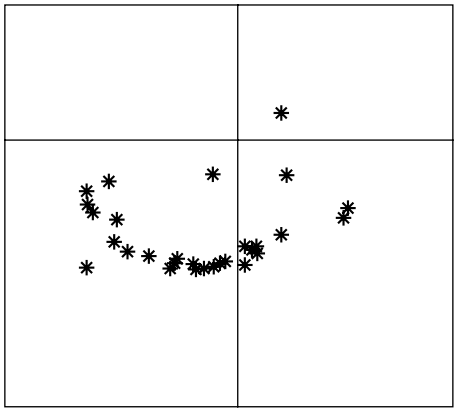

Fig. 9. Evolution of a dust vortex (t = 2 s).

drag force, which drives them into rapid rightward motion. Simultaneously, the dust grains in the central region of the cell experience an upward-directed heat convection force, which, however, does not have enough time to considerably affect the dust grains in their rapid rightward motion through this central region. As the grains approach the electrode (which is positioned perpendicularly to the beam axis in the peripheral region on the right side of the cell and is held at a negative potential), they are decelerated and begin moving downward under the action of three equidirectional forces, namely, the gravitational force, the proton-beam-driven drag force, and the heat convection force (which is directed downward in the cell's peripheral region in question). The grains that have come down to the lower part of the cell begin to experience the leftward-directed proton-beam-driven drag force. Under the action of this force, the dust grains continue moving downward and simultaneously they begin moving leftward and escape from the peripheral region of the cell. In the central part of the cell, the convection force is directed from bottom to top and causes the dust grains to rise upward. As the upwardly moving grains enter the proton beam region, they rapidly begin moving from left to right under the action of the drag force. This cycle of the grain's motion then repeats itself, resulting in the formation of a dust vortex. The grains that occur initially in the upper part of the cell are subject to forces similar to those described above. However, when these grains come into the region near the electrode (on the right side of the cell), they begin moving downward because the upward-directed proton-beam-driven drag force is not strong enough to counterbalance the downward-directed gravity and heat convection forces. As a result, almost all of the grains from the upper part of the cell fall progressively into its lower part and are entrained in the formation of the vortex.

It should be emphasized that, in numerical simulations, such dust motion results from solving the set of Langevin equations with allowance for the transfer of kinetic energy between grains and plasma particles. The mean kinetic energy of dust grains is determined by their mass and size, as well as by the proton beam intensity and the plasma viscosity. When the beam is

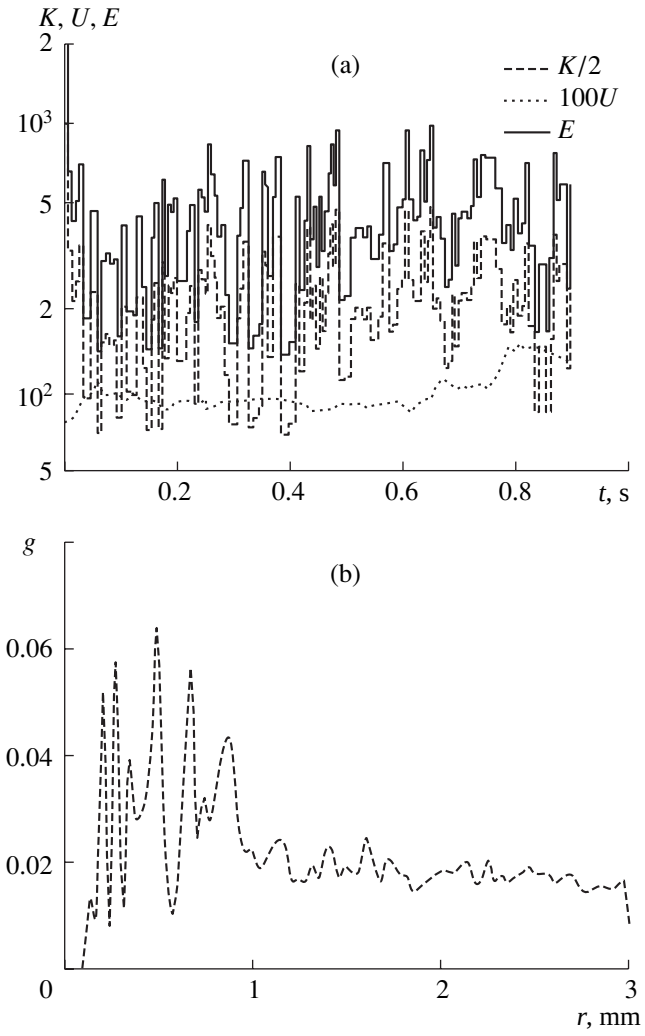

Fig. 10. (a) Time evolution of the kinetic (K), potential (U), and total (E) energies (in units of kT) of the dust plasma component for $T = 300$ K. (b) Pair correlation function as a function of the distance r between the grains.

absent, the mean kinetic energy of the grains is determined by the kinetic energy of the plasma particles and is equal to $3kT/2$. However, under the action of the drag force in the proton beam, the kinetic energy of the grains increases appreciably. With increasing distance from the beam-dominated region, the drag force acting on a grain that has escaped from this region decreases abruptly, and the total force exerted on the grain also decreases. As a result, the grain is decelerated by the plasma viscosity and its kinetic energy decreases. Figure 10a shows how the kinetic, potential, and total energies depend on time (which is given in seconds). The temporal variations in the kinetic and potential energies provide evidence for the presence of irregular oscillations. Figure 10b shows the pair correlation functions for the dust grains. The shape of the correlation functions indicates that, despite the vortex motion, dust grains have short-range order in their spatial positions. In Fig. 10, the distances are given in millimeters.

ACKNOWLEDGMENTS

We are grateful to A.I. Chusov for his help in preparing the experimental device and his assistance in experiments. We are also grateful to the Kernforschungszentrum Jülich (Germany) for providing us with the possibility for carrying out computations. The work was supported in part by the Russian Foundation for Basic Research (project nos. 04-02-97241 and 04-02-08085), the Presidium of the Russian Academy of Sciences under the "Parallel Computations and Multiprocessor Computational Systems" fundamental research program, the US Civilian Research and Development Foundation for the Independent States of the Former Soviet Union (CRDF), the Ministry of Education of the Russian Federation, and the Government of the Republic of Karelia (project no. PZ-013-02).

REFERENCES

1. V. E. Fortov, A. P. Nefedov, V. M. Torchinsky, *et al.*, Phys. Lett. A **258**, 305 (1999).
2. V. E. Fortov, V. I. Vladimirov, L. V. Deputatova, *et al.*, Dokl. Akad. Nauk **366**, 184 (1999) [Dokl. Phys. **44**, 279 (1999)].
3. V. E. Fortov, A. P. Nefedov, V. A. Rykov, *et al.*, Phys. Lett. A **284**, 118 (2001).
4. V. I. Vladimirov, L. V. Deputatova, V. A. Rykov, *et al.*, in *Proceedings of XVII International Conference on Physics of Extremal States of Matter, Elbrus, 2002*, p. 142.
5. Yu. P. Raizer, *Gas Discharge Physics* (Nauka, Moscow, 1987; Springer-Verlag, Berlin, 1991).
6. B. M. Smirnov, *Aerosols in Gases and Plasmas* (IVTAN, Moscow, 1990).
7. V. E. Fortov, V. I. Vladimirov, L. V. Deputatova, *et al.*, Dokl. Akad. Nauk **380**, 610 (2001) [Dokl. Phys. **46**, 697 (2001)].
8. V. I. Vladimirov, L. V. Deputatova, V. A. Rykov, *et al.*, Zh. Éksp. Teor. Fiz. **120**, 353 (2001) [JETP **93**, 313 (2001)].
9. P. P. D'yachenko and V. A. Rykov, At. Energ. **82**, 365 (1997).
10. V. L. Vladimirov, L. V. Deputatova, V. I. Molotkov, *et al.*, Fiz. Plazmy **27**, 37 (2001) [Plasma Phys. Rep. **27**, 36 (2001)].
11. A. V. Zobnin, A. P. Nefedov, V. A. Sinel'shchikov, *et al.*, Fiz. Plazmy **26**, 445 (2000) [Plasma Phys. Rep. **26**, 415 (2000)].
12. A. V. Ivlev, S. K. Zhdanov, S. A. Khrapak, and G. E. Morfill, Plasma Phys. Controlled Fusion **46**, B267 (2004).

Translated by G.V. Shepekina

Plasma Physics Reports, Vol. 31, No. 7, 2005, pp. 577–590. Translated from Fizika Plazmy, Vol. 31, No. 7, 2005, pp. 628–641.

NONLINEAR PHENOMENA

Equations for Nonlinear MHD Convection in Shearless Magnetic Systems

V. P. Pastukhov

Russian Research Centre Kurchatov Institute, pl. Kurchatova 1, Moscow, 123182 Russia

e-mail: past@nfi.kiae.ru

Received September 8, 2004; in final form, December 1, 2004

Abstract—A closed set of reduced dynamic equations is derived that describe nonlinear low-frequency flute MHD convection and resulting nondiffusive transport processes in weakly dissipative plasmas with closed or open magnetic field lines. The equations obtained make it possible to self-consistently simulate transport processes and the establishment of the self-consistent plasma temperature and density profiles for a large class of axisymmetric nonparaxial shearless magnetic devices: levitated dipole configurations, mirror systems, compact tori, etc. Reduced equations that are suitable for modeling the long-term evolution of the plasma on time scales comparable to the plasma lifetime are derived by the method of the adiabatic separation of fast and slow motions. © *2005 Pleiades Publishing, Inc.*

1. INTRODUCTION

The problem of anomalous transport of particles and energy is one of the central concerns of research on the magnetic confinement of high-temperature plasmas. In most theoretical papers on the subject, anomalous transport processes are attributed to the plasma temperature and density fluctuations driven by different types of drift instabilities (see, e.g., [1, 2]). In view of the fact that the transverse scales of such fluctuations are small, the anomalous transport problem is traditionally discussed in terms of the diffusion approximation with local transport coefficients. Numerous recent experiments have shown, however, that anomalous transport may often be of a different physical nature, which cannot in principle be described in the diffusion approximation.

In speaking about nondiffusive transport, note first of all that low-frequency plasma oscillations and resulting transport fluxes observed in many magnetic systems with very different magnetic field topologies and plasma parameters share fairly general regular features [3]. Thus, in tokamaks [4], stellarators [5, 6], tandem mirror systems [7], straight systems with a uniform magnetic field [8–10], and others, the spectra of the low-frequency fluctuations of the electric field and plasma density contain not only individual peaks associated with drift instabilities but also the so-called broadband component—a stochastically irregular spectral component that extends to very low frequencies and decreases according to a power law at higher frequencies. The spectra of this type are characteristic of a strong turbulence dominated by nonlinear structures (e.g., vortices) arising stochastically in the plasma. Accordingly, such turbulence is often called structural turbulence [5, 6, 8]. Fairly long radial and poloidal correlation lengths of the turbulence [4, 6], which are sometimes even comparable to the plasma radius (especially, for the low-frequency part of the broadband component), indicate that the expected nonlinear structures are large-scale and, accordingly, the resulting transport processes are nonlocal and nondiffusive in character.

The statistical properties of fluctuations observed in different magnetic systems (except for some specific details) are also rather similar [5, 6, 8]. For instance, the probability distribution functions (PDFs) that describe the increments of fluctuations and that were obtained by processing experimental data from different devices turn out to be non-Gaussian and to have heavy tails. This circumstance indicates that large-amplitude fluctuations make an enhanced contribution to the PDF and provides additional evidence for the nondiffusive nature of the transport processes.

Finally, in connection with the development of more sophisticated diagnostics, it became possible to clearly detect the presence of relatively long-lived macroscopic structures in some experiments. A striking example of such structures is the so-called blobs, which were first discovered in the scrape-off-layer (SOL) plasma in the DIII-D tokamak [11] and later in many other devices. Moving ballistically or semi-ballistically across the magnetic field, the blobs can carry the bulk of the global particle and energy flux in the SOL.

Hence, nondiffusive transport processes associated with the onset of one or another type of structural turbulence are fairly typical phenomena in the physics of magnetic plasma confinement; hence, they should be thoroughly studied both experimentally and theoretically. The difficulties standing in the way of experimental investigations of structural turbulence are quite

1063-780X/05/3107-0577$26.00 © 2005 Pleiades Publishing, Inc.

obvious. Of course, they will be overcome step by step with the development of more advanced diagnostics. At the same time, in research on such complicated turbulent phenomena, an important task is to provide an adequate theoretical basis, which would make it possible to reveal the fundamental features of the expected turbulence and to develop specific recommendations concerning the ways of controlling this turbulence and the resulting nondiffusive transport.

The presence (and even predominance) of large-scale structures in low-frequency turbulence in various magnetic systems presumably stems from the fact that the structures in a magnetized plasma should be highly stretched out along the magnetic field (as follows from theory and is confirmed by experiment [5–11]). As a result, the turbulence turns out to be two-dimensional (2D) or quasi-two-dimensional and is thereby characterized by both direct and inverse cascade processes, in which the energy is redistributed over the spectrum toward both small and large transverse scales. When dissipation is weak, the strong 2D turbulence should lead to the establishment of fairly universal spectra that decrease according to a power law toward the small scales and are almost independent of the spatial scale of the instability supplying them.

In view of the relatively large-scale and low-frequency nature of the expected dominating structures, a very fruitful approach to the theoretical study of 2D turbulence in a magnetized plasma seems to be that based on direct simulation of the nonlinear plasma dynamics in terms of the hydrodynamic moment equations (namely, the continuity equations, the equations of motion, the energy transport equations, etc.). These equations are a finite set of integral consequences of the basic kinetic equations, supplemented with certain conditions that make the set closed. Although this approach requires smaller amounts of computer time than does the kinetic approach, it is expected to provide a fairly complete self-consistent description of the evolution of the main macroscopic plasma parameters (such as the plasma density, the plasma velocity, and the temperatures of different plasma components). At the same time, it will lead to a better qualitative understanding of the dynamic processes under investigation and will greatly simplify their numerical simulation.

It should be emphasized that, with this approach, the dynamic modeling of the low-frequency turbulence can be further simplified. The reason is that even the aforementioned moment equations describe too many collective degrees of freedom, including stable fast (high-frequency) collective degrees of freedom (such as magnetosonic waves). Since these fast degrees of freedom have very high characteristic frequencies, they are not excited by the low-frequency turbulence under analysis and can be excluded from consideration by appropriately reducing the basic set of moment equations.

The reduced MHD equations for describing the plasma dynamics in tokamaks were originally proposed by B.B. Kadomtsev and O.P. Pogutse [12, 13]. Later on, this idea was developed in [14–16] and in many subsequent papers associated mostly with the name of H. Strauss. In all these papers, the magnetosonic waves were eliminated in one way or another from the equations of the nonlinear low-frequency plasma dynamics in tokamaks and stellarators with the help of the small parameter B_p/B_T (the ratio of the poloidal to the toroidal magnetic field). Later, in my papers [17, 18], a variational method for the adiabatic separation of fast and slow motions in continuous Lagrangian systems was developed. This method makes it possible to remove from consideration fast stable collective degrees of freedom of a dynamic system by using various small parameters and without violating the kinematic and dynamic conservation laws of the basic (unreduced) set of equations. This latter circumstance is important for simulating the long-term dynamic plasma evolution on time scales comparable to the plasma lifetime. This method will serve as a basis for the present study.

That the adiabatically reduced equations hold promise for modeling the nonlinear plasma dynamics was demonstrated in [19, 20], which were devoted to simulating the nonlinear 2D plasma convection that develops near the marginal stability of the plasma against a flute MHD mode in a simple cylindrical nonparaxial magnetic system (an equilibrium Z-pinch configuration with an internal levitated conductor). It was shown that the auxiliary heating and the local transport processes initially present in the plasma can modify the marginally stable plasma pressure profile to make it slightly unstable and to give rise to low-frequency turbulent convection and resulting nondiffusive transport processes. The frequency and spatial spectra of the nascent turbulent convection, as well as its statistical properties, were found to be similar to those observed experimentally [4–10]. In addition, the resulting nondiffusive transport processes calculated in terms of the model proposed in [19, 20] have exhibited some properties that are called, in different experiments, the internal transport barrier, L–H transitions, and impurity pinch.

The magnetic configuration that was discussed in [19, 20] is a simple model of a fairly wide class of highly nonparaxial magnetic confinement systems based on an alternative approach to the problem of MHD plasma stability [19]. This alternative approach utilizes plasma self-organization and assumes neither an absolute nor average minimum B in the plasma confinement region. Typical examples of the class of systems in question are levitated dipole configurations with an internal levitated current-carrying ring [21–23] (see Fig. 1) and straight [24] or toroidally linked [25] systems of mirror cells with so-called “divertor stabilization” (see Fig. 2). Although these two types of magnetic systems are different in appearance, the plasma in them is confined on the basis of the same principles, namely, those associated with the existence of a marginally stable pressure profile that drops to zero at the external separatrix [19]. Because of a growing interest

in such systems and with regard to a number of planned experiments, it is desirable that the dynamic model of nonlinear convection developed in [19, 20] be generalized in order to adequately take into account the high nonuniformity of the magnetic field configurations in actual devices.

In the present work, the method of the adiabatic separation of fast and slow motions [18] is used to construct reduced equations for describing the nonlinear convection and resulting transport processes in weakly dissipative plasmas of magnetic systems based on an alternative principle of MHD plasma stabilization. By analogy with [19, 20], as well as with most of the papers on the equilibrium and MHD stability of toroidal plasmas, the analysis is carried out in terms of a simple one-fluid MHD model with an isotropic plasma pressure. The equations derived make it possible to simulate the low-frequency flutelike plasma dynamics in arbitrary axisymmetric shearless magnetic systems with closed or open magnetic field lines. It can be expected that the results obtained by means of this generalized dynamic model will provide a more detailed comparison with the experimental data from various magnetic systems and will contribute to the development of the general theory of nondiffusive transport processes in a magnetized plasma.

This paper is organized as follows. The questions of the equilibrium and MHD stability of a plasma in the class of magnetic systems under consideration are discussed in Section 2. The adiabatically reduced equations of motion are derived in Section 3 in terms of the one-fluid MHD model with an isotropic plasma pressure. The reduced equations for the plasma density and plasma temperature are obtained in Section 4. In Section 5, the complete set of reduced equations is transformed into a final form consisting of two subsets of equations describing slow transport processes and relatively faster turbulent fluctuations. The main results of the work are briefly summarized in Section 6.

2. EQUILIBRIUM AND MHD PLASMA STABILITY IN AXISYMMETRIC SHEARLESS MAGNETIC SYSTEMS

The first stage of the analysis of any magnetic system consists in the investigation of the equilibrium and MHD stability of the plasma. For the magnetic systems under consideration, the discussion of these problems will enable us to correctly determine the basic plasma state near which the dynamic and transport processes of interest to us develop. As was mentioned above, the well-known one-fluid MHD model with an isotropic plasma pressure will serve as the basic dynamic plasma model. Being relatively simple and highly illustrative, this model can be conveniently used as a first step in investigating the self-consistent plasma dynamics. At the same time, it should be noted that a more adequate

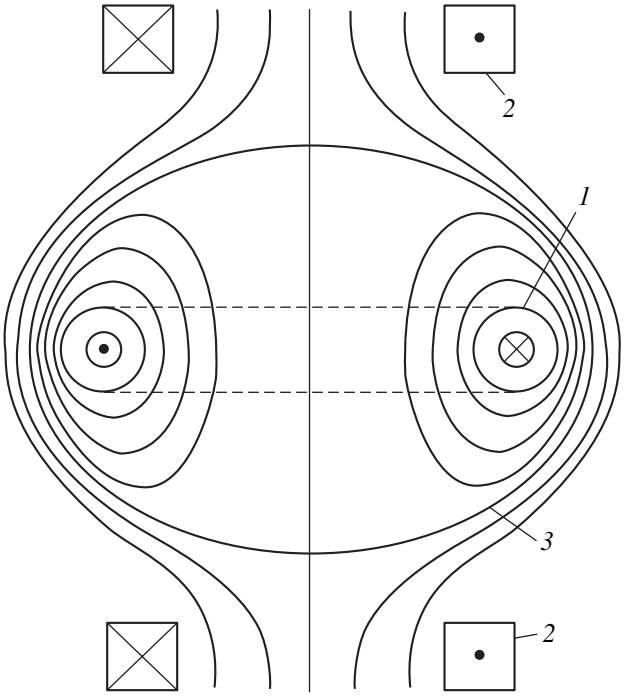

Fig. 1. Configuration of the magnetic field lines in a confinement system with an internal levitated ring: (*1*) internal ring, (*2*) external field coils, and (*3*) separatrix.

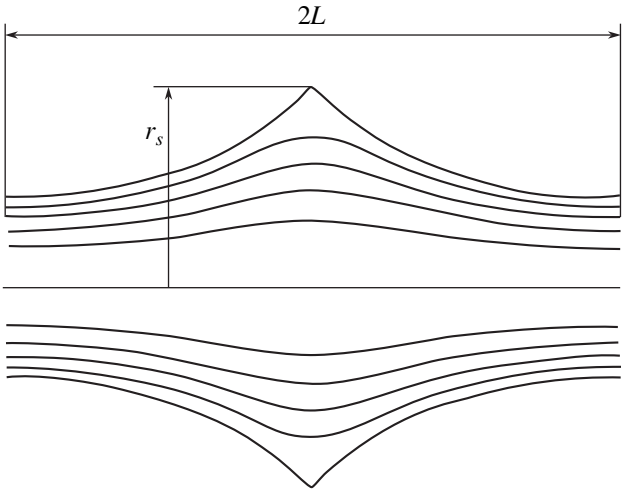

Fig. 2. Configuration of the magnetic field lines in a mirror cell with divertor stabilization.

bounce-averaged Kruskal–Oberman model leads to more optimistic marginally stable pressure profiles [26, 27].

Under the assumptions that the magnetic systems in question are axisymmetric and the plasma pressure is

isotropic, we can describe the plasma equilibrium with the Grad–Shafranov equation

$$\Delta^*\psi + 4\pi r^2 p'(\psi) = 0, \quad \Delta^*\psi \equiv r^2\left(\nabla\cdot\frac{\nabla\psi}{r^2}\right), \quad (1)$$

where r, ϕ, and z are cylindrical coordinates and $\psi(r, z)$ is the poloidal magnetic flux function. It is convenient to relate this flux function to the system axis for mirror devices (Fig. 2) and to the toroidal magnetic axis for tokamaks and for systems with an internal conductor (Fig. 1). The purely poloidal (and, accordingly, shearless) magnetic field of the system can be represented as

$$\mathbf{B} = \nabla\psi\times\nabla\varphi. \quad (2)$$

The class of systems under analysis allows equilibrium plasma states with $\beta = 8\pi p/B^2 \sim 1$ [28, 29].

It is convenient to analyze the stability of the static equilibrium plasma states by using a variational minimum-energy principle [30, 31], according to which arbitrary plasma displacements $\boldsymbol{\xi}$ from equilibrium should satisfy the condition

$$\delta^2 W = \int d^3\mathbf{r}\left\{\frac{1}{4\pi}[\nabla\times(\boldsymbol{\xi}_\perp\times\mathbf{B})]^2 + \gamma p(\nabla\cdot\boldsymbol{\xi})^2 - \frac{1}{4\pi}[\boldsymbol{\xi}_\perp\times(\nabla\times\mathbf{B})]\cdot[\nabla\times(\boldsymbol{\xi}_\perp\times\mathbf{B})] + (\boldsymbol{\xi}_\perp\cdot\nabla p)(\nabla\cdot\boldsymbol{\xi}_\perp)\right\} > 0; \quad (3)$$

where γ is the adiabatic index, the subscript $\perp$ refers to a direction perpendicular to the magnetic field, and the rest of the notation is standard. By minimizing the expression for $\delta^2 W$ with allowance for the fact that the first two terms in this expression are positive definite, we can single out two families of the most dangerous modes. The first family is characterized by the condition $\delta\mathbf{B} = \nabla\times(\boldsymbol{\xi}_\perp\times\mathbf{B}) = 0$, which corresponds to flute interchange modes, and the second family is characterized by the condition $\nabla\cdot\boldsymbol{\xi} = 0$, which corresponds to incompressible Alfvén modes.

In the shearless magnetic systems under consideration, the condition for plasma stability against flutelike modes is easily satisfied for any β value and leads to the following expression for $\boldsymbol{\xi}_\perp$:

$$\boldsymbol{\xi}_\perp\times\mathbf{B} = \nabla\delta\alpha(\psi,\varphi) \longrightarrow \boldsymbol{\xi}_\perp = \frac{1}{B^2}(\mathbf{B}\times\nabla\delta\alpha). \quad (4)$$

In this case, the second, positive definite, term in expression (3) can be minimized with respect to $\boldsymbol{\xi}_\parallel$ to yield the relationship

$$(\nabla\cdot\boldsymbol{\xi})_{\min} = \langle\nabla\cdot\boldsymbol{\xi}_\perp\rangle \equiv U^{-1}\int_-^+(\nabla\cdot\boldsymbol{\xi}_\perp)dl/B,$$
$$U(\psi) = \int_-^+ dl/B. \quad (5)$$

Here and below, the angle brackets $\langle\ldots\rangle$ denote averaging over the specific volume U of a magnetic flux tube. The integration in relationship (5) is carried out over the entire closed magnetic field line or along the entire length of the magnetic field line within the plasma region in an open system.

With expressions (4) and (5), condition (3) gives the following criterion for plasma stability against flute modes [31]:

$$U'(\psi)(p'(\psi) + \gamma p U'/U) > 0, \quad (6)$$

which implies that, in the absence of an average magnetic well (i.e., for $U'(\psi) > 0$), the plasma is stable only when its pressure decreases sufficiently gradually with radius. The marginally stable pressure profile has the form

$$S \equiv pU^\gamma = \text{const}, \quad (7)$$

where S is a single-valued function of the entropy density of a magnetized plasma [19, 20]. In contrast to the flute modes, incompressible Alfvén modes in typical shearless systems are unstable only for $\beta > \beta_{cr} \sim 1$ (see [19, 32–34]).

The existence of a marginally stable pressure profile creates conditions for relatively quiescent confinement based on the self-organization of the plasma according to the following scenario: the auxiliary heating and the initial (e.g., classical) heat conduction distort the original pressure profile to make it weakly unstable, and the resulting instability excites and maintains the nonlinear MHD convection, which tends to restore the marginally stable pressure profile and gives rise to an anomalous nondiffusive transport of heat and plasma particles. In accordance with the above analysis of the MHD plasma stability, it can be concluded that, in shearless magnetic systems with $\beta < \beta_{cr}$, the most dangerous type of plasma motions that is responsible for nondiffusive transport processes is represented by nonlinear flute modes developing near their marginal stability. Due to the closeness to the instability threshold, the frequencies of these modes should be relatively low. In this case, higher-frequency stable modes, such as magnetosonic and Alfvén waves, can be excluded from consideration in further analysis.

3. DERIVATION OF ADIABATICALLY REDUCED EQUATIONS OF MOTION

In accordance with the conclusions reached in the previous section, the task now is to study the nonlinear plasma convection driven by a flute MHD mode near a plasma state with a marginally stable pressure profile S = const. We assume that $\beta < \beta_{cr} \sim 1$; in this case, Alfvén modes are stable. We also assume that, during the development of self-consistent convection, the deviation from the marginally stable pressure profile is on the order of the small parameter $\epsilon^2 \ll 1$. In other words, we assume $a|\nabla S| \sim \epsilon^2 S$, where a is the characteristic transverse plasma size. In this case, the characteristic frequencies of the nonlinear flute convection are on the order of $\omega \sim \epsilon k_\perp c_s$, where c_s is the speed of sound. These frequencies are much lower than the characteristic frequencies of the stable magnetosonic ($\omega \sim k_\perp c_A$) and incompressible Alfvén ($\omega \sim k_\parallel c_A$) waves. It is reasonable to expect that the kinetic energy of this self-consistent convection should saturate at a level of the free potential plasma energy, which in turn is related to the deviation from the marginally stable pressure profile. For this reason, the kinetic energy should be on the order of ϵ^2.

In order to exclude from consideration the fast (high-frequency) collective degrees of freedom of the basic set of dynamic equations, we use the variational method of the adiabatic separation of fast and slow motions (the ASM method) [18]. To do this, we represent the variation of the Lagrangian of the ideal one-fluid MHD model in the form

$$\delta\mathcal{L} = \int d^3\mathbf{r}\left\{\rho\mathbf{v}\cdot\delta\mathbf{v} + \frac{v^2}{2}\delta\rho + \frac{1}{U^\gamma}\frac{\boldsymbol{\xi}\cdot\nabla S}{\gamma-1} - \frac{1}{4\pi}\mathbf{B}\cdot[\nabla\times(\boldsymbol{\xi}_\perp\times\mathbf{B})] + \frac{\gamma p U}{\gamma-1}\nabla\cdot\frac{\boldsymbol{\xi}}{U}\right\}, \quad (8)$$

where, unlike in condition (3), $\boldsymbol{\xi}$ is the plasma displacement from an arbitrary dynamic state.

The ASM method begins with searching for an adiabatic transformation $\boldsymbol{\xi}_a(\mathbf{r}, t)$ that leaves the Lagrangian unchanged to within terms on the order of ϵ^2. According to [18], this transformation has the meaning of an approximate relabeling symmetry transformation with respect to fast motions. In accordance with the above order-of-magnitude estimates, the first three terms in representation (8) for $\delta\mathcal{L}$ are on the order of ϵ^2, while for arbitrary displacements $\boldsymbol{\xi}$, the last two terms are on the order of unity. Consequently, the transformation that converts $\delta\mathcal{L}$ into $\delta_a\mathcal{L} \sim O(\epsilon^2)$ should satisfy the conditions

$$\nabla\times[\boldsymbol{\xi}_{a\perp}\times\mathbf{B}] = 0, \quad \nabla\cdot(\boldsymbol{\xi}_a/U) = 0. \quad (9)$$

The first of these conditions requires that the magnetic field be unperturbed and makes it possible to exclude from analysis magnetosonic and Alfvén modes. The second imposes additional restrictions on the displacement $\boldsymbol{\xi}_{a\parallel}$ and, as can be readily seen, enables us to exclude from consideration stable longitudinal acoustic waves with characteristic frequencies of $\omega \sim k_\parallel c_s$. It is easy to see that these two conditions are equivalent to conditions (4) and (5), which determine the functional structure of the most unstable flute perturbations.

In order to write an explicit expression for $\boldsymbol{\xi}_a$, it is convenient to supplement the coordinates ψ and φ with the third independent flux coordinate ζ satisfying the following two conditions: (i) the Jacobian should be nondegenerate ($J = (\nabla\psi\times\nabla\varphi)\cdot\nabla\zeta \neq 0$), and (ii) the increment in ζ along the entire magnetic field line should not depend on ψ and φ ($\zeta_+ - \zeta_-$ = const). For systems with closed magnetic field lines, these two conditions imply that the role of ζ can be played by any monotonically varying poloidal angular function; in this case, we have $\zeta_+ - \zeta_- = 2\pi$. For mirror systems, it is convenient to choose $\zeta = z$, so we have $J = B_z$. In terms of the three new coordinates, the integration over the flux tube volume becomes

$$\int_-^+ dl/B = \int_-^+ d\zeta/J|_{\psi,\varphi},$$

and the adiabatic transformation $\boldsymbol{\xi}_a(\mathbf{r}, t)$ satisfying conditions (9) can be represented as

$$\boldsymbol{\xi}_a = \frac{1}{B^2}(\mathbf{B}\times\nabla\delta\alpha(\epsilon t, \psi, \varphi)) + \mathbf{B}\lambda\partial_\varphi\delta\alpha(\epsilon t, \psi, \varphi),$$
$$\lambda = U\partial_\psi\int_0^\zeta\frac{d\zeta}{UJ} + \frac{\nabla\psi\cdot\nabla\zeta}{r^2B^2J}. \quad (10)$$

Hereafter, we assume for simplicity that the system is symmetric with respect to $\zeta = 0$, so the functions B, J, and r are even in ζ. The generalization to an asymmetric system is a simple matter but leads to more involved expressions. The dependence on time in the form ϵt symbolizes the slow variation in the corresponding functions in comparison to the characteristic time scales of the fast stable oscillations.

One of the most important principles of the ASM method is the following: the "adiabatic" velocity field $\mathbf{v}_a$ that does not perturb fast stable degrees of freedom and makes it possible to describe the relatively slow (reduced) dynamics of the system should have the same functional structure as the adiabatic transformation $\boldsymbol{\xi}_a$, specifically,

$$\mathbf{v}_a = \frac{1}{B^2}(\mathbf{B}\times\nabla\Phi(\epsilon t, \psi, \varphi)) + \mathbf{B}\lambda\partial_\varphi\Phi(\epsilon t, \psi, \varphi) \sim \epsilon c_s. \quad (11)$$

It should be stressed that, according to relationship (11), the three-dimensional vector field $\mathbf{v}_a$ is completely described by one 2D scalar function $\Phi(\epsilon t, \psi, \varphi)$, which coincides with the electric field potential to within a constant factor.

In accordance with the logic of the ASM method, it is natural to slightly extend and generalize the notions of the *adiabatic transformation* and *adiabatic velocity* by adding to expressions (10) and (11) a *complementary* small displacement $\boldsymbol{\xi}_s \sim \epsilon^2\boldsymbol{\xi}_a$ and *complementary* low velocity $\mathbf{v}_s \sim \epsilon^2\mathbf{v}_a$. In particular, the displacement $\boldsymbol{\xi}_s$ can be represented in the following general form:

$$\boldsymbol{\xi}_s = \frac{1}{B^2}(f_\psi(\mathbf{B}\times\nabla\psi) + f_\varphi(\mathbf{B}\times\nabla\varphi)) + \frac{\mathbf{B}}{B}\xi_{s\|}, \quad (12)$$

where f_ψ, f_φ, and $\xi_{s\|}$ are arbitrary functions on the order of ϵ^2. In this case, the variation of the Lagrangian $\delta\mathcal{L}$ is small only due to the smallness of $\boldsymbol{\xi}_s$; this circumstance does not impose any restriction on the coordinate dependence of the functions f_ψ, f_φ, and $\xi_{s\|}$. On the other hand, in deriving the sought reduced equations of motion, we can use the smallness of the functions $\boldsymbol{\xi}_s$ and $\mathbf{v}_s$ to ignore all inertial terms associated with them. In essence, it is in the ignoring of such inertial terms that the reduced equations of motion differ from the basic complete equations.

Allowance for the inertialess velocity field $\mathbf{v}_s$ indicates that, in the basic equations, we eliminate fast stable oscillations, while keeping slow variations in quasi-steady plasma parameters, associated mainly with dissipative processes. Since the adiabatic velocity field $\mathbf{v}_a$ does not perturb the magnetic field, we can take into account the finite resistivity to reduce the well-known frozen-in equation to the form

$$\partial_t\mathbf{B} = \nabla\times((\mathbf{v}_s\times\mathbf{B}) - D(\nabla\times\mathbf{B})), \quad (13)$$

where $D = c^2/4\pi\sigma$ is the classical resistive diffusion coefficient. From Eq. (13) we see that the velocity $\mathbf{v}_s$ should vary on time scales characteristic of the dissipative processes. At this point, it is appropriate to note that, according to the results of [19, 20], the value of the small parameter ϵ^2, determining the order of magnitude of the plasma deviation from a marginally stable equilibrium state, also results from the competition between the ideal convection and the dissipative processes, which are characterized by the thermal diffusivity χ, the viscosity coefficient η, and the resistive diffusion coefficient D. Consequently, in accordance with [19, 20], we set

$$\epsilon \sim (\chi/ac_s)^{1/3} \ll 1,$$

which leads to the estimate $\partial_t v_s \sim \epsilon^3 kc_s v_s$.

In the previous section, the equilibrium magnetic field was represented as $\mathbf{B} = \nabla\psi\times\nabla\varphi$. The form of the function $\Phi(\epsilon t, \psi, \varphi)$ implies in fact that this representation is conserved throughout the magnetic field evolution. For this to be the case, it is necessary to introduce the functions $\psi(t)$ and $\varphi(t)$ in an appropriate manner. The plasma should evolve in a way that does not break the axial symmetry of the magnetic field. It is, therefore, reasonable to assume that the φ coordinate does not change with time,

$$\partial_t\varphi = -(\mathbf{v}_s\cdot\nabla\varphi) = 0,$$

and to satisfy Eq. (13) only at the expense of temporal variations in $\psi(t)$,

$$\partial_t\psi = -(\mathbf{v}_s\cdot\nabla\psi) + Dr^2(\nabla\cdot(\nabla\psi/r^2)). \quad (14)$$

In this case, the velocity $\mathbf{v}_s$ can be represented as

$$\mathbf{v}_s = u_\psi(\epsilon^3 t, \psi, \zeta)\nabla\psi + u_\|(\epsilon^3 t, \psi, \zeta)\mathbf{B}. \quad (15)$$

Moreover, it is also convenient to choose the ζ coordinate to be time-independent, $\partial_t\zeta = 0$. With representation (15), Eq. (14) takes the form

$$\partial_t\psi = -r^2B^2u_\psi + Dr^2\nabla\cdot(\nabla\psi/r^2). \quad (16)$$

It should be stressed that Eq. (16) in essence determines the function $u_\psi(\epsilon^3 t, \psi, \zeta)$ because the function $\psi(t, \mathbf{r})$ is determined by the quasi-equilibrium condition, as will be shown below. The function $u_\|(\epsilon^3 t, \psi, \zeta)$ in representation (15) will be determined when discussing the reduced equation for the plasma density.

Let us now proceed immediately to the derivation of the reduced equations of motion. The basic equation of motion in ideal one-fluid magnetohydrodynamics can be obtained from Hamilton's principle of least action written in the form

$$\delta\mathcal{A} \equiv \int dt\delta\mathcal{L} \Rightarrow \int dtd^3\mathbf{r}(\boldsymbol{\xi}\cdot\{EoM\}) = 0, \quad (17)$$

where the variation of the Lagrangian $\delta\mathcal{L}$ is given by formula (8) and the symbol $\{EoM\}$ stands for the expression resulting from the integration of $\delta\mathcal{L}$ by parts. Since $\boldsymbol{\xi}$ is an arbitrary function of t and $\mathbf{r}$, the corresponding equation of motion has the form $\{EoM\} = 0$.

In applying the ASM method to derive the reduced equations, we must switch from an arbitrary displacement $\boldsymbol{\xi}(t, \mathbf{r})$ to a displacement of the form $\boldsymbol{\xi} = \boldsymbol{\xi}_a + \boldsymbol{\xi}_s$ with arbitrary functions f_ψ, f_φ, $\xi_{s\|}$, and $\delta\alpha(\epsilon t, \psi, \varphi)$; substitute the latter displacement into Hamilton's principle (17); and equate to zero the expressions in front of these functions, keeping in mind that $\boldsymbol{\xi}_s \sim O(\epsilon^2)$. Consequently, in the expressions in front of the functions f_ψ, f_φ, and $\xi_{s\|}$, we can retain only the terms of the zero order in the small parameter ϵ. In accordance with relationship (11), the inertial terms should be on the order of ϵ^2. For states close to a marginally stable state, we can represent the entropy density function S as a sum of the main (quasi-equilibrium) and fluctuating components,

$S = S_0 + \tilde{S}$, where the fluctuations are on the order of $\tilde{S} \sim \epsilon^2 S_0$. Hence, we must omit the inertial terms and the terms with the entropy fluctuations in the expressions in front of the functions f_ψ, f_φ, and $\xi_{s\|}$ to obtain the equations determining the balance of the main forces to zero order in ϵ^2. As a result, we arrive at the following equations, which have the meaning of the quasi-equilibrium conditions:

$$\begin{aligned} &\partial_\varphi p_0 = 0, \quad \mathbf{B}\cdot\nabla p_0 = 0, \\ &\Delta^*\psi + 4\pi r^2 \partial_\psi p_0(t, \psi) = 0, \end{aligned} \tag{18}$$

where $p_0(t, \psi)$ is the main quasi-equilibrium plasma pressure component. These equations coincide in structure with Grad–Shafranov equation (1), the only difference being that the pressure component $p_0 = S_0(t, \psi)/U^\gamma$ can vary slowly with time in accordance with the transport equations that will be derived below. From Eqs. (18) we see that, in this case, the flux function ψ can also vary slowly with time.

The main equation for the low-frequency (reduced) plasma dynamics is obtained by equating to zero the expression in front of the function $\delta\alpha(\epsilon t, \psi, \varphi)$ in Hamilton's principle (17). Since the function $\delta\alpha(\epsilon t, \psi, \varphi)$ enters the expression for $\boldsymbol{\xi}_a$ through the term $\nabla\delta\alpha$ and is independent of ζ, the sought equation can be derived from Hamilton's principle (17) by integrating by part, by expressing the volume element in terms of the flux coordinates ($d^3\mathbf{r} = d\psi d\varphi d\zeta/J$), and by averaging over the specific volume of the flux tube. As a result of these manipulations, the reduced equation of motion, which has the meaning of the Euler–Lagrange equation corresponding to the generalized coordinate $\alpha(\epsilon t, \psi, \varphi)$ of the adiabatic motion, takes the form

$$\mathcal{R}\{EoM\} \equiv \int_-^+ \frac{d\zeta}{J}\left\{\nabla\cdot\frac{\mathbf{B}\times\{EoM\}}{B^2} - \partial_\varphi(\lambda\mathbf{B}\cdot\{EoM\})\right\} = 0. \tag{19}$$

This equation is an exact consequence of the basic equation of motion $\{EoM\} = 0$. In order to complete the procedure of derivation of the reduced adiabatic equation of motion in ideal magnetohydrodynamics, we must substitute the sum of the velocities $\mathbf{v}_a + \mathbf{v}_s$ for the velocity $\mathbf{v}$ in Eq. (19) and retain the terms of the zero and first orders in $\mathbf{v}_s$. In accordance with the derivation procedure described in [18, 19], the generalized reduced equation of motion with allowance for dissipative processes can be obtained from Eq. (19) by substituting into it the expression for $\{EoM\}$, which includes the corresponding dissipative terms, such as the viscosity tensor, the external momentum source term (associated, e.g., with the charge exchange of a fast neutral beam), etc. It is also necessary to take into account the resistive term in Eq. (16) for u_ψ and the dissipative terms (in particular, the source terms) in the equation for the plasma density.

The reduction procedure, specified by the operator $\mathcal{R}\{EoM\}$ in Eq. (19), leads to an equation for the quantity $\hat{w}$, which can be called the specific dynamic vorticity of a magnetic flux tube. This quantity has the form

$$\begin{aligned} \hat{w}(\epsilon t, \psi, \varphi) &\equiv U\langle w\rangle \\ &= \int_-^+ \frac{d\zeta}{J}\left\{\nabla\cdot\left(\frac{\rho}{B^2}\nabla\Phi\right) + \partial_\varphi(\rho\lambda^2 B^2\partial_\varphi\Phi)\right\} \end{aligned} \tag{20}$$

and, to within a sign, coincides with the generalized momentum $P_\alpha = -\hat{w}$, which is canonically conjugate to the adiabatic coordinate $\alpha(\epsilon t, \psi, \varphi)$. In Section 4, it will be shown that, in the case under analysis, the plasma density can be assumed to be uniform along the magnetic field lines and can be represented as $\rho = \hat{\rho}/U \equiv \langle\rho\rangle$. This allows us to explicitly perform the procedure of averaging over the specific volume of the flux tube in expression (20) in order to convert it into the form

$$\hat{w} = \partial_\psi(\hat{\rho}\langle r^2\rangle\partial_\psi\Phi) + \partial_\varphi\left(\hat{\rho}\left\langle\frac{1}{r^2B^2} + \lambda^2B^2\right\rangle\partial_\varphi\Phi\right). \tag{21}$$

The procedure of calculating the remaining terms in Eq. (19) consists in carrying out fairly involved identity transformations with allowance for the relationship $\rho = \hat{\rho}/U$ and the useful formulas presented in the Appendix. As a result, these transformations put Eq. (19) into the form

$$\begin{aligned} \partial_t|_\psi\hat{w} + [\Phi, \hat{w}] - \left[\hat{\rho}, \left\langle\frac{v_a^2}{2}\right\rangle\right] + \frac{1}{U^\gamma}\partial_\psi U\partial_\varphi\langle\tilde{S}\rangle \\ = \{DT\}. \end{aligned} \tag{22}$$

The left-hand side of this equation contains the terms describing the ideal plasma dynamics and the symbol $\{DT\}$ on the right-hand side stands for the dissipative terms. In what follows, the symbol $\partial_t|_\psi$, which denotes the partial time derivative at fixed ψ and φ, and the symbol

$$[\Phi, f] \equiv \partial_\psi\Phi\partial_\varphi f - \partial_\varphi\Phi\partial_\psi f$$

will be used as standard symbolic notations.

Equation (22) is an essentially 2D equation, although it describes convection with 3D velocity field (11). Moreover, the flux coordinates ψ and φ in Eq. (11) are Eulerian ones, even though the coordinate ψ in actual space can depend on time. These properties of the equation obtained substantially simplify numerical simulation of the low-frequency turbulent convection. In accordance with the ordering of the quantities that were introduced above, all the terms on the right-hand side of Eq. (22) are on the order of ϵ^2. The order of the dissipa-

tive terms on the right-hand side of this equation is higher, $\{DT\} \sim O(\epsilon^4)$. However, since these terms can contain higher order spatial derivatives, they should be retained in order to provide a description of the suppression of small-scale vortices. The explicit form of the dissipative terms in question will be determined below, after the discussion of the reduced equations for the plasma density and temperature.

4. EQUATIONS FOR THE DENSITY AND TEMPERATURE

The basic equation for the plasma density is an exact zeroth moment of the kinetic equation, namely, the continuity equation with a local mass source term Q_ρ. Inserting the velocity field $\mathbf{v} = \mathbf{v}_a + \mathbf{v}_s$ into this equation puts it in the form

$$\partial_t \rho + \nabla \cdot (\rho \mathbf{v}_a) + \nabla \cdot (\rho u_\psi \nabla \psi) + J \partial_\zeta (\rho u_\parallel) = Q_\rho.$$

Averaging this equation over the specific volume of the flux tube converts it into a 2D equation similar to Eq. (22),

$$\partial_t|_\psi \hat{\rho} + [\Phi, \hat{\rho}] = 4\pi \partial_\psi (\hat{\rho} \langle r^2 D \rangle \partial_\psi p_0(\psi)) + Q_\rho^* U. \quad (23)$$

Here, the term Q_ρ^* involves the volume plasma source as well as longitudinal plasma losses (for open confinement systems),

$$Q_\rho^* = \langle Q_\rho \rangle - \rho u_\parallel|_-^+ / U = \langle Q_\rho \rangle + M_i [dn/dt]_\parallel,$$

where M_i is the mass of an ion. The magnitude of the longitudinal plasma losses $[dn/dt]_\parallel$ in different types of open devices was discussed in detail in [35]. The quantity $\hat{\rho} \equiv \langle \rho \rangle U$ is the plasma mass within the specific flux tube volume and, in the set of reduced equations proposed here, it plays the same role as the Lagrangian density function introduced in [19].

Equation (23) describes the 2D function $\hat{\rho}$ (or $\langle \rho \rangle$), averaged over the flux tube volume. Expression (20) for $\hat{w}$, however, contains the local (unaveraged) density, which should be determined from the basic unaveraged equation for the plasma density. The local density can be represented as $\rho = \hat{\rho}(t, \psi, \varphi)/U + \rho_1(t, \psi, \varphi, \zeta)$, where $\langle \rho_1 \rangle = 0$. The form of the functions ρ_1 and $u_\parallel$ is generally governed by the transport processes along the magnetic field lines. It should be noted, however, that we are primarily interested in the case in which the collision frequencies of the plasma particles and the characteristic frequencies of the processes under consideration are much lower than the bounce frequencies of the particles in their longitudinal motion. In this case, the kinetic approach implies that, in the isotropic-pressure plasma model considered here, the plasma density should be uniform along the magnetic field lines (i.e., $\rho_1 = 0$). Actually, in considering the difference between the basic unaveraged equation for the density and Eq. (23), we can show that the solvability condition for the function $u_\parallel(\epsilon^3 t, \psi, \varphi, \zeta)$ can be satisfied when $\rho_1 = 0$. In other words, the function $u_\parallel(\epsilon^3 t, \psi, \varphi, \zeta)$ in representation (15) is determined by the condition for the plasma density to be smoothed out along the magnetic field lines; in the case in question, this smoothing-out condition is satisfied not only for the equilibrium state but also for states with a developed low-frequency turbulent convection. The essential point is that the function $u_\parallel(\epsilon^3 t, \psi, \varphi, \zeta)$, as well as the other auxiliary function $u_\psi(\epsilon^3 t, \psi, \varphi, \zeta)$, which is defined by Eq. (16), drops out of the final set of equations.

Since the plasma density is longitudinally uniform ($\rho = \hat{\rho}/U \equiv \langle \rho \rangle$), 2D equation (23) has the meaning of a reduced mass transport equation. Recall that the assumption of the longitudinal uniformity of ρ has already enabled us to substantially simplify expression (20) for $\hat{w}$ and to reduce it to expression (21), which should now be regarded as an equation with which the function Φ can be reconstructed from the given functions $\hat{w}$ and $\hat{\rho}$. In turn, the functions $\hat{w}$ and $\hat{\rho}$ are determined from Eqs. (22) and (23). It is essential that the problem of determining the specific character of a particular nonuniform magnetic configuration has been reduced to that of calculating the form factors $\langle r^2 \rangle$ and $\langle r^{-2} B^{-2} + \lambda^2 B^2 \rangle$, which enter into Eq. (21) and depend on $(\epsilon^3 t)$ and ψ. A rather interesting point is that, in nonparaxial magnetic systems, the inertia of the radial plasma motion is larger because of the inertia of the longitudinal plasma redistribution, i.e., at the expense of the form factor $\langle \lambda^2 B^2 \rangle$ in Eq. (21).

It should be noted that the resistive diffusion term on the right-hand side of Eq. (23) is somewhat incomplete, because the one-fluid MHD model traditionally makes use of a simplified form of Ohm's law, $\mathbf{j} = \sigma \mathbf{E}$. In order to provide a more adequate description of the dissipative processes, the transport equations for the plasma density should be supplemented with the generalized Ohm's law that follows from the two-fluid MHD model and accounts for the Hall effect and electron pressure gradient. The two-fluid description of the plasma is, however, beyond the scope of the present study. The corresponding generalization is supposed to be done in subsequent papers.

The continuity equation and the equation of motion are, respectively, the zeroth and first moments of the kinetic equation. The next (third) equation to be obtained should correspond to the second moment. This equation is usually derived under additional assumptions that would make it possible to close the set of moment equations. In the case under discussion, one such assumption is that the pressure is isotropic, which reduces the second moment of the distribution function to the scalar pressure. Another assumption is that the third moments, corresponding to the heat fluxes, can be

expressed in terms of the zeroth, first, and second moments; this makes it possible to close the set of moment equations. In accordance with the classic review by Braginskii [36], the basic equation for the plasma pressure in the one-fluid MHD model can be represented as

$$\partial_t p + \mathbf{v}\cdot\nabla p + \gamma p\nabla\cdot\mathbf{v} = -(\gamma-1)\nabla\cdot\mathbf{q} + (\gamma-1)Q_E,$$

where Q_E is the energy density source term. The transverse heat flux $\mathbf{q}_\perp$ in this equation is determined by the initial local thermal diffusivity $\chi_\perp$ (e.g., by the classical ion thermal diffusivity in a magnetized plasma). On the other hand, in the low-collisional limit, the longitudinal heat flux $q_\parallel$ remains a free function, as is the function $u_\parallel$ in the basic equation for ρ.

In deriving the reduced heat transport equation, it is reasonable to suppose that, in the isotropic-pressure plasma model, the temperature T, as well as the density ρ, should be constant along the magnetic field lines not only in the equilibrium state but also in states with a developed low-frequency turbulent convection. It is easy to show that the conditions for the temperature T to be constant along the magnetic field lines and the same condition for the entropy density function S, $S = \langle S\rangle$, are consistent with the solvability condition for the function $q_\parallel(t, \psi, \varphi, \zeta)$. In this case, the condition $S = \langle S\rangle$ determines the form of the function $q_\parallel(t, \psi, \varphi, \zeta)$ in the same way as the constancy of $\hat\rho$ determines the form of the function $u_\parallel$. As a result, instead of the basic equation describing the plasma pressure variations, we can use the corresponding equation averaged over the specific volume of the flux tube. In doing so, it is convenient, following [19], to switch to the function S, which plays the role of the Lagrangian pressure function. After substituting $\mathbf{v} = \mathbf{v}_a + \mathbf{v}_s$ into the above equation for the plasma pressure, we arrive at the following resulting equation for S, which is similar in form to Eq. (23):

$$\partial_t|_\psi S + [\Phi, S] = (\gamma-1)U^\gamma(-U^{-1}\partial_\psi(U\langle\mathbf{q}\cdot\nabla\psi\rangle) - \partial_\varphi\langle\mathbf{q}\cdot\nabla\varphi\rangle + Q_E^*) + 4\pi\gamma S^{\frac{\gamma-1}{\gamma}}\partial_\psi(S^{1/\gamma}\langle r^2 D\rangle\partial_\psi p_0). \quad (24)$$

The left-hand side of this equation contains the terms describing the ideal convection, while the terms on the right-hand side describe various dissipative processes. The effective energy source term Q_E^* is given by the expression

$$Q_E^* = \langle Q_E\rangle - \frac{1}{U}\left(\frac{q_\parallel}{B} + \frac{\gamma}{\gamma-1}pu_\parallel\right)\Bigg|_-^+ = \langle Q_E\rangle - Q_{E\parallel}\big|_-^+,$$

which accounts for both the volume energy source and the longitudinal energy losses (see [35]).

Under the assumption that the electron-to-ion temperature ratio is constant over the entire plasma volume, T_e/T_i = const, the components of the classical transverse heat flux have the form

$$\langle\mathbf{q}\cdot\nabla\psi\rangle = -\left\langle r^2B^2\rho\chi_\perp\partial_\psi\left(\frac{p_i}{\rho}\right)\right\rangle = -X_M\rho^2\langle r^2\rangle\partial_\psi\left(\frac{p}{\rho}\right)^{1/2},$$

$$\langle\mathbf{q}\cdot\nabla\varphi\rangle = -\left\langle\frac{\rho\chi_\perp}{r^2}\partial_\varphi\left(\frac{p_i}{\rho}\right)\right\rangle = -X_M\rho^2\left\langle\frac{1}{r^2B^2}\right\rangle\partial_\varphi\left(\frac{p}{\rho}\right)^{1/2}.$$

Here, X_M is a constant having the meaning of the renormalized thermal diffusivity,

$$X_M = \chi_M\frac{B_M^2}{\rho_M}\left(\frac{p_M}{\rho_M}\right)^{1/2}\left(\frac{4T_i}{T_i+T_e}\right)_M^{1/2} = \text{const},$$

where the subscript M labels the values of the quantities at a certain arbitrarily chosen point (e.g., at the point of intersection of the axis with the midplane of the mirror cell) that is convenient for the subsequent transformation of the set of equations under analysis into a dimensionless form. By analogy with the thermal diffusivity, the classical resistive diffusion coefficient D, which is proportional only to $T_e^{-3/2}$ and, therefore, is constant along the magnetic field lines, can also be conveniently renormalized by introducing a constant coefficient d_M:

$$D = d_M(\rho_0/p_0)^{3/2}, \quad d_M = D_M(p_M/\rho_M)^{3/2} = \text{const}.$$

It is easy to see that the classical heat flux is proportional to $\nabla(p/\rho) = \nabla(S/\hat\rho\, U^{\gamma-1})$. Recall that, for small deviations from the marginally stable pressure profile, the function S can be represented as $S = S_0(\epsilon^3 t, \psi) + \tilde S(\epsilon t, \psi, \varphi)$, where the term $S_0 = \int_0^{2\pi} S d\varphi/2\pi$ is the quasi-steady part of S and the term $\tilde S \sim \epsilon^2 S_0$ describes small but relatively fast fluctuations. The function $\hat\rho$ can be represented in a similar manner: $\hat\rho = \hat\rho_0(\epsilon^3 t, \psi) + \tilde\rho(\epsilon t, \psi, \varphi)$, where $\tilde\rho \sim \epsilon^2\hat\rho_0$. Since the functions $\tilde S$ and $\hat\rho$ are small, the expression for the classical heat flux can be linearized in them. However, the linearization of the classical heat flux with respect to $\hat\rho$ leads to a "negative-diffusion" term, which may lead to certain difficulties in numerical modeling. In order to avoid them, we introduce a new function $\hat T = S/\hat\rho$, which, in analogy to $\hat\rho$, has the meaning of the Lagrangian temperature function and is related to the actual electron and ion temperatures by the relationship $\hat T = (T_e + T_i)U^{(\gamma-1)}/M_i$. Representing this function as a sum of the main (quasi-steady) and fluctuating components, $\hat T = \hat T_0(\epsilon^3 t, \psi) + \tilde T(\epsilon t, \psi, \varphi)$, we can linearize the ratio p/ρ in $\tilde T \sim \epsilon^2\hat T_0$,

instead of linearizing it separately in $\tilde{S}$ and in $\tilde{\rho}$. In terms of the function $\hat{T}$, Eq. (24) reads

$$\begin{aligned}
&\partial_t|_\psi \hat{T} + [\Phi, \hat{T}] \\
&= -(\gamma-1)\frac{U^\gamma}{\hat{\rho}}\left(\frac{1}{U}\partial_\psi(U\langle \mathbf{q}\cdot\nabla\psi\rangle) + \partial_\varphi\langle \mathbf{q}\cdot\nabla\varphi\rangle\right) \\
&\quad + Q_T^*\frac{U^\gamma}{\hat{\rho}} + 4\pi d_M(\partial_\psi\hat{T})\langle r^2\rangle\left(\frac{U^{(\gamma-1)}}{\hat{T}_0}\right)^{3/2}\partial_\psi p_0 \\
&\quad + 4\pi d_M(\gamma-1)\hat{T}\partial_\psi\left(\langle r^2\rangle\left(\frac{U^{(\gamma-1)}}{\hat{T}_0}\right)^{3/2}\partial_\psi p_0\right),
\end{aligned} \tag{25}$$

where, for convenience, we have introduced the effective temperature source term

$$\begin{aligned}
Q_T^* &= (\gamma-1)\langle Q_E\rangle + \left[\frac{d(2nT)}{dt}\right]_\parallel \\
&\quad - \frac{\hat{T}}{U^{\gamma-1}}\left(\langle Q_\rho\rangle + M_i\left[\frac{dn}{dt}\right]_\parallel\right).
\end{aligned}$$

5. FAST AND SLOW SUBSETS OF THE REDUCED EQUATIONS

Equations (23) and (25) describe both the main (slowly varying) components of the density and temperature and relatively fast fluctuations of these plasma parameters. This is why it is natural to separate the set of Eqs. (23) and (25) into a "slow" and a "fast" subset. By virtue of the axial symmetry of the magnetic configurations under discussion, the main density and temperature components are independent of the angle φ; this allows us to separate the equations by averaging them over φ. In addition, keeping in mind further applications of the resulting reduced equations to practical calculations, we set the adiabatic index equal to $\gamma = 5/3$.

Averaging Eq. (23) over φ yields the 1D equation

$$\begin{aligned}
&\partial_t|_\psi \hat{\rho}_0 - \partial_\psi(\overline{\tilde{\rho}\partial_\varphi\Phi}) \\
&= 4\pi d_M\partial_\psi(\hat{\rho}_0\langle r^2\rangle(U/\hat{T}_0^{3/2})\partial_\psi(\hat{\rho}_0\hat{T}_0/U^{5/3})) + \overline{Q}_\rho^* U,
\end{aligned} \tag{26}$$

which describes the evolution of the main density component $\hat{\rho}_0(\epsilon^3 t, \psi)$. According to the traditional terminology, this equation should be called the density transport equation. The second term on the right-hand side of Eq. (26) accounts for fluctuations of the radial plasma velocity and plasma density and describes the mean convective density flux, which is just the nondiffusive turbulent transport flux whose fundamental role was discussed in the Introduction. Hereafter, a bar above one or another expression indicates its average over φ. In accordance with the above ordering of the quantities, all the terms on both sides of Eq. (26) are on the order of ϵ^3. In terms of the functions $\hat{\rho}$ and $\hat{T}$ introduced above, the main quasi-equilibrium plasma pressure component has the form $p_0 = \hat{\rho}_0\hat{T}_0/U^\gamma$, provided that the terms on the order of ϵ^4 are ignored.

Subtracting from Eq. (23) its component that is uniform in φ (i.e., Eq. (26)), we obtain the equation for the plasma density fluctuations,

$$\begin{aligned}
&\partial_t|_\psi\tilde{\rho} + [\Phi, \tilde{\rho}] + \partial_\psi(\overline{\tilde{\rho}\partial_\varphi\Phi}) - \partial_\varphi\Phi\partial_\psi\hat{\rho}_0 \\
&= 4\pi d_M\partial_\psi(\tilde{\rho}\langle r^2\rangle(U/\hat{T}_0^{3/2})\partial_\psi(\hat{\rho}_0\hat{T}_0/U^{5/3})) + \tilde{Q}_\rho^* U.
\end{aligned} \tag{27}$$

As in Eq. (26), all the terms on the left-hand side of Eq. (27) are on the order of ϵ^3. The resistive diffusion term on the right-hand side of Eq. (27) is on the order of ϵ^5 (because $D \sim \epsilon^3$ and $\tilde{\rho} \sim \epsilon^2$) and contains the spatial derivatives of $\tilde{\rho}$ of an order no higher than one. The latter circumstance results from the use of the simplified Ohm's law and is a drawback of the one-fluid MHD model applied here; as a result, the suppression of small-scale density fluctuations by dissipation in the model will be weaker than in actuality.

Averaging Eq. (25) over φ, we arrive at the 1D heat transport equation,

$$\begin{aligned}
&\partial_t|_\psi\hat{T}_0 - \partial_\psi(\overline{\tilde{T}\partial_\varphi\Phi}) = X_M\frac{2U^{2/3}}{3\hat{\rho}_0}\partial_\psi\left(\frac{\hat{\rho}_0^2\langle r^2\rangle}{U}\partial_\psi\left(\frac{\sqrt{\hat{T}_0}}{U^{1/3}}\right)\right) \\
&\quad + \frac{u^{5/3}}{\hat{\rho}}\overline{Q}_T^* + \frac{8\pi d_M}{3\sqrt{\hat{T}_0}}\partial_\psi\left(\langle r^2\rangle U\partial_\psi\left(\frac{\hat{\rho}_0\hat{T}_0}{U^{5/3}}\right)\right),
\end{aligned} \tag{28}$$

in which the quantity $\mathbf{q}_\perp$ has been substituted by the expression for the classical heat flux and the rest of the notation was introduced above. As in Eq. (26), all the terms in Eq. (28) are on the order of ϵ^3. The second term on the left-hand side of Eq. (28) describes the convective heat flux, which may be turbulent and nondiffusive, as is the case with the convective density flux.

Subtracting from Eq. (25) its averaged component yields the following equation for the fluctuations of the temperature function:

$$\begin{aligned}
&\partial_t|_\psi\tilde{T} + [\Phi, \tilde{T}] + \partial_\psi(\overline{\tilde{T}\partial_\varphi\Phi}) - \partial_\varphi\Phi\partial_\psi\hat{T}_0 \\
&= X_M\frac{U^{2/3}}{3\hat{\rho}_0}\partial_\psi\left(\frac{\hat{\rho}_0^2\langle r^2\rangle}{U}\partial_\psi\left(\frac{\tilde{T}}{U^{1/3}\sqrt{\hat{T}_0}}\right)\right) \\
&\quad + \frac{X_M\hat{\rho}_0}{3U^{2/3}\sqrt{\hat{T}_0}}\left\langle\frac{1}{r^2B^2}\right\rangle\partial_{\varphi\varphi}^2\tilde{T} + \frac{U^{5/3}}{\hat{\rho}}\tilde{Q}_T^*,
\end{aligned} \tag{29}$$

where $\tilde{Q}_T^*$ is the component of the effective temperature source Q_T^* that is nonuniform in φ. As in Eq. (27),

all the terms on the right-hand side of Eq. (29) are on the order of ϵ^3. The first term on the right-hand side of Eq. (29) accounts for the classical thermal conductivity. Although this term is on the order of ϵ^5 (by virtue of $\chi \sim \epsilon^3$ and $\tilde{T} \sim \epsilon^2$), it plays an important role because it contains second-order spatial derivatives of $\tilde{T}$ and describes the suppression of the small-scale fluctuations of the temperature function. In Eq. (29), the resistive diffusion terms that involve spatial derivatives of $\tilde{T}$ of an order no higher than one are omitted, in contrast to the term with the thermal conductivity.

Transport equations (26) and (28), supplemented with quasi-equilibrium equation (18), constitute a subset of slow reduced equations describing the evolution of the main macroscopic plasma parameters. Equations (26) and (28) contain the averaged convective fluxes, which are determined by the fluctuations of the plasma density, temperature, and radial velocity. These fluctuations are in turn determined from 2D nonlinear equations (22), (27), and (29), which, together with Eq. (21), constitute a subset of fast reduced equations, whose solution depends substantially on the magnetic field configuration and also on the profiles of the macroscopic plasma parameters. In particular, the last terms on the right-hand sides of Eqs. (22), (27), and (29) are responsible for the development of flute instability. These subsets of slow and fast equations constitute a complete set of the adiabatically reduced equations for describing low-frequency MHD plasma convection. In order to accomplish the derivation of the full set of reduced equations, we are left with the problem of finding an explicit form of the dissipative terms in Eq. (22).

The dissipative terms on the right-hand side of Eq. (22) originate from the divergence of the viscous stress tensor, $\nabla \cdot \overleftrightarrow{\pi}$, and the term $\rho((\mathbf{v}_a \cdot \nabla)\mathbf{v}_s + (\mathbf{v}_s \cdot \nabla)\mathbf{v}_a)$ in the basic equation of motion as well as from the dissipative right-hand side of Eq. (23). Recall that all the terms on the left-hand side of Eq. (22) are on the order of ϵ^2, while the dissipative terms on the right-hand side of this equation are on the order of ϵ^4. In other words, the dissipative terms in Eq. (22) are of a higher order of magnitude than the "ideal" terms on its right-hand side, as in Eqs. (27) and (29) for the density and temperature fluctuations. It is therefore necessary to preferentially retain those dissipative terms that include the higher spatial derivatives. In particular, such terms are contained in the viscous stress tensor.

The contribution of the viscous stress tensor to Eq. (22) comes through the operation $\mathcal{R}\{\nabla \cdot \overleftrightarrow{\pi}\}$, which leads to a very involved and complicated expression containing various combinations of the spatial derivatives of Φ from the first to the fourth order. However, proceeding in a manner analogous to that in [19] and using the classical expression for the viscous stress tensor that was obtained in [36], we can write the following approximate representation for $\mathcal{R}\{\nabla \cdot \overleftrightarrow{\pi}\}$:

$$\mathcal{R}\{\nabla \cdot \overleftrightarrow{\pi}\} \approx \partial_\psi \left\{ \hat{\rho} \langle r^2 \rangle \partial_\psi \left((\eta B^2) \frac{a^2}{\hat{\rho} \langle r^2 \rangle} \hat{w} \right) \right\} + \frac{a^2}{\langle r^2 \rangle} \left\langle \frac{1}{r^2 B^2} \right\rangle (\eta B^2) \partial^2_{\varphi\varphi} \hat{w}, \tag{30}$$

which has the same divergence form as the basic representation for this operation and in which we explicitly keep all the terms with the highest spatial derivatives of Φ and retain the terms with the lower spatial derivatives in such a way that the potential Φ enters only into the function $\hat{w}$, defined by expression (21). In representation (30), we have also introduced the characteristic spatial scale $a^2(\psi) = \langle r^4 \rangle / \langle r^2 \rangle$ and the classical kinematic viscosity coefficient $\eta = 3\chi/20$. Representation (30) was derived with allowance for the fact that the product ηB^2 is constant along the magnetic field lines. In Eq. (22), viscous term (30) plays the same role as the viscous term in the Navier–Stokes equation in conventional hydrodynamics. In particular, it is responsible for the dissipation of small-scale vortices generated in flows with a high Reynolds number.

It can be shown that the remaining dissipative terms on the right-hand side of Eq. (22) contain spatial derivatives of Φ of an order no higher than two. These terms can be discarded because, in contrast to viscous term (30), their contribution is small both for long and short spatial scales. Also, in expressing the function $\tilde{S}$, which stands on the left-hand side of Eq. (22), in terms of the functions $\hat{\rho}$ and $\hat{T}$, it is sufficient to take into account only linear terms: $\tilde{S} \approx \hat{\rho}_0 \tilde{T} + \hat{T}_0 \tilde{\rho}$.

It is easy to see that Eq. (22) without dissipative terms implies the conservation law for the dynamic plasma vorticity. Therefore, even a relatively weak source of the transverse momentum of the plasma can significantly change the nonuniform profile of the plasma rotation velocity and thereby can have a strong impact on the development of plasma turbulence. In experiments, the momentum source can be provided, e.g., by the charge exchange and ionization of the injected neutral beams or by controlling the radial electric field with the help of end-plates in open devices.

With allowance for the above estimates and remarks, we arrive at the following final form of Eq. (22):

$$\partial_t|_\psi \hat{w} + [\Phi, \hat{w}] - \left[\hat{\rho}, \left\langle \frac{v_a^2}{2} \right\rangle\right] + \frac{1}{U^\gamma}\partial_\psi U \partial_\varphi(\hat{\rho}_0 \tilde{T} + \hat{T}_0 \tilde{\rho}) = UQ_w^* + \frac{3X_M}{20}\left(\frac{T_i + T_e}{2T_i}\right)\left\{\partial_\psi\left(\hat{\rho}\langle r^2\rangle \partial_\psi\left(\frac{1}{U^{2/3}\sqrt{T_0}\langle r^2\rangle}\frac{a^2}{}\hat{w}\right)\right)\right. + \left.\frac{a^2}{\langle r^2\rangle}\left\langle \frac{1}{r^2B^2}\right\rangle \frac{\hat{\rho}}{U^{2/3}\sqrt{T_0}}\partial_{\varphi\varphi}^2 \hat{w}\right\}, \quad (31)$$

where Q_w^* is the effective source of the specific dynamic vorticity, which is calculated according to the same rules as the above source terms Q_ρ^* and Q_T^*. For completeness, we also present an explicit expression for $\langle v_a^2\rangle$,

$$\langle v_a^2\rangle = \langle r^2\rangle(\partial_\psi\Phi)^2 + \left\langle \frac{1}{r^2B^2} + \lambda^2 B^2\right\rangle(\partial_\varphi\Phi)^2.$$

Hence, we have completed the derivation of the closed set of reduced dynamic equations under discussion. The equations have been represented in a form convenient for designing appropriate computer codes for simulations of the self-consistent nonlinear plasma dynamics and resulting transport processes.

6. CONCLUSIONS

In the present paper, the ASM method has been used to derive a closed set of adiabatically reduced dynamic equations for describing nonlinear low-frequency MHD plasma convection and resulting transport processes in weakly dissipative plasmas of axisymmetric shearless magnetic systems with closed or open magnetic field lines. The equations have been obtained on the assumption that the plasma is maintained near a marginally stable state against pressure-gradient-driven flute interchange modes. It has also been assumed that the plasma pressure is below the instability threshold for Alfvén modes ($\beta < \beta_{cr} \sim 1$). Under these assumptions, the ASM method makes it possible to exclude from consideration relatively high-frequency stable collective degrees of freedom corresponding to magnetosonic, Alfvén, and longitudinal acoustic modes of oscillations. The remaining nonlinear low-frequency convection can be self-consistently generated as a result of the development of a flute interchange instability (similar to the Rayleigh–Taylor instability) and also of a secondary instability associated with the presence of nonuniform plasma flows (similar to the Kelvin–Helmholtz instability). The ASM method preserves the invariant properties of the basic ideal MHD equations, thereby making it possible to use the resulting set of reduced equations to simulate the long-term evolution of the plasma on time scales comparable to its lifetime or even longer.

The final set of reduced equations consists of two subsets of equations: slow and fast. The subset of slow equations, which is represented by quasi-equilibrium equation (18) and transport equations (26) and (28), describes a relatively slow evolution of the main macroscopic plasma parameters. In the quasi-steady (or quasi-Eulerian) flux coordinates $\{\psi, \varphi, \zeta\}$, transport equations (26) and (28) have a traditional 1D form, the only difference from traditional equations being that they contain the averaged convective flux terms accounting for the plasma density, temperature, and radial velocity fluctuations. These fluctuations are in turn described by 2D nonlinear equations (22), (27), and (29), which, together with Eq. (21), constitute the subset of fast equations.

The set of equations constructed here is a generalization of the set of reduced equations obtained in [19] for a simpler model magnetic configuration. The proposed equations make it possible to simulate transport processes and establishment of the self-consistent plasma temperature and density profiles for a broad class of axisymmetric nonparaxial shearless magnetic systems, such as levitated dipole configurations, mirror devices, and compact tori. The essential point is that the specific character of a particular magnetic system is fully described by a finite number of functions that depend on the ψ coordinate and either vary only slowly with time or do not vary at all, namely, the functions U, $\langle r^2\rangle$, $\langle r^4\rangle$, $\langle r^{-2}B^{-2}\rangle$, and $\langle \lambda^2 B^2\rangle$, which play the role of form factors in the final reduced equations. In the approach developed here, quasi-equilibrium equation (18) should be solved only for sufficiently high β values, such that the magnetic configuration differs substantially from a vacuum one. For lower plasma pressures, it can be assumed that $\beta \ll 1$ and the form factors just indicated can be calculated for a vacuum magnetic field configuration, because quasi-equilibrium equation (18) has already been taken into account in deriving the transport equations and the equations for the fluctuations of plasma parameters.

That the adiabatically reduced MHD equations provide an efficient tool for modeling the nonlinear low-frequency MHD convection and resulting transport processes in a weakly dissipative plasma was demonstrated in [19, 20]. It was shown that the resulting transport fluxes are turbulent, nonlocal, and nondiffusive. Computer simulations revealed that transport processes possess specific properties that are qualitatively similar to those of some experimentally observed phenomena, such as the internal transport barrier, L–H transition, and impurity pinch. A generalized dynamic transport model based on the above set of reduced equations is expected to provide a more adequate simulation of the low-frequency plasma turbulence and resulting transport processes, to yield the results that can then be used for a detailed comparison with the experimental data

obtained from various magnetic systems, and also to contribute to the development of the general theory of nondiffusive transport processes in a magnetized plasma.

As was mentioned above, the use of the simplest MHD model with isotropic plasma pressure may be considered merely as a first step in simulating the self-consistent low-frequency plasma dynamics. In further investigations, it is proposed to utilize a more adequate bounce-averaged collisionless Kruskal–Oberman model. Nevertheless, the results obtained in the present study, together with the results of computer simulations carried out in [19, 20], suggest that the set of adiabatically reduced equations in the Kruskal–Oberman model should yield qualitatively the same basic properties of the nonlinear low-frequency plasma dynamics. Thus, the conclusion that the plasma tends to maintain a marginally stable state should remain valid, as well as the conclusion that fast stable degrees of freedom can be removed from consideration. The main quantitative difference from the above results will be associated with the two new adiabatic functions that will characterize the longitudinal and transverse plasma pressures and will appear in the equations in place of the entropy density function defined by Eq. (7). This will lead to the corresponding modification of the marginally stable pressure profile as well as of the form factors describing the specific character of a magnetic system. At the same time, the Kruskal–Oberman model should give approximately the same spatial scales of the self-consistent fluctuations and of the resulting transport processes as those in the model with isotropic plasma pressure.

ACKNOWLEDGMENTS

This work was supported in part by the RF Presidential Program for State Support of Leading Scientific Schools, project no. NSh-2024.2003.2.

APPENDIX

Here, a number of useful formulas are presented that are required to carry out the averaging over the specific flux tube volume in deriving Eqs. (22), (23), and (25) and in performing some other manipulations. The time derivatives of the quantities related to the flux coordinates are as follows:

$$\partial_t J = \nabla(\partial_t\psi)\cdot(\nabla\varphi\times\nabla\zeta) = J\partial_\psi(\partial_t\psi),$$

$$\partial_t\big|_\psi\frac{1}{J} = -\partial_\psi\left(\frac{\partial_t\psi}{J}\right), \quad \partial_t\big|_\psi U = -\partial_\psi\int_-^+\frac{d\zeta}{J}\partial_t\psi.$$

The operation of divergence in the flux coordinates is given by the relationship

$$\nabla\cdot\mathbf{f} = J\left(\partial_\psi\left(\frac{\mathbf{f}\cdot\nabla\psi}{J}\right)+\partial_\varphi\left(\frac{\mathbf{f}\cdot\nabla\varphi}{J}\right)+\partial_\zeta\left(\frac{\mathbf{f}\cdot\nabla\zeta}{J}\right)\right).$$

Finally, the expressions related to the averaging of the fluxes associated with adiabatic velocity field (11) have the form

$$\nabla\cdot(\mathbf{v}_a/U) = 0, \quad \langle\nabla\cdot(\mathbf{v}_aF)\rangle = U^{-1}[\Phi,(U\langle F\rangle)].$$

REFERENCES

1. B. B. Kadomtsev and O. P. Pogutse, in *Reviews of Plasma Physics*, Ed. by M. A. Leontovich (Atomizdat, Moscow, 1967; Consultants Bureau, New York, 1970), Vol. 5.
2. W. Horton, in *Basic Plasma Physics*, Ed. by A. A. Galeev and R. N. Sudan (North-Holland, Amsterdam, 1984; Énergoatomizdat, Moscow, 1984), Vol. 2.
3. J. W. Connor, P. Buratti, J. D. Cordey, *et al.*, Plasma Phys. Controlled Fusion **41**, 693 (1999).
4. M. V. Ossipenko and T-10 Team, in *Proceedings of the 19th IAEA Fusion Energy Conference, Lyon, 2002* (IAEA, Vienna, 2003), Report OV/5-2.
5. G. M. Batanov, L. V. Kolik, A. E. Petrov, *et al.*, Fiz. Plazmy **29**, 395 (2003) [Plasma Phys. Rep. **29**, 363 (2003)].
6. G. M. Batanov, V. E. Bening, V. Yu. Korolev, *et al.*, Pis'ma Zh. Éksp. Teor. Fiz. **78**, 974 (2003) [JETP Lett. **78**, 502 (2003)].
7. T. Cho, M. Yoshida, H. Higaki, *et al.*, J. Plasma Fusion Res. **80**, 81 (2004).
8. V. V. Abrakov, A. E. Petrov, K. A. Sarksyan, and N. N. Skvortsova, Fiz. Plazmy **20**, 1069 (1994) [Plasma Phys. Rep. **20**, 959 (1994)].
9. G. Y. Antar, S. I. Krasheninnikov, P. Devynck, *et al.*, Phys. Rev. Lett. **87**, 065001 (2001).
10. N. Ohno, D. Nishijima, S. Takamura, *et al.*, Nucl. Fusion **41**, 1055 (2001).
11. J. A. Boedo, D. L. Rudakov, R. Moyer, *et al.*, Phys. Plasmas **8**, 4826 (2001).
12. B. B. Kadomtsev and O. P. Pogutse, Zh. Éksp. Teor. Fiz. **65**, 575 (1973) [Sov. Phys. JETP **38**, 283 (1974)].
13. B. B. Kadomtsev and O. P. Pogutse, Zh. Éksp. Teor. Fiz. **66**, 2067 (1974) [Sov. Phys. JETP **39**, 1017 (1974)].
14. R. White, D. Monticello, M. N. Rosenbluth, *et al.*, in *Proceedings of the 5th International Conference on Plasma Physics and Controlled Nuclear Fusion Research, Tokyo, 1974* (IAEA, Vienna, 1975), Vol. 1, p. 495.
15. H. Strauss, Phys. Fluids **19**, 134 (1976).
16. H. Strauss, Phys. Fluids **20**, 1354 (1977).
17. V. P. Pastukhov, Pis'ma Zh. Éksp. Teor. Fiz. **67**, 892 (1998) [JETP Lett. **67**, 940 (1998)].
18. V. P. Pastukhov, Fiz. Plazmy **26**, 566 (2000) [Plasma Phys. Rep. **26**, 529 (2000)].
19. V. P. Pastukhov and N. V. Chudin, Fiz. Plazmy **27**, 963 (2001) [Plasma Phys. Rep. **27**, 907 (2001)].
20. V. P. Pastukhov and N. V. Chudin, in *Proceedings of the 19th IAEA Fusion Energy Conference, Lyon, 2002* (IAEA, Vienna, 2003), Report TH/2-5.
21. A. Hasegava, L. Chen, and M. E. Mauel, Nucl. Fusion **30**, 2405 (1990).

22. A. I. Morozov, V. P. Pastukhov, and A. Yu. Sokolov, in *Proceedings of the Workshop on D-3He-Based Reactor Studies, Moscow, 1991*, p. 1C1.

23. J. Kesner, L. Bromberg, D. T. Garnier, and M. E. Mauel, in *Proceedings of the 17th IAEA Fusion Energy Conference, Yokohama, 1998* (IAEA, Vienna, 1999), Vol. 3, p. 1165.

24. V. P. Pastukhov and A. Yu. Sokolov, Fiz. Plazmy **17**, 1043 (1991) [Sov. J. Plasma Phys. **17**, 603 (1991)].

25. V. V. Arsenin, E. D. Dlougach, V. M. Kulygin, *et al.*, Nucl. Fusion **41**, 945 (2001).

26. A. Yu. Sokolov, Fiz. Plazmy **18**, 657 (1992) [Sov. J. Plasma Phys. **18**, 343 (1992)].

27. V. V. Arsenin and A. Yu. Kuyanov, Fiz. Plazmy **27**, 675 (2001) [Plasma Phys. Rep. **27**, 635 (2001)].

28. P. A. Popovich and V. D. Shafranov, Fiz. Plazmy **26**, 519 (2000) [Plasma Phys. Rep. **26**, 484 (2000)].

29. V. V. Arsenin and A. Yu. Kuyanov, Fiz. Plazmy **26**, 793 (2000) [Plasma Phys. Rep. **26**, 741 (2000)].

30. A. Bernstein, in *Basic Plasma Physics*, Ed. by A. A. Galeev and R. N. Sudan (North-Holland, Amsterdam, 1984; Énergoatomizdat, Moscow, 1983), Vol. 1.

31. B. B. Kadomtsev, in *Reviews of Plasma Physics*, Ed. by M. A. Leontovich (Gosatomizdat, Moscow, 1963; Consultants Bureau, New York, 1966), Vol. 2.

32. S. Krasheninnikov, P. Catto, and R. D. Hazeltine, Phys. Rev. Lett. **82**, 2689 (1999).

33. D. T. Garnier, J. Kesner, and M. E. Mauel, Phys. Plasmas **6**, 3431 (1999).

34. V. V. Arsenin, Fiz. Plazmy **28**, 843 (2002) [Plasma Phys. Rep. **28**, 776 (2002)].

35. V. P. Pastukhov, in *Reviews of Plasma Physics*, Ed. by B. B. Kadomtsev (Énergoatomizdat, Moscow, 1984; Consultants Bureau, New York, 1987), Vol. 13.

36. S. I. Braginskii, in *Reviews of Plasma Physics*, Ed. by M. A. Leontovich (Gosatomizdat, Moscow, 1963; Consultants Bureau, New York, 1965), Vol. 1.

Translated by I.A. Kalabalyk

Plasma Physics Reports, Vol. 31, No. 7, 2005, pp. 591–595. Translated from Fizika Plazmy, Vol. 31, No. 7, 2005, pp. 642–646.

PLASMA DYNAMICS

A Simple Criterion for the Snowplowing Efficiency of the Working Gas in a kJ Plasma Focus

V. Ya. Nikulin, S. N. Polukhin, and A. A. Tikhomirov

Lebedev Physical Institute, Russian Academy of Sciences, Leninskiĭ pr. 53, Moscow 117924 Russia

Received December 15, 2003; in final form, October 22, 2004

Abstract—Correlation between the appearance of the second peculiarity in the current-derivative signal and the drop in the neutron yield is observed experimentally in a plasma focus discharge. The time-resolved photographs of the current sheath lead to the conclusion that, at the instant of maximum compression, the main current is shunted by the second current sheath, which is formed from the rest of the gas after the passage of the first one. It is also suggested that the generation of the second current sheath is a consequence of two competing processes: filamentation of the first sheath, which thus becomes transparent to the working gas, and magnetization of the residual plasma by the field of the main discharge current. © *2005 Pleiades Publishing, Inc.*

1. INTODUCTION

It has been found experimentally that the neutron yield from a plasma focus (PF) is proportional to the square of the stored energy only in the energy range of 1–100 kJ. For MJ devices, the neutron yield remains at a level of 10^{11}–10^{12} n/pulse instead of the expected 10^{13} n/pulse.

It is commonly accepted that reduced neutron yield is related to the shunting of the current by the residual plasma surrounding the discharge column or by the low-density plasma at the periphery of the discharge. The first effect is peculiar to all high-power Z-pinch discharges and is of fundamental importance for plasma physics [1], whereas the second is typical of plasma focus discharges and is directly related to the efficiency of gas snowplowing by the current sheath moving from the insulator.

In the present paper, based on an analysis of the current-derivative signal, electron-optical photographs of the discharge, and the data on the neutron yield, we formulated a criterion for determining the snowplowing efficiency. With this criterion, the effect of the parasitic shunting of the discharge current by the residual plasma at the periphery of the discharge may be easily estimated from the behavior of the current-derivative signal.

2. EXPERIMENTAL SETUP

Experiments were carried out in a PF device with hemispheric electrodes 25 and 50 mm in diameter (Fig. 1) [2, 3]. The electrodes were powered from a 20-μF capacitor bank up to 12–16 kV, which corresponded to a stored energy of 1.5–2.5 kJ. The current rise time was 1.6 μs, and the current amplitude was $I_{max} \cong 3 \times 10^5$ A. The working gas was deuterium at a pressure of $P \cong 1$–3 torr.

In each shot, we recorded the current-derivative signal with a Tektronix TDS210 oscillograph, measured the total neutron yield using the neutron-activation technique (paraffin + In + Geiger counter), and took photographs of the current sheath using an image converter operating in the single-frame mode with a time resolution of 3–10 ns and spatial resolution of 0.1–0.2 mm. The images were recorded by a Nikon Coolpix 700 digital camera and then were stored in a PC. The image converter was placed perpendicular or parallel to the PF axis at a distance of 15–20 cm from the electrode ends.

3. EXPERIMENTAL RESULTS

Figure 2 shows typical oscilloscope traces of the current-derivative signal measured during the initial ten to twenty shots before stable operation of the device is

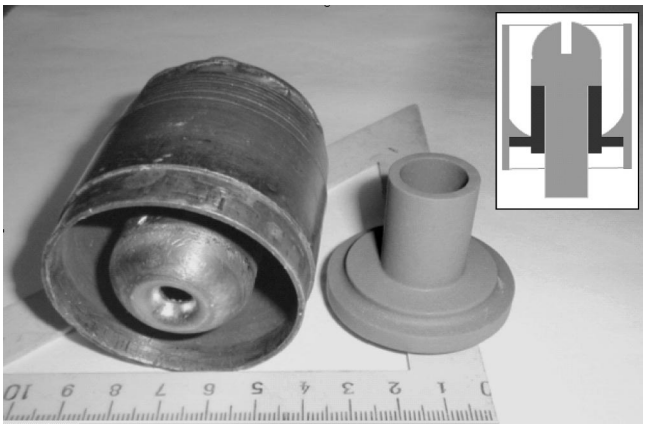

Fig. 1. Photograph of a PF with hemispheric electrodes.

1063-780X/05/3107-0591$26.00 © 2005 Pleiades Publishing, Inc.

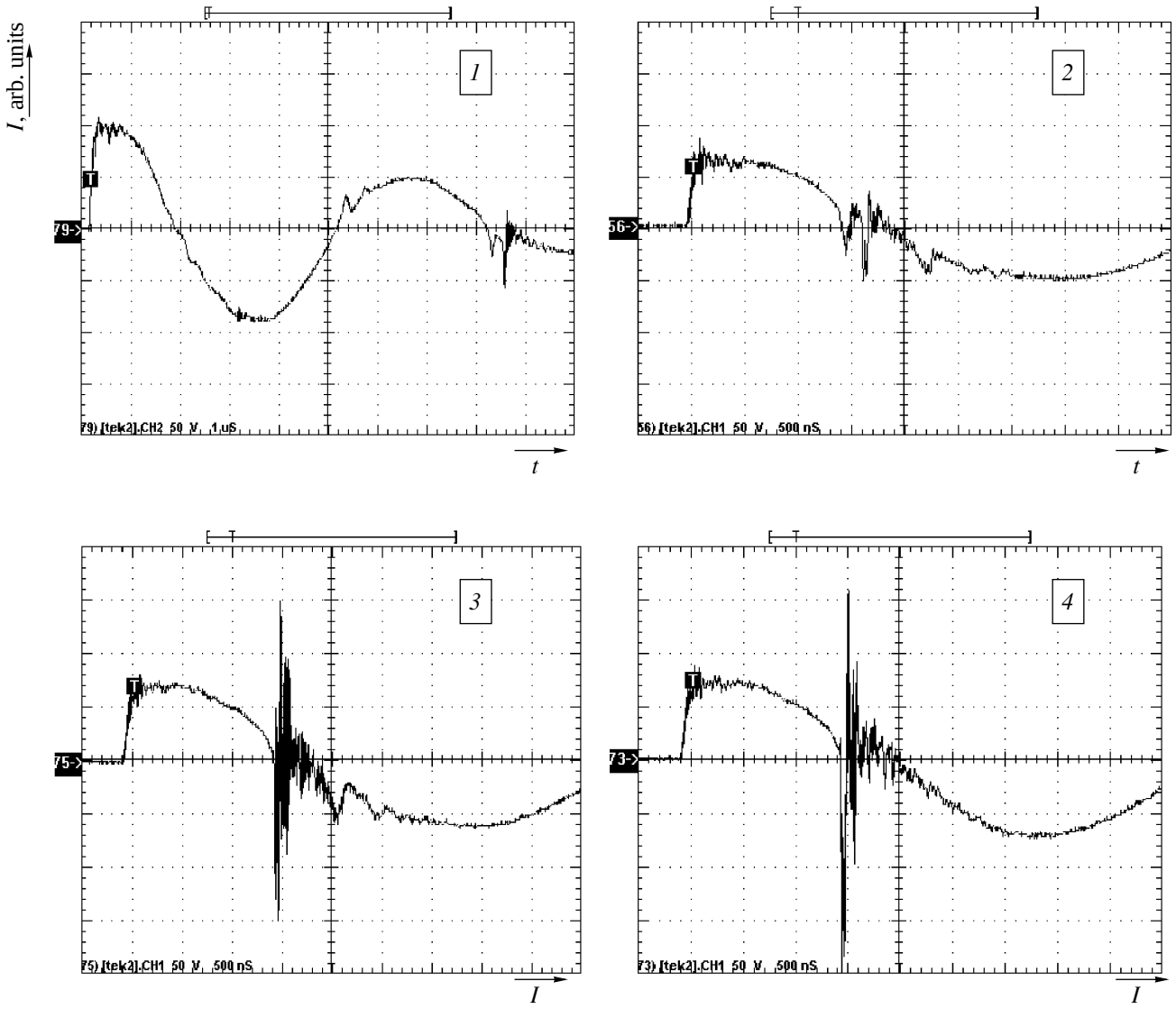

Fig. 2. Evolution of the current-derivative signal at the course of training shots. The time scale is 1 μs/division in the first oscillogram and 0.5 μs/division in the other.

achieved. In these shots, peculiarities in the current-derivative signal initially appear in the third half-period of the discharge current, then in the second half-period, and finally in the first one. Thereafter, the peculiarities in the second and third half-periods disappear, whereas the peculiarity in the first half-period becomes more pronounced. After the peculiarity amplitude exceeds the amplitude of the current-derivative signal, the first neutrons (~10^6 neutrons per shot) appear. A further increase in the amplitude of the peculiarities is accompanied by an increase in the neutron yield to 10^7. Finally, there remains only one large-amplitude peculiarity with an acute peak, and the neutron yield increases to 10^8.

Figure 3 shows photographs taken across the chamber axis near the instant at which a peculiarity in the current-derivative signal appears. The time is counted from the appearance of the peculiarity. It is clearly seen that the current sheath slips along the anode surface. Before the sheath collapses on the chamber axis, its radial velocity reaches a value on the order of 10^7 cm/s. As a result, a cumulative plasma jet is produced that propagates along the chamber axis with a velocity of 2×10^7 cm/s.

Pinch objects are rather difficult to reveal in visible-light photographs because the optical electronic levels in the fully ionized deuterium plasma have already been depleted almost completely (according to [4], a plasma with a density of $\sim 4 \times 10^{14}$ cm^{-3} at a temperature of several electronvolts has the maximum brightness in this spectral region). However, in some shots, millimeter-

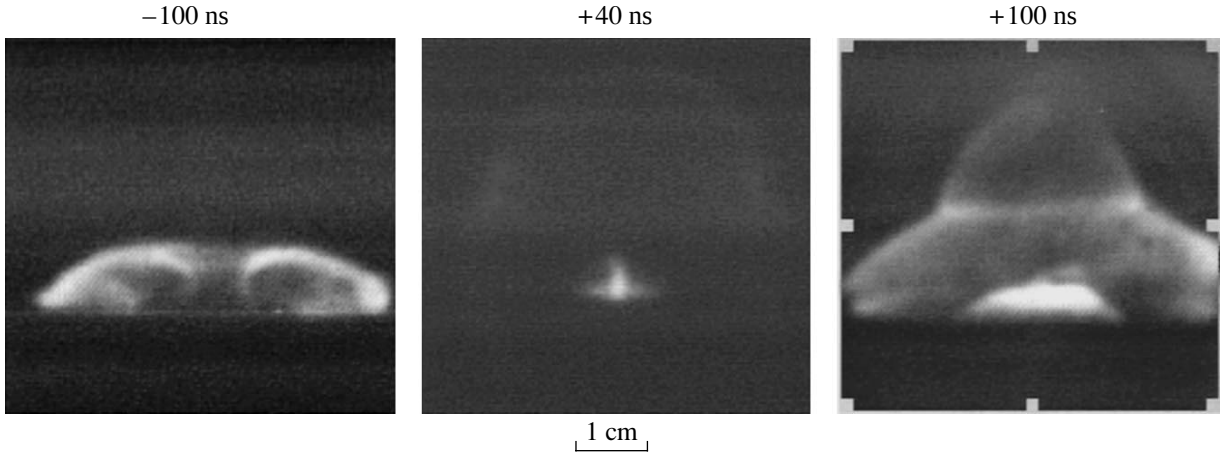

Fig. 3. Typical discharge photographs taken across the chamber axis. The time is counted from the appearance of the first peculiarity.

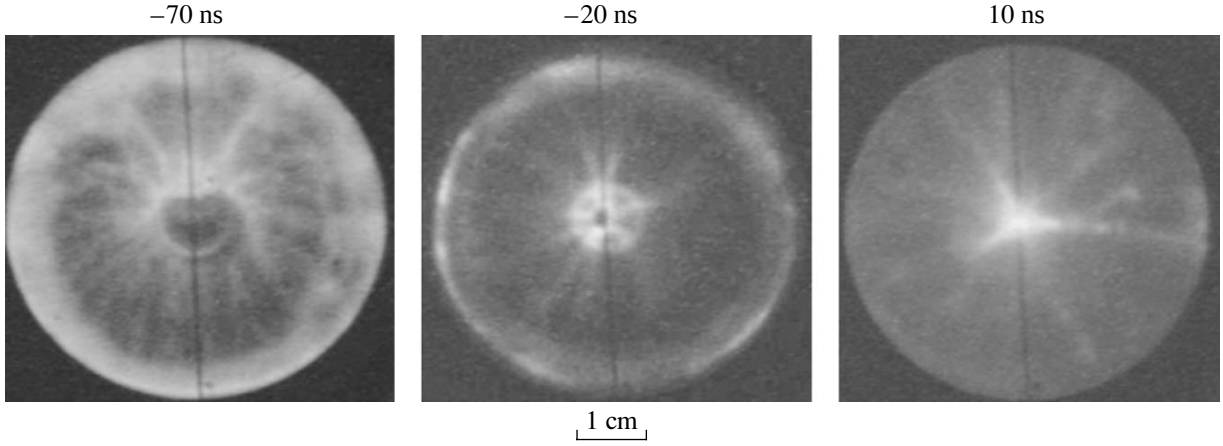

Fig. 4. Filamentation of the current sheath at different stages of the discharge. The photographs were taken along the discharge axis.

size pinches (or more precisely, their "coats") can be seen near the anode.

Figure 4 shows typical discharge photographs taken from the end of the PF at different times. A filamentary structure of the sheath is clearly seen. It was found that, when this structure is asymmetric, the peculiarity in the current-derivative signal is usually small and the neutron yield is low.

4. DISCUSSION OF THE RESULTS

It is well known that the amplitude of the peculiarity in the current-derivative signal correlates with the neutron yield. The new result is that the appearance of the second peculiarity in the first half-period of a discharge (or in other half-periods) usually correlates with a decrease in the amplitude of the first peculiarity and with a substantial decrease in the neutron yield. A comparison of oscilloscope traces with discharge photographs shows that the appearance of the second peculiarity in the first half-period correlates with the appearance of the second current sheath (rather than with the time evolution of the plasma column, as in large devices). In this case, the sheaths resemble nested hats (see Fig. 5). It is interesting that even three peculiarities are sometimes observed in the first half-period.

It is evident that considering (even roughly) the process of the formation of the first sheath [4, 5] can furnish insight into the mechanism for the formation of the second sheath. After the voltage is applied to the electrodes, the following processes occur: (i) the working gas in the chamber is ionized; (ii) the skinning of the current near the insulator leads to the formation of a current sheath and its subsequent filamentation; (iii) and, finally, the sheath separates from the insulator. The merging of the filaments into a continuous current sheath begins after the separation of the sheath [4, 6] and continues up to the pinch compression phase [7–9].

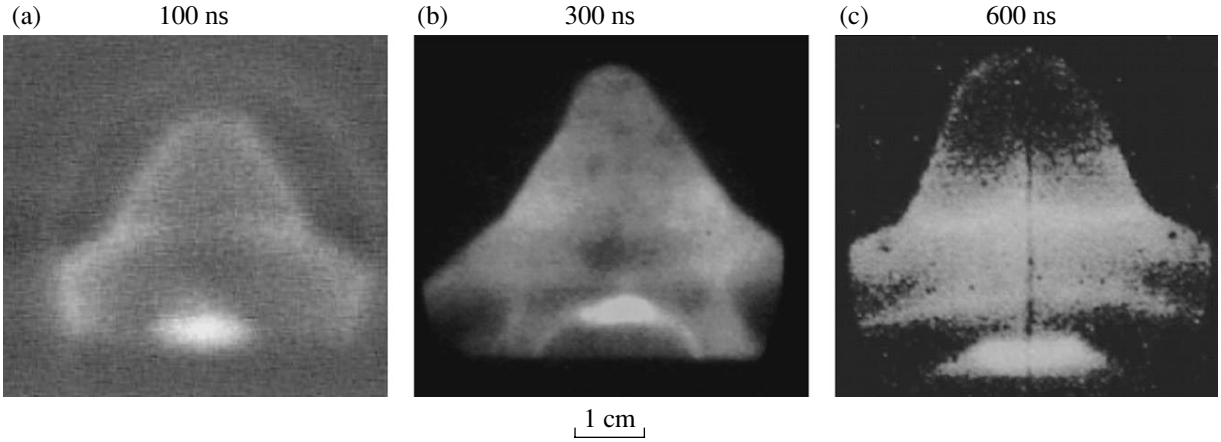

Fig. 5. Discharges with (a) one, (b) two, and (c) three current sheaths.

In our experiments, the filamentary structure was observed in each shot throughout the first half-period of the discharge current until the produced cumulative jet obstructed the field of view of the electron-optical shutter 300–500 ns after the first peculiarity.

The material for the formation of the secondary current structure was probably the gas remaining after the passage of the first sheath, because other possible sources, namely, the gas expelled upward by the current sheath and the gas evaporated from the insulator have no time to fill the discharge gap (their velocity is on the order of the thermal velocity, i.e., 10^4–10^5 cm/s, whereas the characteristic time of the process is 10^{-6}–10^{-7} s).

It is known [4] that a 1-cm-thick homogeneous (without filaments) current sheath with a density of 3×10^{14} cm^{-3} plows the neutral gas almost completely; i.e., the sheath becomes "opaque" in an early stage of the discharge, when the degree of ionization is as low as 10^{-2}. However, when the sheath separates from the insulator, there remains an undragged gas layer with a thickness comparable to the sheath thickness. Another (probably more important) cause of the existence of the residual gas is the filamentary structure of the current sheath, which leads to an incomplete snowplowing of the working gas. The characteristic diameter of the filaments is limited from above by the skin depth [4]. It is clear that, in a thin layer, filaments are located more closely to one another and a smaller amount of gas passes through the sheath. In any case, the contributions from these two gas sources are proportional to the thickness of the current sheath.

For the second current sheath to form, it is necessary that the shunting current flow through the residual plasma in the magnetic field of the main current. The current in the residual plasma flows without substantial losses when this plasma is weakly magnetized, i.e., when $\nu_{ei} > \omega_{Be}$. For simplicity, we assume that the residual plasma is fully ionized and its temperature T is no higher than 10 eV. Substituting the electron–ion collision frequency $\nu_{ei} = 2 \times 10^{-5} n/T^{3/2}$ [10] (where n is the electron density of the residual plasma) and the magnetic field of the axial current $B = 0.2I/R$ into the above inequality, we obtain

$$n > 10^{11} I/R,$$

where R is the average radius of the discharge gap (in cm) and I is the discharge current (in A). When this condition is satisfied, the residual plasma density is high enough to shunt the axial current.

In our experiments, the threshold value for the residual plasma density at a current of 10^5 A and discharge gap radius of ~1 cm is ~10^{16} cm^{-3}, which corresponds to nearly 10% of the initial density of the working gas in the discharge chamber. Hence, in order to efficiently shunt the discharge current, no less than 10% of the working gas should penetrate through the first current sheath. Note, that this lower estimate is obtained under the assumption that the residual plasma is fully ionized.

The snowplow model assumes that the current sheath is impenetrable; this is confirmed by the large cross section for the ion–neutral resonance charge exchange [4, 10]. According to this model, the time at which the sheath arrives at the axis depends slightly on the initial gas density (it is proportional to the fourth root of the initial gas density). For this reason, although the 10% transparency of the sheath has little effect on its motion, it has a substantial effect on the degree of the current shunting in the stage of maximum compression.

The working gas most easily penetrates through the sheath when the current filaments are distributed nonuniformly in the azimuthal direction. Such a nonuniformity may by caused by two effects: the overheating of the sheath and the presence in it of impurities arriving from the constructional elements of the discharge chamber. The impurities decrease the conductivity of the sheath and enlarge and loosen its skin layer; this leads to the onset of large-scale instabilities. The sheath

overheating means that the ratio of the energy stored in the capacitor bank to the initial area of the plasma sheath surface (which coincides with the working area of the insulator surface) exceeds the threshold value above which instabilities develop and the sheath breaks. For the Speed-2 device (300 kV, 180 kJ), this threshold was estimated experimentally at ~100 J/cm^2 [11]. Therefore, a substantial decrease in the insulator radius with the aim of improving magnetic insulation can lead not only to an increase in the inductance and a decrease in the total current, but also to the destruction of the current sheath already in the initial phase of the discharge.

The above considerations allow us to explain why the peculiarity in the current-derivative signal passes from the third and second half-periods of the discharge current to the first half-period as the number of shots increases. In the first discharges, a considerable amount of impurities is evaporated from the insulator surface; this leads to the formation of the subsequent sheaths. Each subsequent sheath carries away a portion of gas from the discharge gap until the residual plasma density decreases to a value satisfying the condition for plasma magnetization. Thereafter, the current flowing through the sheath is no longer shunted and the plasma column is even compressed tightly; this is accompanied by a sharp increase in the discharge inductance and the appearance of a peculiarity in the current-derivative signal. The number of sheaths arising during one shot depends on their transparency, which is determined by the content of impurities affecting the sheath filamentation. The impurity concentration in the sheath decreases from shot to shot; therefore, starting from a certain shot, the working gas can be efficiently snowplowed by the first sheath and a peculiarity in the current-derivative signal appears already in the first half-period of the discharge current.

5. CONCLUSIONS

Based on the experimental data, a criterion for the snowplowing efficiency of the working gas in a plasma-focus discharge can be formulated as follows: The presence of the second peculiarity in the current-derivative signal indicates that the snowplowing of the gas by the current sheath is inefficient. This leads to the shunting of the discharge current by the residual plasma and to a decrease in the neutron yield. The criterion is formulated based on the results from experiments with 1- to 2-kJ plasma focus discharges, in which the current-derivative signal has the shape of a damping sinusoid. In large devices with a stored energy of higher than 100 kJ, the current-derivative signal is much more complicated and the peculiarity in the current-derivative signal lasts over a few hundred nanoseconds. In this case, the effect of shunting by the residual plasma is less pronounced.

ACKNOWLEDGMENTS

This work was supported in part by the “Unique Devices” program of the RF Ministry of Science, Industry, and Technologies (reg. no. 01-07); the RF Presidential Program for Support of Leading Scientific Schools (Studies of Pulsed High-Temperature Plasma; project no. NSh-59-2003.2); the “Integration” special-purpose program (Fundamental Optics and Spectroscopy; project no. B0049); and the “Problems of Plasma Stability and the Achievement of the Limiting Parameters in Magnetic Confinement Systems” Russian academician program.

REFERENCES

1. B. A. Trubnikov, Fiz. Plazmy **12**, 468 (1986) [Sov. J. Plasma Phys. **12**, 271 (1986)].
2. V. A. Evtikhin, Nukleonika **46** (Suppl. 1), 113 (2001).
3. E. P. Bogoljubov, V. D. Bochkov, V. A. Veretennikov, *et al.*, Phys. Scr. **57**, 488 (1998).
4. S. I. Braginskii and V. V. Vikhrev, *Reviews of Plasma Physics*, Ed. by M. A. Leontovich (Atomizdat, Moscow, 1980; Consultants Bureau, New York, 1986), Vol. 10.
5. V. A. Burtsev, V. A. Gribkov, and T. I. Filippova, Itogi Nauki Tekh., Ser. Fiz. Plazmy **2**, 226 (1981).
6. Yu. A. Kolesnikov, Zh. Tekh. Fiz. **38**, 833 (1968) [Sov. Phys. Tech. Phys. **13**, 626 (1968)].
7. J. W. Mather and A. I. Williams, Phys. Fluids **9**, 2080 (1966).
8. I. C. Kvartskhava *et al.*, Nucl. Fusion **5**, 181 (1966).
9. E. Yu. Khautiev, V. I. Kraus, V. V. Vikhrev, and V. M. Fadeev, in *Proceedings of XXIV International Conference on Phenomena in Ionized Gases, Warsaw, 1999*, Vol. 5, p. 89.
10. L. A. Artsimovich, *Controlled Thermonuclear Reactions* (Fizmatgiz, Moscow, 1961; Gordon & Breach, New York, 1964).
11. W. Kies, Plasma Phys. Controlled Nucl. Fusion Res. **28**, 1645 (1986).

Translated by N.F. Larionova

Plasma Physics Reports, Vol. 31, No. 7, 2005, pp. 596–603. Translated from Fizika Plazmy, Vol. 31, No. 7, 2005, pp. 647–654.

PLASMA OSCILLATIONS AND WAVES

On the Dispersion Properties of Waveguides Filled with a Magnetized Plasma

G. I. Zaginaylov*, V. I. Shcherbinin*, and K. Shuenemann**

**Karazin National University, pl. Svobody 4, Kharkov, 61077 Ukraine*

***Technische Universität Hamburg–Harburg, Hamburg, 21073 Germany*

Received August 2, 2004

Abstract—A study is made of the dispersion properties of waveguides filled with a magnetized plasma. It is shown that the eigenmodes of the waveguides filled with a low-density magnetized plasma fall into two families, which are weakly coupled to one another at all frequencies, in particular, in the cyclotron resonance frequency range. These families differ in transverse wavenumbers and the modes in them have hybrid polarization. Attention is focused on the study of the modes that have predominantly TE polarization at frequencies close to the cutoff frequency. The dependence of the critical frequencies of the TE modes on the plasma frequency, as well as the influence of the plasma on the energy flux and energy density of these modes, is investigated. The effect of mode crowding (the existence of an arbitrarily large number of dispersion curves in a finite frequency range between the cyclotron frequency and the upper hybrid frequency) is examined in detail. The results obtained are used to analyze how the plasma affects the electromagnetic properties of the cavity of the 1-MW 140-GHz continuous-wave gyrotron developed at the Institute of Pulsed and Microwave Technology of the Research Center in Karlsruhe, Germany (Institut für Hochleistungsimpuls- und Mikrowellentechnik Forschungszentrum Karlsruhe) for plasma heating in the W7-X stellarator, which is being constructed in Greifswald, Germany. © *2005 Pleiades Publishing, Inc.*

1. INTRODUCTION

Investigation of the electromagnetic properties of plasma waveguide structures is very important for a number of technological applications, such as the generation of high-power electromagnetic radiation, the transport of high-current charged particle beams, and the development of efficient methods for charged particle acceleration. The waveguide structures that are most widely used in such applications are those based on circular plasma-filled waveguides with constant or periodically varying radii in a longitudinal magnetic field.

To efficiently use plasma waveguide structures in various applications, it is necessary to have reliable information about the spectra of their eigenmodes and the details of the field distributions in them.

Most theoretical studies of plasma waveguides are carried out by assuming that the magnetic field is infinitely strong; this makes it possible to substantially simplify the analysis. In some cases, however, this simplification is undesirable and even inappropriate. In particular, this concerns the description of such topics as cyclotron modes of a plasma waveguide, electromagnetic modes of plasma waveguides at frequencies close to the cyclotron frequency, and cyclotron mechanisms for the interaction of a beam with the eigenmodes of a plasma waveguide structure. The dispersion properties of plasma-filled waveguide structures in a finite magnetic field have received insufficient study, even in their simplest form and for the simplest plasma models. The key problem in investigating plasma waveguide structures in a finite magnetic field is that of a cylindrical waveguide filled with a homogeneous cold collisionless plasma and placed in a longitudinal magnetic field. A detailed and comprehensive analysis of this idealized problem is necessary, because it provides basic knowledge and facilitates the examination of more realistic (and, accordingly, more complicated) problems about the influence of the finite magnetic field on the electromagnetic properties of periodic plasma waveguide structures, about waveguide structures filled with an inhomogeneous plasma, etc. By now, however, despite numerous efforts [1–5], even this simplest problem has not been investigated in full measure. It is known (see, e.g., [1]) that, in a finite magnetic field, modes with different polarizations are mutually coupled and there are hybrid waves whose electromagnetic field has all six nonzero components. In this case, the spatial field distribution, as well as the dispersion relation, becomes far more complicated. The transverse field structure is described by two terms containing different transverse wavenumbers. The relevant dispersion relation was obtained in analytic form rather a long time ago (see, e.g., [1, 2]); however, it is so complicated that many its properties still remains unclear. At present, the best studied cases are those in which the wave fields can be approximately divided according to their polarization into TE- and TM-type fields [3–5], i.e., those in which the effects related to the finite magnetic field are weak and can be considered using pertur-

1063-780X/05/3107-0596$26.00

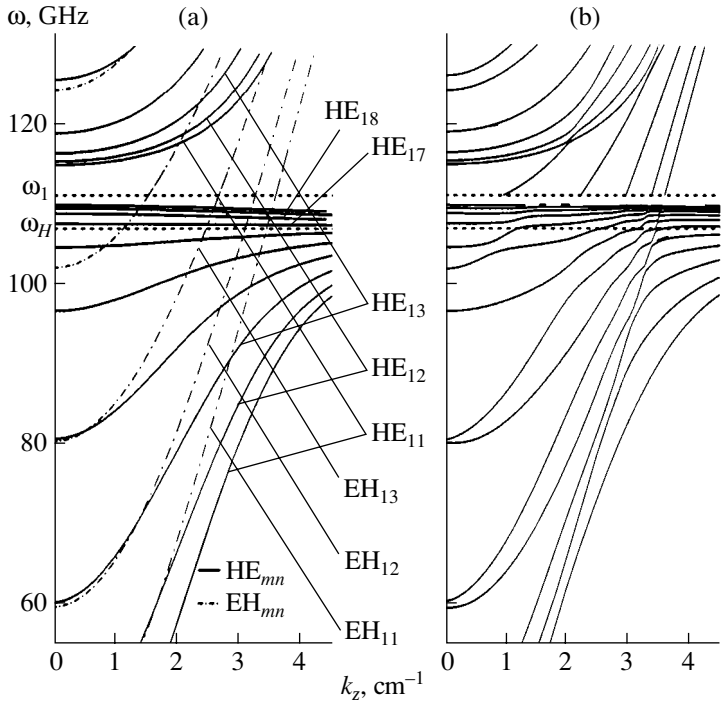

Fig. 1. Dispersion curves for a waveguide filled with a magnetized plasma: (a) the dispersion curves for the first (EH) and second (HE) mode families, $D_{1,2}(\omega, k_z) = 0$, and (b) the dispersion curves described by the simplified dispersion relation (7).

bation theory. For this to be the case, it is necessary that the plasma density be sufficiently low and the perturbation frequency be sufficiently different from the electron-cyclotron frequency,

$$\omega_p^2/(\omega^2 - \omega_H^2) \ll 1, \qquad (1)$$

where $\omega_p = (4\pi e^2 n/m)^{1/2}$ is the electron plasma frequency, $\omega_H = eH/mc$ is the cyclotron frequency of the plasma electrons, e and m are the charge and mass of an electron, n is the electron plasma density, and c is the speed of light in vacuum.

In the case of an arbitrary plasma density, too, the modes with different polarizations can be approximately divided into two families provided that the longitudinal wavenumber k_z is small, $(k_z c/\omega)^2 \ll 1$. For $k_z = 0$, the modes can be divided into two completely different families and it is possible to obtain analytic expressions for the cutoff frequencies of the TE and TM modes. In this case, in the frequency range $\omega_H < \omega < (\omega_p^2 + \omega_H^2)^{1/2}$, there are an infinite number of cutoff frequencies for the TE modes and, accordingly, there are an infinite number of dispersion curves. The effect of the crowding of dispersion curves has received insufficient study, so its physical nature and essence are not quite clear as yet. Since the dispersion relation in the general case is rather complicated and can be analyzed only numerically and since numerical methods cannot provide an exhaustive description of the crowding of dispersion curves, new results can be obtained only by applying novel analytic techniques.

It should be noted that the dispersion curves at frequencies sufficiently different from the electron cyclotron frequency $\omega \sim \omega_H$ were investigated numerically by Kuzelev *et al.* [6]. They found that, unlike in vacuum waveguides, the dispersion curves of waveguides filled with a magnetized plasma have unusual, meandering shapes, which are rather difficult to interpret. In [4], it was shown that such an unusual shape of the dispersion curves is attributed to the existence of an opaque region, which expands with increasing plasma density and has the effect of expelling the dispersion curves and of deforming them (see, e.g., [4], Fig. 3). Onishchenko and Sotnikov [7], however, showed that, within these opaque regions, there also may be dispersion curves. On the other hand, at low plasma densities, such that an opaque region is essentially absent, the dispersion curves are nonetheless appreciably deformed in comparison to those for a vacuum waveguide. Therefore, the mechanism for the formation of dispersion curves that was proposed in [4] is not unique.

In what follows, based on analytical and numerical investigations, we obtain some new results on the dispersion properties of plasma-filled waveguides in a finite magnetic field. In contrast to earlier studies, in which the main attention was paid to slow TM waves, we focus on fast TE modes. In particular, we show that the expressions for the cutoff frequencies of the TE modes differ from those obtained earlier and depend on

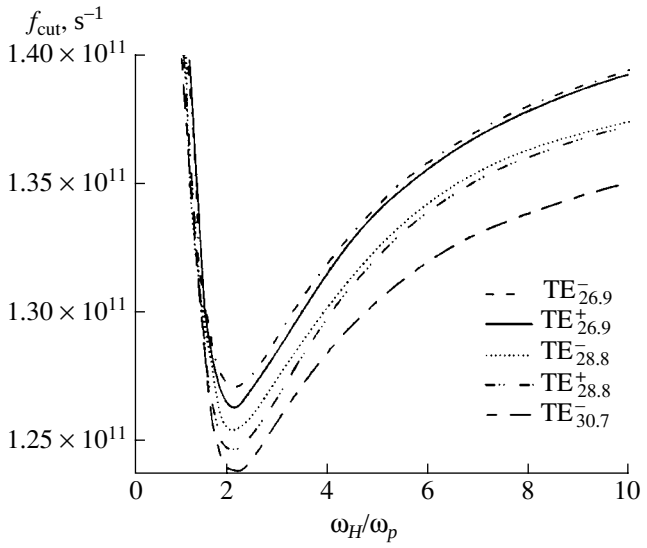

Fig. 2. Critical frequencies of the TE modes of a waveguide filled with a magnetized plasma vs. plasma density for B = 5.56 T and R = 2.045 cm.

the sign of the azimuthal mode number. We qualitatively investigate the effect of the crowding of dispersion curves and also the mechanism by which the dispersion curves of the waveguides filled with a magnetized plasma are deformed. We concentrate primarily on the case of a plasma of comparatively low density, $\omega_p^2/\omega^2 \ll 1$. However, we do not rule out the possibility that inequality (1) may fail to hold, i.e., that the waves under consideration may be, in essence, hybrid waves that comprise strongly coupled perturbations of the TE and TM types. We will show that, in this case, the analysis of the dispersion relation can be significantly simplified. The solutions to the dispersion relation describe two families of hybrid modes that are weakly coupled to one another at all frequencies, in particular, in the cyclotron resonance frequency range $\omega \approx \omega_H$. The only exception is the immediate vicinities of the points where the dispersion curves of one family intersect those of the other family (the dispersion curves of the same family are nonintersecting). In other words, these are points of "reconnection" of the dispersion curves. It is this reconnection that acts as a mechanism for the deformation of the dispersion curves, in addition to the mechanisms that were proposed earlier (see, e.g., [4]). The higher the plasma density, the larger the reconnection regions and the more conditional the division of the modes into two families. Note, however, that the hydrodynamic description developed here remains qualitatively valid for arbitrary plasma densities; its applicability is limited by the condition $k_z^2 v_T^2/(\omega - \omega_H)^2 \ll 1$ (where v_T is the thermal velocity of the plasma electrons), which is routinely used in studies of a magnetized plasma.

Our paper is organized as follows. In Section 2, we describe the method for simplifying the dispersion relation for a cylindrical waveguide filled with a homogeneous low-density ($\omega_p^2/\omega^2 \ll 1$) cold plasma in a longitudinal magnetic field of finite amplitude. We show that

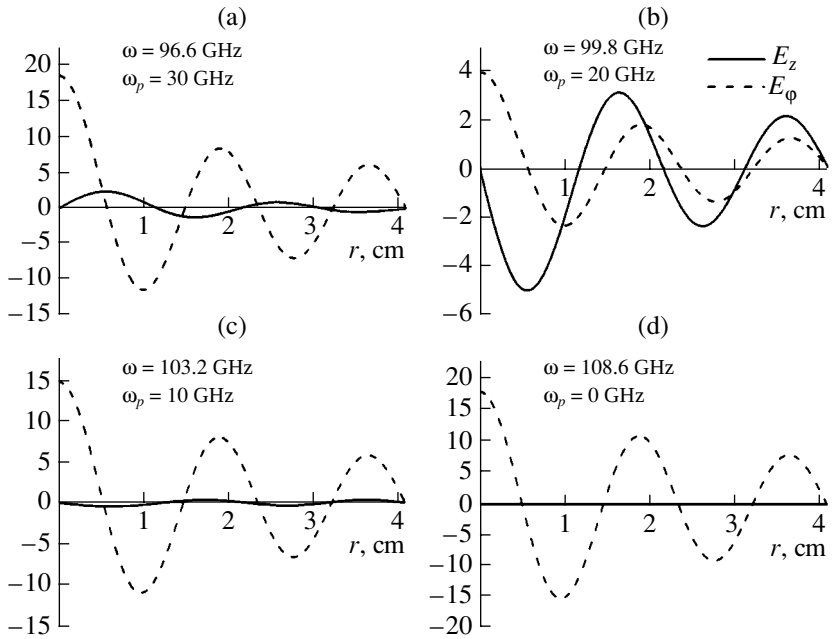

Fig. 3. Distribution of the fields of the $TE_{1,5}$ mode at different plasma densities for k_z = 0.1 cm^{-1}, ω_H = 107 GHz, and R = 4.1 cm.

the dispersion relation refers to two families of modes that are weakly coupled to one another and are described by simpler dispersion relations, which admit thorough and illustrative investigations by analytical and numerical methods. In Section 3, we analyze the two families of hybrid modes and give insight into the mechanism for the formation of the dispersion curves that reconnect at the intersection points and are thus common to both families. In Section 4, we examine the influence of the plasma on the redistribution of the fields over the waveguide cross section. We show that, in the case of TE modes, the plasma acts to reduce heat loads to the waveguide wall and to increase the energy of microwave perturbations in comparison to that in a vacuum waveguide with the same heat loads to the wall. In the Conclusions, we summarize and discuss the main results of our study.

2. DISPERSION RELATION FOR A CYLINDRICAL WAVEGUIDE FILLED WITH A MAGNETIZED PLASMA AND ITS SIMPLIFICATION IN THE CASE OF A LOW-DENSITY PLASMA

The general dispersion relation for a cylindrical waveguide filled with a magnetized plasma and placed in a longitudinal magnetic field of arbitrary amplitude has the form (see, e.g., [1–7])

$$\begin{aligned} &J_l'(k_2R)J_l(k_1R)k_2\{k_zk\varepsilon_2 - i\chi^2 b_2\} \\ &- J_l'(k_1R)J_l(k_2R)k_1\{k_zk\varepsilon_2 - i\chi^2 b_1\} \\ &+ \frac{l}{R}\frac{k}{k_z}\varepsilon_1(k_1^2 - k_2^2)J_l(k_1R)J_l(k_2R) = 0, \end{aligned} \quad (2)$$

where

$$\chi^2 = k_z^2 - \varepsilon_1 k^2, \quad b_{1,2} = \frac{i}{kk_z\varepsilon_2}(\varepsilon_3\chi^2 + \varepsilon_1 k_{1,2}^2),$$

$$2\varepsilon_1 k_{1,2}^2 = -(\varepsilon_1 + \varepsilon_3)\chi^2 - k^2\varepsilon_2^2 \pm \sigma,$$

$$\sigma = \sqrt{[(\varepsilon_1 - \varepsilon_3)\chi^2 + k^2\varepsilon_2^2]^2 + 4k_z^2\varepsilon_2^2k^2\varepsilon_3},$$

$$\varepsilon_1 = 1 - \frac{\omega_p^2}{\omega^2 - \omega_H^2}, \quad \varepsilon_2 = \frac{\omega_p^2\omega_H}{\omega(\omega^2 - \omega_H^2)}, \quad \varepsilon_3 = 1 - \frac{\omega_p^2}{\omega^2},$$

$k = \omega/c$ is the wave vector in free space, and R is the waveguide radius.

In deriving this dispersion relation, it was assumed that the fields are described by the expressions

$$A(r, t) = A(r)\exp(-i\omega t + ik_z z + il\varphi),$$

$$l = 0, \pm 1, \pm 2, \ldots.$$

However, because of its complexity, dispersion relation (2) is very difficult to analyze (both analytically and numerically), especially in the frequency range $\omega \sim \omega_H$. Even when the plasma frequency is much lower than the perturbation frequency, $\omega_p^2/\omega^2 \ll 1$, numerous terms proportional to ω_p^2 cannot be discarded, because some of them have the resonant denominators $\omega^2 - \omega_H^2$ and the others are proportional to k_z^2, so they, too, can increase resonantly as $\omega \longrightarrow \omega_H$. Moreover, the rate of increase of k_z is not known a priori and can only be determined after dispersion relation (2) has been solved. Hence, even with the above small parameter, it is not obvious how the terms of this dispersion relation should be grouped according to their orders of smallness. This is why we will utilize a comparatively simple analytic technique, which will make dispersion relation (2) far simpler and, accordingly, far easier to analyze.

In this way, we begin by presenting a few exact relationships between the elements of the plasma dielectric tensor:

$$\varepsilon_1^2 - \varepsilon_2^2 = \varepsilon_1 - \varepsilon_3 + \varepsilon_1\varepsilon_3, \quad \varepsilon_1 - \varepsilon_3 = -\varepsilon_2\frac{\omega_H}{\omega}. \quad (3)$$

With these relationships, which can be readily verified by direct substitution, the expression for σ can be transformed to

$$\sigma = (\varepsilon_3 - \varepsilon_1)\sqrt{(k_z^2 - k^2)^2 + 4k^2k_z^2\varepsilon_3\frac{\omega^2}{\omega_H^2}}$$

$$= (\varepsilon_3 - \varepsilon_1)\sqrt{(k_z^2 + k^2)^2 + 4k^2k_z^2\left(\frac{\omega^2 - \omega_p^2}{\omega_H^2} - 1\right)}.$$

For $\omega_p^2 \ll \omega_H^2$, the second term under the square root symbol is much less than the first term, provided that any of the following three conditions is satisfied:

$$k_z^2 \ll k^2, \quad k_z^2 \gg k^2, \quad |\omega^2 - \omega_H^2|/\omega_H^2 \ll 1. \quad (4)$$

Under conditions (4), this second term can be ignored in the zeroth approximation, so the expressions for the transverse wavenumbers $k_{1,2}$ can be greatly simplified:

$$k_1^2 = \varepsilon_3 k^2 - k_z^2,$$

$$k_2^2 = \frac{\varepsilon_1 - \varepsilon_3 + \varepsilon_1\varepsilon_3}{\varepsilon_1}k^2 - \frac{\varepsilon_3}{\varepsilon_1}k_z^2. \quad (5)$$

Dispersion relation (2), too, can be converted into a much simpler form that makes its properties far easier to investigate:

$$D_1(\omega, k_z)D_2(\omega, k_z) + \alpha(\omega, k_z) = 0, \quad (6)$$

where

$$D_1(\omega, k_z) = J_l(k_1R),$$

$$D_2(\omega, k_z) = \frac{k_1^2}{k_z^2 + k^2} J_l'(k_2R) + \frac{l}{k_2R}\frac{\varepsilon_2}{\varepsilon_1} J_l(k_2R),$$

$$\alpha(\omega, k_z) = \frac{k_1 k_2 k_z^2}{k^2(k_z^2 + k^2)} J_l(k_2R) J_l'(k_1R).$$

In the limit $\alpha(\omega, k_z) \ll 1$, dispersion relation (6) describes two families of waves that are weakly coupled to one another and whose dispersion curves satisfy the dispersion relations $D_1(\omega, k_z) = 0$ and $D_2(\omega, k_z) = 0$, the transverse wavenumbers k_1 and k_2 being given by expressions (5). This is true for the range $k_z^2 \ll k^2$ and also for $k_z \sim k$. In the range $k_z > k$, the function $D_1(\omega, k_z)$ cannot vanish because the wavenumber k_1 is purely imaginary and only the second wave family can exist. However, for $k_z \gg k$, the dispersion curves of the second family approach those described by the equation $\alpha(\omega, k_z) = 0$, or equivalently $J_l(k_2R) = 0$, and, in the limit $k_z \longrightarrow \infty$, they become the dispersion curves of the potential TM waves that were considered earlier in [3].

Hence, the properties of dispersion relation (6) are mainly governed by the properties of the two simpler dispersion relations $D_1(\omega, k_z) = 0$ and $D_2(\omega, k_z) = 0$ and the dispersion curves of relation (6) are close to those of these two relations, except for the vicinities of the points where the dispersion curves of one family intersect those of the other, i.e., where the functions $D_{1,2}(\omega, k_z)$ vanish simultaneously.

The dispersion curves of both families can be investigated in exhaustive detail, both analytically and numerically.

In the case under consideration, the dispersion curves of the first family differ insignificantly from those of the TM modes of a vacuum waveguide and are very close to the dispersion curves of the TM modes in a plasma-filled waveguide in an infinitely strong magnetic field. The dispersion properties of the last modes have been studied in sufficient detail (see, e.g., [8] and the literature cited therein).

The dispersion relation for the waves from the second family can be conveniently represented as

$$J_l(x) + b(\omega, k_z) x J_l'(x) = 0, \quad (7)$$

where $x = k_2R$ and the function $b(\omega, k_z)$ is equal to $b(\omega, k_z) = \frac{k_1^2}{k^2 + k_z^2}\frac{\varepsilon_1}{\varepsilon_2}\frac{}{l}$ for $k_z < k$ and for $k_z \sim k$ and approaches zero for $k_z \gg k$.

It is known [9] that, for an arbitrary finite value of the function $b(\omega, k_z)$, all positive roots of dispersion relation (7) regarded as an equation for x are simple (unrepeated) and lie between the roots $\mu_{l,n}$ ($n = 1, 2, \ldots$) of the lth-order Bessel function. In terms of these simple positive roots, which will be denoted by $\nu_{l,n}(\omega, k_z)$, the equation determining the dispersion curves can be rewritten in the form $k_2R = \nu_{l,n}(\omega, k_z)$, whose analysis is far easier and much more convenient than the direct analysis of dispersion relation (7) because the roots $\nu_{l,n}(\omega, k_z)$ increase monotonically with n and none of them is a crowding point. On the other hand, in accordance with [8] and with the examination to follow, the dispersion curves described by Eq. (7) are subject to crowding in the (ω, k_z) plane; this considerably complicates their analysis. Using formulas (5), we can express the wavenumber k_z in terms of the roots $\nu_{l,n}(\omega, k_z)$:

$$k_z^{l,n} = \sqrt{\frac{k^2(\varepsilon_1 - \varepsilon_3 + \varepsilon_1\varepsilon_3) - \varepsilon_1\nu_{l,n}^2(\omega, k_z^{l,n})/R^2}{\varepsilon_3}}. \quad (8)$$

The qualitative shape of the dispersion curves from both families is illustrated in Fig. 1a. By comparing Fig. 1a to Fig. 1b, which presents the dispersion curves of Eq. (7), we arrive at the following obvious conclusion: the dispersion curves of Eq. (7) are formed by both of the two families of dispersion curves, which reconnect at the intersection points. A comparison of the dispersion curves of the simplified dispersion relation (7) with those of the exact dispersion relation (2) shows that, for the parameter values under consideration, they are essentially identical.

In the frequency range $\omega_H < \omega < \omega_1$ (where $\omega_1 = \sqrt{\omega_H^2 + \omega_p^2}$ is the upper hybrid frequency), there is an infinite number of dispersion curves from the second family. This fact can be inferred by analyzing expression (8). As the frequency approaches ω_H from below, the wavenumbers $k_z^{l,n}$ increase without bound. The number of branches that asymptotically approach the straight line $\omega = \omega_H$ is determined by the condition $k^2(\varepsilon_1 - \varepsilon_3 + \varepsilon_1\varepsilon_3) - \varepsilon_1\nu_{l,n}^2(\omega, k_z)/R^2\big|_{\omega \to \omega_H, k_z \to \infty} > 0$. By virtue of the relationship $\nu_{l,n}(\omega_H, \infty) = \mu_{l,n}$, this condition can be transformed to

$$\mu_{l,n} < (2 - \omega_p^2/\omega_H^2)^{1/2}\omega_H R/c. \quad (9)$$

All the dispersion curves $HE_{l,n}$ of the modes from the second family (see Fig. 1a) for which l and n satisfy this condition have two branches, one of which lies below the frequency ω_H and the other lies above the frequency ω_1. The number of these modes is always finite. For $(2 - \omega_p^2/\omega_H^2)^{1/2}\omega_H R/c < \mu_{0,1}$, none of the curves lie below the frequency ω_H. The number of modes from the second family for which the inequality opposite to inequality (9) is satisfied is always infinite. The dispersion curves of such modes, too, have two branches. One of them lies above the frequency ω_1 and essentially coincides with the corresponding branch for a vacuum waveguide. The other branch lies within the frequency range $\omega_H < \omega < \omega_1$ and is characterized by an anomalous dispersion. For the case illustrated in Fig. 1, we have $\mu_{1,6} < (2 - \omega_p^2/\omega_H^2)^{1/2}\omega_H R/c < \mu_{1,7}$; consequently,

all the dispersion curves $HE_{l,n}$ with n greater than 6 lie within the range $\omega_H < \omega < \omega_1$. In Fig. 1, we plot only some of these dispersion curves.

Hence, we have clearly demonstrated that, in the frequency range in question, there is an infinite number of dispersion curves with the numbers l and n for which inequality (9) fails to hold.

Let us consider in more detail the cutoff frequencies of the modes from the second family. Setting $k_z = 0$ in dispersion relation (7), we see that the cutoff frequencies satisfy the equation

$$J_l(x(\omega)) + \frac{\varepsilon_1}{\varepsilon_2 l} x(\omega) J_l'(x(\omega)) = 0, \qquad (10)$$

where $x(\omega) = k_2 R|_{k_z = 0} = \sqrt{\dfrac{(\omega^2 - \omega_p^2)^2 - \omega_H^2 \omega^2}{\omega^2 - \omega_p^2 - \omega_H^2}} \dfrac{R}{c}$.

In contrast to Eq. (7), dispersion relation (10) is exact and is valid for any value of the plasma density. From dispersion relation (10), we see that the cutoff frequencies of the right-polarized ($l > 0$) modes differ from those of the left-polarized ($l < 0$) modes—the result that was not mentioned earlier.

The dependence of the cutoff frequencies of the TE modes on the plasma density is illustrated in Fig. 2, which shows the results of calculations carried out for the resonant cavity of the 1-MW $TE_{28.8}$-mode-based continuous-wave gyrotron developed in Karlsruhe (Germany) for plasma heating in the W7-X stellarator. A possible reason for a reduction in the operating frequency of the gyrotron may be the appearance of plasma in the cavity [10].

As the plasma density increases in the range of its low values such that $\omega_H/\omega_p > 2$, the cutoff frequencies of both the right- and left-polarized modes decrease. As the plasma density increases further, the critical frequencies stop decreasing and begin to increase. For $l = 0$, dispersion relation (10) coincides with the corresponding dispersion relation presented earlier in [4].

3. POLARIZATION, FIELD DISTRIBUTIONS, ENERGY DENSITY, AND ENERGY FLUX OF THE ELECTROMAGNETIC WAVES IN A PLASMA-FILLED WAVEGUIDE IN A FINITE MAGNETIC FIELD

In the limit of an infinitely low plasma density, electromagnetic waves from the first family tend to become TM waves of a vacuum waveguide. According to the classification proposed by Liu *et al.* [11], such waves should be treated as EH waves. In the same limit, electromagnetic waves from the second family tend to become TE modes; consequently, in accordance with [11], they should be classified as HE waves. It is necessary to note, however, that, for an arbitrarily low (but finite) plasma density, the second family contains slow waves, which disappear completely (in a jumplike manner) only at $\omega_p = 0$.

In studying the effect of the plasma on the field distributions in a plasma-filled waveguide, we restrict ourselves to considering as an example HE modes with frequencies close to the cutoff frequency ($k_z^2 \ll k^2$) in a waveguide filled with a low-density plasma ($\omega_p^2/\omega^2 < 1/2$). The HE modes in question are polarized in essentially the same manner as the TE waves and thereby can be conveniently called TE modes of a plasma-filled waveguide. It is this case that is of primary interest in studying the effect of the plasma on the operation of high-power gyrotrons [10] and also in analyzing such issues as the generation of microwave radiation and the development of plasma-filled microwave devices whose operation is based on the cyclotron instability of an electron beam. It should be emphasized that, in comparison to the TM modes of a vacuum waveguide, the TE modes of a plasma-filled waveguide have a number of qualitatively new properties. These properties, which manifest themselves even in the case of a very low plasma density, can be important for the above applications. Specifically, the frequencies of the right- and left-polarized modes are different and the dispersion curve of each of the TE modes splits into two branches with different cutoff frequencies. The second cutoff frequency is attributed to the presence of plasma and has no analogue in vacuum waveguides: it exists at an arbitrarily low (but finite) plasma density and disappears completely (in a jumplike manner) only at $\omega_p = 0$. Its other properties are as follows: it depends weakly on the radial and axial numbers of the TE modes and approaches the electron cyclotron frequency ω_H as the plasma density decreases.

When the plasma density is low, the plasma does not significantly affect the polarization of the fields of TE modes at frequencies close to the cutoff frequencies, as well as the distribution of these fields over the waveguide cross section (see Figs. 3a, 3c). This is, however, true only for those TE modes whose cutoff frequencies are not close to the cutoff frequencies of the TM modes with the same azimuthal number. Otherwise, the polarization and distribution of the fields of the TE modes can be appreciably distorted even by a very low-density plasma (see Fig. 3b).

It is of great interest to investigate the effect of the plasma on the energy density of the TE modes and on the energy flux in them. Using the general formula for the density and flux of the electromagnetic energy in an anisotropic dispersive medium [12],

$$W = \frac{1}{16\pi}\left(\frac{\partial(\omega\varepsilon_{ik}(\omega))}{\partial\omega} E_i E_k^* + |\mathbf{H}|^2\right),$$
$$\mathbf{S} = \frac{c}{8\pi}\mathbf{E} \times \mathbf{H}^*, \qquad (11)$$

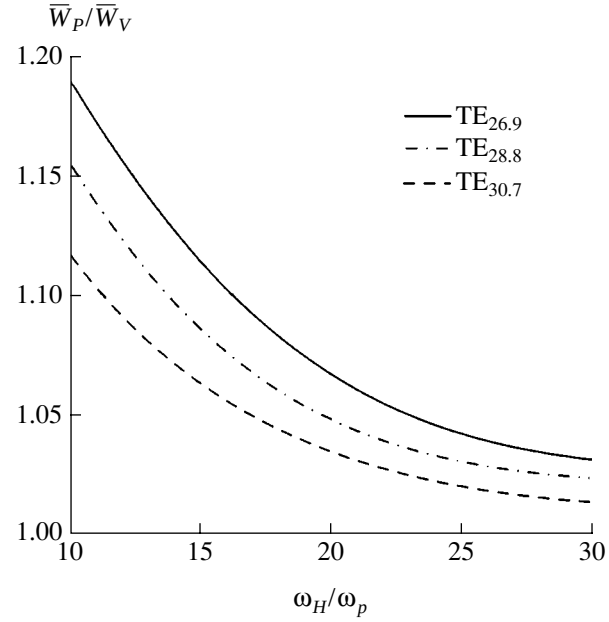

Fig. 4. Normalized line energy density vs. plasma density for B = 5.56 T and R = 2.045 cm. Here, $\overline{W}_P$ is the line energy density in a plasma-filled waveguide and $\overline{W}_V$ is the line energy density in a vacuum waveguide.

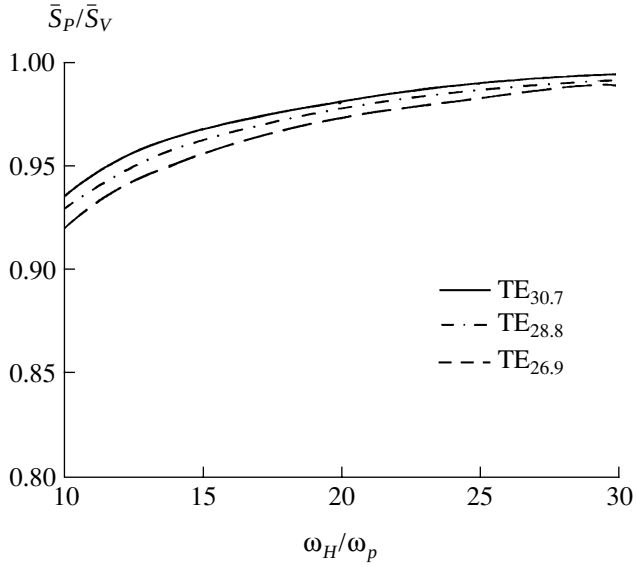

Fig. 5. Normalized line energy flux vs. plasma density for B = 5.56 T and R = 2.045 cm. Here, $\bar{S}_P$ is the line energy flux in a plasma-filled waveguide and $\bar{S}_V$ is the line energy flux in a vacuum waveguide.

we can obtain analytic representations for the line energy density (i.e., the energy density per unit length of the waveguide) $\overline{W} = \int_S W ds$ and the energy flux through the waveguide cross section, $\bar{S}_z = \int_S S_z ds$, in the case $k_z^2 \ll k^2$. It is expedient to express these parameters in terms of the tangential magnetic field at the waveguide wall because this field characterizes the heat loads to it. For illustrative purposes, we present the expressions obtained for the case of a low-density plasma with allowance for the terms on the order of ε_2^2:

$$\overline{W} \approx \frac{1}{16\varepsilon_1}\left(1 + \frac{1}{\varepsilon_1}\left(1 + \frac{\omega_p^2(\omega^2 + \omega_H^2)}{(\omega^2 - \omega_H^2)^2}\right)\right) \times |H_\tau(R)|^2 (k_2^2 R^2 - l^2), \quad (12)$$

$$\bar{S}_z \approx \frac{ck_z}{8}\frac{|H_\tau(R)|^2}{k^3\varepsilon_1^4}[\varepsilon_1^2(k_2^2R^2 - l^2) + 2l\varepsilon_1\varepsilon_2]. \quad (13)$$

Figures 4 and 5 illustrate the difference between the line energy density and energy flux in a plasma-filled waveguide and those in a vacuum waveguide with the same heat loads to the wall.

4. CONCLUSIONS

The investigation of the dispersion properties of waveguide structures is the first, the most natural, and a fairly important step in the analysis of their electromagnetic properties and their possible practical applications. The mathematical technique for a description of the waveguide's dispersion properties has already been well developed; however, because of the complexity of the dispersion relation for a waveguide filled with a magnetized plasma, the properties of its solutions have received insufficient study. In plasma-filled waveguides, a number of new effects are possible in comparison to vacuum waveguides, in particular, the effect of mode crowding (the existence of an arbitrarily large number of dispersion curves in a finite frequency range). The investigation of the dispersion properties of waveguides filled with a magnetized plasma is also complicated because it is necessary to take into account the coupling between the TM and TE waves and the appearance of hybrid modes. Moreover, this coupling, which is attributed to the anisotropy of the dielectric tensor of a cold magnetized plasma, can be fairly strong even when the plasma density is low. This is the case in the cyclotron resonance frequency range $\omega \sim \omega_H$, in which the elements of the plasma dielectric tensor increase resonantly, and in the vicinities of the points where the branches of the dispersion curves of the TE modes intersect those of the TM modes.

In the present paper, we have proposed to classify the modes in terms of their transverse wavenumber (rather than according to polarization). We have shown that, for $\omega_p^2 \ll \omega_H^2$, the solutions to the general dispersion relation for the modes over the entire range of frequencies, including those close to the cyclotron resonance frequency, $\omega \sim \omega_H$, can be divided into two

weakly coupled families. The modes from these families do not necessarily have the same polarization as the TM or TE modes but they tend to become TM and TE modes in the limit of an infinitely low plasma density. According to the classification adopted in [11], the modes of the first and second families should be treated as EH and HE modes, respectively. At the points of their intersection, the dispersion curves of these two families reconnect to become wavy and more complicated structurally (a situation typical of magnetized plasma waveguides). We have also rigorously proved that, in the frequency range $\omega_H < \omega < \sqrt{\omega_H^2 + \omega_p^2}$, there are an infinite number of dispersion curves.

We have investigated the dependence of the critical frequencies of TE modes on the plasma density and have shown that these critical frequencies depend on the sign of the azimuthal mode number and, as functions of plasma density, have a minimum at $\omega_p \cong 0.5\omega_H$ regardless of the radial and azimuthal mode numbers. We have studied the effect of the plasma on the structure and distribution of the fields of TE modes with frequencies close to the cutoff frequencies and have shown that a plasma of low density (such that $\omega_p \leq 0.5\omega_H$) does not significantly affect the distribution and structure of the fields of the TE modes, except when the cutoff frequencies of the TE modes are close to those of the TM modes (Fig. 3b). The line energy density of the TE modes in a plasma-filled waveguide can be substantially higher than that in a vacuum waveguide with the same radius and with the same heat loads to the wall. On the other hand, the energy flux in a plasma-filled waveguide is less intense than that in a vacuum waveguide with the same parameters. At low plasma densities, however, this difference in the energy flux intensities is not large.

The results of our investigations can be of interest in connection with the development of devices for plasma electronics and interpretation of the operating modes of high-power gyrotrons that are being developed for use in fusion devices [10].

ACKNOWLEDGMENTS

We are grateful to Prof. M. Thumm, the director of the Institute of Pulsed and Microwave Technology of the Research Center in Karlsruhe, Germany (Institut für Hochleistungsimpuls- und Mikrowellentechnik Forschungszentrum Karlsruhe), for his interest in this work and fruitful discussions. One of the authors (V.I. Shcherbinin) expresses his gratitude to the German Academic Exchange Service for the award of Euler's research studentship.

REFERENCES

1. W. P. Allis, S. J. Buchsbaum, and A. Bers, *Waves in Anisotropic Plasmas* (MIT Press, Cambridge, Mass., 1963; Atomizdat, Moscow, 1966).
2. R. E. Vanderplas, *Electron Waves and Resonances in Bounded Plasmas* (Wiley, New York, 1968).
3. A. N. Kondratenko, *Plasma Waveguides* (Atomizdat, Moscow, 1976).
4. N. S. Erokhin, N. V. Kuzelev, S. S. Moiseev, *et al.*, *Nonequilibrium and Equilibrium Processes in Plasma Radiophysics* (Nauka, Moscow, 1982).
5. A. A. Rukhadze, A. S. Bogdankevich, S. E. Rosinskiĭ, and V. G. Ruhlin, in *Physics of High-Current Relativistic Electron Beams* (Atomizdat, Moscow, 1980).
6. M. V. Kuzelev, E. V. Liperovskaya, and A. A. Rukhadze, Fiz. Plazmy **4**, 433 (1978) [Sov. J. Plasma Phys. **4**, 242 (1978)].
7. I. N. Onishchenko and G. V. Sotnikov, Fiz. Plazmy **18**, 335 (1992) [Sov. J. Plasma Phys. **18**, 175 (1992)].
8. *Encyclopedia of Low-Temperature Plasma*, Ed. by V. E. Fortov (Nauka, Moscow, 2000), Vol. 4.
9. E. Jahnke, F. Emde, and F. Losch, *Tables of Higher Functions* (McGraw-Hill, New York, 1960; Nauka, Moscow, 1977).
10. G. Dammertz, S. Alberti, A. Arnold, *et al.*, IEEE Trans. Plasma Sci. **30**, 808 (2002).
11. S. Liu, R. J. Barker, D. Zhu, *et al.*, IEEE Trans. Plasma Sci. **28**, 2135 (2000).
12. L. D. Landau and E. M. Lifshitz, *Electrodynamics of Continuous Media* (Fizmatgiz, Moscow, 1959; Pergamon, Oxford, 1960).

Translated by O.E. Khadin

Plasma Physics Reports, Vol. 31, No. 7, 2005, pp. 604–615. Translated from Fizika Plazmy, Vol. 31, No. 7, 2005, pp. 655–666.

PLASMA OSCILLATIONS AND WAVES

Some Properties of the Angular Power Distribution of Electromagnetic Waves Multiply Scattered in a Collisional Magnetized Turbulent Plasma

V. G. Gavrilenko*, A. V. Sorokin*, G. V. Jandieri, and V. G. Jandieri****

** Lobachevsky State University, pr. Gagarina 23, Nizhni Novgorod, 630950 Russia*

*** Georgian Technical University, M. Kostaz str. 77, Tbilisi, 380075 Georgia*

Received November 19, 2003; in final form, October 15, 2004

Abstract—A study is made of oblique incidence of a small-amplitude plane electromagnetic wave on a semi-infinite slab of a collisional turbulent plasma in an external uniform magnetic field. In the small-angle scattering approximation, the condition for neutralizing the effects of oblique incidence and plasma anisotropy on the statistical properties of radiation multiply scattered in the absorbing plasma medium is determined by using the methods of geometrical optics. The validity of this condition was confirmed by numerical calculations based on the statistical modeling technique. The effect of the shape of the spectrum of the electron density fluctuations on the shape of the angular power distribution of a multiply scattered radiation is investigated. © *2005 Pleiades Publishing, Inc.*

1. INTRODUCTION

The analysis of the statistical properties of small-amplitude electromagnetic waves that have passed through a plane turbulent plasma slab is very important in many practical applications associated with both natural and laboratory plasmas [1–4]. It has been recently established that the energy loss due to collisions between plasma particles can lead not only to a decrease in the amplitude of the electromagnetic waves with distance from the slab boundary but also to an appreciable distortion of the angular spectrum of radiation in the events of multiple scattering by random smooth inhomogeneities of the medium.

In [5–9], it was shown that, when a plane wave is incident at a small angle on the interface between an isotropic collisional turbulent plasma and vacuum, the width of the angular spectrum of the scattered radiation increases monotonically with distance from the plasma boundary and approaches a certain asymptotic value (the so-called deep-penetration regime). Subsequent papers demonstrated that, at sufficiently large angles of incidence of radiation, some new effects appear. In [10–13], it was found that the maximum in the angular spectrum shifts monotonically toward the normal to the plasma boundary, as in the case of small incidence angles. However, as the distance from the boundary increases, the spectrum width changes nonmonotonically. When the absorption is sufficiently strong, there exists an interval of distances from the boundary within which the spectrum width substantially exceeds its asymptotic value. Within this interval, as well as near the plasma boundary, the width of the angular spectrum increases with the absorption coefficient, all other conditions being the same (the so-called anomalous broadening). Moreover, within this interval of distances from the plasma boundary, the angular spectrum is highly asymmetric with respect to its maximum (the third central moment is essentially nonzero). These effects are a consequence of the asymmetry of the problem. Such an asymmetry occurs not only in the case of oblique incidence of radiation on a plasma–vacuum interface; it can also be an intrinsic property of the plasma in an external magnetic field. The multiple scattering of waves in a magnetized plasma has been studied less than the wave scattering in chaotic isotropic media.

In [14–18], it was shown that, for a fixed collision frequency between particles, the degree to which the absorption influences the angular spectrum of the scattered waves depends strongly on the propagation direction of the original incident wave with respect to the plasma boundary and also on the strength of the external magnetic field, as well as on its inclination angle (i.e., the angle it makes with the plasma boundary). Those five papers were aimed mainly at considering particular examples (for different directions of the wave vector of the incident wave and the external magnetic field) in which absorption qualitatively changed the angular spectrum of the scattered waves in comparison to that in a collisionless plasma.

In the present work, using the complex geometrical-optics approximation, we construct a general algorithm that allows one to estimate the efficiency with which collisions between the particles in a turbulent plasma affect the angular spectrum of multiply scattered short waves at arbitrary angles of refraction at the plasma boundary and arbitrary angles of inclination of the magnetic field. In order to confirm the predictions made in the geometrical-optics approximation, we have car-

1063-780X/05/3107-0604$26.00

ried out Monte Carlo (MC) simulations for the interval of distances from the plasma boundary within which the small-angle scattering approximation does not work.

The numerical method developed here also makes it possible to investigate the influence of the shape of the spectrum of turbulent fluctuations of the plasma density on the shape of the angular spectrum of the scattered radiation for those values of the plasma parameters at which the wave absorption is significant. In the above-cited papers [14–18], no such investigation was performed: the fluctuations of the plasma density were described either by a Gaussian spectrum or by a power-law spectrum with a certain value of the spectral index.

2. GEOMETRY OF THE PROBLEM AND THE NOTATION ADOPTED

Let a plane electromagnetic wave with frequency ω be incident from vacuum on a semi-infinite slab of a collisional magnetized turbulent plasma. We choose a Cartesian coordinate system such that the *xy* plane is the plasma–vacuum interface, the *z* axis is directed into the plasma slab, and the *xz* plane is generated by the external magnetic field vector $\mathbf{B}_0$ and the wave vector $\mathbf{k}$ of the refracted wave. For the angles, we introduce the following notation (see Fig. 1):

θ_0 is the angle between the magnetic field and the *z* axis, and

θ is the angle between the vectors $\mathbf{B}_0$ and $\mathbf{k}$.

The electron density in the plasma slab is represented as the sum $N(\mathbf{r}) = N_0 + N_1(\mathbf{r})$, where N_0 is a constant density component and $N_1(\mathbf{r})$ is a coordinate-dependent random function describing the electron density fluctuations. The parameters of the scattered radiation within the plasma are searched for as functions of the distance H from the plasma boundary.

For the characteristic frequencies of the processes occurring in the plasma, we introduce the following notation:

$\omega_p = e(4\pi N/m)^{1/2}$ is the electron plasma frequency,

$\omega_B = eB_0/mc$ is the electron gyrofrequency, and

ν_{eff} is the effective electron collision.

In these formulas, e and m are the charge and mass of an electron, c is the speed of light in vacuum, and B_0 is the induction of the external magnetic field.

In addition, we assume that the characteristic spatial scale on which the plasma density varies is much greater than the wavelength λ; this assumption will enable us to utilize the methods of geometrical optics for determining the parameters of the scattered field in the plasma at relatively small distances z from its boundary and to ignore the interaction between the normal waves.

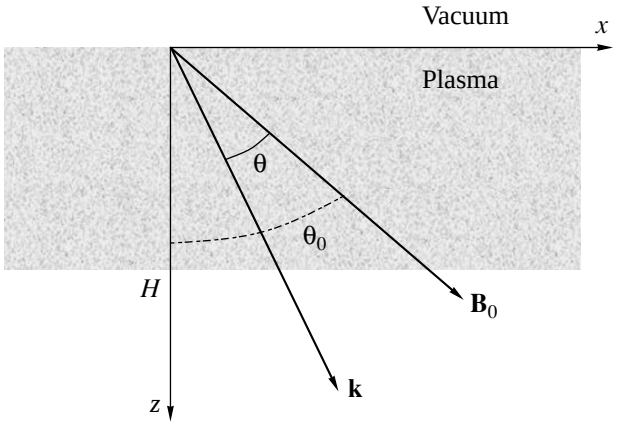

Fig. 1. Geometry of the problem.

3. ANALYSIS OF THE EFFECTS OF ABSORPTION IN THE PLASMA AND THE PLASMA ANISOTROPY ON THE STATISTICAL PROPERTIES OF THE SCATTERED RADIATION BY THE METHODS OF COMPLEX GEOMETRICAL OPTICS

Let us calculate the electric field $\tilde{\mathbf{E}}$ in the *xz* plane (here and below, the tilde identifies complex quantities and the asterisk denotes the complex conjugate). A normal electromagnetic wave propagating in a smoothly inhomogeneous plasma can be described by the eikonal equation [1]

$$\tilde{\mathbf{k}}^2 = \frac{\omega^2}{c^2}\tilde{n}^2, \tag{1}$$

where $\tilde{\mathbf{k}}(\mathbf{r}) = -\nabla\tilde{\varphi}$ is the complex wave vector at a given spatial point, $\tilde{\varphi}$ is the complex wave phase, and $\tilde{n}$ is the complex index of refraction.

The wave vector of an original plane wave incident from vacuum on a plasma slab has purely real x and z components. After refraction at the plasma–vacuum interface, the wave becomes nonuniform; i.e., according to the boundary conditions, the x component k_x of its wave vector remains real while the z component $\tilde{k}_z$ becomes complex,

$$\tilde{k}_z = \sqrt{\frac{\omega^2}{c^2}\tilde{n}^2 - k_x^2}. \tag{2}$$

If the random smooth inhomogeneities of the plasma are ignored ($N_1 = 0$), then, in the zeroth approximation, it is only this refracted wave that contributes to the resulting field. Recall that the refracted wave is nonuniform. An important point for further analysis is that the only parameter that changes with changing the angle of incidence of the wave on the plasma–vacuum interface (i.e., the wave vector component k_x) or the

angle of inclination of the external magnetic field (all other conditions being the same) is the imaginary part of the wave vector component $\tilde{k}_z$, i.e., the rate of decrease of the wave amplitude with distance from plasma boundary.

The chaotic variations of the electron density in the plasma slab give rise to the wave field fluctuations at the observation point. In the case of small-angle scattering, the statistical parameters of the wave field are mostly determined by the fluctuations of the complex phase $\tilde{\varphi}$ of a nonuniform plane wave [19].

The eikonal equation can be rewritten as

$$\nabla\tilde{\varphi}\cdot\nabla\tilde{\varphi} = \frac{\omega^2}{c^2}\tilde{n}^2, \tag{3}$$

where $\tilde{n}^2 = \tilde{n}^2(N(\mathbf{r}), \omega, \tilde{\mathbf{k}})$.

Assuming that the electron density fluctuations are sufficiently small,

$$N = N_0 + N_1(\mathbf{r}), \quad N_1 \ll N_0, \tag{4}$$

we can use the following series expansions for the phase and for the wave vector:

$$\begin{aligned}\tilde{\mathbf{k}} &= \tilde{\mathbf{k}}_0 + \tilde{\mathbf{k}}_1(\mathbf{r}) + \ldots,\\ \tilde{\varphi} &= \tilde{\varphi}_0 + \tilde{\varphi}_1 + \ldots.\end{aligned} \tag{5}$$

Formula (2) describes the z component of the unperturbed wave vector $\tilde{\mathbf{k}}_0$. The fluctuating terms $\tilde{\mathbf{k}}_1$ and $\tilde{\varphi}_1$ are proportional to the dimensionless small parameter N_1/N_0. Substituting expansions (5) into eikonal equation (3) and taking into account only first-order terms, we obtain

$$\begin{aligned}2\nabla\tilde{\varphi}_0\cdot\nabla\tilde{\varphi}_1 &= \frac{\omega^2}{c^2}\frac{\partial\tilde{n}^2}{\partial N_0}N_1 + \frac{\omega^2}{c^2}\frac{\partial\tilde{n}^2}{\partial\tilde{\mathbf{k}}_0}\cdot\tilde{\mathbf{k}}_1,\\ -2\tilde{\mathbf{k}}_0\cdot\nabla\tilde{\varphi}_1 &= \frac{\omega^2}{c^2}\frac{\partial\tilde{n}^2}{\partial N_0}N_1 - 2\frac{\omega^2}{c^2}\tilde{n}\frac{\partial\tilde{n}}{\partial\tilde{\mathbf{k}}_0}\cdot\nabla\tilde{\varphi}_1,\\ \left(\tilde{\mathbf{k}}_0 - \frac{\omega^2}{c^2}\tilde{n}\frac{\partial\tilde{n}}{\partial\tilde{\mathbf{k}}_0}\right)\cdot\nabla\tilde{\varphi}_1 &= -\frac{1}{2}\frac{\omega^2}{c^2}\frac{\partial\tilde{n}^2}{\partial N_0}N_1.\end{aligned} \tag{6}$$

Differentiating the expression $\tilde{\mathbf{k}}_0$ with respect to the vector $\tilde{\mathbf{k}}_0$ · $\tilde{\mathbf{k}}_0 = \omega^2(\tilde{\mathbf{k}}_0)c^{-2}\tilde{n}^2$, we arrive at the following familiar relationship, generalized to the case of an absorbing medium:

$$\tilde{\mathbf{k}}_0 - \frac{\omega^2}{c^2}\tilde{n}\frac{\partial\tilde{n}}{\partial\tilde{\mathbf{k}}_0} = \frac{\omega^2}{c^2}\tilde{n}\frac{\partial(\tilde{n}\omega)}{\partial\omega}\frac{\partial\omega}{\partial\tilde{\mathbf{k}}_0}. \tag{7}$$

With allowance for relationship (7), Eq. (6) in its final form reads

$$\frac{\partial\omega}{\partial\tilde{\mathbf{k}}_0}\cdot\nabla\tilde{\varphi}_1 = -\frac{\omega}{\dfrac{\partial(\tilde{n}\omega)}{\partial\omega}}\frac{\partial\tilde{n}}{\partial N_0}N_1. \tag{8}$$

For a transparent medium, this is clearly the equation describing the transport of the wave phase perturbations with the group velocity. In our case (i.e., for an unperturbed wave propagating in the xz plane, which contains the magnetic field vector), Eq. (8) can be written in the form

$$\frac{\partial\tilde{\varphi}_1}{\partial z} + \frac{\partial\omega/\partial k_x}{\partial\omega/\partial\tilde{k}_z}\frac{\partial\tilde{\varphi}_1}{\partial x} = -\frac{\omega}{\dfrac{\partial(\tilde{n}\omega)}{\partial\omega}\dfrac{\partial\omega}{\partial\tilde{k}_z}}\frac{\partial\tilde{n}}{\partial N_0}N_1. \tag{9}$$

Here and below, the superscript 0 in the components of the wave vector $\tilde{\mathbf{k}}_0$ is omitted for brevity.

Using the condition that the wave frequency in a stationary medium is constant,

$$\omega[k_x, \tilde{k}_z(k_x, \omega)] = \text{const}, \tag{10}$$

we can generalize another familiar relationship to the case of an absorbing medium. Differentiation of equality (10) gives $\partial\omega/\partial k_x + \partial\omega/\partial\tilde{k}_z \cdot \partial\tilde{k}_z/\partial k_x = 0$, so Eq. (9) becomes

$$\frac{\partial\tilde{\varphi}_1}{\partial z} - \frac{\partial\tilde{k}_z}{\partial k_x}\frac{\partial\tilde{\varphi}_1}{\partial x} = -\frac{\omega}{\dfrac{\partial(\tilde{n}\omega)}{\partial\omega}\dfrac{\partial\omega}{\partial\tilde{k}_z}}\frac{\partial\tilde{n}}{\partial N_0}N_1. \tag{11}$$

We expand the function $\tilde{\varphi}_1$ in a two-dimensional Fourier integral, substitute the expansion into Eq. (11), and solve the resulting differential equation with the boundary condition $\tilde{\varphi}_1|_{z=0} = 0$. After these manipulations, we obtain

$$\begin{aligned}\tilde{\varphi}_1 = \tilde{\alpha}\int_{-\infty}^{+\infty}\int_{-\infty}^{+\infty} e^{i\kappa_x x + i\kappa_y y}d\kappa_x d\kappa_y \int_0^z \tilde{N}_1(\kappa_x, \kappa_y, \xi)\\ \times\exp\left\{-i\kappa_x\frac{\partial\tilde{k}_z}{\partial k_x}(z-\xi)\right\}d\xi,\end{aligned} \tag{12}$$

where the electron density fluctuations are expressed in terms of their two-dimensional Fourier transform,

$$N_1(x, y, \xi) = \int_{-\infty}^{+\infty}\int_{-\infty}^{+\infty}\tilde{N}_1(\kappa_x, \kappa_y, \xi)e^{i\kappa_x x + i\kappa_y y}d\kappa_x d\kappa_y \tag{13}$$

and the following notation is introduced:

$$\tilde{\alpha} = -\frac{\omega}{\dfrac{\partial(\tilde{n}\omega)}{\partial\omega}\dfrac{\partial\omega}{\partial\tilde{k}_z}}\frac{\partial\tilde{n}}{\partial N_0}. \tag{14}$$

Let us now calculate the transverse correlation function of the phase. In the definition of this function,

$$R_{\tilde{\varphi}} = \langle \tilde{\varphi}_1(x, y, z)\tilde{\varphi}_1^*(x+\rho_x, y+\rho_y, z)\rangle$$
$$= \tilde{\alpha}^2 \int_{-\infty}^{+\infty}\int_{-\infty}^{+\infty} e^{i\kappa_x(x+\rho_x) - i\kappa_x' x + i\kappa_y(y+\rho_y) - i\kappa_y' y}$$
$$\times \int_0^z\int_0^z \langle \tilde{N}_1(\kappa_x, \kappa_y, \xi)\tilde{N}_1^*(\kappa_x', \kappa_y', \xi')\rangle \quad (15)$$
$$\times \exp\{-i\kappa_x(\beta + i\gamma)(z-\xi)$$
$$+ i\kappa_x'(\beta - i\gamma)(z-\xi')\}d\kappa_x d\kappa_y d\kappa_x' d\kappa_y' d\xi d\xi',$$

we switch to the new variables,

$$\rho_z = \xi - \xi', \quad \eta = \frac{\xi + \xi'}{2}, \quad (16)$$

and integrate over them with allowance for the correlation scale length of the parameters of the medium being much less than the penetration depth z of radiation into the plasma. As a result, we obtain

$$R_{\tilde{\varphi}}(\rho_x, \rho_y, z) = 2\pi\tilde{\alpha}^2 \int_{-\infty}^{+\infty}\int_{-\infty}^{+\infty} e^{i\kappa_x\rho_x + i\kappa_y\rho_y}\frac{e^{2\kappa_x\gamma z}}{2\kappa_x\gamma} \quad (17)$$
$$\times [1 - e^{2\kappa_x\gamma z}]\Phi(\kappa_x, \kappa_y, -\beta\kappa_x)d\kappa_x d\kappa_y,$$

where $\Phi(\kappa_x, \kappa_y, \kappa_z)$ is the three-dimensional spatial power spectrum of the statistically uniform electron density fluctuations and $\partial\tilde{k}_z/\partial k_x = \beta + i\gamma$. In the limit of weak damping of the field over one wavelength, this expression is close to that for the correlation function of the real phase. We are interested, however, in the case in which the wave damping over the entire penetration distance z is sufficiently strong and the function $\exp(2\kappa_x\gamma z)$ appreciably exceeds unity for those values of κ_x at which the spectrum $\Phi(\kappa_x, \kappa_y, -\beta\kappa_x)$ of the electron density fluctuations is essentially nonzero. For $\gamma \longrightarrow 0$, expression (17) yields the familiar result [20], namely, a linear increase in the wave phase dispersion with distance from the plasma–vacuum interface. It should also be kept in mind that this expression was derived by the method of expansion in small perturbations in the small-angle scattering approximation, which is valid only for finite distances z from the plasma boundary.

By definition, the correlation function of the complex field (the spatial coherence function) can be written as

$$R_E = \langle \tilde{E}(x, y, z)\tilde{E}^*(x+\rho_x, y+\rho_y, z)\rangle$$
$$= E_0^2 \exp\{-2z\,\mathrm{Im}(\tilde{k}_z) + ik_x\rho_x\} \quad (18)$$
$$\times \langle \exp\{i\tilde{\varphi}_1(x, y, z) - i\tilde{\varphi}_1(x+\rho_x, y+\rho_y, z)\}\rangle.$$

Taking into account the fact that the field is damped insignificantly over one wavelength, we can ignore the imaginary part of the perturbed wave phase ($\tilde{\varphi}_1 \approx \varphi_1$, $\tilde{\alpha} = \alpha$). In this case, it should be kept in mind that the imaginary part of the derivative $\partial\tilde{k}_z/\partial k_x$, equal to γ, plays an important role because it enters into expressions (12) and (17) through the argument of the exponentials and its contribution to the statistical parameters of the phase fluctuations increases with distance z from the plasma boundary.

In the most interesting case of multiple scattering, the fluctuations of the phase are strong, $\langle \tilde{\varphi}_1\tilde{\varphi}_1^*\rangle \gg 1$, so we can as usual [20] assume that they obey a normal distribution. Since, in this case, the correlation function decreases sharply as ρ_x and ρ_y increase, the argument of the second exponential in expression (18) can be expanded in a series,

$$R_E(\rho_x, \rho_y) = E_0^2 \exp\{-2z\,\mathrm{Im}(\tilde{k}_z) + ik_x\rho_x\}$$
$$\times \exp\left\{\frac{\partial R_{\tilde{\varphi}}}{\partial\rho_x}\rho_x + \frac{1}{2}\frac{\partial^2 R_{\tilde{\varphi}}}{\partial\rho_x^2}\rho_x^2 + \frac{1}{2}\frac{\partial^2 R_{\tilde{\varphi}}}{\partial\rho_y^2}\rho_y^2\right\}, \quad (19)$$

where the correlation function $R_{\tilde{\varphi}}$ is given by expression (17). The derivatives in the correlation function of the phase are taken at the point $\rho_x = \rho_y = 0$.

The spatial (angular) spectrum of the scattered field, which is of great practical importance for us, is the Fourier transformed correlation function of the field [20]:

$$S(\kappa_x, \kappa_y, z)$$
$$= \frac{1}{4\pi^2}\int_{-\infty}^{+\infty}\int_{-\infty}^{+\infty} d\rho_x d\rho_y R_E(\rho_x, \rho_y)\exp\{-i\kappa_x\rho_x - i\kappa_y\rho_y\}. \quad (20)$$

This characteristic of the scattered radiation is equivalent to the ray intensity (brightness), which usually enters the radiation transport equation [20]. In [19], it was shown that the solution to the radiation transport equation that was obtained in the small-angle scattering approximation and the solution obtained in the geometrical-optics approximation yield the same angular spectrum. We think, however, that the second approach is simpler and more illustrative.

For strong fluctuations of the phase, the spatial power spectrum is Gaussian in shape,

$$S(\kappa_x, \kappa_y, z) = S_0\exp\left\{-\frac{(\kappa_x - k_x - \Delta\kappa_x)^2}{2\langle\kappa_x^2\rangle} - \frac{\kappa_y^2}{2\langle\kappa_y^2\rangle}\right\}. \quad (21)$$

Here, S_0 is the peak value of the spectral curve; the quantity $\Delta\kappa_x$ describes the shift of the peak due to the random variations in the plasma density; and the quantities $\langle\kappa_x^2\rangle$ and $\langle\kappa_y^2\rangle$ describe the widths of the spectrum in the xz and yz planes, respectively. The formulas

for $\Delta\kappa_x$, $\langle\kappa_x^2\rangle$, and $\langle\kappa_y^2\rangle$ can be derived by taking the derivatives in expression (19):

$$\Delta\kappa_x = \frac{2}{i}\frac{\partial R_\varphi}{\partial\rho_x}\bigg|_{\substack{\rho_x=0\\ \rho_y=0}}, \quad \langle\kappa_x^2\rangle = -\frac{\partial^2 R_\varphi}{\partial\rho_x^2}\bigg|_{\substack{\rho_x=0\\ \rho_y=0}},$$
$$\langle\kappa_y^2\rangle = -\frac{\partial^2 R_\varphi}{\partial\rho_y^2}\bigg|_{\substack{\rho_x=0\\ \rho_y=0}}. \tag{22}$$

As a result, we obtain

$$\Delta\kappa_x = \frac{2\pi}{\gamma}\alpha^2\int\limits_{-\infty}^{+\infty}\int\limits_{-\infty}^{+\infty}\Phi(\kappa_x, \kappa_y, -\beta\kappa_x)[e^{2\kappa_x\gamma z}-1]d\kappa_x d\kappa_y, \tag{23}$$

$$\langle\kappa_x^2\rangle = \frac{\pi}{\gamma}\alpha^2\int\limits_{-\infty}^{+\infty}\int\limits_{-\infty}^{+\infty}\Phi(\kappa_x, \kappa_y, -\beta\kappa_x)\kappa_x[e^{2\kappa_x\gamma z}-1]d\kappa_x d\kappa_y, \tag{24}$$

$$\langle\kappa_y^2\rangle = \frac{\pi}{\gamma}\alpha^2\int\limits_{-\infty}^{+\infty}\int\limits_{-\infty}^{+\infty}\Phi(\kappa_x, \kappa_y, -\beta\kappa_x)\frac{\kappa_y^2}{\kappa_x}[e^{2\kappa_x\gamma z}-1]d\kappa_x d\kappa_y. \tag{25}$$

Formulas (23)–(25) imply that the effects mentioned in the Introduction, namely, the effect of the marked shift of the spectral peak and the anomalous broadening effect, take place when the imaginary part of the derivative $\partial\tilde{k}_z/\partial k_x$ is nonzero. These effects stem from the fact that the damping of the waves scattered in a turbulent plasma depends strongly on their propagation direction because of the oblique incidence of the original wave on the plasma boundary and also because of the inclination of the external magnetic field.

Let us analyze the applicability conditions for expressions (17) and (23)–(25) in more detail. These expressions have been derived from the eikonal equation by the method of perturbative expansions in powers of the small parameter N_1/N_0. Consequently, the parameter range in which expressions (17) and (23)–(25) (when substituted into expression (21)) correctly describe the spatial power spectrum of the wave is determined by the inequalities

$$|\Delta\kappa_x| \ll 2\pi/\lambda, \quad \sqrt{\langle\kappa_x^2\rangle} \ll 2\pi/\lambda, \quad \sqrt{\langle\kappa_y^2\rangle} \ll 2\pi/\lambda.$$

These three inequalities justify the use of the above small-angle scattering approximation and make it possible to keep only the first terms in expansion (5). The consistency of these inequalities with the condition that the wave absorption play a significant role, $\exp(2\kappa_x\gamma z) \geq 1$, is ensured by the smallness of the dispersion of the plasma density fluctuations, $\langle N_1^2\rangle \ll N_0^2$, which determines the normalization of the spectrum $\Phi(\kappa_x, \kappa_y, \kappa_z)$ in the integral in expression (35) (see below). The restrictions indicated do not contradict the assumption that the wave phase fluctuations are strong, because, in a smoothly inhomogeneous plasma medium, the transverse scale on which the correlation function of the phase varies corresponds to the mean spatial scale of the plasma inhomogeneities, $l \gg \lambda$ [20], and the characteristic angle between the random wave front and the normal to the plasma boundary, $\Delta\theta \approx \sqrt{\langle\kappa_x^2\rangle}/|k_z| \approx \frac{\sqrt{\langle\kappa_x^2\rangle}\lambda}{2\pi}$, can remain small for $\langle\varphi_1^2\rangle \gg 1$. The reason is that formulas (17) and (24) agree with the familiar estimate $\sqrt{\langle\kappa_x^2\rangle} \propto \sqrt{\langle\varphi_1^2\rangle}/l$; therefore, for $\sqrt{\langle\varphi_1^2\rangle} \gg 1$, the angle $\Delta\theta \propto \sqrt{\langle\varphi_1^2\rangle}\frac{\lambda}{l}$ can be small by virtue of the very strong inequality $\lambda/l \ll 1$. Analogous estimates are valid for the quantities given by expressions (23) and (25) as well. It is also pertinent to note that, in the region that makes the dominant contribution to the integrals in expressions (17) and (23)–(25), the argument of the exponential function in these expressions can be estimated by $2\kappa_x\gamma z \propto \mathrm{Im}(\tilde{n})\frac{z}{l}$. Consequently, the inequality $2\kappa_x\gamma z \geq 1$ leads to the condition $\mathrm{Im}(\tilde{k}_z)z \approx \mathrm{Im}(\tilde{n})\frac{z}{\lambda} \gg 1$, which implies that, at the distances z from the plasma boundary that are of interest to us, the wave amplitude decreases strongly according to an exponential law. It is this circumstance that makes the angular radiation spectrum considerably distorted, because the power is redistributed to the directions along which the waves are damped relatively more weakly. As for the exponential dependence of the width and shift of the spectral peak on z, it is valid only over a limited range of distances from the plasma boundary to which the small-angle scattering approximation is applicable. Numerical calculations show that, for longer distances z from the plasma boundary, this exponential increase changes into a slower one [18].

For the case in which the external magnetic field is absent, formulas similar to expressions (23)–(25) were derived in [10] but in a different way, namely, by solving the radiation transport equation, i.e., the transport equation for the angular power distribution of the wave in a chaotic isotropic absorbing medium. In this case, the coefficient γ is nonzero for an oblique incidence of the original wave on the boundary of the medium.

For $\gamma = 0$, the spatial (and, accordingly, angular) power spectrum in the small-angle scattering approximation is independent of the absorption. In this case, expression (23) implies that $\Delta k_x = 0$ because, for the statistically isotropic electron density fluctuations in

which we are interested here, the dependence of $\Phi(\kappa_x, \kappa_y, -\beta\kappa_x)$ on κ_x is even. For $\gamma = 0$, the quantities $\langle \kappa_x^2 \rangle$ and $\langle \kappa_y^2 \rangle$ increase linearly with z, as in the case of a nonabsorbing medium, for which this linear increase agrees with the familiar decrease in the transverse correlation length, $\propto 1/\sqrt{z}$, when the wave phase fluctuations are strong [20]. Of course, formulas (17) and (23)–(25) cannot be applied to describe the processes occurring at sufficiently large distances z from the boundary of the medium, i.e., at distances for which the basic small-angle scattering approximation fails to hold.

Form formula (2) we see that, in the case under consideration, the quantity γ is contributed by the oblique incidence of radiation (the wave vector component k_x) and also by the anisotropy of the medium itself. Depending on the conditions in the medium, one or another of these two factors can predominate. For instance, when the magnetic field is very strong, the effects of the anisotropy almost completely predominate over those of the oblique incidence (see [17]) and vice versa when the magnetic field is weak or even is absent. In the latter case, the radiation is scattered in the plasma in essentially the same manner as in an isotropic medium (see [12]). However, the scattering of radiation produces the most interesting effects when the plasma anisotropy and the oblique incidence are of comparable importance. It is this case that will be considered below. The most reliable way of calculating the quantity γ in this complicated case is as follows.

When a wave is incident obliquely on the boundary of a magnetized plasma, the components of the wave vector $\tilde{\mathbf{k}} = \frac{\omega}{c}\{p, 0, \tilde{q}\}$ satisfy the equation [1]

$$a_4\tilde{q}^4 + a_3\tilde{q}^3 + a_2\tilde{q}^2 + a_1\tilde{q} + a_0 = 0. \tag{26}$$

Here, the coefficients are expressed in terms of p through the relationships

$$\begin{aligned}
a_4 &= (1-is)[(1-is)^2 - u] - v[(1-is)^2 - u_z],\\
a_3 &= 2pv\sqrt{u_x u_z},\\
a_2 &= -2(1-is)\{[(1-p^2)(1-is) - v](1 - v - is)\\
&\quad - (1-p^2)u\} + v[p^2 u_x - (1-p^2)u_z - u],\\
a_1 &= -2(1-p^2)pv\sqrt{u_x u_z},\\
a_0 &= [(1-p^2)(1-is) - v]\\
&\quad \times \{[(1-p^2)(1-is) - v](1 - v - is) - (1-p^2)u\}\\
&\quad - (1-p^2)p^2 u_x v,
\end{aligned} \tag{27}$$

and the quantities u, v, and s are introduced to denote the dimensionless parameters that characterize, respectively, the influence of the magnetic field, electron density, and absorption on the plasma properties:

$$\begin{aligned}
u &= \frac{\omega_B^2}{\omega^2}, \quad v = \frac{\omega_p^2}{\omega^2}, \quad s = \frac{\nu_{\text{eff}}}{\omega},\\
u_x &= u\sin^2\theta_0, \quad u_z = u\cos^2\theta_0.
\end{aligned} \tag{28}$$

Since this equation is very difficult to solve analytically, we analyzed it numerically. As a result of this analysis, we can plot the dependence of the imaginary part $\text{Im}(\tilde{q})$ of $\tilde{q}$ on p for both of the normal waves. In this case, the quantity $\gamma = \text{Im}\,\partial\tilde{q}/\partial p$ is defined as the tangent of the angle between the abscissa and a line tangent to the curve. This definition clearly shows that the quantity γ determines how much the rate of decrease of the wave amplitude along the z axis depends on p, i.e., on the wave propagation direction. As was mentioned above, it is the dependence of the damping of the wave on its propagation direction that leads to a substantial distortion of the angular spectrum of multiply scattered waves because of their absorption. Near the points where $\gamma = 0$, the wave damping depends on the wave propagation direction to a much smaller extent. We thus arrive at the following problem: for particular values of the different plasma parameters (the electron density, the magnetic field induction, and the collision frequency), it is necessary to determine those values of the angle of refraction and the angle of inclination of the magnetic field at which, for a given type of wave, the quantity γ vanishes or, conversely, is essentially nonzero. Formulas (23)–(25) imply that, when the quantity γ vanishes, the absorption has no impact on the angular spectrum in the geometrical-optics approximation (the effects of the oblique refraction and of the anisotropy neutralize each other). This neutralization effect was first pointed out in [18], in which, however, the imaginary part of the derivative $\partial\tilde{k}_z/\partial k_x$ was calculated using an approximate expression that is valid only for small angles between the wave vector and the magnetic field. In the absence of the neutralization effect, the situation is as follows: the larger the quantity γ, the more pronounced the anomalous effects of the absorption on the angular spectrum. There are sound reasons to suppose that, for a wave that penetrates deeper in the region where the small-angle scattering approximation fails to hold and the solution to the equations of geometrical optics by the perturbation method is invalid, the qualitative dependence on the parameter γ will remain the same; i.e., for $\gamma = 0$, the absorption will influence the angular spectrum in the same fashion as in the case of normal incidence of a wave on the boundary of an isotropic turbid medium, leading to a narrowing of the angular spectrum in comparison to that in an analogous transparent medium [6]. For essentially nonzero values of γ, it is natural to expect that, at large penetration depths, the shape of the angular spectrum will be distorted by absorption to a far greater extent.

In order to confirm this supposition, in subsequent sections of this paper, we will consider the results of a numerical solution of the problem by the MC method.

4. SOME SPECIFIC FEATURES OF THE MONTE CARLO METHOD AS APPLIED TO THE PROBLEM AS FORMULATED

Since the problem has not yet been solved analytically, it is necessary to utilize numerical methods. One of the most convenient techniques is that based on MC simulations, i.e., statistical numerical calculations of the processes of propagation, scattering, and absorption of radiation in a chaotically inhomogeneous medium. The general scheme and mathematical justification of the MC method have been elucidated in sufficient detail in [21]. Here, we mention only some specific features of the MC method that have been used in our work.

Since our main task is to investigate how absorption influences the angular spectrum of the scattered radiation, the statistical computational scheme should be capable of adequately describing this influence. In the classical version of the MC method, the absorption is accounted for through the so-called "survival probability" Λ, which, in quantum-physical language, corresponds to the probability for a photon to be absorbed in its scattering by the inhomogeneities of the medium. The photon that has been absorbed is treated as nonexistent, so the resulting power distribution is formed only by those photons that have survived after scattering. For isotropic media, the following relationship holds:

$$\Lambda = \frac{\sigma_s}{\sigma_s + \sigma_a}, \tag{29}$$

where σ_s and σ_a are the extinction coefficients associated with scattering and absorption, respectively. Hence, the survival probability provides a relationship between the scattering and absorbing properties of an isotropic medium. By assigning specific values to the survival probability, the wavelength, and the refractive index, we can derive exhaustive information for modeling the scattering properties of isotropic media. The classical version of the MC method is advantageous in that it has a clear physical meaning and can relatively easily be expressed in an algorithmic language. The drawback of the classical version is that, in the case of a large number of scattering events, it requires a very large amount of computer time, even when the survival probability is close to unity. This is why, in our study, we used a "weighted" version of the MC method, which makes it possible to greatly hasten the computational process in comparison to that based on the classical version. The essence of the weighted version is that the random ray trajectory being simulated is assigned a "weight," i.e., a fraction of the original radiation energy that remains within the ray tube as the radiation travels along this trajectory. The resulting angular power distribution is calculated with allowance for the weight of the radiation coming from different directions. A detailed discussion of the weighted scheme can be found in [21].

In statistical simulations of a single scattering process, the probability density for the deviation of a ray trajectory in a given direction is traditionally described by a function proportional to the differential cross section $\frac{\partial\sigma_s}{\partial\Omega}(\alpha, \varphi)$, where α and φ are, respectively, the zenithal and azimuthal angles through which the ray deviates from its original direction. The proportionality coefficient is chosen so that the total integral of the probability density over all possible scattering directions is unity.

For a cold magnetized turbulent plasma with statistically isotropic fluctuations, the differential cross section is described by the formula [22]

$$\frac{d\sigma_s}{d\Omega} = \frac{1}{2\pi}\frac{e^4}{m_e^2c^2}\frac{\omega^4}{\omega_p^4}\Phi(\Delta k)\frac{\tilde{n}_s^3\left|\tilde{\mathbf{e}}_s^* \cdot (\hat{\varepsilon} - 1)\tilde{\mathbf{e}}_i\right|^2}{\tilde{n}_i(\left|\tilde{\mathbf{e}}_i\right|^2 - \left|\tilde{\mathbf{k}} \cdot \tilde{\mathbf{e}}_i\right|^2/k^2)(\tilde{\mathbf{e}}_s^* \cdot \hat{\varepsilon}\tilde{\mathbf{e}}_i)}. \tag{30}$$

Here, $\hat{\varepsilon}$ is the plasma dielectric tensor and $\tilde{\mathbf{k}}_s$, $\tilde{\mathbf{e}}_s$, and $\tilde{n}_s$ are the wave vector, the polarization vector of the electric field, and the index of refraction of the scattered wave along its propagation direction, respectively. Similar parameters $\tilde{\mathbf{k}}_i$, $\tilde{\mathbf{e}}_i$, and $\tilde{n}_i$ describe the wave before it has been scattered. The quantity Δk denotes the absolute value of the difference $\tilde{\mathbf{k}}_s - \tilde{\mathbf{k}}_i$. Formula (30) is a generalization of an analogous well-known formula for isotropic media [20],

$$\frac{\partial\sigma_s}{\partial\Omega}(\alpha, \varphi) = \frac{1}{2}\pi\frac{\omega^4}{c^4}\Phi(\Delta k). \tag{31}$$

Formula (30) differs from formula (31) not only in that it contains the proportionality coefficient but mainly in that it involves the factor $F = \frac{\tilde{n}_s^3\left|\tilde{\mathbf{e}}_s^* \cdot (\hat{\varepsilon} - 1)\tilde{\mathbf{e}}_i\right|^2}{\tilde{n}_i(\left|\tilde{\mathbf{e}}_i\right|^2 - \left|\tilde{\mathbf{k}} \cdot \tilde{\mathbf{e}}_i\right|^2/k^2)(\tilde{\mathbf{e}}_s^* \cdot \hat{\varepsilon}\tilde{\mathbf{e}}_i)}$, which describes the dependence of the scattering properties of the plasma on the wave propagation direction.

It can be shown that, for a single small-angle scattering event, the expression for F, as well as expression (30) as a whole, can be substantially simplified. In particular, one can discard a small error resulting from the use of the approximate equality $\tilde{\mathbf{e}}_i \approx \tilde{\mathbf{e}}_s$. This approximation implies that, for fixed plasma parameters, the function F depends only on one argument—the angle θ between the wave vector and the external magnetic field. The change in the refractive index of the plasma

in a single scattering event can also be ignored; in this case, we have $k \approx k_s \approx k_i$ (for an isotropic medium, these approximate relationships would be exact) and arrive at the following expression for the quantity Δk in terms of the zenithal deviation angle α:

$$\Delta k = \frac{1}{2}k\sin\frac{\alpha}{2}. \quad (32)$$

We thus see that the differential cross section for a single scattering event is independent of the azimuthal deviation angle φ.

In view of the fact that the function F is independent of the zenithal scattering angle α, the probability density for the deviation of the ray is proportional to the function $\Phi(k\sin(\alpha/2)/2)$ and is independent of the angle θ because the factor $F(\theta)$ drops out in normalizing the spectrum. The anisotropy of the medium is taken into account in the computation stage in which a random number generator produces the value of the distance the radiation passes between two successive scattering interactions with density inhomogeneities. For an isotropic medium, this distance is a random quantity having an exponential distribution. The mean value of this random quantity is constant and is equal to σ_s^{-1}. For the magnetized plasma under consideration, the coefficient of extinction in scattering (or equivalently the total cross section per unit volume of the scattering medium) is [20]

$$\sigma_s = \int_{\Omega_s}\frac{\partial\sigma_s}{\partial\Omega}d\Omega = C_1\int_0^{\alpha_{\max}}\Phi\left(\frac{k}{2}\sin\frac{\alpha}{2}\right)F(\theta)d\alpha = C_2F(\theta), \quad (33)$$

where C_1 and C_2 are the α- and θ-independent proportionality coefficients, Ω_s is the solid angle into which the radiation can be scattered, and $\alpha_{\max}$ is the maximum possible zenithal angle of the deviation of the ray in a single scattering event. This is why the mean distance between the positions at which the scattering events occur depends on the angle θ.

For a collisional magnetized plasma, the coefficient of extinction in scattering can be found from a fairly simple expression, $\sigma_a = 2\omega c^{-1}\mathrm{Im}\,\tilde{n}(\theta)$. In the case in question, the imaginary part of the refractive index can be obtained from the formula [1]

$$\tilde{n}^2 = 1 - \frac{2\nu(1-\nu-is)}{2(1-is)(1-\nu-is) - u\sin^2\theta \pm \sqrt{u^2\sin^4\theta + 4u(1-\nu-is)^2\cos^2\theta}}. \quad (34)$$

In order to calculate the coefficient C_2, the spectrum Φ should be normalized to the mean square of the electron density fluctuations, $\langle N_1^2\rangle$:

$$4\pi\int_0^\infty \kappa^2\Phi(\kappa_x, \kappa_y, \kappa_z = 0)d\kappa = \langle N_1^2\rangle. \quad (35)$$

Having made this normalization, we must treat the quantity $\langle N_1^2\rangle$ as an independent numerical parameter and substitute it into the formula for the spectrum. However, the mean square of the electron density fluctuations is, as a rule, obtained from experimental data in an indirect way and thus can depend in a fairly complicated manner on a large number of external factors. This is why, in the present work, we simplify the computational process and make it more illustrative by assuming that, for given values of the plasma parameters u, ν, and s, the coefficient of extinction in scattering, σ_s', along the magnetic field is equal to unity,

$$\sigma_s'(\theta) = \frac{\sigma_s(\theta)}{\sigma_s(0)}. \quad (36)$$

This choice implies in fact that all the distances are expressed in units of the mean free path L_f of radiation between two scattering events in its propagation along the magnetic field, because the scale L_f is nothing more than the reciprocal of σ_s. In this case, however, in order for the absorption to be taken into account correctly, the coefficient σ_a should be expressed in terms of the same scale of distances. This can be done in the following way. Let the quantities σ_a' and l' be expressed in terms of a scale in which the unit of distance is accepted to be the mean free path of radiation between two successive scattering events in the direction along the magnetic field. For the intensity I of the mean wave field, we can then write the formula $I = I_0\exp(-\sigma_a' l')$. On the other hand, this intensity is equal to $I = I_0\exp(-2k_0\mathrm{Im}(\tilde{n})l)$, where l is the total path expressed in the same units of distance as k_0. Consequently, we have

$$2k_0\mathrm{Im}(\tilde{n})l = l\frac{2\pi}{\lambda}\mathrm{Im}(\tilde{n}) = \frac{l}{L_f}\times 2\pi\frac{L_f}{\lambda}\mathrm{Im}(\tilde{n}) = l'\times 2\pi\,\mathrm{Im}(\tilde{n})\frac{L_f}{\lambda} \quad (37)$$

and, as a result, obtain $\sigma_a' = \pi\mathrm{Im}(\tilde{n})L_f/\lambda$. In other words, in order to calculate the coefficient of extinction in scattering in units of the reciprocal of the mean free path, it is necessary to know how many wavelengths fit along the mean free path of radiation between two successive scattering interactions by plasma density inho-

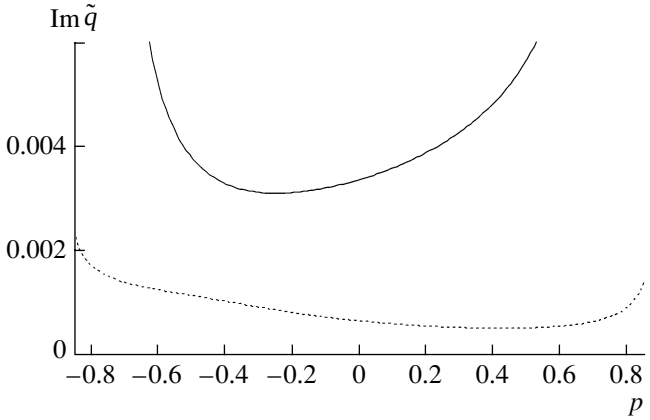

Fig. 2. Dependence $\mathrm{Im}\,\tilde{q}(p)$ for an extraordinary (solid curve) and an ordinary (dotted curve) normal wave in a plasma with the parameters $u = 0.22$, $v = 0.28$, and $s = 0.0053$, the angle of inclination of the magnetic field being $\theta_0 = 40°$. The angle between the neutralization direction and the normal to the slab is ≈23.5° for an ordinary ($p \approx 0.4$) wave and ≈ –14.5° for an extraordinary ($p \approx -0.25$) wave.

mogeneities. This implies that, in the simulation algorithm, the quantity $\langle N_1^2 \rangle$ should be replaced by the ratio L_f/λ; this makes it possible to calculate the coefficient σ_a in terms of the above scale of distances. Of course, these two parameters are very closely related to one another: an increase in the fluctuation intensity $\langle N_1^2 \rangle$ leads to a decrease in the mean free path L_f (and, accordingly, in the ratio L_f/λ), and, vice versa, a decrease in the fluctuation intensity leads to an increase in the ratio L_f/λ.

Having derived expressions for σ_s and σ_a in terms of the same scale of distances, we can calculate the survival probability Λ in the case of a collisional magnetized plasma from the same formula as that used for an isotropic medium, specifically, from formula (29). For a plasma, however, the survival probability is not generally constant and depends on the angle θ.

5. RESULTS OF NUMERICAL SIMULATIONS

All numerical simulations were carried out for the frequencies $\omega_B \approx 8.8 \times 10^6$ rad/s, $\omega_p \approx 10^7$ rad/s, and $\nu \approx 10^5$ s^{-1}, which correspond to the mean values of the parameters in the F region of the Earth's ionosphere. The wavelength was chosen to be 100 m; in this case, the plasma parameters in question are equal to $u = 0.22$; $v = 0.28$, and $s = 0.0053$. The plots of the dependence $\mathrm{Im}(\tilde{q}(p))$ for both of the normal waves propagating into a plasma slab with these parameters, the angle of inclination of the magnetic field being $\theta_0 = 40°$, are shown in Fig. 2, in which the solid and dotted curves refer to the extraordinary and ordinary normal waves, respectively. By the extraordinary wave we mean a normal wave for which the refractive index approaches unity as the magnetic field increases, all other parameters being fixed. Figure 2 clearly shows that each of the normal waves is characterized by its own neutralization direction, i.e., the direction along which we have $\mathrm{Im}(\partial\tilde{q}/\partial p) = 0$ and along which the neutralization effect occurs. From the plots we see that, in the cases under analysis, the neutralization directions correspond to those values of p and k_x for which the waves suffer the weakest damping over z (the wave vector component $\tilde{k}_z$ is minimum). In order to check our assumptions about the character of distortion of the angular spectrum of the scattered radiation, we carried out a series of simulations of the propagation of waves in a plasma slab of thickness $\sigma_s|_{\theta=0} \cdot H = 50$ for a ratio L_f/λ of 100. For the u, v, and s values chosen above, this corresponds to a plasma slab with a thickness of about 500 km for which the extinction coefficient and survival probability along the magnetic field are equal to $\sigma_s \approx 0.0001$ m^{-1} and $\Lambda \approx 0.75$, respectively. Note that, for such penetration depths, the solution obtained by the perturbation method is inapplicable because the scattering angles are not small and the inequality $k_1 \ll k_0$ in expansion (5) fails to hold. The spatial spectrum of the electron density fluctuations, $\Phi(\Delta k)$, is given by the model expression

$$\Phi(\Delta k) = C\begin{cases}\left(\frac{\sqrt{2}}{90}k_i\right)^{-g}, & \Delta k \in \left[0, \frac{\sqrt{2}}{90}k_i\right] \\ \Delta k^{-g}, & \Delta k \in \left[\frac{\sqrt{2}}{90}k_i, \sqrt{2}k_i\right] \\ 0, & \Delta k > \sqrt{2}k_i,\end{cases} \quad (38)$$

where g is the spectral index, k_i is the absolute value of the wave vector of the wave before it has been scattered, and C is the normalizing coefficient calculated from formula (35).

The results of simulating the propagation of an ordinary wave for $g = 2.6$ are illustrated in Fig. 3. We can see that, at a qualitative level, the geometrical-optics solution correctly reflects the main properties of the propagation and scattering of waves in a collisional magnetized turbulent plasma, namely, the neutralization direction and also the anomalous effects of the shift of the centroid position of the peak in the angular spectrum and its broadening. For comparison, Fig. 4 shows the angular spectra of the scattered radiation in a nonabsorbing plasma that were calculated for the same parameters of the problem as those in Fig. 3. Our new result is the realization that the shape of the angular distribution can always be calculated for any physically meaningful values of the plasma parameters and of the angle of refraction and the angle of inclination of the magnetic field. In earlier studies, the shape of the angular spectrum was calculated only for a few particular cases (those of normal incidence on a plasma slab or of

a plasma in a very strong magnetic field). From Fig. 3 we see that the angular spectrum can sometimes have a double-humped shape, which stems from the mutual influences of anisotropy, absorption, and the shape of the single-scattering indicatrix.

The fact that the angular spectrum can be double-humped in shape provides a clearer insight into the cause of anomalous broadening of the asymmetric spectrum of a multiply scattered wave (see the Introduction). In an asymmetric case, there are two preferential directions in an absorbing medium: the propagation direction of the original plane wave and the direction along which the wave propagates a given distance from the plasma boundary being damped to the smallest extent. As the radiation propagates away from the plasma boundary, it deviates progressively from its original direction due to multiple scattering (preferentially through small angles) by random smooth inhomogeneities. Nevertheless, a relatively small portion of the scattered waves occurs in a narrow angular interval along the direction of weakest damping. When the absorption is sufficiently strong, the amplitude of these waves decreases far more gradually than the amplitudes of other waves, so a second peak can form in the angular power spectrum. This is indeed the case when the angle between the two preferential directions mentioned above is sufficiently large. Under such conditions, the width of the angular spectrum is anomalously large in comparison to that in a similar nonabsorbing medium. If the original wave propagation direction coincides with the direction of weakest damping, then the problem is symmetric and the absorption does not lead to anomalous effects.

Let us now examine the influence of the shape of the single-scattering indicatrix in more detail. As was mentioned above (see also [18]), the double-humped shape of the angular power spectrum stems from the fact that the waves that have been scattered through large angles with low probability and propagate nearly along the neutralization direction can suffer a substantially weaker damping as the distance z from the plasma boundary increases. The scattering through large angles is governed by the asymptotic behavior of the electron density fluctuation spectrum $\Phi(\Delta k)$ (which yields the resulting shape of the single-scattering indicatrix) at relatively large values of Δk. In order to investigate how the shape of $\Phi(\Delta k)$ affects the shape of the angular spectrum of multiply scattered radiation, we performed numerical simulations for different values of the spectral index g. The plasma parameters were taken to be the same as in the previous simulation version, the depth of penetration into the slab was $\sigma_s|_{\theta=0} \cdot H = 60$, the angle of refraction for the wave was 0°, and the angle of inclination of the magnetic field was 60°. The resulting angular spectra of multiply scattered radiation are displayed in Fig. 5. It can be seen that, when the angle between the direction of refraction and the neutralization direction is sufficiently large, the angular

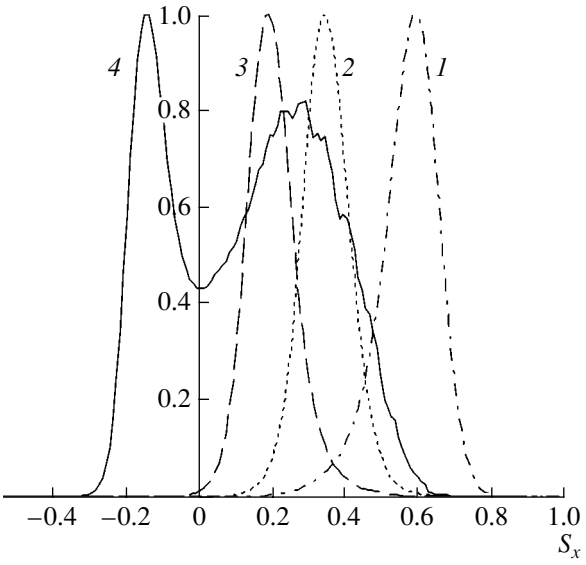

Fig. 3. Angular spectra of the multiply scattered radiation in a plasma slab with the parameters $u = 0.22$, $v = 0.28$, and $s = 0.0053$ at a distance of $\sigma_s|_{\theta=0} \cdot H = 50$ from the plasma boundary for $L_f/\lambda = 100$, the angle of inclination of the magnetic field being $\theta_0 = 40°$. In this and other subsequent figures, the abscissa represents the parameter $S_x = k_x/k$. All the spectra are normalized to their peak values. Curves *1*, *2*, *3*, and *4* were calculated for angles of refraction equal to 40°, 23.5° (the neutralization direction for the ordinary wave in question), 10°, and –10°, respectively.

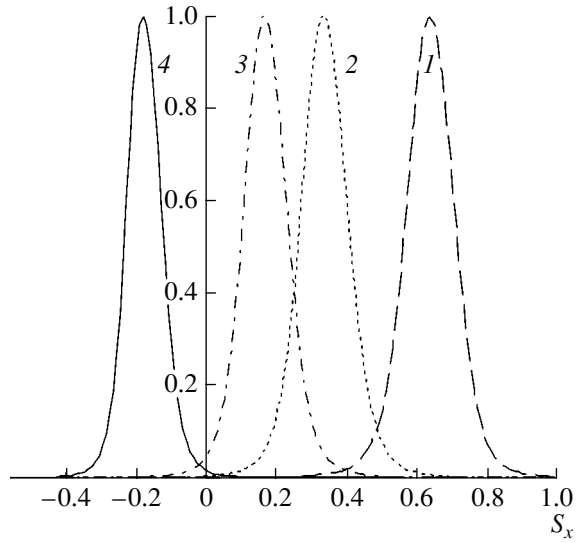

Fig. 4. Angular spectra of the multiply scattered radiation in a plasma slab with the parameters $u = 0.22$, $v = 0.28$, and $s = 0$ at a distance of $\sigma_s|_{\theta=0} \cdot H = 50$ from the plasma boundary for $L_f/\lambda = 100$, the angle of inclination of the magnetic field being $\theta_0 = 40°$. All the spectra are normalized to their peak values. Curves *1*, *2*, *3*, and *4* were calculated for angles of refraction equal to 40°, 20°, 10°, and –10°, respectively.

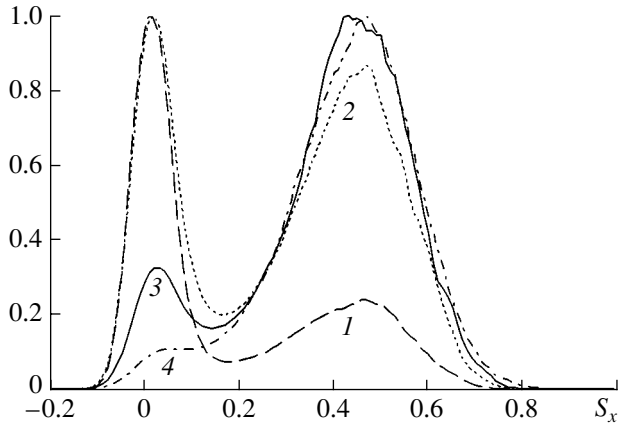

Fig. 5. Angular spectra of the multiply scattered radiation in a plasma slab with the parameters $u = 0.22$, $v = 0.28$, and $s = 0.0053$ at a distance of $\sigma_s|_{\theta=0} \cdot H = 60$ from the plasma boundary for $L_f/\lambda = 100$, the angle of inclination of the magnetic field being $\theta_0 = 60°$. All the spectra are normalized to their peak values. Curves *1*, *2*, *3*, and *4* were calculated for a wave incident normally on the slab and for the values $g = -3.2$, -2.9, -2.6, and -2.3 of the power index of the electron density fluctuation spectrum.

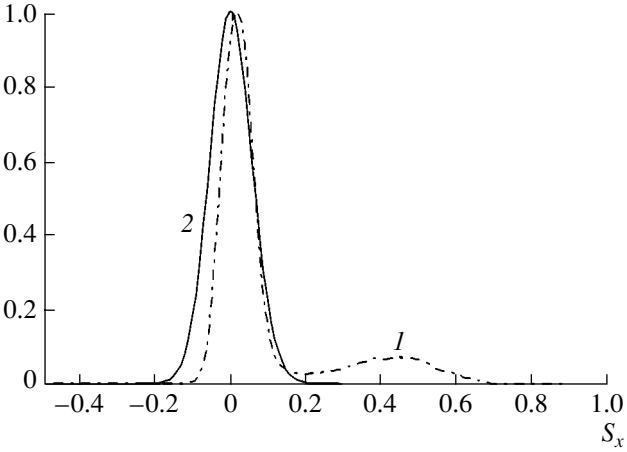

Fig. 6. Angular spectra of the multiply scattered radiation in a plasma slab with the parameters $u = 0.22$, $v = 0.28$, and $s = 0.0053$ at a distance of $\sigma_s|_{\theta=0} \cdot H = 60$ from the plasma boundary for $L_f/\lambda = 100$, the angle of inclination of the magnetic field being $\theta_0 = 60°$. All the spectra are normalized to their peak values. Curve *1* corresponds to a power-law electron density fluctuation spectrum with the index $g = -3.5$, and curve *2* refers to a Gaussian fluctuation spectrum. In both cases, the wave is incident normally onto the slab and the dispersion of the fluctuation spectra is the same.

spectrum in the transitional and deep-penetration regimes is formed by the strongly scattered radiation. The shape of the single-scattering indicatrix determines not only the shape of the angular spectrum but also the ranges of depths over which the waves propagate in the near-surface, transitional, or deep-penetration regimes, all other conditions being the same. In particular, the smaller the portion of the strongly scattered radiation in the single-scattering spectrum, the larger the penetration depth for which the geometrical-optics solution obtained perturbatively is valid. To illustrate, Fig. 6 depicts two angular spectra with the same width that were calculated for a Gaussian single-scattering indicatrix and for a single-scattering indicatrix obeying a power law with the index $g = -3.5$. Since the tails of the Gaussian indicatrix decrease very sharply with increasing scattering angle, its half-width at half-maximum is approximately three times that of the power-law indicatrix. As a result, in the Gaussian indicatrix, the portion of radiation scattered through large angles is very small in comparison to that in the power-law spectrum. This is why the resulting spectrum contains no hint of the anomalous effects and coincides fairly well with the geometrical-optics solution to first order in the parameter N_1/N_0.

6. CONCLUSIONS

Hence, analytic calculations in the small-angle scattering approximation by the methods of complex geometrical optics and a numerical analysis by statistical modeling technique have shown that, in a collisional magnetized turbulent plasma, the degree to which the absorption of electromagnetic waves influences the shape of the angular spectrum of a multiply scattered radiation depends substantially on the original direction of incidence, the angle of inclination of the magnetic field to the plasma boundary, and the spatial spectrum of fluctuations of the plasma density.

We have proposed and tested an algorithm for determining those propagation directions of the original wave at which the absorption is either weakened (the neutralization effect) or, conversely, at which the absorption is very pronounced. As an example, we carried out numerical simulations for plasma parameters close to those in the Earth's ionosphere.

Estimates show that the range of heights corresponding to the F region is not wide enough for the anomalous effects of the absorption on the angular spectrum to manifest themselves markedly; moreover, these effects are unlikely to be observed in the unperturbed ionosphere in full measure. Nevertheless, we think that the neutralization effect may well be detected in a quiet ionosphere. The shift of the centroid position of the peak in the angular power distribution of the radiation scattered in the Earth's ionosphere is also a quite readily measurable quantity. To be specific, by substituting the plasma parameters averaged along the ray trajectory into formulas (26) and (27), one can determine the direction along which the quantity $\mathrm{Im}(\partial\tilde{q}/\partial p)$ equals zero. It can be expected that this direction, being associated with the centroid position of the spectrum of the scattered radiation from a remote radio-frequency cosmic source, will coincide with (or will have a mini-

mum deviation from) the line of sight toward the source. The phenomena that have been analyzed above may also become quite readily observable in the presence of strong artificial or natural perturbations in the Earth's ionosphere when the plasma density and the collision frequency increase considerably.

ACKNOWLEDGMENTS

This work was supported in part by the Russian Foundation for Basic Research under the Leading Scientific Schools program (project no 0015-96741, the scientific school of V.A. Zverev and N.S. Stepanov).

REFERENCES

1. V. L. Ginzburg, *The Propagation of Electromagnetic Waves in Plasmas* (Nauka, Moscow, 1967; Pergamon, Oxford, 1970).
2. V. N. Tsytovich, *Theory of Turbulent Plasma* (Atomizdat, Moscow, 1971; Plenum, New York, 1974).
3. A. Z. Dolginov, Yu. Ya. Gnedin, and N. A. Silant'ev, *Propagation and Polarization of Radiation in Space* (Nauka, Moscow, 1979).
4. B. N. Gershman, L. M. Erukhimov, and Yu. Ya. Yashin, *Wave Phenomena in the Ionosphere and Space Plasma* (Nauka, Moscow, 1984).
5. *Optics of Ocean*, Ed. by A. S. Monin (Nauka, Moscow, 1983), Vol. 1.
6. L. S. Dolin and I. M. Levin, *Theory of Underwater Vision (Handbook)* (Gidrometeoizdat, Leningrad, 1991).
7. L. S. Dolin, Dokl. Akad. Nauk SSSR **260**, 1344 (1981) [Sov. Phys. Dokl. **26**, 976 (1981)].
8. V. S. Remizovich and Sh. A. Shekhmamet'ev, Izv. Vyssh. Uchebn. Zaved., Radiofiz. **33**, 202 (1990).
9. É. P. Zege, I. N. Polonskiĭ, and L. I. Chaĭkovskaya, Izv. Akad. Nauk SSSR, Fiz. Atmos. Okeana **23**, 486 (1987).
10. V. G. Gavrilenko and S. S. Petrov, Izv. Vyssh. Uchebn. Zaved., Radiofiz. **28**, 1408 (1985).
11. A. V. Aistov, V. G. Gavrilenko, and S. S. Petrov, Izv. Akad. Nauk SSSR, Fiz. Atmos. Okeana **27**, 297 (1991).
12. V. G. Gavrilenko and S. S. Petrov, Waves Random Media **2**, 237 (1992).
13. A. V. Aistov and V. G. Gavrilenko, Opt. Spektrosk. **72**, 672 (1992) [Opt. Spectrosc. **72**, 360 (1992)].
14. A. V. Aistov and V. G. Gavrilenko, Fiz. Plazmy **22**, 712 (1996) [Plasma Phys. Rep. **22**, 643 (1996)].
15. V. G. Gavrilenko, A. A. Semerikov, and V. G. Jandieri, Waves Random Media **9**, 427 (1999).
16. A. V. Aistov, V. G. Gavrilenko, and G. V. Dzhandieri, Izv. Vyssh. Uchebn. Zaved., Radiofiz. **42**, 1165 (1999).
17. V. G. Gavrilenko, S. S. Petrov, A. A. Semerikov, *et al.*, Izv. Vyssh. Uchebn. Zaved., Radiofiz. **43**, 28 (2000).
18. V. G. Gavrilenko and A. V. Sorokin, Izv. Vyssh. Uchebn. Zaved., Radiofiz. **45**, 963 (2002).
19. L. A. Apresyan and Yu. A. Kravtsov, *Theory of Radiative Transfer: Statistical and Wave Aspects* (Nauka, Moscow, 1983).
20. S. M. Rytov, Yu. A. Kravtsov, and V. I. Tatarskiĭ, *Introduction to Statistical Radiophysics* (Nauka, Moscow, 1974).
21. S. M. Ermakov and G. A. Mikhaĭlov, *Statistical Modeling* (Nauka, Moscow, 1982).
22. *Plasma Electrodynamics*, Ed. by A. I. Akhiezer, I. A. Akhiezer, R. V. Polovin, *et al.* (Nauka, Moscow, 1974; Pergamon, Oxford, 1975).

Translated by O.E. Khadin

Plasma Physics Reports, Vol. 31, No. 7, 2005, pp. 616–620. Translated from Fizika Plazmy, Vol. 31, No. 7, 2005, pp. 667–672.

LOW-TEMPERATURE PLASMA

The Properties of High-Current High-Pressure Discharges

É. A. Azizov, S. A. Kravchenko, and S. G. Solodovnikov

Troitsk Institute for Innovation and Fusion Research, Troitsk, Moscow oblast, 142090 Russia

Received September 14, 2004

Abstract—The properties of high-current high-pressure gas discharges (I = 60 kA, p = 1 atm, $\tau_{1/2}$ = 1.6 ms, $r \sim 10$ cm) just before the end of the discharge are investigated experimentally. It is shown that the anomalously high rate of gas cooling after the current is switched off is related to the turbulent hydrodynamic processes induced by the Rayleigh–Taylor instability at the discharge boundary in the stage of volume radiative cooling of the discharge channel. The turbulent thermal conductivity is estimated using experimental data on the recovery of the electric strength of the discharge gap. © *2005 Pleiades Publishing, Inc.*

1. INTRODUCTION

Direct measurements of free high-current high-pressure discharges have shown that the rate of electric-strength recovery (ESR) in the discharge gap after the current is switched off exceeds the rate of diffusion processes [1, 2] by several orders of magnitude. This effect finds a natural explanation in the case of low-pressure ($p < 0.1$ atm) low-current ($I < 1$ A) discharges, in which the plasma is highly nonequilibrium [3] and the fast ESR is provided by volume recombination. However, the higher the pressure and current, the closer the plasma is to equilibrium, and at $p \sim 1$ atm and $I \sim 10^3$ A, the plasma state is usually close to a local thermodynamic equilibrium (though it somehow depends on the gas mixture composition) [3]. For discharges with such high values of p and I (they are generally called high-current high-pressure discharges), the electric strength is recovered due to the cooling of the entire mass of the gas heated during the discharge. In the absence of current and any other forced action (e.g., forced air cooling), the cooling of the gas in the discharge channel is determined by the state of the gas itself before the current is switched off. Hence, it is necessary to examine the discharge structure and the related physical processes just before the end of the discharge. In this paper, we present and analyze the results of such investigations.

The preextinction stage can be conveniently examined by considering so-called "subsonic" free discharges with a characteristic current growth rate of $dI/dt \sim 10^8$ A/s [4]. In such discharges, the hydrodynamic flow velocities are lower than the speed of sound, the ponderomotive forces are of minor importance, and the gas pressure is quite uniform. Under certain conditions, a cylindrically symmetric discharge with a fairly wide current-carrying channel can be produced. This allows one to use probe diagnostics; as a result, the reliability of the results obtained increases significantly.

"Slow" discharges display features characteristic of steady-state free arcs, which are dominated by turbulent convection at the interface with a cold ambient gas. Such convection disturbs the shape of the discharge and significantly complicates its inner structure [5].

In discharges with high current growth rates ($dI/dt \geq 10^{10}$ A/s), nonlinear hydrodynamic phenomena related to the formation of intense shock waves become important and instabilities caused by the high magnetic pressure arise [6].

2. EXPERIMENTAL SETUP AND MEASUREMENT TECHNIQUE

A schematic of the experimental setup is shown in Fig. 1. The discharge is supplied from capacitor bank C, which is connected to the discharge circuit via spark gap SG. Inductance L serves to form a current pulse of required duration. The discharge chamber is a sealed stainless-steel cylinder with a diameter of 46 cm. Along its axis, two electrodes in the shape of truncated cones with major and minor diameters of 70 and 55 mm are installed. At the side wall of the chamber, there are openings for probe diagnostics and four viewing windows.

The discharge was ignited by exploding a 0.1-mm-diameter copper wire set between the electrodes along their axis. Special experiments showed that perturbations introduced during such ignition into the discharge structure rapidly decayed. Thorough studies of another ignition technique with the use of a slipping arc dis-

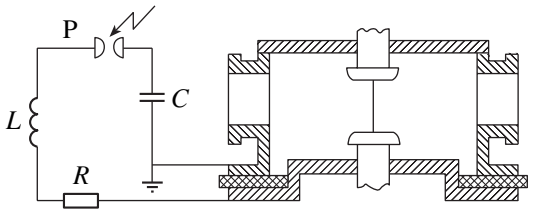

Fig. 1. Schematic of the experimental setup.

1063-780X/05/3107-0616$26.00 © 2005 Pleiades Publishing, Inc.

charge [7] showed that the discharge features were almost similar to those observed in our study.

The discharge current was measured using a coaxial shunt, and the arc voltage was measured using a resistive divider. The spatial distribution of the magnetic field generated by the discharge current was measured by magnetic probes, and the electric field was measured by double passive electric probes (see [8] for details).

The total radiation energy emitted from the discharge was measured with a calorimeter, and the time evolution of the emission intensity was determined with the use of an electrodynamic shutter.

The discharge was photographed with a fast framing camera through the viewing windows of the discharge chamber. The arc plasma temperature was determined from spectral measurements by the method of relative intensities.

The ESR process was studied using a double active electric probe by a method similar to that used in [1]. The measurements began after the discharge current was switched off. The voltage applied to the two probe electrodes was increased until either the probe current or the voltage reached its critical value, I_m or U_m, respectively. As either of these critical values was achieved, the voltage abruptly (over a time much less than its rise time) dropped to zero. After a certain pause needed for the relaxation of the excessive charge around the probe, the voltage was increased again. This process was repeated many times. The time during which the envelope of the voltage pulses arrived at the plateau $U = U_m$ was identified as the time t_u required for the recovery of a given electric strength unambiguously determined by the U_m value. The cutoff current I_m was chosen such that the energy deposited by the probe voltage pulses was much smaller than the energy stored in the plasma. An electronic circuit enabling such an algorithm is described in detail in [9].

The measurements were performed in the central cross section (equally distant from the discharge electrodes). The probe electrodes were set parallel to the discharge axis at the same distance r from it. The bare ends of the electrodes made of 1-mm-diameter wire were separated by a distance of $z = 2$ cm. In our experiments, the critical values of the probe voltage and current were $U_m = 18$ kV and $I_m \approx 2$ mA, respectively.

The value of t_u depends on the gap length z. For $z <$ 7 mm, an electric breakdown of a cold gas occurred. For $z \geq 1$ cm, the scatter in the times during which the envelope of the voltage pulses arrived at the plateau did not exceed the measurement error (~10%). This effect may be attributed to the fact that the distribution of the electric field between the probe electrodes is highly nonuniform. The field is maximum near the electrodes and depends slightly on the distance between them if this distance is much larger than the probe radius.

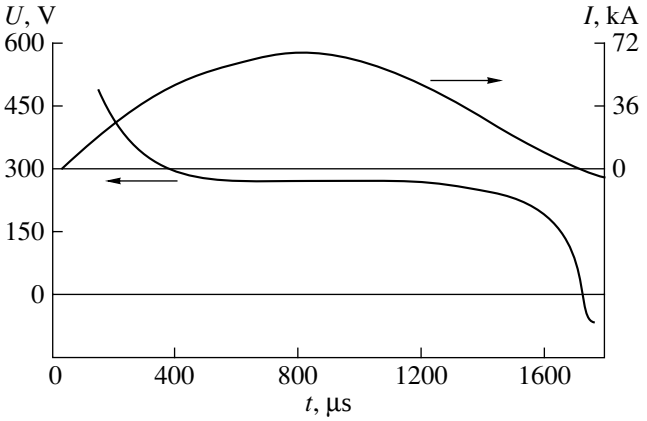

Fig. 2. Waveforms of discharge current and voltage.

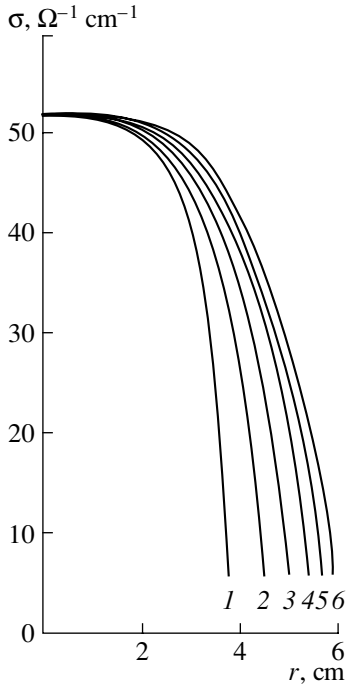

Fig. 3. Radial profiles of the discharge plasma conductivity $\sigma(r, t)$ at t = (*1*) 300, (*2*) 400, (*3*) 500, (*4*) 600, (*5*) 700, and (*6*) 800 μs.

3. EXPERIMENTAL RESULTS

Our experiments were performed at $C = 1.6 \times 10^{-2}$ F and $L = 1.6 \times 10^{-5}$ H. The initial stored energy was 70 kJ, the active resistance of the discharge circuit was $R = 1.5 \times 10^{-2}$ Ω, and the interelectrode distance was 12 cm. The working gases were nitrogen and air at atmospheric pressure. The inner structure and current–voltage characteristics of electric discharges in these gases are very similar. Thereafter, unless otherwise indicated, the results from experiments with nitrogen are presented.

The data obtained with two fast framing cameras oriented at a right angle to one another in the plane per-

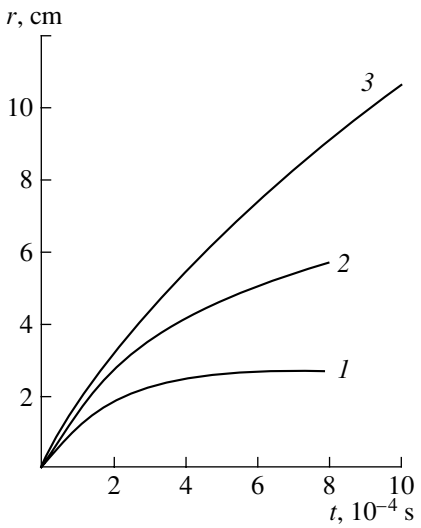

Fig. 4. Time evolution of the boundaries of plasmas with different conductivities: σ = (*1*) $0.9\sigma_{max}$, (*2*) $0.2\sigma_{max}$, and (*3*) $2 \times 10^{-6}\sigma_{max}$ where $\sigma_{max} = 55\ \Omega^{-1}\ cm^{-1}$.

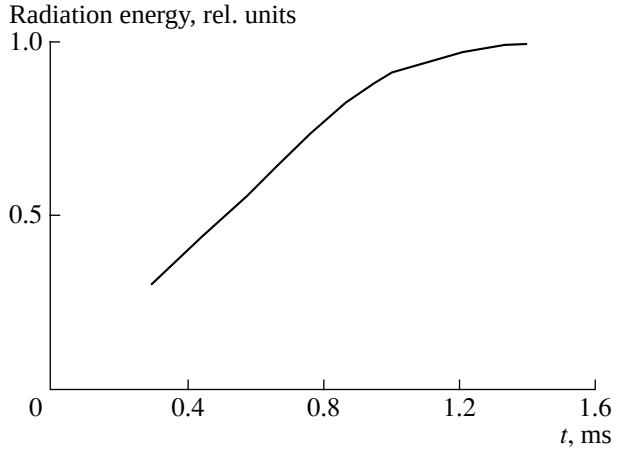

Fig. 5. Total radiation energy emitted from a discharge vs. time.

pendicular to the chamber axis show that the glowing part of discharge is nearly cylindrical in shape and its radius increases in time. The axial symmetry of the discharge is also confirmed by the data from magnetic probes installed in the same plane at an angle of 120° to one another.

Figure 2 shows waveforms of the discharge current and voltage. The shape of the current pulse is close to a sinusoid with an amplitude of 60 kA and a half-period of 1.6 ms. The voltage spike at the initial instant is attributable to the breakdown caused by the explosion of the copper wire. At $t \sim 300$ μs, the voltage decreases to 240 V and remains almost constant up to $t \sim 1000$ μs. After this, it gradually decreases and then drops to zero together with the current.

The data from magnetic and passive electric probes were used to determine the time evolution of the radial profile of the plasma conductivity $\sigma(r, t)$ (Fig. 3). The time evolution of the plasma boundaries with different σ values is shown in Fig. 4. The upper curve was obtained by estimating the conductivity near the electrodes of a passive electric probe at the instant when the probe signal appeared [8].

In an equilibrium plasma, the conductivity is a function of state: for a fixed pressure, there is a one-to-one relation between the conductivity and temperature. In our case, the discharge core conductivity of $\sigma_{max} = 55\ \Omega^{-1}\ cm^{-1}$ corresponds to a temperature of $T \approx 13000$ K. This is in good agreement with the results from spectroscopic measurements, according to which the temperature of the copper vapor at the discharge axis is $T \approx 12500$ K.

Figure 5 shows the total radiation energy emitted from the discharge as a function of the time elapsed from the beginning of the discharge. The radiation energy is normalized to the energy measured by the calorimeter without a shutter when the discharge current flows for only during one half-period.

Figure 6 illustrates the dynamics of the ESR process for different rates with which the current was switched to the shunt connected in parallel to the discharge [1]. Curve *1* corresponds to a relatively fast (over a time of about 100 μs) switching at the instant of the current maximum, whereas curve *2* corresponds to a relatively slow decrease in the current during the natural development of the discharge. The electric strength of 15 kV is completely recovered over 4 ms and over about 8 ms after the fast and slow switching-off of the current, respectively.

The radial profile of the time required for the recovery of the electric strength of air when the current is switched off slowly is shown in Fig. 7. As was expected, the ESR rate is maximum at the discharge periphery and minimum at the center. For $r \le 4$ cm, this dependence has an explicit plateau.

4. DISCUSSION OF THE RESULTS

An analysis of the data from Figs. 2 and 3 shows that the transient processes related to discharge ignition decay almost completely by the time $t \sim 300$ μs. Starting from this instant, the discharge can be conditionally divided into three regions: central, intermediate, and peripheral. In the central region ($r \approx 3$–4 cm), the current density; the electric conductivity; and, accordingly, the temperature are nearly constant over space and time. The main variations in the current density and electric conductivity occur in the intermediate region, whereas in the peripheral region, the temperature decreases to the temperature of the cold ambient gas. The dimensions of all the regions increase with time. The peripheral region expands much faster than the central one (see Fig. 4). The contributions from different transfer mechanisms can be estimated using the Hellenbaas–Heller energy balance equation. It follows

from these estimates that, in the central region, the main fraction of the deposited Joule energy is carried away by freely escaping radiation [8], whereas in the intermediate region, the energy is mainly lost by heat conduction. A significant fraction (~50%) of the radiation emitted from the central region is absorbed in the peripheral region. The main mechanism for the arc expansion in this region is convection; i.e., it is related to the hydrodynamic flow of a relatively cold gas.

The behavior of a discharge in the current-rise stage was described in [10–13], which were devoted to the modeling of discharges with a current-carrying channel transparent to its own emission. In those papers, a self-consistent analytic physical model was developed that predicted all the most important discharge parameters (the electric field, the temperature, and the radius and the expansion rate of the current-carrying channel) for any growth rate of the discharge current and without making any additional assumptions about the temperature dependence of the transport coefficients. It was shown that, for each working gas, there is a region in the (I, dI/dt) phase plane that corresponds to a universal self-regulating regime of arc operation to which the discharge evolves, whatever the initial conditions were. A consequence of such self-regulation is stabilization of the discharge parameters: as the current increases by one order of magnitude, the temperature and the electric field vary by only a few tens of percent.

In the current-rise stage, a regime is established in which Joule heating and radiative cooling nearly balance one another. A decrease in the current is accompanied by a decrease in the energy deposition; this leads to a decrease in the temperature due to volume cooling. However, volume radiative losses may dominate in the energy balance only at relatively high temperatures. In atmospheric-pressure nitrogen at $T < 8000$–9000 K, this effect is almost absent. This is confirmed by direct calorimetric measurements of the total radiation energy emitted from the discharge (see Fig. 5). As was expected, radiative losses are most intense in the current-rise stage and near the current maximum and then rapidly decrease to zero.

Simple estimates show that, for laminar flows, the characteristic cooling time of a gas column with a diameter of about 10 cm and an initial temperature of 8000 K is a few tenths of a second. Hence, the observed ESR rate can be attributed only to turbulent hydrodynamic processes.

The reason for such turbulent mixing can be the onset of Rayleigh–Taylor instability at the interface between the cold and hot gases. Radiative cooling of the current-carrying channel after the current is switched off causes intense reverse gas flow. As the temperature decreases, the emission power reduces to zero and the motion of the cold gas towards the center slows down. As a result, the inertia force directed toward the center arises. This force is similar to the force of gravity exerted by a heavy gas on an underlying light gas. In this case, the gradients of the pressure and density are oppositely directed. This provokes the development of the Rayleigh–Tailor instability, which leads to the generation of, first, laminar and, then, vortex flows of the cold gas into the hot one. Finally, the flow pattern becomes chaotic; i.e., the turbulent mixing of the hot and cold gases occurs.

The process of cooling depends on which harmonics dominate during the onset of instability. When the translational energy of the cold gas is transformed into the lower harmonics with a wavelength on the order of the channel radius, the instability substantially disturbs the geometry of the discharge and leads to its fragmentation. If the energy is transferred to short-wavelength perturbations, then heat transfer immediately becomes

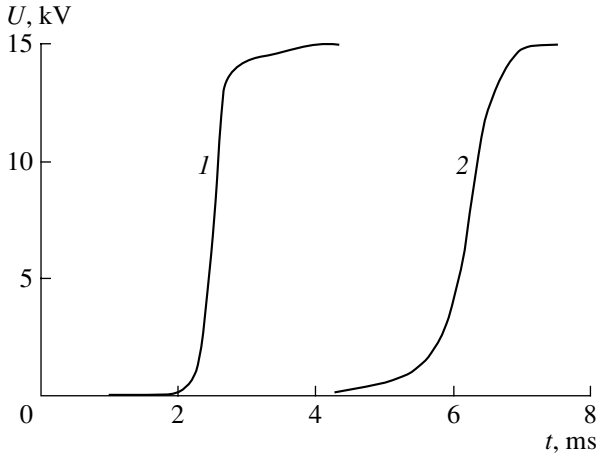

Fig. 6. ESR dynamics for two different decay rates of the discharge current.

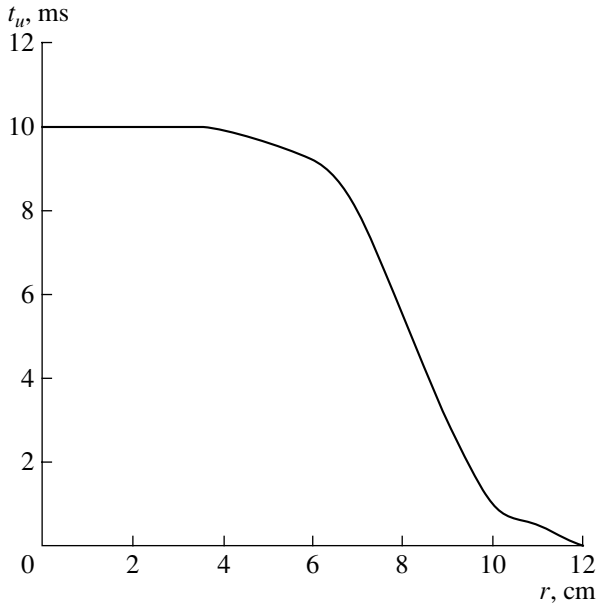

Fig. 7. The radial profile of the time t_u, needed for recovering the electric strength of air in the case where the discharge current was switched off slowly.

diffusive in character and the effective thermal conductivity λ_{eff} substantially exceeds its classical value.

The linear stage of this process was considered in [14]. The velocity of the reverse flows v and, consequently, the instability growth rate γ depend on the initial plasma temperature and the current decay rate. Under the conditions corresponding to curve *1* in Fig. 6, the velocity v reaches a few hundred meters per second and the deceleration is $dv/dt \sim 10^6$ m/s^2, which is 10^5 times higher than the gravitational acceleration near the Earth's surface. The gas density varies by two orders of magnitude, and the growth rate of the lower harmonics is $\gamma \sim 10^4$ s^{-1}.

Let us estimate λ_{eff} using the data from Fig. 7 and assuming that the gas cooling in the final stage of ESR is diffusive in character. The insufficient measurement accuracy did not allow us to resolve variations in the ESR rate in the central region ($r_c \approx 4$ cm). When cooling is caused by diffusion, the inner region is always cooled more slowly than the outer one. Hence, the time τ of heat diffusion through the central region is no longer than the experimental error $\delta t_u \sim 1$ ms in determining the ESR time. On the other hand, we have $\tau \sim r_c^2 C_p \rho/\lambda$ by definition, where C_p and ρ are the specific heat capacity and specific density of the gas, respectively. From this, we obtain the lower estimate for the sought quantity: $\lambda_{eff} \sim r_c^2 C_p \rho/\delta t_u \approx 1$ W/(cm K), which is more than 100 times higher than the thermal conductivity of air in the temperature range in which ESR begins (i.e., at $T < 4000$ K).

5. CONCLUSIONS

In this study, the properties of high-current high-pressure gas discharges have been examined using an optimal experimental model. The model incorporates all the features characteristic of the preextinction stage of high-current high-pressure discharges, whereas all the side effects hampering direct measurements and their interpretation are excluded.

The experimental results have revealed the main features of a discharge in the current rise stage. The available literature data on the mechanisms responsible for the spatiotemporal structure of a discharge are contradictory. This is partially explained by the fact that the use of optical methods for determining the radial profiles of the arc parameters is impeded by the large uncertainty in the spectral characteristics of the working mixture and by the difficulty of accounting for the absorption of radiation in cold gas layers. The fairly large dimensions of the discharge produced allowed us to use probe diagnostics, which, together with high-speed photorecording, calorimetric measurements, and parallel measurements of the gas temperature by the relative intensities of the spectral lines, furnished a clear insight into the discharge. With these data, it is much easier to study the decay stage, which begins immediately after the current is switched off, because the initial conditions of the problem are well defined.

An analysis of the data obtained has shown that the anomalously high cooling rate of the gas stems primarily from the fact that, at the very beginning of the cooling process, the radiation escapes from the central region of the discharge within a relatively short time interval. Thereafter, the instability that develops at the interface between the hot and cold gases provokes their turbulent mixing.

The data obtained have lain the basis for the development of an adequate physical model of the discharge decay. Hopefully, further experimental studies in combination with theoretical analysis and numerical simulations will provide a deeper insight into this complicated phenomenon.

The results obtained go beyond the scope of gas discharge physics and are related to an important branch of contemporary hydrodynamics—turbulent mixing. They can also be applied to the development of new types of arc switches.

REFERENCES

1. N. A. Akhmerov, V. A. Vorob'ev, Yu. G. Gendel, and I. P. Shed'ko, in *Proceedings of the 6th International Conference on Switching Arc Phenomena, Lodz, 1989*, Part II, p. 114.
2. E. P. Bel'kov, Zh. Tekh. Fiz. **44**, 1946 (1974) [Sov. Phys. Tech. Phys. **19**, 1210 (1974)].
3. V. L. Granovskiĭ, *Electric Current in a Gas* (Gostekhteoretizdat, Moscow, 1952), Vol. 1.
4. V. I. Petrenko and R. V. Mitin, Zh. Tekh. Fiz. **45**, 1225 (1975) [Sov. Phys. Tech. Phys. **20**, 765 (1975)].
5. V. L. Granovskiĭ, *Electric Current in a Gas: Steady-State Current* (Nauka, Moscow, 1971).
6. A. F. Aleksandrov and A. A. Rukhadze, *Physics of High-Current Electric-Discharge Light Sources* (Atomizdat, Moscow, 1976).
7. É. A. Azizov, N. A. Akhmerov, G. G. Gladush, and I. P. Shed'ko, Teplofiz. Vys. Temp. **22**, 655 (1984).
8. Yu. Yu. Abramov, É. A. Azizov, N. A. Akhmerov, *et al.*, Preprint No. 4169/7 (Kurchatov Inst. of Atomic Energy, Moscow, 1985).
9. E. A. Kuznetsov, S. A. Kravchenko, V. A. Yagnov, and I. Ya. Shipuk, Prib. Tekh. Éksp., No. 2, 64 (1997).
10. Yu. Yu. Abramov, É. A. Azizov, and S. G. Solodovnikov, Preprint No. 4243/7 (TsNIIatominform, Moscow, 1986).
11. Yu. Yu. Abramov, É. A. Azizov, and S. G. Solodovnikov, Preprint No. 4504/6 (TsNIIatominform, Moscow, 1987).
12. Yu. Yu. Abramov, É. A. Azizov, and S. G. Solodovnikov, Dokl. Akad. Nauk SSSR **295**, 353 (1987) [Sov. Phys. Dokl. **32**, 578 (1987)].
13. Yu. Yu. Abramov, É. A. Azizov, and S. G. Solodovnikov, Fiz. Plazmy **15**, 97 (1989) [Sov. J. Plasma Phys. **15**, 57 (1989)].
14. Yu. Yu. Abramov, É. A. Azizov, and S. G. Solodovnikov, Fiz. Plazmy **15**, 1128 (1989) [Sov. J. Plasma Phys. **15**, 655 (1989)].

Translated by N.N. Ustinovskiĭ